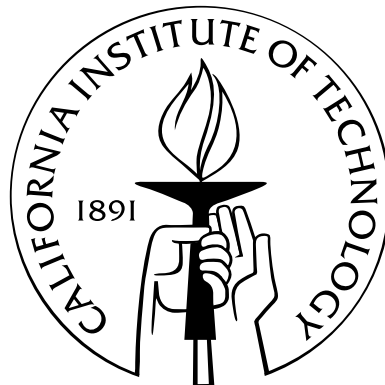# Towards a Quantum Network with Atomic Ensembles

Thesis by

Chin-wen Chou

In Partial Fulfillment of the Requirements

for the Degree of

Doctor of Philosophy

California Institute of Technology

Pasadena, California

2006

(Defended May 22, 2006)

ii

Acknowledgements

I would like to thank all those who made this work possible. People worked with me on the experiments: Jeff, Alex, Warwick, Andreea, Dave, Sergey, Daniel, Hugues, Julien, and Erik; and all other members of the Caltech Quantum Optics Group, past and present: Akira, Tiancai, Win, Peter, Jason, Joe, Theresa, Kevin, Tracy, Russ, Takao, Barak, Liz, Dal, and Andrey. Of course I will not forget the great help from our theorists friends: Lumin and Steven. To all of you, I would like to say: thank you, it has been great working with you!

Abstract

The experiments discussed in this thesis investigate the application of atomic ensembles in building a quantum network. Specifically, the atomic ensembles refer to cesium atoms trapped and cooled in magneto-optical traps.

Chapter 1 gives a general introduction to quantum networks, along with the difficulty in extending the range due to the optical loss of communication channels, e.g., optical fibers.

Chapter 2 describes the protocol proposed by Duan, Lukin, Cirac, and Zoller (DLCZ) for overcoming the limit of channel loss on scaling up a quantum network, exploiting relatively simple setups with atomic ensembles. The protocol introduces many capabilities and simplifies many tasks in quantum information processing with atoms and light. The scaling of the required resources with the range of the network is also discussed.

Chapter 3 summarizes the first step in our lab toward realizing the DLCZ protocol. In particular, we observed nonclassical correlation between two optical fields generated from one atomic ensemble.

Chapter 4 is a sidetrack apart from the DLCZ protocol. We demonstrated that the atomic ensemble can be used as a conditional source of single photons. In addition

to a description of the experiment, details of the simple model we used to fit the data are also included.

Chapter 5 augments chapter 4 in that the temporal behavior of the nonclassical correlation is investigated. We found that the correlation decayed rapidly, which is a major obstacle for further implementation of the DLCZ protocol.

Chapter 6 describes our effort to fight the fast decay of correlation observed in the experiment. A theoretical model is used to better understand the source of decoherence.

Chapter 7 is the follow-up in the direction of implementing the DLCZ protocol. Two atomic ensembles located in vacuum chambers on two optical tables are entangled in a heralded fashion. The details on controlling the phases of the interferometers and data processing are elaborated.

Chapter 8 is a practical proposal on how to proceed further toward realization of the DLCZ protocol. Four atomic ensembles are involved in the proposed setup, which merely requires relative phase stability.

Chapter 9 concludes the thesis and provides several possible directions toward building a large-scale quantum network through the DLCZ protocol.

Contents

List of Figures

xviii

List of Tables

Chapter 1

Introduction

1.1 Introduction to the quantum network

The quantum network is a fast-growing field in quantum information science. Specifically, a quantum network will consist of quantum nodes connected by quantum channels. The quantum nodes generate, process, and store information encoded in the quantum states of physical systems. The information is exchanged through quantum channels by way of sending photons from one node to the other, or through quantum entanglement shared by the nodes.

The ability to distribute quantum resources over long distances is a key element for the development of several practical applications in the field of quantum information [1]. Major efforts have been made in the past decade to extend the maximum distances for the observation of entanglement or for the realization of quantum cryptography between remote nodes in a quantum network. Using optical fibers as the quantum channel, entanglement has already been achieved between photons separated by 50 km of fiber [2], and quantum cryptography is now a commercial technology [3] that allows quantum key distribution over distances up to around 100 km [4, 5]. Progress has also been made toward entanglement distribution in free space, with the achieved distances of about 10 km in ground atmosphere [6, 7] being a substantial step toward the development of satellite-based quantum communication [8, 9].

1.2 Overcoming the limit on the range of a quantum network

In spite of all these developments, the quantum communication protocols that have been tested up to now suffer from some fundamental limitations on the maximum achievable distance [10]. The problem is the absorption of photons in the quantum channel, which grows exponentially with the length of the channel. In classical communication, the attenuation problem is solved in a straightforward way by amplification of the signal. It is not possible, however, to generate perfect copies of unknown quantum states [11], which prevents the amplification techniques from being used for quantum communication.

A first step to solve this problem was the development of techniques for entanglement purification [12, 13]. These techniques were inspired by quantum algorithms for error correction, and are designed to obtain a set of transmitted states of high fidelity (i.e., high overlap with a maximally entangled state) out of a larger set with lower fidelity, if this fidelity is still above a certain value F_{min}. Based on these ideas, a solution for the long-distance problem in quantum communication was then formulated with the development of the concept of the quantum repeater [14, 15]. The idea is to divide the quantum channel in several segments with lengths that allow the transmission of quantum states with fidelity $F > F_{min}$, and then apply the entanglement purification algorithms in a hierarchical way, beginning with shorter seqments and going up to longer ones until a high fidelity is obtained for the entanglement of pairs of particles located on the extremes of the communication channel. The connection be-

tween the different segments is done by entanglement swapping [16, 17]. The essential advantage of the quantum repeater protocol is that the number of trials to entangle a pair of particles grows only polynomially with the distance, not exponentially as in the protocols usually used for quantum communication.

The development of quantum repeaters, however, introduces new challenges that need to be addressed. It is necessary to entangle distant qubits, store them over operational time scales, and perform collective local operations on several of these qubits. Quantum memory is essential, since all entanglement purification protocols have a probabilistic nature. If the system had no memory, the purification of all segments would have to succeed at the same time for the algorithm to work, which is improbable. The requirement of quantum memory implies, in practice, that the local qubits need to be stored in atomic internal states. Since the communication between distant sites still needs to be done by photons, a quantum repeater should rely on systems that present strong atom-photon coupling. Usually this strong coupling is obtained with the aid of high finesse cavities, in the field known as Cavity Quantum Electrodynamics (CQED). However, in spite of important recent advances [18, 19], these techniques still require a reasonably complicated experimental setup, which could prevent the application on a larger scale of quantum communication and error correction protocols for CQED, as the ones described in Refs. [20] and [21], respectively.

This was the context in which Duan, Lukin, Cirac and Zoller (DLCZ) proposed an alternative protocol [22] for the implementation of quantum repeaters with atomic ensembles, which would require a much simpler experimental apparatus. The DLCZ protocol introduces many novel ideas, including the physical process that couples light

to atoms, the way entanglement is achieved between distant atomic ensembles, and the details of the entanglement purification process. The DLCZ protocol is explained in detail in Chapter 2.

Chapter 2

The Duan-Lukin-Cirac-Zoller (DLCZ) Protocol

2.1   Outline

In this chapter the theoretical framework of the Duan-Lukin-Cirac-Zoller (DLCZ) protocol is elaborated. In Sec. 2.2, a widely exploited principle, the superposition from indistinguishability, is discussed. This provides an intuitive approach to understanding the protocol. Sec. 2.3 describes the key idea of the protocol: generation of light fields sharing quantum mechanical correlation with an ensemble of atoms. Secs. 2.4 and 2.5 explain the ways to exploit the correlation, including entangling two ensembles and extending the range of entanglement by entanglement swapping.

2.2   Superposition from indistinguishability

In quantum mechanics, if there is more than one possible pathway for a physical event to occur, and the pathways are in principle indistinguishable, the probability for that event to take place can be obtained by summing the probability amplitudes corresponding to the various pathways and taking the square of the absolute value. Feynman is the one who uses this concept the most. His path integral approach to quantum electrodynamics utilizes the concept to the extreme. This concept can also be applied when one tries to determine the quantum state of a physical system. If after some evolution, the system can end up in several states which are, even in principle, indistinguishable, the system is in a coherent superposition of all the possible states, with the coefficients reflecting the probabilities of each state. For instance, consider an atom that is initially in an excited state with two radiatively allowed (equally probable) decay paths and thus two possible final states (Fig. 2.1). After the atom
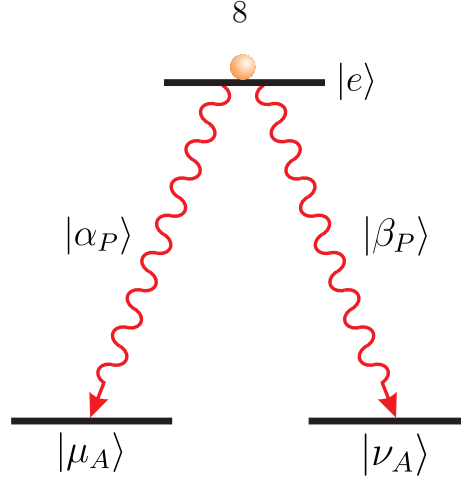
Figure 2.1: Two possible decay paths for an atom. State $|e\rangle$ denotes the excited state of the atom. States $(|\alpha_P\rangle, |\beta_P\rangle)$ and $(|\mu_A\rangle, |\nu_A\rangle)$ stand for the possible final states of the emitted photon and the atom, respectively.

decays to the ground states and emits a photon, the state of the system composed of the atom and the emitted photon can be written as:

$$|\Psi\rangle = \frac{1}{\sqrt{2}}\Big(|\alpha_P\rangle|\mu_A\rangle + e^{i\phi}|\beta_P\rangle|\nu_A\rangle\Big), \tag{2.1}$$

where each term stands for the final state of the atom (A) and the emitted photon (P) for the two possible decay paths. This concept provides an intuitive way to gain insight in the quantum communication protocol proposed by Duan, Lukin, Cirac, and Zoller.

2.3 Light-atoms coupling in DLCZ protocol

2.3.1 Introduction: an intuitive approach

In the DLCZ protocol [22], the authors consider an ensemble of N_a identical atoms with lambda-type energy level configuration as shown in Fig. 2.2. Initially all the

atoms are prepared in the ground state, $|g\rangle$. A weak light pulse near resonant with the $|g\rangle \rightarrow |e\rangle$ transition, called the write pulse, illuminates the atoms and generates a forward-scattered field, field 1, near resonant with the $|e\rangle \rightarrow |s\rangle$ transition through spontaneous Raman scattering. The field 1 can have different polarization or frequency from the write pulse. If a photon is scattered into field 1, an atom is transferred to $|s\rangle$. However, the spatial modes of the write pulse and collection optics for field 1 are arranged in such a way that it is impossible to tell which atom is transferred since all the atoms illuminated by the weak write pulse are equally probable to create the forward-scattered photon. Thus in the event of one photon scattered into field 1, the state of the atoms is

$$|1_a\rangle = \frac{1}{\sqrt{N_a}} \sum_{i=1}^{N_a} |g\rangle_1 \cdots |s\rangle_i \cdots |g\rangle_{N_a}, \tag{2.2}$$

which is a superposition of all the possible final states with one of the atoms transferred to $|s\rangle$. Similarly, we can get the state of the atoms when more than one photon is scattered into field 1. The states are denoted as $|2_a\rangle$, $|3_a\rangle$, etc. When no photon is scatted into field 1, the atoms are all in the initial state, $|g\rangle$. In this case, the state of the atoms is $|0_a\rangle \equiv \bigotimes_i^{N_a} |g\rangle_i$.

Denote as p the probability of a photon scattered into field 1 by the atoms illuminated by the weak light pulse (write pulse). Then the probability of two photons scattered into field 1 is just p^2, since the events are independent from each other. Before any measurement, it is impossible, even in principle, to know the number of photons excited in field 1. Along with the observation above that a $|g\rangle \rightarrow |s\rangle$ transfer
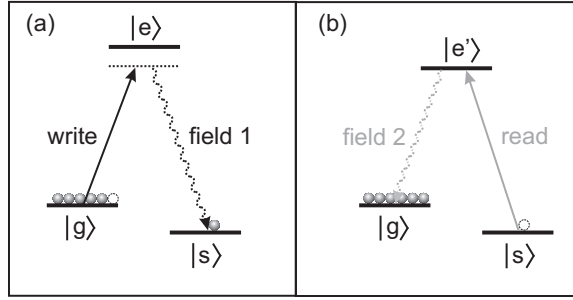
Figure 2.2: Relevant level structure of the atoms in the ensemble for (a) writing and (b) reading processes. In this chapter, the (write, read) pulses and the scattered (1, 2) fields are represented by solid (black, gray) and wavy dashed (black, gray) lines, respectively.

accompanies a scattered photon, after illumination of the write pulse, the state of the ensemble-field system should be of the form

$$|\phi\rangle \propto |0_a\rangle|0_1\rangle + e^{i\beta}\sqrt{p}\,|1_a\rangle|1_1\rangle + O(p), \tag{2.3}$$

which is a superposition of states with various numbers of photons created in field 1 along with the corresponding numbers of atoms transferred to $|s\rangle$, with the coefficients corresponding to the square roots of the probabilities each term would occur. In Eq. (2.3), $|n_1\rangle$ stands for the state of the forward-propagating light field, field 1, with n excitations, and β is an phase that is determined by that of the write pulse. Note that $|\phi\rangle$ is an entangled state between the ensemble and field 1.

2.3.2   Details from the protocol

The metastable lower states $|g\rangle$ and $|s\rangle$ can be, e.g., hyperfine or Zeeman sublevels of the electronic ground state of alkali-metal atoms, thus ensuring a long coherence lifetime.

A key element of the protocol is the collective enhancement of the spontaneous Raman scattering in a forward direction, which is determined by the spatial mode of the laser pulse and the geometry of the addressed region [23]. The spatial distribution of the atoms contributing to Raman scattering and transferred from $|g\rangle$ to $|s\rangle$ can be understood in the same way one understands the distribution of photons in light. The transferred atoms can be distributed in various ways (spatial modes) in the region addressed by the write field, and the quantum state of the atoms can be in various forms. The states in the form of superpositions of all possibilities for n atoms being transferred, with Eq. (2.2) as an example ($n = 1$), are called symmetrical collective states [22, 23] (or dark-state polaritons [24, 25]). If the atoms are in this kind of state and distributed in a region of pencil shape, the scattered field will be concentrated in the elongated direction, in which the amplitudes of scattering from each atom add up coherently (thus the term "collective enhancement"). States of other forms, even with the atoms in the same region, do not show this enhanced emission in a particular direction. Therefore the detection of photons in the forward direction is highly correlated with the case in which the atoms are prepared in the symmetrical collective states. After the detection, the atoms might end up in a state different from the symmetrical collective states, but with much lower probability. If the addressed region is not elongated, one can define a cylindrical region in the addressed region using the imaging system for the detection of photons in field 1 [26, 27, 28]. A detection event "click" then heralds that the atoms in the imaged cylinder are prepared in the state (2.2) with high probability.

By sending in a second ("read") pulse resonant with the $|s\rangle \rightarrow |e'\rangle$ transition, the

symmetrical collective state of the atomic ensemble can be transferred (read out) to another forward-propagating light field 2 at the $|e'\rangle \to |g\rangle$ transition (see Fig. 2.2(b)). The readout can be achieved with high efficiency due to the collective effect that the probability amplitude of all the atoms returning to the original state $|g\rangle$ is enhanced by the number of atoms. In this way, it is possible to access the quantum state of the atoms. For resonant excitation, the reading process is closely related to low-light-level Electromagnetically Induced Transparency [25, 29]. The case in which $|e\rangle = |e'\rangle$ is called, in the following Chapters, a three-level scheme of excitation, while for four-level excitation shemes, $|e\rangle \neq |e'\rangle$. Note also that the resultant state of the two forward-scattered modes (1,2) can be written, in the ideal case, as

$$|\phi_{1,2}\rangle = |0_1\rangle|0_2\rangle + e^{i\beta'}\sqrt{p}\,|1_1\rangle|1_2\rangle + O(p), \tag{2.4}$$

where β' takes into account the additional phase introduced in the readout process. The photon numbers in the two modes are correlated so that $|\phi_{1,2}\rangle$ is an entangled state, precisely as in the case of parametric down conversion [30].

We have experimentally demonstrated the generation of the two forward-scattered fields from an atomic ensemble and verified the nonclassical correlation between them, as described in Chapter 3. The correlation between the photon numbers in the two fields can be exploited to generate single photons in field 2 conditioned on the detection events in field 1 (Chapter 4). The temporal dynamics of the generation of single photons from an ensemble is studied in Chapter 5.
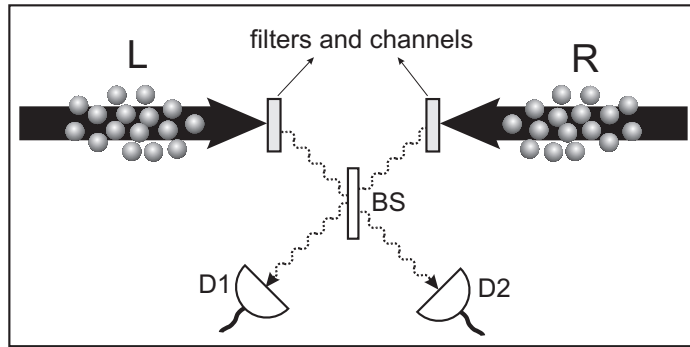
Figure 2.3: Setup for generating entanglement between two atomic ensembles L and R. The ensembles are pencil shaped, and excited by synchronized write pulses. After filtering, the scattered fields are collected and coupled to optical channels. The pulses after the transmission channels interfere at a 50-50 beam splitter BS, with outputs directed towards two single-photon detectors D_1 and D_2. Ideally, if D_1 or D_2 records a detection event, the process is finished and entanglement is successfully generated. Otherwise, the system is restored to its initial state and the process is repeated until D_1 or D_2 records a click.

2.4   Entangling two ensembles

2.4.1   Intuitive approach

After establishing the correlation between the number of photons in field 1 and the number of atoms transferred to $|s\rangle$, the state in Eq. (2.3) can be exploited to create entanglement between two ensembles of atoms. We send two write pulses into two ensembles, L and R, combine the respective fields 1 on a 50-50 beam splitter, and monitor the two output ports with two single-photon detectors capable of registering single photons (Fig. 2.3). If one of the detectors registers a photo-electric event ("click"), we know that at least one photon has been emitted from the ensembles and thus at least one excitation is created. In the ideal case, with the beam splitter, the information about which ensemble has the excitation is inaccessible. Thus the state of the two ensembles is the coherent superposition of the cases where either ensemble

has the excitation. Specifically, in the ideal case, the state can be written as:

$$|\phi_{L,R}\rangle = \frac{1}{\sqrt{2}} \left(|0_a\rangle_L|1_a\rangle_R \pm e^{i\eta_1}|1_a\rangle_L|0_a\rangle_R\right) + O(\sqrt{p}). \tag{2.5}$$

The sign between the two terms depends on which detector registers the photon, which results from the reversability for a lossless beam splitter. Note that correlation between the photon numbers and the number of excitations alone cannot result in the entangled state (2.5); coherence between the terms in the state (2.3) is also required. In particular, if after illuminated by the write pulse, the state of the ensemble and field 1 is an incoherent mixture of the form

$$\rho_{a,1} \propto |0_a\rangle|0_1\rangle\langle0_1|\langle0_a| + p|1_a\rangle|1_1\rangle\langle1_1|\langle1_a|, \tag{2.6}$$

then the state of the ensembles after one detector "clicks" would be

$$\rho_{L,R} = \frac{1}{2} \left(|0_a\rangle_L|1_a\rangle_R\langle1_a|_R\langle0_a|_L + |1_a\rangle_L|0_a\rangle_R\langle0_a|_R\langle1_a|_L\right) + O(p^2), \tag{2.7}$$

and is not entangled.

2.4.2   Details on entangling two ensembles

After two write pulses are sent into the two ensembles, at the output the scattered fields and the ensembles are, ideally, in the state:

$$
\begin{aligned}
|\Phi_{LR}\rangle \;&=\; |\Phi_L\rangle \otimes |\Phi_R\rangle \\
&=\; \left[|0_a\rangle_L |0_1\rangle_L + e^{i\beta_L}\sqrt{p}\,|1_a\rangle_L |1_1\rangle_L + O_L(p) \right] \\
&\qquad \otimes \left[|0_a\rangle_R |0_1\rangle_R + e^{i\beta_R}\sqrt{p}\,|1_a\rangle_R |1_1\rangle_R + O_R(p) \right] .
\end{aligned}
\tag{2.8}
$$

Detection of a photon in either detector $(D_1,\ D_2)$ then projects the state of the ensembles as follows:

$$
\begin{aligned}
|\phi_{L,R}\rangle \;&=\; Tr_{1L,1R}(a_\pm |\Phi_{LR}\rangle) = Tr_{1L,1R}\!\left[\frac{1}{\sqrt{2}}\left(a_{1L} \pm e^{i\phi} a_{1R}\right)|\Phi_{LR}\rangle \right] \\
&\propto\; \frac{1}{\sqrt{2}}\left(|0_a\rangle_L |1_a\rangle_R \pm e^{i\eta_1} |1_a\rangle_L |0_a\rangle_R \right) + O(\sqrt{p}) ,
\end{aligned}
\tag{2.9}
$$

where $Tr_{1L,1R}$ stands for tracing over the states of fields $1L$ and $1R$; a_{1L}, a_{1R}, and $a_\pm$ are the annihilation operators associated with fields $1L$, $1R$, and the output modes of the beam splitter, respectively; η_1 relates to the initial phase difference $\beta_L - \beta_R$ and the difference ϕ between phase shifts in the two channels connecting the ensembles to the beam splitter. The sign $\pm$ depends on which detector records the event.

The presence of certain sources of noise, especially dark noise in the detectors, modifies the above pure state to

$$
\hat{\rho}_{LR} = \frac{1}{c_0 + 1}\left(c_0 |0_a\rangle_L |0_a\rangle_R \langle 0_a|_R \langle 0_a|_L + |\phi_{L,R}\rangle\langle\phi_{L,R}| \right) ,
\tag{2.10}
$$

where $c_0/(1+c_0)$ gives the probability for a detection not related to excitations in the ensembles. This state is called an effective maximally entangled (EME) state [22]. The DLCZ protocol is designed to be resilient to this important kind of noise, since it always requires further detection events to proceed. The detection events without excitations in the relevant atomic modes have then a high probability of being discarded right after they occur. This is the main origin of the "built-in entanglement purification" characteristic of the protocol [22]. Unlike the conventional purification [12, 14], which starts with multiple copies of entangled pairs and ends with a heralded pair with higher degree of entanglement, the built-in entanglement purification in the DLCZ protocol proceeds in time. The trials which fail to entangle the ensembles are "purified" to yield a heralded entangled pair. Note that in writing Eq. (2.10), we have neglected higher-order terms involving pairs of excitations (one in each ensemble) and two excitations in either ensemble, which are intrinsic to the protocol of DLCZ, as well as diverse imperfections relevant to actual experimental implementations.

We have experimentally entangled two remote atomic ensembles following the DLCZ protocol, as described in Chapter 7.

2.5 Extending the distance between entangled ensembles by entanglement swapping

The maximum distance between the above entangled ensembles is limited by the attenuation length of the communication channels of fields $1L$ and $1R$. To extend
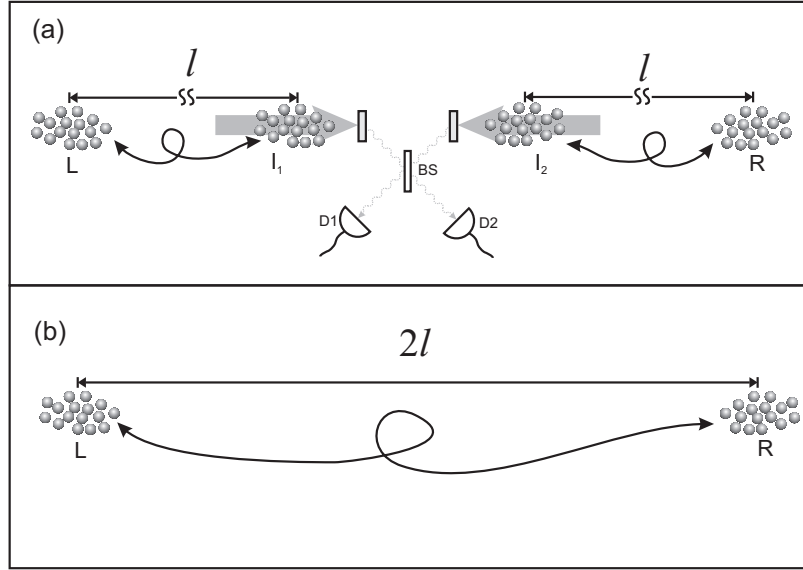
Figure 2.4: Setup for extending the distance between entangled ensembles (entanglement swapping). Two pairs of ensembles—L and I_1, and I_2 and R—are initially distributed at three sites L, I, and R. Each of the pairs is prepared in an EME state in the form of Eq. (2.10). (a) The stored atomic excitations of two nearby ensembles I_1 and I_2 are converted into light by two simultaneous read pulses. The emitted fields 2 interfere at a 50-50 beam splitter, and then are detected by the single-photon detectors D_1 and D_2. (b) If either D_1 or D_2 clicks, the protocol is successful and an EME state is established between the ensembles L and R with twice the distance. Otherwise, the process fails, and the previous entanglement generation and swapping need to be repeated until a click is recorded in D_1 or D_2.

the distance between entangled ensembles, one applies the entanglement swapping scheme, shown in Fig. 2.4. In this scheme, two pairs of ensembles need first to be prepared in the entangled state described by Eq. (2.9). Once the two entangled pairs are obtained, two read pulses are sent into ensembles I_1 and I_2 located in the middle, and the scattered fields are combined on a 50-50 beam splitter (Fig. 2.4a). A single click in either detector prepares the ensembles L and R in an EME state like the one in Eq. (2.10) (Fig. 2.4b). The "vacuum" coefficient c_0 now also includes the probability of reading the two excitations from the pairs (I_1, I_2) at the same time, leaving no remaining excitation in L or R.

Note that, since the entanglement process is probabilistic, the two pairs of ensembles do not necessarily become entangled at the same time. Due to the system memory, however, once a pair is entangled, one can hold the entangled state and wait for the other pair to attain entanglement. This is an important advantage of the quantum repeater idea, which is responsible for the polynomial growth in number of trials with the distance between the final entangled pair. Other quantum communication schemes, e.g., the quantum relay [31], that require all parts to be entangled at the same time present an exponential growth with distance.

2.6 Quantum communication with entangled ensembles

The EME states created between distant ensembles can be used to implement several entanglement-based communication schemes, such as quantum cryptography, teleportation, and Bell inequality measurements. In order to appreciate the broad applicability of the DLCZ protocol, it is important to note that a pair of entangled ensembles can be used to represent a qubit, with the states $\{|0_a\rangle_L|1_a\rangle_R, |1_a\rangle_L|0_a\rangle_R\}$ mapping to the usual qubit basis, $\{|0\rangle, |1\rangle\}$, in the ideal case. An experiment in this context has been recently reported by Matsukevich and Kuzmich [32].

To implement entanglement-based quantum cryptography or Bell's inequality detection, we use two pairs of entangled ensembles between the communication parties, as shown in Fig. 2.5. Keeping the terms of lowest order in the excitation probability p,

ideally, the state of the ensembles before read out can be written as:

$$|\Psi_{LU,LD,RU,RD}\rangle = \frac{1}{2}\big(|1_a\rangle_{LU}|0_a\rangle_{RU} + e^{i\eta_U}|0_a\rangle_{LU}|1_a\rangle_{RU}\big)$$

$$\otimes\big(|1_a\rangle_{LD}|0_a\rangle_{RD} + e^{i\eta_D}|0_a\rangle_{LD}|1_a\rangle_{RD}\big) , \qquad (2.11)$$

where η_U and η_D are the relative phases similar to the η_1 in Eq. (2.9). The state of

the ensembles is then transferred to fields 2 by read pulses. The fields 2 are combined

on 50-50 beam splitters with the relative phases ϕ_L and ϕ_R controlled by the phase

shifters. If we only record the coincidence events when one of the detectors on the left,

D_{L1} or D_{L2}, registers one click, and one of those on the right, D_{R1} or D_{R2}, registers

another, the effective state of the ensembles that would result in those events is

$$|\Psi_{LU,LD,RU,RD}\rangle_{eff}$$

$$= \frac{1}{\sqrt{2}}\big(e^{i\eta_D}|1_a\rangle_{LU}|0_a\rangle_{RU}|0_a\rangle_{LD}|1_a\rangle_{RD} + e^{i\eta_U}|0_a\rangle_{LU}|1_a\rangle_{RU}|1_a\rangle_{LD}|0_a\rangle_{RD}\big).(2.12)$$

Transferred to fields, the effective state for the fields 2 is, in the ideal case,

$$|\Psi_{2LU,2LD,2RU,2RD}\rangle_{eff}$$

$$= \frac{1}{\sqrt{2}}\big(e^{i\eta'_D}|1_2\rangle_{LU}|0_2\rangle_{RU}|0_2\rangle_{LD}|1_2\rangle_{RD} + e^{i\eta'_U}|0_2\rangle_{LU}|1_2\rangle_{RU}|1_2\rangle_{LD}|0_2\rangle_{RD}\big),(2.13)$$

where η'_U and η'_D include the extra phases introduced in the readout process.

The rate of coincidences between a pair of detectors, one on the left and the other
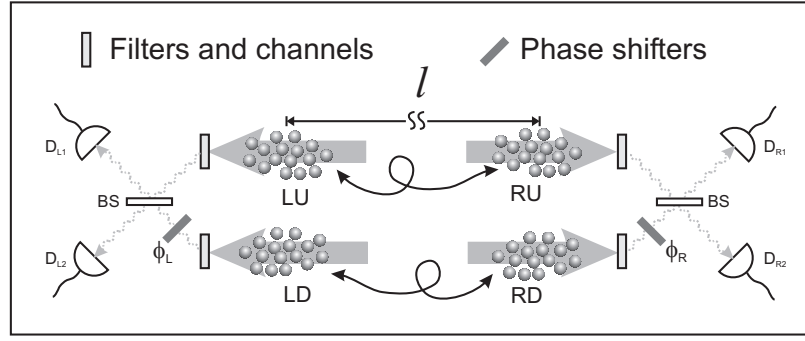
Figure 2.5: Setup for implementing entanglement-based quantum cryptography.

on the right, say D_{L1} and D_{R2}, is proportional to

$$\langle a_{L1}^\dagger a_{R2}^\dagger a_{R2} a_{L1}\rangle$$

$$= \frac{1}{4}\langle\left(a_{2LU} + e^{i\phi_L}a_{2LD}\right)^\dagger\left(a_{2RU} - e^{i\phi_R}a_{2RD}\right)^\dagger\left(a_{2RU} - e^{i\phi_R}a_{2RD}\right)\left(a_{2LU} + e^{i\phi_L}a_{2LD}\right)\rangle$$

$$(2.14)$$

where a_{mode} are the annihilation operators for the corresponding modes. The nonvanishing terms result in

$$\frac{1}{4}\Big(\langle a_{2LU}^\dagger a_{2RD}^\dagger a_{2RD} a_{2LU}\rangle + \langle a_{2LD}^\dagger a_{2RU}^\dagger a_{2RU} a_{2LD}\rangle$$

$$- e^{-i(\phi_R-\phi_L)}\langle a_{2LU}^\dagger a_{2RD}^\dagger a_{2RU} a_{2LD}\rangle$$

$$- e^{i(\phi_R-\phi_L)}\langle a_{2LD}^\dagger a_{2RU}^\dagger a_{2RD} a_{2LU}\rangle\Big)$$

$$= \frac{1}{4}\big[1 - cos(\phi_R - \phi_L + \eta_D' - \eta_U')\big] \,, \qquad (2.15)$$

which, when $\phi_R - \phi_L + \eta_D' - \eta_U'$ is varied, traces out a fringe with 100% visibility in the ideal case. When the relative phase $\eta_D' - \eta_U'$ is held constant, the coincidence rate depends on the difference $\phi_R - \phi_L$ induced by the two phase shifters of the

communication parties. The dependence on $\phi_R - \phi_L$ is characteristic of entangled states and can be used to perform entanglement based quantum cryptography and to check the violation of Bell's inequality [22].

In Chapter 8, an experimental scheme, involving four atomic ensembles, proposed for the demonstration of entanglement swapping and the implementation of entanglement-based quantum cryptography is discussed.

2.7   The requirement on the coherence time

The probabilistic character of the DLCZ scheme imposes stringent requirements for the coherence times for the quantum memories at the various sites of the communication chain (Fig. 2.4). Namely, the coherence time τ_{memory} for each memory is required to be much longer than the time Δt_c taken to establish entanglement between two nodes in the network. We require roughly

$$\tau_{memory} \gg \Delta t_c \approx (P_1 R_1)^{-1} \ . \tag{2.16}$$

Here P_1 gives the probability of detection of a scattered photon from a write pulse in each trial of the experiment and R_1 gives the rate at which successive trials can be carried out. The maximum repetition rate is given by the inverse of the time light takes to travel from one site to the other, so that $R_1 < c/l$. Since the excitation probability p needs to be kept low to minimize undesirable multiphoton events and the propagation and detection efficiencies are also small, commonly $P_1 \sim 10^{-2}$, which

with $l \gtrsim 10$ km implies $\tau_{memory} \gg 10^{-3}$ seconds. Notice that τ_{memory} results, in practice, in another limit for the maximum distance for communication with this protocol. The search for larger memory times is then one of the main goals in the actual implementation of the protocol, as discussed in more detail in Chapter 6.

Chapter 3

Generation of Nonclassical Photon Pairs from an Atomic Ensemble

3.1 Introduction

In this experiment, we demonstrate a basic primitive integral to the *DLCZ* scheme. Specifically, an initial *write* pulse of (classical) light is employed to create a state of collective atomic excitation as heralded by photoelectric detection of a first photon 1. After a programmable delay δt, a subsequent *read* pulse interrogates the atomic sample, leading to the emission of a second (delayed) photon 2. The manifestly quantum (or *nonclassical*) character of the correlations between the initial photon 1 and the subsequent photon 2 is verified by way of the observed violation of a Cauchy-Schwarz inequality for coincidence detection of the $(1, 2)$ fields [33]. Explicitly, we find $[\tilde{g}_{1,2}^2(\delta t) = (5.45 \pm 0.11)] \not\leq [\tilde{g}_{1,1}\tilde{g}_{2,2} = (2.97 \pm 0.08)]$, where $\tilde{g}_{i,j}$ are normalized correlation functions for the fields (i, j) and $\delta t = 405$ ns is the time separation between the emissions of the $(1, 2)$ photons. The capabilities realized in this experiment provide an important initial step toward the implementation of the full protocol of DLCZ, which would enable the distribution and storage of entanglement among atomic en-

sembles distributed over a quantum network. Extensions of these capabilities could facilitate scalable long-distance quantum communication [22]. By employing spin-polarized samples in optical-dipole or magnetic traps [34], it should be possible to extend the interval δt to times of several seconds.

This experiment arises within the context of prior work on spin squeezing [35, 36], and in particular on atomic ensembles, where significant progress has been made in the development of methods to exploit collective enhancement of atom-photon interactions provided by optically thick atomic samples [37, 38, 39, 40, 41, 42]. Instead of homodyne or heterodyne detection of light as used in spin-squeezing experiments [40, 41, 42], the $DLCZ$ scheme involves photon-counting techniques, which present stringent requirements for broad bandwidth detection and for the suppression of stray light from the atomic ensemble.

This chapter is largely based on Ref. [43].

3.2   Experiment

3.2.1   Apparatus and timing sequence

As illustrated in Fig. 3.1, an optically thick cloud of cold Cs atoms, trapped and cooled in a magneto-optical trap (MOT) [34], is exploited to produce correlated photons. The Cs hyperfine manifolds $\{|6S_{1/2}, F = 4\rangle, |6S_{1/2}, F = 3\rangle, |6P_{3/2}, F' = 4\rangle\}$ correspond to the levels $\{|g\rangle, |s\rangle, |e\rangle\}$, respectively. As shown in the timing diagram in Fig. 3.2, the MOT beams are chopped from ON to OFF with $\Delta t = 4\ \mu$s to prepare
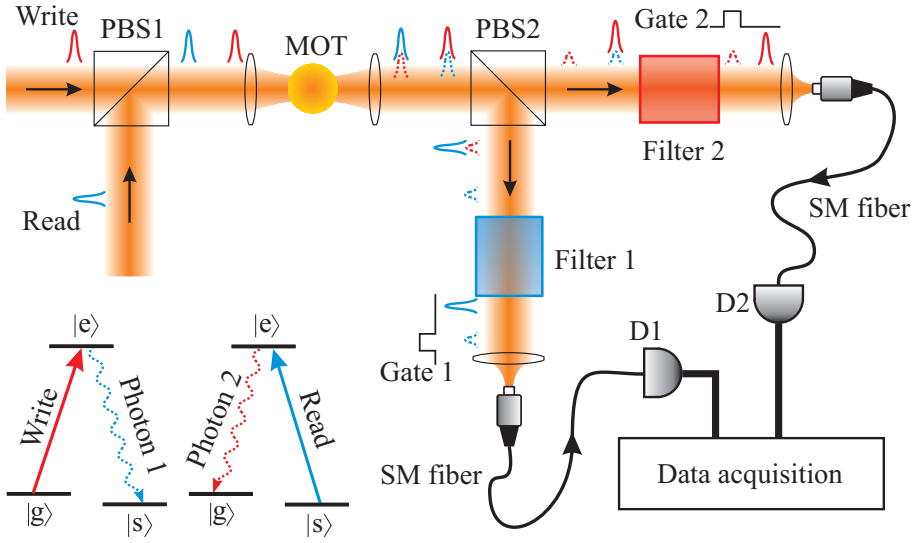
Figure 3.1: A diagram of the apparatus for the generation of nonclassical photon pairs from an atomic ensemble. Fields with frequency near that of the $|g\rangle \leftrightarrow |e\rangle$ ($|s\rangle \leftrightarrow |e\rangle$) transition are colored red (blue) here and in the subsequent two figures. The *write* pulse generates forward-scattered (anti-Stokes) Raman light around frequency $\omega_{3,4}$ from the $F' = 4$ excited level to the $F = 3$ ground level ($|e\rangle \rightarrow |s\rangle$) that is directed onto a single-photon detector *D1*. Raman (Stokes) light generated by the *read* pulse around frequency $\omega_{4,4}$ from $F' = 4$ to $F = 4$ ($|e\rangle \rightarrow |g\rangle$) is directed onto a second single-photon detector *D2*. PBS: polarizing beam splitter; SM: single-mode; Filter 1 and Filter 2: glass cells of Cs vapor.

the setting for a trial of the protocol. The MOT repumper is turned off about 300 ns later than the trapping beams to prepare the atoms in the $|g\rangle$ ($F = 4$) level. Less than 0.1% of atoms are measured to remain in the $|s\rangle$ ($F = 3$) level at this stage. The duration of the "dark" period is 1 μs. The jth trial of the protocol for single photon generation is initiated by a *write* pulse which is resonant with the $|g\rangle \rightarrow |e\rangle$ ($6S_{1/2}, F = 4 \rightarrow 6P_{3/2}, F' = 4$) transition at frequency $\omega_{4,4}$ and that has duration $\simeq 51$ ns (FWHM). The write pulse induces spontaneous Raman scattering to the initially empty level $|s\rangle$ via the $|e\rangle \rightarrow |s\rangle$ transition at time $t^{(1)}$. The *write* pulse is made sufficiently weak so that the probability to scatter one Raman photon into the preferred forward propagating mode $\psi^{(1)}(\vec{r}, t)$ is much less than unity for each pulse.
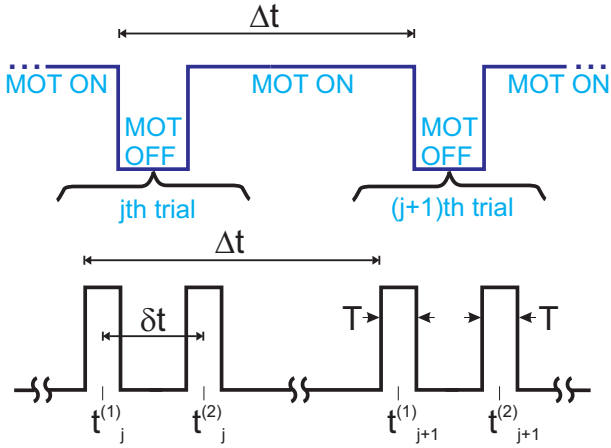
Figure 3.2: The timing sequence for data acquisition. Gating windows for the joint detection of photons (1,2) are centred at times $(t_j^{(1)}, t_j^{(2)})$ for the jth trial of the experiment during intervals when the MOT is "OFF".

Detection of a photon in the mode $\psi^{(1)}(\vec{r}, t)$ produced by the $|e\rangle \to |s\rangle$ transition results in a single excitation in the atomic level $|s\rangle$. In the ideal case, this coherently symmetrized state is [22]

$$|\Phi_{1A}\rangle \sim \sum_{j=1}^{N} |g\rangle_1 \cdots |s\rangle_j \cdots |g\rangle_N. \tag{3.1}$$

A critical parameter for the experiment is the resonant optical thickness $\gamma_{4,4}$ of the atomic sample [23]. We measure $\gamma_{4,4} \simeq 4 - 5$ for cw excitation, corresponding to an attenuation of intensity $\exp(-\gamma_{4,4})$ in propagation through the MOT.

Although the initial detection of photon 1 generated by the *write* beam is probabilistic, the detection of photon 1 results in the conditional state $|\Phi_{1A}\rangle$ with one collective atomic "excitation." This excitation can subsequently be converted into an excitation of the light field with high probability "on demand" with a specified emission direction and a programmable pulse shape [21, 22, 23, 24]. In order to achieve the conversion from atoms to field, a laser pulse from the *read* beam tuned near

the $|s\rangle \rightarrow |e\rangle$ transition illuminates the atomic sample, thereby affecting the transfer

$|s\rangle \rightarrow |g\rangle$ for the sample with the accompanying emission of a second Raman photon 2

on the $|e\rangle \rightarrow |g\rangle$ transition. For an optically thick atomic sample, photon 2 is emitted

with high probability into a specified mode $\psi^{(2)}(\vec{r}, t)$ offset in time by $t^{(2)} = t^{(1)} + \delta t$.

The spatial and temporal structures of the modes $\psi^{(1,2)}(\vec{r}, t)$ are set by the geometry

of the atomic sample and by the shape and timing of the *write* and *read* beams [23].

In our experiment, the read pulse is tuned to the $6S_{1/2}, F = 3 \rightarrow 6P_{3/2}, F' = 4$ transi-

tion at frequency $\omega_{3,4}$ with duration $\simeq 34$ ns (FWHM). The modes of the (*write*, *read*)

beams are spatially mode matched, with measured visibility greater than 95% for the

case of equal frequency and polarization. The time delay δt is limited in principle

only by the coherence time between the levels $|g\rangle$ and $|s\rangle$.

3.2.2   Filtering, efficiencies, and electronic gating

The *write* and *read* pulses have orthogonal polarizations. They are combined into a

single input at PBS1 (PBS: polarizing beam splitter) and then focused into the Cs

MOT with a waist of approximately 30 μm. The output fields are split by PBS2,

which also serves as the first stage of filtering the (*write*, *read*) beams from the $(1, 2)$

fields. For example, field 2 is transmitted by PBS2 to be subsequently registered by

detector *D2*, while the *read* pulse itself is reflected by 90° at PBS2 and then blocked

by an acousto-optical modulator that serves as gate 1. Further filtering is achieved

by passing each of the outputs from PBS2 through separate frequency filters each

of which consists of a glass cell of Cs vapor optically pumped to place atoms into

either $6S_{1/2}, F = 3$ or $F = 4$ [44]. The small residual reflected (transmitted) light of the *write* (*read*) pulse from PBS2 at frequency $\omega_{4,4}$ ($\omega_{3,4}$) passes through a filter cell with atoms in the $F = 4$ (3) level. It is thereby strongly attenuated ($>10^6$), while the accompanying Raman-scattered light as photons 1 (2) at frequency $\omega_{3,4}$ ($\omega_{4,4}$) is transmitted with high efficiency ($\simeq 80\%$). Transmission efficiencies from the MOT to detectors ($D1$, $D2$) are both about 30% for light with the spatial shape of the *write* and *read* beams and of the correct polarization.

The detected photons are converted to TTL pulses at the output of the detectors. ($D1$, $D2$) have overall quantum efficiencies of approximately 50% (photon *in* to TTL pulse *out*). Electronic gates are used to block TTL pulses with rising edges outside of predefined time windows. The time windows for the joint detection of photons $(1, 2)$ are centered at times $(t_j^{(1)}, t_j^{(2)})$ for the jth trial of the experiment during intervals when the MOT is *OFF*.

3.3   Observations and results

3.3.1   Temporal dynamics

By interchanging the frequencies for optical pumping of the filter cells described in Fig. 3.1, the (*write*, *read*) beams can be detected at ($D1$, $D2$) in place of the $(1, 2)$ fields. An example of the resulting pulse profiles accumulated over many trials $\{j\}$ is presented in Fig. 3.3, where the origin in time is set to coincide with the approximate center of the *write* pulse, with the *read* pulse following after a delay
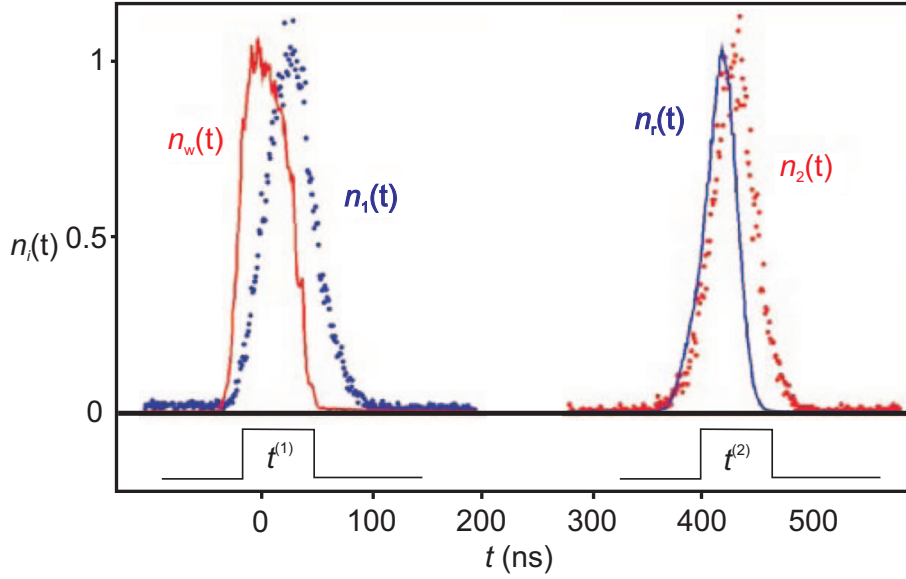
Figure 3.3: Normalized singles counts $n_i(t)$ are shown for the *write*, *read*, and $(1,2)$ fields. The pulses around $t = 0$ are from detector *D1* for the *write* beam $n_w(t)$ (solid trace) and for photon 1, $n_1(t)$ (points). The pulses around $t = 410$ ns are from detector *D2* for the *read* beam $n_r(t)$ (solid trace) and for photon 2, $n_2(t)$ (points).

$\simeq 415$ ns determined by external control logic.

With the filter cells set to transmit the $(1,2)$ photons to the $(D1, D2)$ detectors, respectively, we record histograms of the numbers $(n_1(t), n_2(t))$ of photoelectric events versus time, which are also displayed in Fig. 3.3. For the data presented here, the intensity of the *write* pulse is kept low ($\sim 10^3$ photons per pulse), resulting in a time lag for the onset of the $n_1(t)$ counts in Fig. 3.3. The probability $p_{write}^{(1)}$ to generate an anti-Stokes photon 1 within the solid angle of our imaging system is $p_{write}^{(1)} \simeq 10^{-2}$ per pulse.

The *read* pulse is about 100 times more intense than the *write* pulse. Examples of the resulting detection events $n_2(t)$ are shown in Fig. 3.3. In contrast to the behavior of $n_1(t)$, the intense *read* beam generates $n_2(t)$ counts promptly. This can be understood by noting that while the photons 1 are generated through a spontaneous

process started by the weak write pulse, the photons 2 are created in a process that is driven by the much stronger read pulse and also enhanced by the vast number of involved atoms (collective enhancement, see [22] and Sec. 6.2). More extensive investigations of the timing characteristics of the emitted fields $(1, 2)$ will be elaborated in Chapter 5 and 6.

Note that in addition to the symmetrized excitation, each *write* pulse also transfers several hundred atoms into the $F = 3$ level due to spontaneous emission from its near-resonant character. However, atoms transferred into $F = 3$ via spontaneous decay are spatially uncorrelated, so that their contribution to the signal from the *read* channel is strongly suppressed (by roughly the fractional solid angle collected, $\delta\Omega/4\pi \simeq 4 \times 10^{-5}$).

3.3.2 Observation of the nonclassical correlation between the (1,2) photons

A virtue of the *DLCZ* protocol is its insensitivity to a variety of loss mechanisms, including inefficiencies in transport and detection of the $(1, 2)$ photons. However, in an actual experiment, various nonideal characteristics of the atom-field interaction (as in our MOT) do lead to deterioration of correlation for the $(1, 2)$ photons (e.g., imperfect filtering and background fluorescence). Fortunately, there exists a well-defined border between the classical and quantum domains for the $(1, 2)$ fields that can be operationally accessed via coincidence detection, as was first demonstrated in the pioneering work of Clauser [33].

As illustrated in Fig. 3.2, electronic pulses from detectors ($D1$, $D2$) are separately gated with windows of duration $T = 60$ ns centered on times $(t^{(1)}, t^{(2)})$ corresponding to the approximate peaks of the $(n_1(t), n_2(t))$ pulses shown in Fig. 3.3. Photoelectric events that fall within the gate windows are directed to a time-interval analyzer (TIA) configured in a standard fashion for measurement of photoelectric correlations [30]. For a *start* event from $D1$ within the interval $t_j^{(1)} \pm T/2$ for the jth trial of the experiment, the TIA records the times of *stop* events from $D2$ within successive intervals $t_k^{(2)} \pm T/2$. Over many repetitions of the experiment, we thereby acquire time-resolved coincidences $n_{1,2}(\tau)$ between the $(1, 2)$ fields, both within the same trial $k = j$ and for subsequent trials $k = j + 1, j + 2,$ ... (i.e., a *start* event from trial j around time t_j and a *stop* event from trial k around time t_k, where $t_k = t_j + (k - j)\Delta t$ for $k = j, j + 1, \cdots$). By a 50-50 beam splitter, the field 1 can be directed to detectors ($D1$, $D2$), and then in turn the field 2 to ($D1$, $D2$) (we only had two detectors at hand at that time). We thus also acquire the time-resolved coincidences $n_{1,1}(\tau)$ and $n_{2,2}(\tau)$.

Figure 3.4 displays an example of data accumulated in this manner for coincidences $n_{\alpha,\beta}(\tau)$ between the $(1, 2)$, $(1, 1)$, and $(2, 2)$ fields, with successive peaks separated by the time between trials $\Delta t = 4\,\mu$s. Note that there is an *excess* of coincidence counts in each of the initial peaks for joint detections from the same trial ($\tau < \Delta t$) as compared to $n_{\alpha,\beta}(\tau)$ from different trials ($\tau > \Delta t$). This excess is shown more clearly in the plots in the right column, which expand the time axis from the left column in Fig. 3.4. Here, data from successive trials $k = j + 1, \cdots, j + 10$ have been offset to $\tau < \Delta t$ and then averaged for comparison with $n_{\alpha,\beta}(\tau)$ from the same trial j by introducing
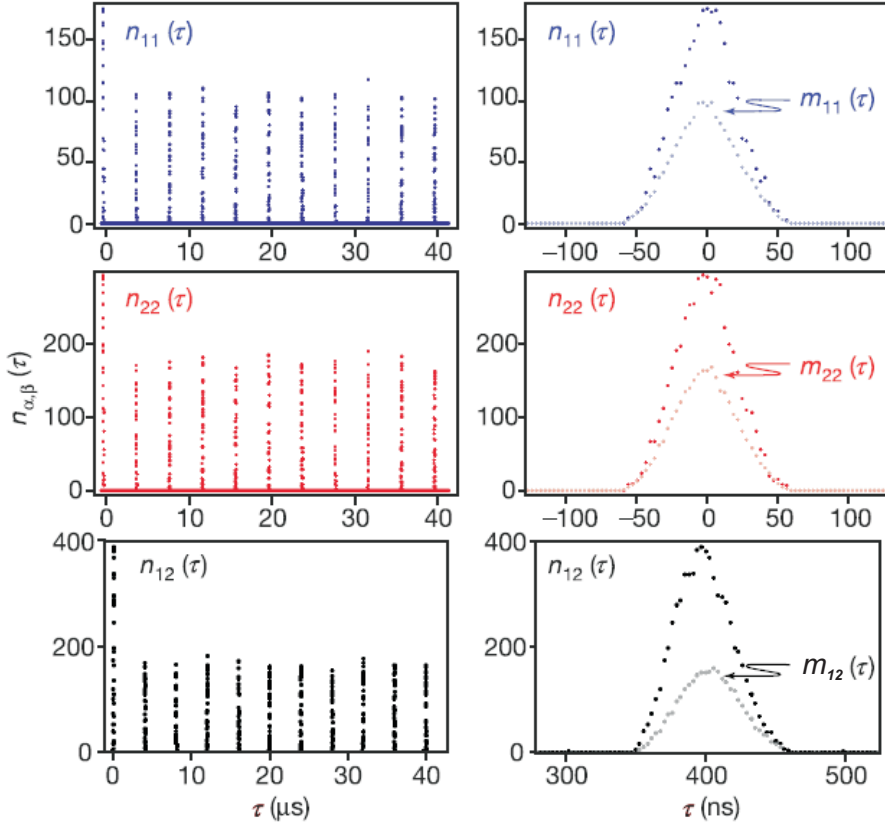
Figure 3.4: Time-resolved coincidences $n_{\alpha,\beta}(\tau)$ between the $(1,1)$, $(2,2)$, and $(1,2)$ fields are displayed versus time delay τ. *Left column*, $n_{\alpha,\beta}(\tau)$ is shown over 11 successive repetitions of the experiment. *Right column*, the time axis is expanded to a total duration of 250 ns with $\tau = 0$ set to the center of the gating window $(t^{(1)}, t^{(2)}, t^{(1)})$ for (n_{11}, n_{22}, n_{12}), respectively. The larger peak $n_{\alpha,\beta}(\tau)$ corresponds to detection pairs from the same trial j, while the smaller peak $m_{\alpha,\beta}(\tau)$ is for pairs from different trials.

the quantity $m_{\alpha,\beta}(\tau) = \frac{1}{10} \sum_{k=j+1}^{j+10} n_{\alpha,\beta}(\tau + (k-j)\Delta t)$. Statistical independence for

trials with $k \neq j$ is enforced by the experimental protocol of reapplying the MOT

and repumping beams after each trial (see Sec. 3.5.5).

From the data in Fig. 3.4, we determine the total number of coincidences $N_{\alpha,\beta} =$

$\sum_{\{\tau_i\}} n_{\alpha,\beta}(\tau_i)$ with $(\alpha, \beta) = (1, 2)$ obtained by summing over time bins $\{\tau_i\}$ for detec-

tion within the same trial j, and $M_{\alpha,\beta} = \sum_{\{\tau_k\}} m_{\alpha,\beta}(\tau_k)$ obtained from *start* and *stop*

events from different trials $(j \neq k)$. Fields for which the Glauber-Sudarshan phase-

space function is well behaved (i.e., *classical* fields) are constrained by a Cauchy-Schwarz inequality for the various coincidence counts (Sec. 3.5 and [30]), namely

$$[\tilde{g}_{1,2}(\delta t)]^2 \leq \tilde{g}_{1,1}\tilde{g}_{2,2} , \tag{3.2}$$

where $\tilde{g}_{1,1} \equiv \frac{N_{1,1}}{M_{1,1}}$, $\tilde{g}_{2,2} \equiv \frac{N_{2,2}}{M_{2,2}}$, $\tilde{g}_{1,2}(\delta t) \equiv \frac{N_{1,2}}{M_{1,2}}$.

For the data displayed in Fig. 3.4, we find $\tilde{g}_{1,1} = (1.739 \pm 0.020)$ and $\tilde{g}_{2,2} = (1.710 \pm 0.015)$, in correspondence to the expectation that the $(1,2)$ fields should each exhibit Gaussian statistics with $\tilde{g}_{1,1} = \tilde{g}_{2,2} = 2$ for the protocol of *DLCZ* in the ideal case, but here degraded by diverse sources of background counts (see Sec. 4.3.1). By contrast, for the cross-correlations of the $(1,2)$ fields, we record $\tilde{g}_{1,2}(\delta t) = (2.335 \pm 0.014)$, with $\delta t = 405$ ns. *Hence the inequality of Eq. (3.2) for classical fields is strongly violated, namely* $[\tilde{g}_{1,2}^2(\delta t) = 5.45 \pm 0.11] \nleq [\tilde{g}_{1,1}\tilde{g}_{2,2} = 2.97 \pm 0.08]$, where all errors indicate the statistical uncertainties. This violation of the Cauchy-Schwarz inequality clearly demonstrates the nonclassical character of the correlations between photons $(1,2)$ generated by the (*write, read*) beams. In addition, $\tilde{g}_{1,2} > 1$ also indicates that the coincidence rate between the detection of photons (1,2) is higher than that from uncorrelated atomic emission and background light. This also supports the claim of cooperative emission of photons (1,2) into the collection solid angle of our detection setup [45].

Typical acquisition parameters are as follows. Detectors (*D1, D2*) have average count rates of about (400/s, 250/s), respectively, while background counts with no MOT present are about 100/s. Counts due to the MOT itself (with *write* and *read*

beams blocked) are less than (10/s, 20/s) for (*D1, D2*). Dark counts with the inputs to the fibers blocked are less than 5/s. All these numbers are for the gated-output mode of data acquisition as in Fig. 3.1 with $T = 60$ ns.

The temporal extent of the photon wave packet $\psi(\vec{r}, t)$ for the $(1, 2)$ photons is also of some interest. To investigate this issue, we have carried out the experiment with expanded gate windows of duration $T = 140$ ns that then encompass the entire domains over which counts $n_1(t)$ and $n_2(t)$ are observed in Fig. 3.3. In this case, we record $\tilde{g}_{1,1} = (1.72 \pm 0.04), \tilde{g}_{2,2} = (1.52 \pm 0.05)$, and $\tilde{g}_{1,2}(\delta t) = (2.45 \pm 0.10)$, now with δt set to be 320 ns. *The classical inequality of Eq. (3.2) is once again not satisfied;* $[\tilde{g}_{1,2}^2(\delta t) = 6.00 \pm 0.50] \nleq [\tilde{g}_{1,1}\tilde{g}_{2,2} = 2.61 \pm 0.11]$. These results with $T = 140$ ns also confirm that dead-time effects do not play a significant role in the current experiment.

As described in Sec. 3.5, the violation of the Cauchy-Schwarz inequality of Eq. (3.2) in the ideal case can be much larger than we have observed, namely $[\tilde{g}_{1,2}(\delta t)]^2 / [\tilde{g}_{1,1}\tilde{g}_{2,2}] \simeq [(1 + p)/(2p)]^2 \gg 1$, where $p \ll 1$ is the excitation probability. In our experiment, the size of the violation of the inequality was limited mostly by uncorrelated fluorescence from individual atoms in the atomic sample. This contribution is made smaller in future experiments by moving to off-resonant excitation, which necessitates higher optical density, as detailed in the subsequent Chapters. There is also a significant limitation due the presence of the leakage light from the *read* pulse. This classical pulse is only 9 GHz away from the single-photon field 2 of interest, and is filtered by a factor exceeding 10^{-9}. To achieve even stronger violation of the inequality, we have further improved the filtering capability (Chapter 4).

3.4   Summary

Our observations of nonclassical correlations between the $(1,2)$ photons represent the first important step in the realization of the *DLCZ* protocol [22] for scalable quantum communication with atomic ensembles, although it is not yet sufficient for realization of the full protocol. Beyond the nonclassical correlations, our experiment also demonstrates successful filtering of the various fields and collective enhancement by the atomic ensemble, all of which are critical for realization of the full quantum repeater protocol. More generally, the capabilities that we have demonstrated should help to enable other advances in the field of quantum information, including implementation of quantum memory [24, 46] (Chapter 6) and fully controllable single-photon sources [47] (Chapter 4), which, combined, help to pave the avenue for realization of universal quantum computation [48].

3.5   A Cauchy-Schwarz inequality for coincidence detection of the (1, 2) fields

3.5.1   Introduction

A critical aspect of the experiment described in this chapter is the demonstration of the violation of a Cauchy-Schwarz inequality for two fields $(1,2)$ generated sequentially by the (*write, read*) pulses. A principal purpose of this section is to offer a detailed derivation of the relevant inequality specific to the setting of the measurement. In essential content, the analysis of Sections 3.5.2 and 3.5.3 is based upon the

discussion in the pioneering paper by J. Clauser [33], extended here to the setting of nonstationary fields as appropriate to the pulses of light in our experiment. The subsequent Sections 3.5.4 and 3.5.5 address in turn the question of the expected violations of the Cauchy-Schwarz inequality for the states relevant to our experiment, and the issue of statistical independence for the various trials of our experiment.

3.5.2 Joint probabilities for photodetection

Consider photoelectric detection at locations $(\vec{r}_A, \vec{r}_B)$ with the timing sequence shown in Figure 3.2, where j denotes the jth trial of the experiment. The joint probability p_2 for detection at $(\vec{r}_A, t_j^{(A)})$ and at $(\vec{r}_B, t_j^{(B)})$ within the time intervals $t_j^{(A,B)} \pm T/2$ is given by [30]

$$p_2(\vec{r}_A, t_j^{(A)}; \vec{r}_B, t_j^{(B)}) = \eta_A \eta_B \int_{-\frac{T}{2}}^{+\frac{T}{2}} \int_{-\frac{T}{2}}^{+\frac{T}{2}} dt' dt'' \langle : \hat{I}(\vec{r}_A, t_j^{(A)} + t') \hat{I}(\vec{r}_B, t_j^{(B)} + t'') : \rangle \ , \ \ (3.3)$$

where η_A and η_B are efficiency factors as defined in Ref. [30], $: \hat{O} :$ denotes normal and time ordering for the operator $\hat{O}$, and $\hat{I}$ denotes the intensity operator. In our experiment, we record photoelectric coincidences associated with cross- and auto-correlations of the $(1, 2)$ fields produced with a time separation δt, as depicted in Fig. 3.2. For cross-correlations $(1, 2)$, we direct the field 1 generated by the *write* beam and the field 2 produced by the *read* beam to the detectors at $(\vec{r}_A, \vec{r}_B)$, respectively, in which case $\hat{I}(\vec{r}_A, t_j^{(A)}) \mapsto \hat{I}_1(t_j^{(1)})$ and $\hat{I}(\vec{r}_B, t_j^{(B)}) \mapsto \hat{I}_2(t_j^{(2)})$. For autocorrelation of either field 1 or 2 with itself, we rearrange the detection geometry so that either field 1 or 2 is split and directed in equal parts to the detectors at $(\vec{r}_A, \vec{r}_B)$. For field 1, we

then have that $\hat{I}(\vec{r}_A, t_j^{(A)}) \mapsto r^2 \hat{I}_1(t_j^{(1)})$ and $\hat{I}(\vec{r}_B, t_j^{(B)}) \mapsto t^2 \hat{I}_1(t_j^{(1)})$, while for field 2, $\hat{I}(\vec{r}_A, t_j^{(A)}) \mapsto t^2 \hat{I}_2(t_j^{(2)})$ and $\hat{I}(\vec{r}_B, t_j^{(B)}) \mapsto r^2 \hat{I}_2(t_j^{(2)})$, where (r, t) are the transmission and reflection coefficients for the beam splitter. The vacuum state input to the beam splitter makes no contribution to the various normally ordered expectation values. The joint probabilities for photodetection required to describe our coincidence measurements can then be compactly written as

$$p_2^{(\alpha,\beta)}(\vec{r}_A, t_j^{(\alpha)}; \vec{r}_B, t_j^{(\beta)}) = \eta_{A,B}(\alpha, \beta) \int_{-\frac{T}{2}}^{+\frac{T}{2}} \int_{-\frac{T}{2}}^{+\frac{T}{2}} dt' dt'' \langle I_\alpha(t_j^{(\alpha)} + t') I_\beta(t_j^{(\beta)} + t'') \rangle_\varphi \; , \quad (3.4)$$

where $(\alpha, \beta) = (1, 2)$, $\eta_{A,B}(\alpha, \beta) = \eta_A \eta_B$ for $\alpha \neq \beta$ and $\eta_{A,B}(\alpha, \beta) = r^2 t^2 \eta_A \eta_B$ for $\alpha = \beta$. Here, we have employed the Optical Equivalence Theorem to convert the normally ordered expectation value from Eq. (3.3) into an average of the intensities with respect to the Glauber-Sudarshan phase-space function φ [30].

Define

$$x_i(t_j^i) \equiv \eta \int_{-\frac{T}{2}}^{+\frac{T}{2}} dt' I_i(t_j^i + t'), \; i = (1, 2). \quad (3.5)$$

In those cases for which φ is positive definite, the cross-correlations between x_1 and x_2 are constrained relative to the product of autocorrelations by the Cauchy-Schwarz inequality,

$$\left[\frac{\langle x_1(t_j^{(1)}) x_2(t_j^{(2)}) \rangle_\varphi}{\langle x_1(t_j^{(1)}) \rangle_\varphi \langle x_2(t_j^{(2)}) \rangle_\varphi} \right]^2 \leq \frac{\langle [x_1(t_j^{(1)})]^2 \rangle_\varphi}{\langle x_1(t_j^{(1)}) \rangle_\varphi^2} \frac{\langle [x_2(t_j^{(2)})]^2 \rangle_\varphi}{\langle x_2(t_j^{(2)}) \rangle_\varphi^2} \; . \quad (3.6)$$

This relation implies a constraint on the joint probabilities of photodetection from

Eq. (3.4) for fields with well-behaved φ (i.e., classical fields), namely that

$$\left[\frac{p_2^{(1,2)}(\vec{r}_A, t_j^{(1)}; \vec{r}_B, t_j^{(2)})}{p_2^{(1,2)}(\vec{r}_A, t_j^{(1)}; \vec{r}_B, t_k^{(2)})}\right]^2 \leq \frac{p_2^{(1,1)}(\vec{r}_A, t_j^{(1)}; \vec{r}_B, t_j^{(1)})}{p_2^{(1,1)}(\vec{r}_A, t_j^{(1)}; \vec{r}_B, t_k^{(1)})} \frac{p_2^{(2,2)}(\vec{r}_A, t_j^{(2)}; \vec{r}_B, t_j^{(2)})}{p_2^{(2,2)}(\vec{r}_A, t_j^{(2)}; \vec{r}_B, t_k^{(2)})} \tag{3.7}$$

with $j \neq k$. Note that to reach this relation, we assume statistical independence between the various trials $\{j\}$, so that

$$p_2^{(\alpha,\beta)}(\vec{r}_A, t_j^{(\alpha)}; \vec{r}_B, t_k^{(\beta)}) = p_1^{(\alpha)}(\vec{r}_A, t_j^{(\alpha)}) p_1^{(\beta)}(\vec{r}_B, t_k^{(\beta)}) \ , \ j \neq k \ . \tag{3.8}$$

In our experiment, the required detection probabilities $p_2^{(\alpha,\beta)}$ are estimated by way of coincidence detection among various channels. As illustrated in Figure 3.4, over many trials of the experiment we acquire time-resolved coincidences $n_{\alpha,\beta}(\tau)$ between the $(1,2)$, $(1,1)$, and $(2,2)$ beams, both within the same trial j and for subsequent trials $k = j+1, j+2, \cdots$, with the acquisition gated in correspondence to the timing sequence shown in Fig. 3.2. The quantity $m_{\alpha,\beta}(\tau) = \frac{1}{10}\sum_{k=j+1}^{j+10} n_{\alpha,\beta}(\tau + (k-j)\Delta t)$ allows us to more easily compare coincidence events from different trials ($\tau > \Delta t$) with those from the same trial ($n_{\alpha,\beta}(\tau)$ with $\tau < \Delta t$) by offsetting successive trials to $\tau < \Delta t$ and then averaging the results for improved statistical uncertainty (here over 10 subsequent trials).

From the time-resolved coincidence measurements as in Figure 3.4, we determine the total number of coincidences $N_{\alpha,\beta} = \sum_{\{\tau_i\}} n_{\alpha,\beta}(\tau_i)$ obtained by summing over time bins $\{\tau_i\}$ within the duration T of the gating window for detection within the same trial j and $M_{\alpha,\beta} = \sum_{\{\tau_k\}} m_{\alpha,\beta}(\tau_k)$ obtained from subsequent trials $k = $

$j + 1, j + 2, \cdots, j + 10$. Since the quantities $(N_{\alpha,\beta}, M_{\alpha,\beta})$ are directly proportional to the joint probabilities for photoelectric detection required for Eq. (3.7), we can construct an experimentally testable inequality in correspondence to the Cauchy-Schwarz inequality of Eq. (3.6), namely

$$\left[\frac{N_{1,2}}{M_{1,2}} \right]^2 \leq \frac{N_{1,1}}{M_{1,1}} \frac{N_{2,2}}{M_{2,2}} \ . \tag{3.9}$$

With the definitions

$$\tilde{g}_{1,1} \equiv \frac{N_{1,1}}{M_{1,1}}, \qquad \tilde{g}_{2,2} \equiv \frac{N_{2,2}}{M_{2,2}}, \qquad \tilde{g}_{1,2}(\delta t) \equiv \frac{N_{1,2}}{M_{1,2}} \ , \tag{3.10}$$

this inequality can be compactly written as

$$\left[\tilde{g}_{1,2}(\delta t) \right]^2 \leq \tilde{g}_{1,1} \tilde{g}_{2,2} \ , \tag{3.11}$$

which is the form employed in Sec. 3.3.2.

From the data displayed in Fig. 3.4, we perform sums over the time-resolved coincidences to deduce the quantities $(N_{1,1}, N_{2,2}, N_{1,2})$ and $(M_{1,1}, M_{2,2}, M_{1,2})$. We thereby find

$$\tilde{g}_{1,1} = (1.739 \pm 0.020), \qquad \tilde{g}_{2,2} = (1.710 \pm 0.015), \qquad \tilde{g}_{1,2}(\delta t = 405 \text{ ns}) = (2.335 \pm 0.014),$$
$$\tag{3.12}$$

where the quoted uncertainties arise from the statistics of the finite numbers of counts

for the various $(N_{\alpha,\beta}, M_{\alpha,\beta})$. The inequality (3.11) is thus strongly violated,

$$[\tilde{g}_{1,2}^2(\delta t) = 5.45 \ \pm \ 0.11] \nleq [\tilde{g}_{1,1}\tilde{g}_{2,2} = 2.97 \ \pm \ 0.08], \tag{3.13}$$

clearly demonstrating the nonclassical character of the correlations between photons $(1,2)$ generated by the (*write*, *read*) beams.

3.5.3 Conditional probabilities for photodetection

Our experimental protocol records the times of *stop* events within the gating window at $t_j^{(\beta)}$ given an initial *start* event within the window centered at $t_j^{(\alpha)}$. Strictly speaking, the recorded data thus correspond to the *conditional* probability p_c of a *stop* event given a *start* event, which is given by Eq. $(14.7-7)$ in Ref. [30],

$$p_c^{(\alpha,\beta)}(\vec{r}_B, t_j^{(\beta)}|\vec{r}_A, t_j^{(\alpha)}) = \frac{p_2^{(\alpha,\beta)}(\vec{r}_A, t_j^{(\alpha)}; \vec{r}_B, t_j^{(\beta)})}{p_1^{(\alpha)}(\vec{r}_A, t_j^{(\alpha)})} \ . \tag{3.14}$$

The conditional probabilities $p_c^{(\alpha,\beta)}$ are thus related to the joint probabilities $p_2^{(\alpha,\beta)}$ by simple scale factors $p_1^{(\alpha)}$ that can be obtained from the counting rates in the individual channels.

Somewhat more straightforwardly, Eq. (3.14) together with Eq. (3.7) leads to another Cauchy-Schwarz inequality of precisely the same form as Eq. (3.7),

$$\left[\frac{p_c^{(1,2)}(\vec{r}_B, t_j^{(2)}|\vec{r}_A, t_j^{(1)})}{p_c^{(1,2)}(\vec{r}_B, t_k^{(2)}|\vec{r}_A, t_j^{(1)})}\right]^2 \leq \frac{p_c^{(1,1)}(\vec{r}_B, t_j^{(1)}|\vec{r}_A, t_j^{(1)})}{p_c^{(1,1)}(\vec{r}_B, t_k^{(1)}|\vec{r}_A, t_j^{(1)})} \frac{p_c^{(2,2)}(\vec{r}_B, t_j^{(2)}|\vec{r}_A, t_j^{(2)})}{p_c^{(2,2)}(\vec{r}_B, t_k^{(2)}|\vec{r}_A, t_j^{(2)})} \ , \tag{3.15}$$

In deriving this relation, we make use of the assumed statistical independence of the trials (which is supported by data as in Figure 3.4), so that the conditional probability for photoelectric detection in trial k given an initial event in a prior trial j (with $j \neq k$) is just the unconditional probability p_1 for the event in k, namely

$$p_c^{(\alpha,\beta)}(\vec{r}_B, t_k^{(\beta)} | \vec{r}_A, t_j^{(\alpha)}) = p_1^{(\beta)}(\vec{r}_B, t_k^{(\beta)}) \ . \tag{3.16}$$

By utilizing Eq. (3.16), we can proceed precisely as before to estimate the various conditional probabilities $p_c^{(\alpha,\beta)}$ from the data via the ratios $\frac{N_{\alpha,\beta}}{M_{\alpha,\beta}}$. We then arrive at exactly the same result for the nonclassical character of the $(1,2)$ fields as was presented in Eq. (3.13). We have chosen to frame the discussion in this chapter in terms of *coincidence* counts rather than *conditional* counts for greater clarity and compactness of presentation.

3.5.4 Expected violations of the Cauchy-Schwarz inequality

Under ideal conditions, the respective signal modes 1 and 2 from the *write* and *read* processes are perfectly correlated, and they are in the following state (see Refs. [22, 23])

$$|\Phi_{12}\rangle = |00\rangle + \sqrt{p}|11\rangle + p|22\rangle + O(p^{3/2}) \ , \tag{3.17}$$

where $p \ll 1$ is the excitation probability in the signal mode for each pulse. The state $|\Phi_{12}\rangle$ has this form, since after the *write* (first) pulse, the signal mode 1 and the collective atomic mode should be in a two-mode squeezed state under ideal conditions.

Then, after the *read* (second) pulse, the collective atomic mode is mapped to the signal mode 2. So, under ideal conditions, the signal modes $(1, 2)$ should be in the two-mode squeezed state $|\Phi_{12}\rangle$ as given in Eq. (3.17).

In this ideal case, the traced density operator for the mode 1 or 2 is a thermal state. From Eq. (3.17) one can easily calculate the normalized correlations $(\tilde{g}_{1,1}, \tilde{g}_{2,2}, \tilde{g}_{1,2})$, and find (see Appendix A)

$$\tilde{g}_{1,1} = \tilde{g}_{2,2} = 2, \quad \tilde{g}_{1,2} = 1 + \frac{1}{p} \ .$$

Hence the Cauchy-Schwarz inequality should be violated with the ratio between $[\tilde{g}_{1,2}]^2$ and $\tilde{g}_{1,1} \times \tilde{g}_{2,2}$ being

$$R \equiv \frac{[\tilde{g}_{1,2}]^2}{\tilde{g}_{1,1} \times \tilde{g}_{2,2}} \simeq (\frac{1+p}{2p})^2 \gg 1 \ ,$$

for $p \ll 1$ and $p \neq 0$. Note that $p \lesssim 10^{-2}$ in our experiments, so that this condition is well satisfied.

In contrast to this ideal case, in our actual experiment there are a number of imperfections due to leakage of the pumping light from non-ideal filtering, low efficiency mode matching of the $(1, 2)$ fields with the detection system, and background fluorescence from uncorrelated atoms. These imperfections reduce the observed photoelectric correlations and thus the ratio R between the cross- and autocorrelations. However, we emphasize that in our experiment, $R > 1$ (i.e., a violation of the Cauchy-Schwarz inequality) has clearly demonstrated the nonclassical character of the correlation between the $(1, 2)$ fields. The Glauber-Sudarshan phase-space function cannot

exist as a positive probability distribution for the fields generated in our experiment.

3.5.5 Statistical independence of experimental trials

An important aspect of the connection between the formal derivation of the Cauchy-Schwarz inequality and the coincidence data in Figure 3.4 is the statistical independence of the various experimental trials. There are two principal issues here. (1) In a strict theoretical sense, statistical independence for a set of events requires that the joint probabilities factorize for the events or any subset. Section 3.5.2 refers to this requirement as part of a formal derivation. (2) However, in any real experiment, this formal requirement can never be strictly satisfied but only approximated. In our experiment, we endeavor to confirm operationally the statistical independence of various underlying joint probabilities by a variety of direct and indirect means.

The data in Fig. 3.4 strongly support statistical independence. There is no excess correlation observed between different experimental trials $j \neq k$ extending over 10 subsequent trials in the data shown in Figure 3.4, and over 25 trials for the actual data acquired in the experiment. This situation is enforced by the experimental protocol. After each trial, the MOT is reapplied together with an optical pumping field to incoherently repump population back from the $F = 3$ ground level.

Since we take data sequentially and in an interleaved fashion for the $(1, 1)$, $(2, 2)$, and $(1, 2)$ correlations, the raw coincidence counts in Figure 3.4 cannot be directly compared. These quantities are total coincidence counts for different acquisition times and rates for the three cases. No inequality can be inferred directly from the

coincidence counts. For example, if we double the acquisition time for any one of the quantities, the number of accumulated coincidences for that quantity alone would double.

By contrast, there is a nonclassical inequality for the *ratios* of summed coincidences $N_{1,1}/M_{1,1}$, $N_{2,2}/M_{2,2}$, and $N_{1,2}/M_{1,2}$. For the ratios, the total counting times are irrelevant, except to ultimately set the statistical uncertainty of the results.

Chapter 4

Single-Photon Generation from Stored Excitation in an Atomic Ensemble

4.1 Introduction

A critical capability for quantum computation and communication is the controlled generation of single-photon pulses into well-defined spatial and temporal modes of the electromagnetic field. Indeed, early work on the realization of quantum computation utilized single-photon pulses as quantum bits (*flying qubits*), with nonlinear interactions mediated by an appropriate atomic medium [49, 50]. More recently, a scheme for quantum computation by way of linear optics and photoelectric detection has been developed that again relies upon single-photon pulses as qubits [48]. Protocols for the implementation of quantum cryptography [51] and of distributed quantum networks also rely on this capability [22, 52], as do some models for scalable quantum computation [53].

Efforts to generate single-photon wavepackets can be broadly divided into techniques that provide photons "on demand" (e.g., quantum dots [47, 54, 55] or single

atoms [56] coupled to microcavities) and those that produce photons as a result of conditional measurement on a correlated quantum system. For conditional generation, the detection of one photon from a correlated pair results in a one-photon state for the second photon, as was first achieved using "twin" photons from atomic cascades [33, 57] and parametric down conversion [58], with many modern extensions [59, 60, 61, 62]. The DLCZ protocol [22] suggests a new avenue for producing single photons via conditional measurement of the light from optically thick atomic samples [63, 25].

In this chapter we report a significant advance in the creation of single photons for diverse applications in quantum information science, namely the generation and storage of single quanta in an atomic ensemble. In particular, single photons are generated from an ensemble of cold Cs atoms via the DLCZ protocol. Conditioned upon an initial detection from field 1 at 852 nm, a photon in field 2 at 894 nm is produced in a controlled fashion from the excitation stored within the atomic ensemble. The single-quantum character of field 2 is demonstrated by the violation of a Cauchy-Schwarz inequality, namely $w(1_2, 1_2|1_1) = 0.24 \pm 0.05 \not\geq 1$, where $w(1_2, 1_2|1_1)$ describes detection of two events $(1_2, 1_2)$ in field 2 conditioned upon an initial detection 1_1 in field 1, with $w \to 0$ for single photons.

This chapter is largely based on Ref. [64].
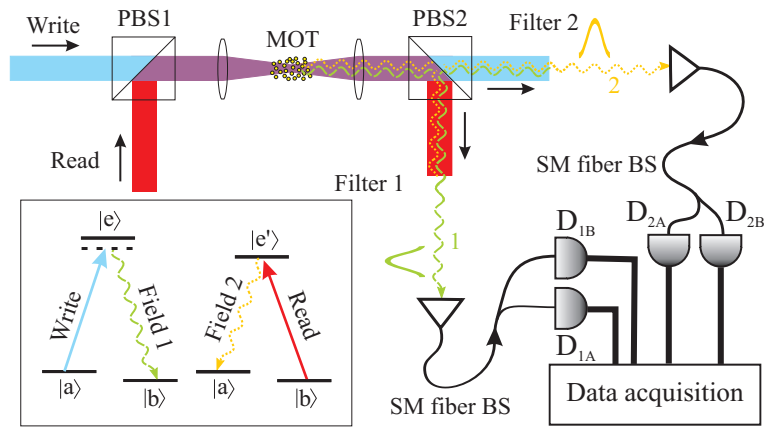
Figure 4.1: Schematic of experiment for conditional generation of single photons. *Write* and *read* pulses sequentially propagate into a cloud of cold Cs atoms (MOT), generating the correlated output fields $(1, 2)$. A detection event for field 1 at D_{1A} or D_{1B} leads to an approximate one-photon state for field 2, as confirmed with detectors D_{2A} and D_{2B}. (P)BS: (polarizing) beam splitter, SM: single-mode. The inset illustrates the relevant atomic level scheme.

4.2 Experiment

4.2.1 Apparatus and timing sequence

Figure 4.1 provides an overview of our experiment for producing correlated photons from an optically thick sample of four-level atoms in a magneto-optical trap (MOT) [34, 43]. The ground states $\{|a\rangle; |b\rangle\}$ correspond to the $6S_{1/2}, F = \{4; 3\}$ levels in atomic Cs, while the excited states $\{|e\rangle; |e'\rangle\}$ denote the $\{6P_{3/2}, F = 4; 6P_{1/2}, F = 4\}$ levels of the D_2, D_1 lines at $\{852; 894\}$ nm, respectively. Exploiting the D_1 line for the reading process is the major difference between this experiment and the experiment in Chapter 3.

The timing sequence is similar to that described in Sec. 3.2.1. We start the protocol for single photon generation by shutting off all light responsible for trapping and cooling for 1 μs, with the trapping light turned off approximately 300 ns before

the re-pumping light in order to empty the $F = 3$ hyperfine level in the Cs $6S_{1/2}$ ground state, thus preparing the atoms in $|a\rangle$. During the "dark" period, the jth trial is initiated at time $t_j^{(1)}$ when a rectangular pulse from the *write* laser beam, 150 ns in duration (FWHM) and tuned 10 MHz below the $|a\rangle \rightarrow |e\rangle$ transition, induces spontaneous Raman scattering to level $|b\rangle$ via $|a\rangle \rightarrow |e\rangle \rightarrow |b\rangle$. Detuning write pulses from resonance reduces the population transfer from $|a\rangle$ to $|e\rangle$ and thus decreases the probability of generating uncorrelated photons. The *write* pulse is sufficiently weak so that the probability to scatter one Raman photon into a forward propagating wavepacket $\psi^{(1)}(\vec{r}, t_j^{(1)})$ is much less than unity for each pulse. Detection of one photon from field 1 results in a "spin" excitation to level $|b\rangle$, with this excitation distributed in a symmetrized, coherent manner throughout the sample of N atoms illuminated by the *write* beam.

Given this initial detection, the stored atomic excitation can be converted into one photon at a user-controlled time $t_j^{(2)} = t_j^{(1)} + \delta t$. To implement this conversion, a rectangular pulse from the *read* beam, 120 ns in duration (FWHM) and resonant with the $|b\rangle \rightarrow |e'\rangle$ transition, illuminates the atomic sample. This pulse affects the transfer $|b\rangle \rightarrow |e'\rangle \rightarrow |a\rangle$ with the accompanying emission of field 2 on the $|e'\rangle \rightarrow |a\rangle$ transition described by the wavepacket $\psi^{(2)}(\vec{r}, t_j^{(2)})$. The spatial and temporal structure of $\psi^{(1,2)}(\vec{r}, t)$ are discussed in detail in Refs. [23] and [26]. The trapping and re-pumping light for the MOT are then turned back on to prepare the atoms for the next trial $j + 1$. The whole process is repeated at 250 kHz.

4.2.2   Filtering and detection

The forward-scattered Raman fields (1, 2) from the (*write, read*) pulses are directed
to two sets of single-photon detectors ($D_{1A,1B}$ for field 1 and $D_{2A,2B}$ for field 2).
Light from the (*write, read*) pulses is strongly attenuated (by $\simeq 10^6$) by the filters
(1,2) shown in Fig. 4.1, while the associated fields $(1, 2)$ are transmitted with high
efficiency ($\simeq 80\%$) [43]. Before it is coupled into a single-mode fiber, field 1 (2)
passes through a bandpass (long-pass) filter. The bandpass filter has a 5 nm wide
passband centered at 852 nm, and the long-pass filter has a cutoff wavelength at 888
nm. Both filters are purchased from Omega Optical. The disparate wavelengths of
the writing and reading processes facilitate the filtering of the write (read) classical
pulse and prevent contamination of field 1 (2) signal by the quiescent level of the read
(write) pulses. The acousto-optical modulators (AOMs) switching the fields in the
former experiment (Chapter 3) can thus be removed from the setup. Thus, the losses
associated with the AOMs are also removed. Detection events from $D_{1A,1B}$ within
the intervals $[t_j^{(1)}, t_j^{(1)} + T]$ and from $D_{2A,2B}$ within $[t_j^{(2)}, t_j^{(2)} + T]$ are time stamped
(with a resolution of 2 ns) and stored for later analysis. $T = 200$ ns for all of our
measurements.

4.3   Observations and results

For a particular set of operating conditions, we determine the single p_l and joint
$p_{l,m}$ event probabilities from the record of detection events at $D_{1A,1B}, D_{2A,2B}$, where
$(l, m) = 1$ or 2. The total singles probability p_l for events at D_{lA}, D_{lB} due to field l

is found from the total number of detection events n_{lA}, n_{lB} recorded by D_{lA}, D_{lB} during the intervals $[t_j^{(l)}, t_j^{(l)} + T]$ over M_{tot} repeated trials $\{j\}$, with then $p_l = (n_{lA} + n_{lB})/M_{tot}$. To determine $p_{l,l}$ for joint detections at D_{lA}, D_{lB}, we count the total number of coincidences $N_{lA,lB}$ recorded by D_{lA}, D_{lB}, with then $p_{l,l} = N_{lA,lB}/M_{tot}$. Joint detections between the $(1, 2)$ fields are described by $p_{1,2}$, which is determined by summing coincidence events between the four pairs of detectors for the $(1, 2)$ fields (i.e., between pairs $[D_{1A}, D_{2A}]$, $[D_{1A}, D_{2B}]$, $[D_{1B}, D_{2A}]$, and $[D_{1B}, D_{2B}]$), and $p_{1,2} = (N_{1A,2A} + N_{1A,2B} + N_{1B,2A} + N_{1B,2B})/M_{tot}$.

From $(p_l, p_{l,m})$ we derive estimates of the normalized intensity correlation functions $\tilde{g}_{l,m}$, where $\tilde{g}_{l,m} = 1$ for coherent states. For example, the autocorrelation function $\tilde{g}_{1,1} = p_{1,1}/(p_{1A}p_{1B})$ for field 1, and similarly for the functions $\tilde{g}_{2,2}, \tilde{g}_{1,2}$ for the auto-correlation of field 2 and the cross-correlation between fields $(1, 2)$. The first column in Figure 4.2 displays $\tilde{g}_{1,1}, \tilde{g}_{2,2}$, and $\tilde{g}_{1,2}$ as functions of p_1, p_2, and $\sqrt{p_1 p_2}$. A virtue of $\tilde{g}_{l,m}$ is its independence from the propagation and detection efficiencies. In the ideal case, the state for the fields $(1, 2)$ is [22, 23, 45]

$$|\Phi_{12}\rangle = |0_1 0_2\rangle + \sqrt{\chi}|1_1 1_2\rangle + \chi|2_1 2_2\rangle + O(\chi^{3/2}) , \qquad (4.1)$$

where $\sqrt{\chi}$ is the excitation amplitude for field 1 in each trial of the experiment and $|n_i\rangle$ is the Fock state for field i with n photons. For $\chi \ll 1$, $\tilde{g}_{1,1} = \tilde{g}_{2,2} = 2$ and $\tilde{g}_{1,2} = 1 + 1/\chi$. By contrast, for reasons that we will shortly address, our measurements in Fig. 4.2 give $\tilde{g}_{1,1} \simeq 1.7$ and $\tilde{g}_{2,2} \simeq 1.3$, with $\tilde{g}_{1,2}$ exhibiting a sharp rise with decreasing $\sqrt{p_1 p_2}$, but with considerable scatter.
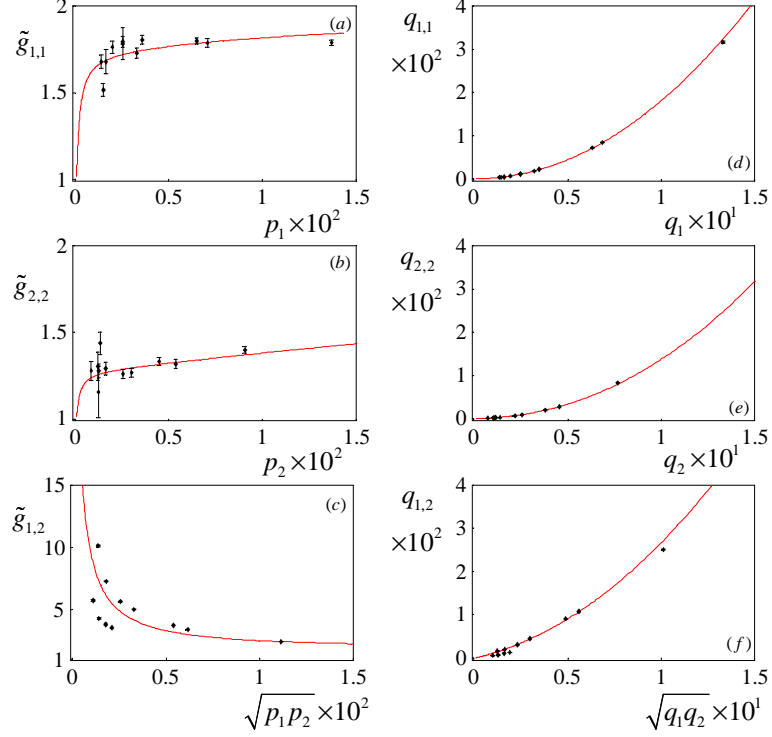
Figure 4.2: Left column (a)–(c) Normalized intensity correlation functions $\tilde{g}_{1,1}$, $\tilde{g}_{2,2}$, $\tilde{g}_{1,2}$ versus observed detection probabilities p_1, p_2, $\sqrt{p_1 p_2}$, respectively. Right column (d)–(f) $q_{1,1}$, $q_{2,2}$, $q_{1,2}$ for joint detection versus q_1, q_2, $\sqrt{q_1 q_2}$ for single detection, with q_l, $q_{l,m}$ referenced to the output of the MOT. Statistical uncertainties are indicated by the error bars. The full curves are from the model calculation described in the text with $(\kappa_1, \kappa_2) = (0.17, 0.90)$ and $(|v_{1b}|^2, |v_{2b}|^2) = 0.006$.

To provide a characterization of fields $(1, 2)$ that is independent of the efficiency of our detection setup, we convert the photodetection probabilities $(p_l, p_{l,m})$ to the quantities $(q_l, q_{l,m})$ for the field modes collected by our imaging system at the output of the MOT. Explicitly, for single events for fields $(1, 2)$, we define $q_l \equiv p_l/\alpha_l$, while for joint events, $q_{l,m} \equiv p_{l,m}/\alpha_l \alpha_m$, where α_l gives the overall efficiencies for fields $(1, 2)$. The second column in Fig. 4.2 displays the measured dependence of $q_{l,m}$ for joint events on $q_1, q_2, \sqrt{q_1 q_2}$ for single events over a range of operating conditions. As expected from Eq. (4.1), $q_{1,1}, q_{2,2}$ exhibit an approximately quadratic dependence on
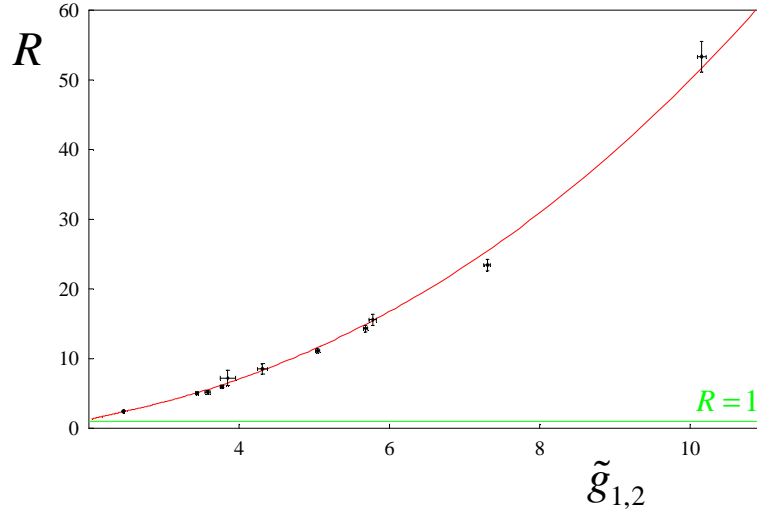
Figure 4.3: Ratio $R \equiv [\tilde{g}_{1,2}]^2 / \tilde{g}_{1,1}\tilde{g}_{22}$ versus the normalized cross-correlation $\tilde{g}_{1,2}$, where $R > 1$ for manifestly quantum (nonclassical) fields. The points are from our experiment with statistical uncertainties indicated by the error bars. The full curve is from the model calculation with (κ_1, κ_2) and $(|v_{1b}|^2, |v_{2b}|^2)$ as in Fig. 4.2.

q_1, q_2, while $q_{1,2}$ is linear for $\sqrt{q_1 q_2} \ll 1$.

The overall efficiencies $\alpha_l = \xi_l T_l \varsigma_l$, $l = (1, 2)$, where $\xi_1 = 0.41 \pm 0.04$ and $\xi_2 = 0.47 \pm 0.04$ for light with the spatial shape of the *write* and *read* beams propagating from the MOT to the input beam splitters for detectors $D_{1A,1B}$ and $D_{2A,2B}$, which have quantum efficiencies $\varsigma_1 \simeq 0.5$ and $\varsigma_2 \simeq 0.4$ (i.e., photon *in* to TTL pulse *out*), respectively. The efficiencies $T_1 = T_2 = 0.50$ for PBS2 in Fig. 4.1 account for the presumed unpolarized character of the $(1, 2)$ fields in our experiment. Note that from the theory developed in Sec. 6.2, or simply from the selection rules, we can infer that with the polarization arrangement for the (*write*, *read*) classical pulses and the detection settings for the (1,2) fields depicted in Fig. 4.1, conditioned on a detection at either D_{1A} or D_{1B}, field 2 will be linearly polarized orthogonal to the polarization of the read pulse. Thus conditioned on the detection events at D_1s, the efficiency T_2 is close to 1 instead of 0.5.

4.3.1   Estimation of collection efficiencies and noise level

In our experiment there are a number of imperfections that lead to deviations from the ideal case expressed by $|\Phi_{12}\rangle$ [22, 23, 45]. To quantify this, we developed a simple model that assumes the total fields $(1,2)$ at the output of the MOT consist of contributions from $|\Phi_{12}\rangle$ and background fields in coherent states $|v_{1,2}\rangle$. Operationally, p_1, p_2 are controlled by the intensity of the *write* beam, with only minor adjustments to that of the *read* beam. Hence, we parameterize our model by taking $\chi = |v_w|^2$, with v_w as the (scaled) amplitude of the *write* beam. Since important sources of noise are light scattering from the *write* and *read* beams and background fluorescence from uncorrelated atoms in the sample [23], we assume that $v_{1,2} = \sqrt{\kappa_{1,2}}v_w$. We further allow for fixed incoherent backgrounds v_{1b}, v_{2b} to account for processes that do not depend upon increases in *write* beam intensity.

    With this model, we compute the quantities that appear in Figs. 4.2–4.4. The parameters $(\kappa_1, \kappa_2) = (0.17, 0.90)$ and $(|v_{1b}|^2, |v_{2b}|^2) = 0.006$ are obtained directly by optimizing the comparison between the model results and our measurements of normalized correlation functions (e.g., $\tilde{g}_{1,1}$ versus $\tilde{g}_{1,2}$) without requiring absolute efficiencies. $\kappa_1 = 0.17$ implies that the photon number for "good" events associated with $|\Phi_{12}\rangle$ exceeds that for "bad" (background) events from $|v_1\rangle$ by roughly 6-fold for detection at D_{1A}, D_{1B}. For the curves in Fig. 4.2, we must also obtain the efficiencies β_l, η_l that convert expectation values for normally ordered photon number operators $\hat{n}_l$ for fields $l = (1,2)$ in the model into the various $(p_l, p_{l,m})$ and $(q_l, q_{l,m})$ (e.g., $p_l = \beta_l\langle\hat{n}_l\rangle, q_l = \eta_l\langle\hat{n}_l\rangle, q_{1,2} = \eta_1\eta_2\langle:\hat{n}_1\hat{n}_2:\rangle$). Ideally $\beta_l = \alpha_l$ and $\eta_l = 1$; we find instead

$(\beta_l, \eta_l) = (0.013, 0.15)$, where we take $\beta_1 = \beta_2$ and $\eta_1 = \eta_2$ for simplicity. Among various candidates under investigation, values $\beta_l < \alpha_l, \eta_l < 1$ can arise from inherent mode mismatching for capturing collective emission from the atomic ensemble [23].

4.3.2   Details on the simple model

The model assumed that the state of the fields resulting in the detection probabilities takes the form:

$$|\Psi\rangle = |\Phi_{12}\rangle|v_1\rangle|v_2\rangle|v_{1b}\rangle|v_{2b}\rangle \qquad (4.2)$$

from which we can obtain

$$
\begin{aligned}
p_1 &= \beta_1 \langle: \hat{n}_I :\rangle \\
&= \beta_1 (\langle: \hat{n}_1 :\rangle + \langle: \hat{n}_{v_1} :\rangle + \langle: \hat{n}_{v_{1b}} :\rangle) \\
&= \beta_1 (\frac{\chi}{1-\chi} + |v_1|^2 + |v_{1b}|^2) \,, \qquad (4.3)
\end{aligned}
$$

where $\hat{n}_x$ denotes the photon number operator for the mode x, $\langle: \hat{O} :\rangle$ gives the normally ordered expectation value for the operator $\hat{O}$, and $\langle: \hat{n}_I :\rangle$ denotes the mean photon number measured by detector 1s. Similarly,

$$p_2 = \beta_2 (\frac{\chi}{1-\chi} + |v_2|^2 + |v_{2b}|^2) \,. \qquad (4.4)$$

The joint detection probabilities

$$p_{1,1} = \beta_1^2 \langle : \hat{n}_I^2 : \rangle$$

$$= \beta_1^2 \big[\langle : \hat{n}_1^2 : \rangle + \langle : \hat{n}_{v_1}^2 : \rangle + \langle : \hat{n}_{v_b}^2 : \rangle$$

$$+ \ 2(\langle : \hat{n}_1 \hat{n}_{v_1} : \rangle) + 2(\langle : \hat{n}_1 \hat{n}_{v_{1b}} : \rangle) + 2(\langle : \hat{n}_{v_1} \hat{n}_{v_{1b}} : \rangle) \big]$$

$$= \beta_1^2 \big[\frac{2\chi^2}{(1-\chi)^2} + |v_1|^4 + |v_{1b}|^4$$

$$+ \ 2\frac{\chi}{1-\chi}(|v_1|^2 + |v_{1b}|^2) + 2|v_1|^2|v_{1b}|^2 \big] \ , \tag{4.5}$$

$$p_{2,2} = \beta_2^2 \big[\frac{2\chi^2}{(1-\chi)^2} + |v_2|^4 + |v_{2b}|^4$$

$$+ \ 2\frac{\chi}{1-\chi}(|v_2|^2 + |v_{2b}|^2) + 2|v_2|^2|v_{2b}|^2 \big] \ , \tag{4.6}$$

and

$$p_{1,2} = \beta_1\beta_2 \langle : \hat{n}_I \hat{n}_{II} : \rangle$$

$$= \beta_1\beta_2 \big[\frac{\chi + \chi^2}{(1-\chi)^2} + \frac{\chi}{1-\chi}(|v_1|^2 + |v_{1b}|^2 + |v_2|^2 + |v_{2b}|^2)$$

$$+ \ (|v_1|^2 + |v_{1b}|^2)(|v_2|^2 + |v_{2b}|^2) \big] \ . \tag{4.7}$$

The correlation functions $\tilde{g}_{i,j}$ can be calculated from $p_{i,j}/(p_i p_j)$. As described in Sec. 4.3.1, by fitting the calculated relation between efficiency-independent quantities, e.g., $\tilde{g}_{1,1}$ versus $\tilde{g}_{1,2}$, we can obtain the estimation of κ_1, κ_2, $|v_{1b}|^2$, and $|v_{2b}|^2$. The curves in the figures are obtained by substituting $|v_i|^2$ and v_{ib} with $\kappa_i\chi$ and 0.006 $[i = (1, 2)]$ from the fit, respectively, into Eqs. (4.3) to (4.7).

4.3.3 Verifying the nonclassical characteristics of the (1,2) fields

Following Sec. 3.5, the results from Fig. 4.2 are used to address directly the question of the nonclassical character of the $(1, 2)$ fields. The correlation functions $\tilde{g}_{l,m}$ for fields for which the Glauber-Sudarshan phase-space function φ is well behaved (i.e., *classical* fields) are constrained by the inequality $R \equiv [\tilde{g}_{1,2}]^2 / \tilde{g}_{1,1}\tilde{g}_{2,2} \leq 1$ [33, 45]. In Fig. 4.3 we plot the experimentally derived values for R versus the degree of cross-correlation $\tilde{g}_{1,2}$. As compared to previous measurements for which $R = 1.84 \pm 0.06$ [43] and $R = 1.34 \pm 0.05$ [65], we have achieved $R = (53 \pm 2) \gg 1$. In Figs. 4.2, 4.3, and 4.4, all points are taken with $\delta t = 200$ ns, except the points at $\tilde{g}_{1,2} \simeq 10$, which have $\delta t = 50$ ns.

4.3.4 The sub-Poissonian characteristic of field 2 conditioned on detection in field 1

The large degree of quantum correlation between the $(1, 2)$ fields suggests the possibility of producing a single photon in field 2 by conditioning on the detection of field 1. To investigate this, we consider the correlation function $w(1_2, 1_2|1_1)$ for detection with the setup shown in Fig. 4.1, namely $w(1_2, 1_2|1_1) \equiv p^{(c)}(1_2, 1_2|1_1)/[p^{(c)}(1_2|1_1)]^2$, where $p^{(c)}(1_2, 1_2|1_1)$ is the conditional probability for detection of two photons $(1_2, 1_2)$ from field 2 conditioned upon the detection of an initial photon 1_1 for field 1, and $p^{(c)}(1_2|1_1)$ is the probability for detection of one photon 1_2 given a detection event 1_1. Bayes' theorem allows the conditional probabilities to be written in terms of single and joint

probabilities, so that

$$w \equiv w(1_2, 1_2 | 1_1) = \frac{p^{(1)}(1_1) p^{(3)}(1_1, 1_2, 1_2)}{[p^{(2)}(1_1, 1_2)]^2}. \tag{4.8}$$

Classical fields must satisfy the Cauchy-Schwarz inequality $w \geq 1$; for independent coherent states, $w = 1$, while for thermal beams, $w = 2$. However, for the state $|\Phi_{12}\rangle$ of Eq. (4.1), $w = 4\chi \ll 1$ for small χ, approaching the ideal case $w \to 0$ for a "twin" Fock state $|1_1 1_2\rangle$.

From the record of photo-detection events at $D_{lA, lB}$, we calculate estimates of the probabilities appearing in Eq. (4.8), with the results of this analysis shown in Fig. 4.4. Part (a) examines the quantity $w_{i,j}$ obtained from events taken from different trials $i \neq j$ for the $(1, 2)$ fields (i.e., detection 1_1 in trial i for field 1 followed by two detections $(1_2, 1_2)$ in trial j for field 2). In this case, the $(1, 2)$ fields should be statistically independent [45], so that $w_{i,j} = \tilde{g}_{2,2}$. Hence, we also superimpose $\tilde{g}_{2,2}$ from Fig. 4.2 and find reasonable correspondence within the statistical uncertainties (in particular, $w_{i,j} \gtrsim 1$), thereby validating our analysis techniques.

To check various experimental procedures, we have employed white light to make the same measurements of $\tilde{g}_{1,1}, \tilde{g}_{2,2}, \tilde{g}_{1,2}$, and $w_{i,i}$ as were made in Figs. 4.2−4.3, and find that $\tilde{g}_{1,1} = 1.02 \pm 0.01$, $\tilde{g}_{2,2} = 1.01 \pm 0.01$, $\tilde{g}_{1,2} = 1.02 \pm 0.01$, $w_{i,i} = 0.99 \pm 0.2$, and $w_{i,j} = 0.97 \pm 0.02$, where in all cases, these correlation functions should equal unity.
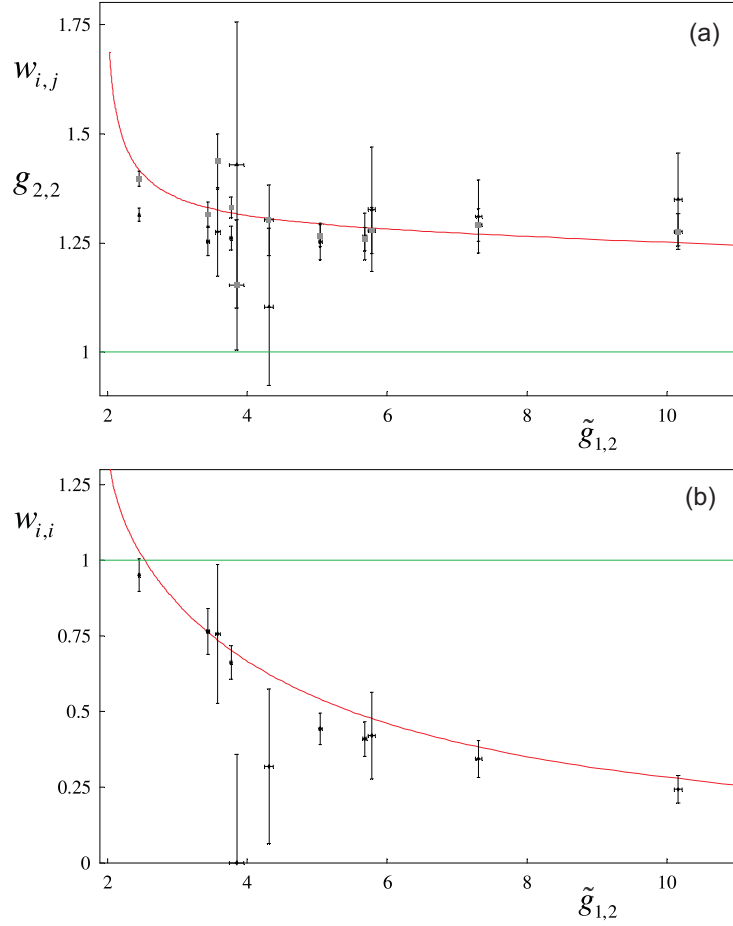
Figure 4.4: Three-fold correlation function w for detection event 1_1 for field 1 followed by two events $(1_2, 1_2)$ for field 2 versus the normalized cross-correlation $\tilde{g}_{1,2}$. (a) $w_{i,j}$ for events $(1_1)_i$ and $(1_2, 1_2)_j$ from different trials $i \neq j$ together with points for $\tilde{g}_{2,2}$. $w_{i,j} = \tilde{g}_{2,2}$ for statistically independent trials. (b) $w_{i,i}$ for events from the same trial i. $w_{i,i} < 1$ for sub-Poissonian fields in support of the single-photon character of field 2. Statistical uncertainties are indicated by the error bars. The red curves are from the model calculation with (κ_1, κ_2) and $(|v_{1b}|^2, |v_{2b}|^2)$ as in Figs. 4.2, 4.3.

Fig. 4.4(b) displays $w_{i,i}$ for events from the same experimental trial i for the $(1, 2)$ fields. Significantly, as the degree of cross-correlation expressed by $\tilde{g}_{1,2}$ increases (i.e., decreasing χ), $w_{i,i}$ drops below the classical level of unity, indicative of the sub-Poissonian character of the conditional state of field 2. With $\delta t = 200$ ns, $w_{i,i} = 0.34 \pm 0.06$ for $\tilde{g}_{1,2} = 7.3$, while with $\delta t = 50$ ns, $w_{i,i} = 0.24 \pm 0.05$ for $\tilde{g}_{1,2} = 10.2$.

Beyond the comparison to our model shown in the figure, empirically we find that $w_{i,i}$ is well approximated by $\tilde{g}_{1,1}\tilde{g}_{2,2}/\tilde{g}_{1,2}$, as in the ideal case of Eq. (4.1). However, independent of such comparisons, we stress that the observations reported in Fig. 4.4 represent a sizable nonclassical effect in support of the conditional generation of single photons for field 2. No corrections for dark counts or other backgrounds have been applied to the data in Fig. 4.4 (nor indeed to Figs. 4.2, 4.3). For the point at $\tilde{g}_{1,2} \approx 3.8$, we did not obtain any triple coincidences, thus $w_{i,i} = 0$ for that data run with a large error bar.

4.4 Conclusion

In conclusion, our experiment represents an important step in the creation of an efficient source of single photons stored within an atomic ensemble, and thereby toward enabling diverse protocols in quantum information science [22, 48, 51, 53]. Our model supports the hypothesis that the inherent limiting behavior of $w_{i,i}$ below unity is set by the efficiency η_l, which leads to prohibitively long times for data acquisition for $\chi \lesssim 0.04$, corresponding to the smallest value of $w_{i,i}$ in Fig. 4.4. We are pursuing improvements to push $\eta_l \simeq 0.15 \rightarrow 1$. Dephasing due to Larmor precession in the quadrupole field of the MOT limits $\delta t \lesssim 300$ ns, which could be extended to several seconds in optical dipole or magnetic traps [34].

Chapter 5

Temporal Dynamics of Photon Pairs Generated by an Atomic Ensemble

5.1   Introduction

With the exception of the verification of the time-delay implicit for the Raman processes employed [66], experiments up to this point have investigated neither the time or spatial dependence of quantum correlations for the emitted fields from the atomic ensemble. The high efficiencies achieved in Chapter 4 now enable such an investigation into the temporal properties of nonclassical correlations between emitted photon pairs, which is described in this Chapter.

Specifically, we study the time dependence of quantum correlations for photons emitted from an ensemble of cold Cesium atoms, with photon pairs created sequentially by classically controlled *write* and *read* pulses. The correlation function $R(t_1, t_2)$ for the ratio of cross- to autocorrelations for the $(1, 2)$ fields at times (t_1, t_2) presents large violations of the Cauchy-Schwartz inequality $R \leq 1$, with $R^{\mathrm{max}} = 292 \pm 57 \nleq 1$. By contrast, previous measurements have reported violations $R \nleq 1$ only for de-

tection events integrated over the entire durations of the *write* and *read* pulses ($R = 1.84 \pm 0.06$ in Ref. [43], $R = 1.34 \pm 0.05$ in Ref. [65], and $R = 53 \pm 2$ in Ref. [64]). We also map the decay of quantum correlations by varying the time delay between the *write* and *read* pulses, and find a decoherence time $\tau_d \simeq 175$ ns. We have developed a model to describe the decoherence and find good correspondence with our measurements. This model is utilized to analyze a new proposal that should extend the correlation times to beyond 10 μs, which would allow for entanglement between atomic ensembles on the scale of several kilometers.

This chapter is largely based on Ref. [67].

5.2 Experiment

Our experimental procedure is the same as in Chapter 4 and is illustrated in Figure 5.1. To investigate the photon statistics, we use four avalanche photodetectors, a pair for each field (1,2), labelled as $D_{iA,iB}$ ($i = (1, 2)$, connected in the same way shown in Fig. 4.1), which are activated in the jth trial at $(T_j, T_j + \Delta t)$, respectively, for 200 ns for all experiments. T_j is the time at which the write pulse illuminates the ensemble in the jth trial, and Δt is the delay between the write and read pulses. We define $p_\tau(t_l, t_m)$ as the joint probability for photoelectric detection from field l in the interval $[T_j + t_l, T_j + t_l + \tau]$ and for an event from field m in the interval $[T_j + t_m, T_j + t_m + \tau]$, where l and m equal 1 or 2. $p_\tau(t_l, t_m)$ is determined from the record of time-stamped detection events at $D_{1A,1B}, D_{2A,2B}$, allowing us to measure autocorrelations and cross-correlations simultaneously. In a similar fashion, $q_\tau(t_l, t_m)$ gives the joint probability
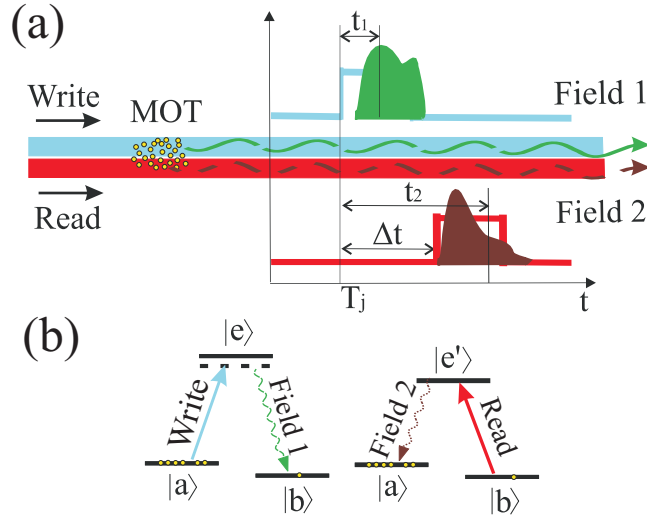
Figure 5.1: (a) Simplified schematic of experiment. *Write* and *read* pulses propagate into a cloud of cold Cs atoms (MOT) at times T_j and $T_j + \Delta t$ respectively, and generate the correlated output fields 1 and 2. Quantum correlations for these fields at times (t_1, t_2) are investigated by way of photoelectric detection. (b) The relevant atomic-level scheme.

for detection for fields (l, m) in the intervals $([T_j + t_l, T_j + t_l + \tau], [T_k + t_m, T_k + t_m + \tau])$

for two trials $k \neq j$.

5.3   Observations and results

Following Chapters 3 and 4, we introduce the time-dependent ratio $R_\tau(t_1, t_2)$ of cross-correlation to autocorrelation for the $(1, 2)$ fields, where

$$R_\tau(t_1, t_2) \equiv \frac{[p_\tau(t_1, t_2)]^2}{p_\tau(t_1, t_1) p_\tau(t_2, t_2)} \ . \tag{5.1}$$

This ratio is analogous to the quantity R defined in Sec. 4.3.3 and is constrained by the inequality $R_\tau(t_1, t_2) \leqslant 1$ for all fields for which the Glauber-Sudarshan phase-space function is well behaved (i.e., *classical* fields) [33, 43]. Beyond enabling a

characterization of the quantum character of the $(1, 2)$ fields in a model-independent fashion, measurements of $R_\tau(t_1, t_2)$ also allow inferences of the quantum state for collective excitations of single spins within the atomic ensemble.

The first step in the determination of $R_\tau(t_1, t_2)$ is the measurement of the joint probability $p_\tau(t_1, t_2)$ for the $(1, 2)$ fields, and for comparison, $q_\tau(t_1, t_2)$ for independent trials. In this experiment, we focus on two cases: (I) nearly simultaneous application of *write* and *read* pulses with offset $\Delta t = 50$ ns less than the duration of either pulse, and (II) consecutive application of *write* and *read* pulses with $\Delta t = 200$ ns longer than the *write*, *read* durations. Results for $p_\tau(t_1, t_2)$ and $q_\tau(t_1, t_2)$ are presented in Fig. 5.2 as functions of the detection times (t_1, t_2) for the fields $(1, 2)$. For both $\Delta t = 50$ and 200 ns, $p_\tau(t_1, t_2) \gg q_\tau(t_1, t_2)$, indicating the strong correlation between fields 1 and 2, with the maximal ratio $g_{1,2}^\tau(t_1, t_2) = p_\tau(t_1, t_2)/q_\tau(t_1, t_2) \gtrsim 30$, which is much greater than reported previously [43, 64, 65]. In Fig. 5.2, $\tau = 4$ ns, leading to statistical errors of about 8% for the largest values shown.

In case (I) for near simultaneous irradiation with *write* and *read* pulses, Fig. 5.2(a) shows that $p_\tau(t_1, t_2)$ peaks along the line $t_2 - t_1 = \delta t_{12} \simeq 50$ ns with a width $\Delta t_{12} \simeq 60$ ns, in correspondence to the delay δt_{12} and duration Δt_2 for readout associated with the transition $|b\rangle \rightarrow |e'\rangle \rightarrow |a\rangle$ given an initial transition $|a\rangle \rightarrow |e\rangle \rightarrow |b\rangle$ [66]. Apparently, the qualitative features of $p_\tau(t_1, t_2)$ depend only upon the time difference between photon detections in fields 1 and 2.

In case (II) with the *read* pulse launched 200 ns after the *write* pulse, excitation is "stored" in the atomic ensemble until the readout. As shown in Fig. 5.2(c), the production of correlated photon pairs now peaks towards the end of the *write* pulse

64
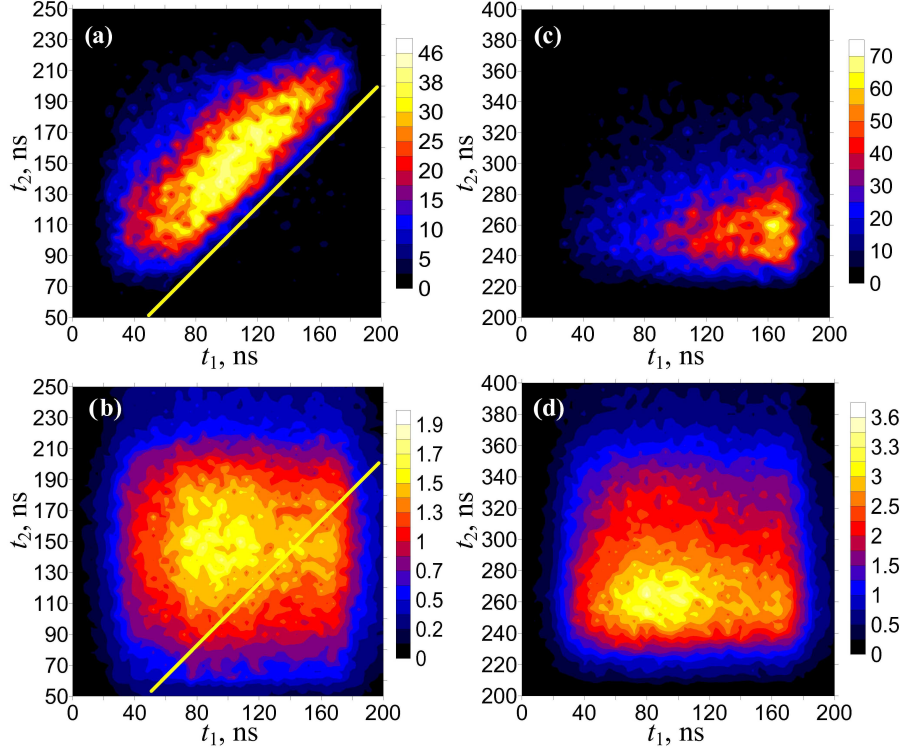
Figure 5.2: Probability for joint detection from the fields $(1, 2)$ at times (t_1, t_2). (a) $p_\tau(t_1, t_2)$ and (b) $q_\tau(t_1, t_2)$ for overlapped *write* and *read* pulses, $\Delta t = 50$ ns, with the solid line corresponding to $t_2 = t_1$. (c) $p_\tau(t_1, t_2)$ and (d) $q_\tau(t_1, t_2)$ for consecutive *write* and *read* pulses, $\Delta t = 200$ ns. In all cases the bin size $\tau = 4$ ns, and the joint probabilities p_τ and q_τ have been scaled by 10^9.

(i.e., $t_1 \gtrsim 100$ ns), and near the beginning of the *read* pulse (i.e., $200 \lesssim t_2 \lesssim 300$ ns), albeit with comparable values for δt_{12} and Δt_2. Early events for field 1 do not lead to correlated events for field 2; rather, $p_\tau(t_1, t_2)$ decays rapidly beyond the line $t_2 - t_1 = \tau_d \simeq 175$ ns. The marked contrast between $p_\tau(t_1, t_2)$ for $\Delta t = 50$ and 200 ns results in a diminished ability for the conditional generation of single photons from excitation stored within the atomic ensemble [64] and, more generally, for the implementation of the *DLCZ* protocol for increasing Δt. The underlying mechanism is decoherence within the ensemble, as will be discussed.

Fig. 5.2(b), (d) display $q_\tau(t_1, t_2)$ for independent trials $j \neq k$. $q_\tau(t_1, t_2)$ is expected
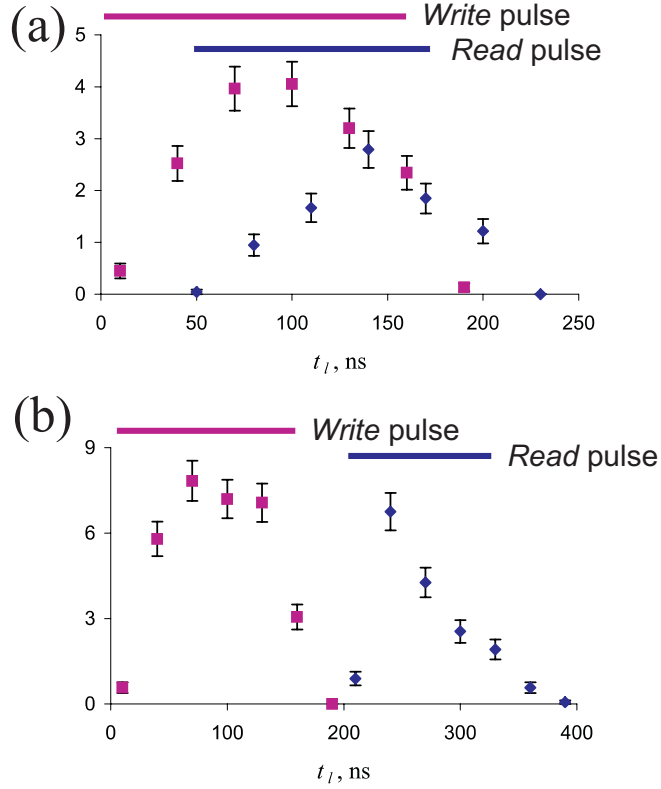
Figure 5.3: Probability of joint detection $p_\tau(t_1, t_1)$ for field 1 (squares) and $p_\tau(t_2, t_2)$ for field 2 (diamonds) as functions of respective detection times t_1 and t_2. (a) Overlapping *write* and *read* pulses, $\Delta t = 50$ ns; (b) Consecutive *write* and *read* pulses, $\Delta t = 200$ ns. The probabilities are scaled by 10^8.

to be proportional to the product of classical intensities of the fields 1 and 2, in reasonable correspondence to the form shown in Fig. 5.2(b), (d) for our roughly rectangular *write*, *read* pulses, but distinctively different from $p_\tau(t_1, t_2)$ in (a), (c).

To deduce $R_\tau(t_1, t_2)$ from Eq. (5.1), we determine the joint detection probabilities $p_\tau(t_1, t_1)$ for field 1 and $p_\tau(t_2, t_2)$ for field 2 from the same record of photoelectric events as for Fig. 5.2 (a, c). Since the rate of coincidences for the autocorrelations are roughly 10^2 times smaller than for the cross-correlations $p_\tau(t_1, t_2)$ from photon pairs for the $(1, 2)$ fields, we must increase the bin size τ to 30 ns to accumulate enough events to reduce the statistical errors to acceptable levels. Fig. 5.3 shows the time

dependence of $p_\tau(t_1, t_1)$ and $p_\tau(t_2, t_2)$ for both cases (I) and (II). While the shape of $p_\tau(t_1, t_1)$ associated with the *write* pulse does not change with Δt, the profile of $p_\tau(t_2, t_2)$ from the *read* pulse is affected and exhibits a rise time that is ~ 3 times shorter for $\Delta t = 200$ ns than for $\Delta t = 50$ ns. This prompt rise in Fig. 5.3(b) is consistent with the observation that a stored excitation is efficiently addressed at the beginning of the *read* pulse for non-overlapping *write*, *read* pulses, while the longer rise time in Fig. 5.3(a) results from overlapping excitation and retrieval of atoms from the state $|b\rangle$.
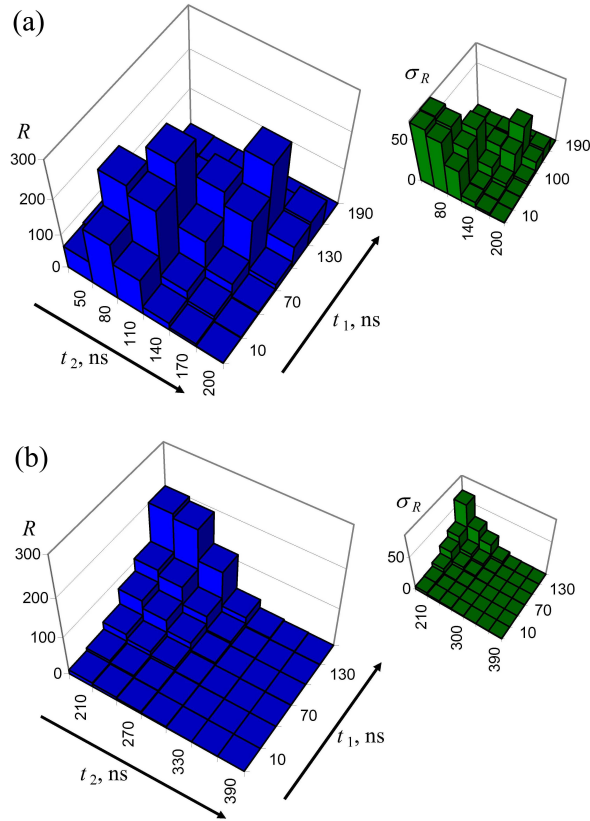
Figure 5.4: The experimentally derived ratio $R_\tau(t_1, t_2)$ as a function of detection times (t_1, t_2) for the $(1, 2)$ fields, with $R_\tau \leq 1$ for classical fields. The left column gives $R_\tau(t_1, t_2)$ for (a) $\Delta t = 50$ ns and (b) $\Delta t = 200$ ns, while the right column gives the associated statistical uncertainties. Bin size $\tau = 30$ ns.

We employ the data in Figs. 5.2, 5.3 together with Eq. (5.1) to construct the ratio $R_\tau(t_1, t_2)$, with the result presented in Fig. 5.4. Before applying Eq. (5.1), we reprocess the data for $p_\tau(t_1, t_2)$ in Fig. 5.2 for $\tau = 30$ ns bin size. Not unexpectedly, the trends for $R_\tau(t_1, t_2)$ closely resemble those of the joint probability $p_\tau(t_1, t_2)$ for correlated pair generation previously discussed. As for the violation of the Cauchy-Schwarz inequality $R_\tau(t_1, t_2) \leq 1$ for classical fields [33, 43], we observe maximal violations with $R_\tau^{\max} = 292 \pm 57$ for $\Delta t = 50$ ns and $R_\tau^{\max} = 202 \pm 60$ for $\Delta t = 200$ ns (with the next largest value in Fig. 5.4 (b) being $R_\tau^{\max} = 198 \pm 33$). The relatively large errors in $R_\tau(t_1, t_2)$ arise predominantly from the uncertainties in $p_\tau(t_1, t_1)$ and $p_\tau(t_2, t_2)$ shown in Fig. 5.3.

To verify the validity of our experimental procedures, we calculate $R(t_1, t_2)$ for detection events for the $(1, 2)$ fields from different trials $j \neq k$, for which $R(t_1^j, t_2^k)$ is expected to equal unity. This result is confirmed experimentally to within a statistical uncertainty of less than 4%.

The forms for $p_\tau(t_1, t_2)$ and $R_\tau(t_1, t_2)$ for the cases $\Delta t = 50$ and 200 ns imply a decoherence process operative on a time scale $\tau_d \sim 175$ ns. To investigate this decay, we have performed a separate set of experiments with the delay Δt varied within $0 \leq \Delta t \leq 400$ ns. For each Δt, we determine the normalized correlation function $g_{1,2}^\tau$ from the ratio of integrated coincidence counts to singles counts over the entire detection window (i.e., $\tau = 200$ ns), with the results presented in Fig. 5.5.

In Fig. 5.5, the initial growth of $g_{1,2}^\tau$ for small Δt is due to the finite time required to produce photons sequentially in the $(1, 2)$ fields, which is already evident in Fig. 5.2 and characterized by $\Delta t_2 \cong 60$ ns. More troublesome is the rapid decay of $g_{1,2}^\tau$ over
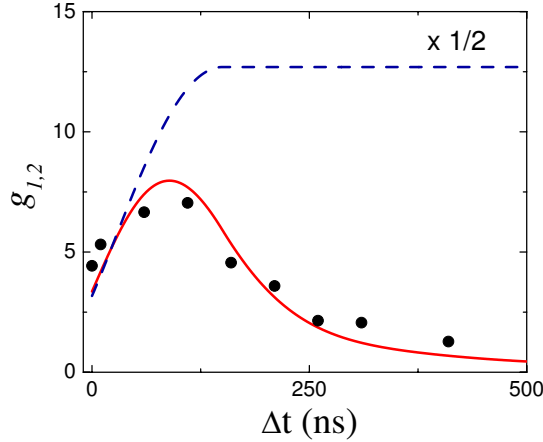
Figure 5.5: Coherence time assessment. Experimentally acquired $g_{1,2}$ (black dots), theoretical description of the current experiment with $K = 1.1$ MHz (solid line), and the theoretical prediction for a spin polarized $m_F = 0$ MOT (dotted line).

times of 100–200 ns. A likely candidate responsible for this decay is Larmor precession among the various Zeeman states of the $F = 3, 4$ hyperfine levels of the $6S_{1/2}$ ground level. Indeed, for our Cs cloud with diameter $L = 3.6$ mm, the quadrupole magnetic field of the MOT reaches 3 G at the edges of the trap [34].

To investigate this possibility, we have extended the treatment of Ref. [23] to include the readout process as well as the full set of Zeeman states for the $F = 3, 4$ hyperfine levels (Chapter 6). The sample of Cs atoms is assumed to be initially unpolarized and uniformly distributed over the MOT's magnetic field. With *write* and *read* pulses that approximate those used in our experiment and separated by Δt, we calculate the joint probability $p_{1,2}^{th}(\Delta t)$ to generate a pair of photons in the $(1,2)$ fields. We compare the quantity $\tilde{p}_{1,2}(\Delta t) \equiv \xi p_{1,2}^{th}(\Delta t)$ to the measured $g_{1,2}(\Delta t)$ by way of a single overall scaling parameter ξ for all Δt. The result is the solid curve in Fig. 5.5 that adequately describes the impact of Larmor precession on our experiment.

The form of $\tilde{p}_{1,2}(\Delta t)$ strongly depends upon the inhomogeneity of Zeeman splitting across the MOT, which is described by the parameter $K = \mu_B g_{F_g} Lb/h$, where b is the gradient of the magnetic field for the MOT and g_{F_g} is the Landé factor. The solid curve in Fig. 5.5 is the theoretical result for an initially unpolarized sample with $K = 1.1$ MHz, which corresponds to our independent estimate of K for our experiment.

A remedy for this dephasing is to eliminate the magnetic field altogether and transfer the sample to a dipole-force trap [34]. Alternatively, we are developing a scheme that should allow for long coherence times even in the presence of the quadrupole field of the MOT by utilizing only magnetic-field insensitive states. The *write, read* beams are circularly polarized $\sigma_{\pm}$ and are aligned along the z-axis of the MOT, which provides the quantization axis. Atoms within the approximately cylindrical volume illuminated by these beams are initially spin polarized into $F = 3(4)$, $m_F = 0$ (note that the beam waist $w_0 = 30$ μm for the *write, read* fields is much smaller than the characteristic dimension $l > 1$mm of the MOT), where m_F marks Zeeman sublevels. The $(1, 2)$ fields are selected to be $\sigma_{\pm}$, which results in spin excitation stored in $F = 4(3)$, $m_F = 0$. The prediction of our model for this new protocol for the same experimental conditions but now with an initially spin polarized sample is shown as the dashed curve in Figure 5.5, resulting in an increase of more than $3\times$ in $g_{1,2}^\tau$, and signifcantly extending the decoherence time to more than $\tau_d \sim 10$ μs.

5.4 Conclusion

In conclusion, we have reported the first observations of the temporal dependence of the joint probability $p_\tau(t_1, t_2)$ for the generation of correlated photon pairs from an atomic ensemble, which is critical for the protocol of Ref. [22]. Our measurements of $p_\tau(t_1, t_2)$ are an initial attempt to determine the structure of the underlying two-photon wavepacket [68]. The time dependence of the ratio $R_\tau(t_1, t_2)$ evidences the nonclassical character of the emitted $(1, 2)$ fields, with $R^{\mathrm{max}} = 292 \pm 57 \nleq 1$. Decoherence due to Larmor precession is characterized and identified as a principal limitation of the current experiment. A new scheme for effectively eliminating this decay process is proposed and analyzed, and could be important for the experimental realization of scalable quantum networks [22] as well as for an improved source for single photons [64].

Chapter 6

Control of Decoherence in the Generation of Photon Pairs from Atomic Ensembles

6.1 Introduction

Quantum memory is a key resource for many quantum information protocols. Usually it is associated with the basic requirements for quantum computation [1, 69], but in recent years quantum communication protocols have also started to rely on it. The requirement of memory was introduced in quantum communication as part of the idea for quantum repeaters [14, 15], a possible solution for the problem of quantum communication over long distances. In this case, memory is essential to increase the probability of success of the chain of conditional steps that underlies the protocol, and makes feasible scalable quantum networks.

In this chapter, we analyze the decoherence processes present in the DLCZ protocol, and describe experiments to mitigate the problem. We construct a theory for the decoherence process in the photon-pair generation. Particularly, our analysis concentrates on its implementation with cold atomic ensembles, but many results should also apply to studies with room-temperature ensembles in vapor cells. We propose various strategies to increase the system's coherence time, and introduce experimental techniques necessary for its characterization and control. We also report experimental steps in this direction, with an increase of more than two order of magnitude in the coherence time with respect to the previously reported works with cold atoms [43, 64, 67, 32, 27].

The coherence times reported up to now by the several groups working on the implementation of the protocol are all shorter or on the order of a couple of microseconds. Furthermore, for all experiments to date, the reported coherence times are of

the order of the excitation pulses duration. However, in order to use this system as a quantum memory, it is important to obtain storage time much longer than the excitation pulses. Moreover, for the DLCZ protocol to become a viable alternative for long distance quantum communication, long coherence time is crucial and major efforts are required to increase it. The main goal of the present chapter is then to provide the initial steps in this direction, and to establish several techniques and ideas for the next steps.

Only two types of systems have been employed in the experiments up to now: vapor cells [65, 70] and cold atoms in magneto-optical traps [27, 32, 43, 64, 67]. In both systems, however, the experiments have not achieved yet their respective state-of-the-art coherence times. The vapor-cell studies, for example, did not employ paraffin-coated cells [71, 72]; the coherence times were effectively limited to the time the atoms take to diffuse out of the excitation region, which is of the order of microseconds. Recently, high fidelity atomic quantum memory of the state of a light pulse was achieved with such paraffin coated cells [73] with memory times of up to 4 ms. Coherence times of tens of milliseconds, however, are commonly achieved in this system [74], and there are reports of coherence times as high as one second [71]. The difference in these values is largely due to measurements of decay of different coherent processes [71]. How the coherence required for the generation of photon pairs from atomic vapors will decay as the atoms collide with the walls of paraffin coated cells is still to be determined.

The use of atomic traps to generate photon pairs for the DLCZ protocol has the advantage of providing a high density of atoms distributed in a small spectral region,

due to the suppression of Doppler broadening by the cooling process. This allows the use of excitation laser pulses tuned closer to resonance, which requires much less power and makes it easier to filter the excitation pulses from the Ramam-scattered photons. However, atomic traps also introduce a different set of complications. In the case of the magneto-optical traps (MOT) used up to now, the magnetic field of the trap induces decoherence on a timescale of the order or smaller than a few hundreds nanoseconds [27, 32, 67]. The first results with the MOT magnetic field off are reported in this chapter, with coherence times on the order of 10 μs. As will be discussed below in detail, a better nulling of the magnetic field combined with optical pumping to specific Zeeman levels might increase the coherence time, in a straightforward way, to hundreds of microseconds.

Further improvements with MOTs would face the problem of diffusion of atoms from the excitation region and, most troublesome, from the MOT itself. This problem can in principle be mitigated by improved cooling techniques. However, along these lines, it would be difficult to increase the coherence time above a couple of milliseconds. A possible solution then is to use an optical dipole trap to hold the atoms during the write-and-read process. Hyperfine coherence times of hundreds of milliseconds have already been observed in such traps [75, 76].

In the following, Sec. 6.2 is devoted to theoretical results and Sec. 6.3 to associated experiments. In Sec. 6.2 we give a general introduction to the photon-pair generation process behind the DLCZ protocol and then derive a theory for the probability of joint detection of these photon pairs generated from an atomic ensemble in a magneto-optical trap. This theory is a direct extension of a previous theoretical treatment

reported in Ref. [23], to which we added explicitly the reading process and the Zeeman structure of the levels. In this way, we are able to model the action of the magnetic field over the atoms, and to study the dependence of the correlations with the light polarization.

Section 6.3 describes an experimental investigation leading to the nulling of the magnetic field in the photon-pair correlation measurements, with the subsequent increase in the system coherence time and degree of correlation. In Sec. 6.3.1, we describe a series of Raman-spectroscopy experiments to characterize the system and optimize the process of zeroing the magnetic field. We determine the set of experimental conditions that result in a good compromise between atomic density and magnetic field cancellation, which we used in the correlation measurements. Section 6.3.2 describes then measurements of nonclassical correlations for the photon pairs generated by the MOT. We compare results with magnetic field on and with magnetic field off. The magnetic field off measurements present a higher degree of correlation, and a hundred times larger coherence time. We compare the shape of the experimental curves with magnetic field on and off to our theory, obtaining good agreement. We also show how the two-photon wavepacket that describes the detailed temporal structure of the photon pair generation is modified by the magnetic field.

Finally, based on the procedure for comparison between theory and experiment described in Sec. 6.3.2, we formulate in Sec. 6.4 a proposal to improve our experimental signal. We suggest using a combination of optical pumping to a specific initial state and polarization of the light fields to increase both our detection efficiency and coherence time. Section 6.5 summarizes and concludes this chapter.

This chapter is largely based on Ref. [77].

6.2 Theory

The basic theory for the DLCZ protocol is described in Refs. [22] and [23]. The general idea of the protocol is treated in Ref. [22], while Ref. [23] gives a detailed analysis of the collective emission of photons through spontaneous Raman scattering following excitation by free-space light. This section provides an extension of the theoretical treatment of Ref. [23] to better account for our experimental conditions. The emphasis here is the modeling of the decoherence process due to external magnetic fields, and in particular for experiments using magneto-optical traps. To model this decoherence, the essential elements to be introduced in the previous theory of Ref. [23] are the Zeeman structure of all levels and an explicit treatment of the reading process. On the other hand, the theory in this section is a simplification of the treatment of Ref. [23] concerning the spatial mode of the photons. We consider only the forward, collectively enhanced emission. The reading process is also treated in a simplified, perturbative way, while the experiments are done with stronger read pulses on resonance. This later difference between theory and experiment will result in some noticeable discrepancy in Sec. 6.3.4, where we discuss measurements of the two-photon wavepacket of the pair-generation process. In general, however, the comparison between theory and experiment performed in Sec. 6.3.2 results in very good agreement, which indicates that the theory here takes into account the essential physical elements behind the decoherence process.

In order to analyze the decoherence process in the generation of pairs from an atomic ensemble as described in Chapter 3, we need to expand the theoretical treatment of Ref. [23] to include other experimentally relevant features. For our experiments in particular, it is essential to include the splitting of the Zeeman structure of the atomic ground states due to the magnetic field. The MOT quadrupole field generates an inhomogeneous distribution of splittings throughout the ensemble. As the system evolves in time, this results in dephasing between different regions of the atomic cloud, and in a respective decay of the coherence of the collective state. It is also important to include explicitly the reading process in the theory. For simplicity, this is done by considering a reading process similar to the writing process, i.e., with small probability of excitation and detuned from the excited state. Note that in the actual experiment, the read beam is stronger than the write beam and is on resonance. This will lead to small discrepancies when comparing the experimental results to the theory that will be discussed in section 6.3.4.

The inclusion of Zeeman structure in the theory allows a detailed discussion of the effect of light polarization in the experiment. This is important to evaluate different excitation and detection schemes. It also gives a better description of the initial state, and of its role on the subsequent coherent pair generation. Together, the analysis of different polarization schemes and of different initial states led to specific proposals of ways to improve the whole process. These features of the theory are not specifically related to the MOT magnetic field, and should apply to pair generation in other systems, like vapor cells or dipole traps.

Our treatment starts by considering a sample of N four-level atoms, such as in

Fig. 6.1. The four levels represent manifolds of Zeeman sublevels and are indicated by their respective F quantum numbers. A specific state of the F_j manifold of the ith atom is represented by its ket $|m_j\rangle_i$, where m_j is the azimuthal quantum number. Two pumping fields act on the system, namely a write field $\vec{\mathcal{E}}_{ga}$ and a read field $\vec{\mathcal{E}}_{sb}$, where

$$\vec{\mathcal{E}}_{ga}(\vec{r},t) = u_w(\vec{r},t)e^{i(k_w z - \omega_w t)}\vec{e}_{p_w}, \qquad (6.1\text{a})$$

$$\vec{\mathcal{E}}_{sb}(\vec{r},t) = u_r(\vec{r},t)e^{i(k_r z - \omega_r t)}\vec{e}_{p_r}, \qquad (6.1\text{b})$$

which couple the transitions $F_g \to F_a$ and $F_s \to F_b$, respectively. The functions u_w and u_r give the slowly varying envelopes of the *write* and *read* pulses, respectively, and $\vec{e}_{p_w}$ and $\vec{e}_{p_r}$ are their polarization vectors. As a result of their action, two Raman fields are spontaneously generated in the sample:

$$\hat{\vec{\mathcal{E}}}_{sa}(\vec{r},t) \propto \sum_{p_1} \int d\vec{k}_1 \hat{a}_{\vec{k}_1 p_1} e^{i(\vec{k}_1 \cdot \vec{r} - \omega_{\vec{k}_1} t)}\vec{e}_{p_1}, \qquad (6.2\text{a})$$

$$\hat{\vec{\mathcal{E}}}_{gb}(\vec{r},t) \propto \sum_{p_2} \int d\vec{k}_2 \hat{b}_{\vec{k}_2 p_2} e^{i(\vec{k}_2 \cdot \vec{r} - \omega_{\vec{k}_2} t)}\vec{e}_{p_2}, \qquad (6.2\text{b})$$

where $\omega_{\vec{k}_i} = |\vec{k}_i|c$ and p_i is a label for the field polarization. $\hat{a}_{\vec{k}_1 p_1}$ and $\hat{b}_{\vec{k}_2 p_2}$ are the annihilation operators for the Raman fields 1 and 2, respectively, which couple the transitions $F_s \to F_a$ and $F_g \to F_b$. The state of field 1 with just one photon excited in mode $\vec{k}_1 p_1$ will be designated by $|1_{\vec{k}_1 p_1}\rangle$. A similar notation will be used for field 2.
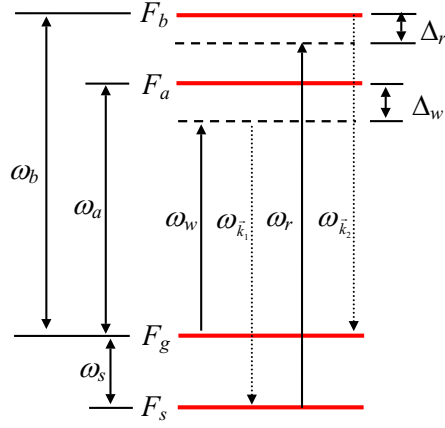
Figure 6.1: Energy level scheme considered for the atomic ensembles.

The Hamiltonian for the system of N atoms can be written as

$$\hat{H}(t) = \hat{H}_0 + \hat{V}(t) \,, \tag{6.3}$$

where

$$
\begin{aligned}
\hat{H}_0 = \sum_{i=1}^{N} \Bigg\{ & \sum_{m_s=-F_s}^{F_s} \left(-\hbar\omega_s + \mu_B g_s m_s B_{z_i} \right) |m_s\rangle_i \langle m_s| \\
& + \sum_{m_g=-F_g}^{F_g} \mu_B g_g m_g B_{z_i} |m_g\rangle_i \langle m_g| \\
& + \sum_{m_a=-F_a}^{F_a} \hbar\omega_a |m_a\rangle_i \langle m_a| + \sum_{m_b=-F_b}^{F_b} \hbar\omega_b |m_b\rangle_i \langle m_b| \Bigg\}
\end{aligned}
\tag{6.4}
$$

is the free-atom Hamiltonian, and

$$
\begin{aligned}
\hat{V}(t) = \sum_{i=1}^{N} \Bigg\{ & \sum_{m_a=-F_a}^{F_a} \sum_{m_g=-F_g}^{F_g} \left(-\vec{d}_{m_a m_g} \cdot \vec{\mathcal{E}}_{ga} \right) |m_a\rangle_i \langle m_g| \\
& + \sum_{m_s=-F_s}^{F_s} \sum_{m_a=-F_a}^{F_a} \left(-\vec{d}_{m_s m_a} \cdot \hat{\vec{\mathcal{E}}}_{sa}^{\dagger} \right) |m_s\rangle_i \langle m_a| \\
& + \sum_{m_b=-F_b}^{F_b} \sum_{m_s=-F_s}^{F_s} \left(-\vec{d}_{m_b m_s} \cdot \vec{\mathcal{E}}_{sb} \right) |m_b\rangle_i \langle m_s| \\
& + \sum_{m_g=-F_g}^{F_g} \sum_{m_b=-F_b}^{F_b} \left(-\vec{d}_{m_g m_b} \cdot \hat{\vec{\mathcal{E}}}_{gb}^{\dagger} \right) |m_g\rangle_i \langle m_b| \Bigg\} + h.c.
\end{aligned}
\tag{6.5}
$$

gives the time-dependent interaction Hamiltonian. $\vec{d}_{jk}$ is the dipole moment for the $j \rightarrow k$ transition, μ_B the Bohr magneton, g_j the hyperfine Landé factor for level F_j, B_{z_i} is the magnetic field in the position of the ith atom, and $h.c.$ stands for the Hermitian conjugate. The magnetic field direction is assumed to be in the quantization z axis. We neglect the Zeeman splitting of the excited states since we want to investigate a situation where it is always smaller than the excited states' natural linewidths. The factors $-\vec{d}_{jk} \cdot \vec{\mathcal{E}}_{kj}$ can also be written as

$$
-\vec{d}_{m_a m_g} \cdot \vec{\mathcal{E}}_{ga} = K_{m_a m_g} u_w(\vec{r}_i, t) e^{i(k_w z_i - \omega_w t)} ,
\tag{6.6a}
$$

$$
-\vec{d}_{m_s m_a} \cdot \hat{\vec{\mathcal{E}}}_{sa}^{\dagger} = \sum_{p_1} \int d\vec{k}_1 K_{m_s m_a}^{\vec{k}_1 p_1} \hat{a}_{\vec{k}_1 p_1}^{\dagger} e^{-i(\vec{k}_1 \cdot \vec{r} - \omega_{\vec{k}_1} t)} ,
\tag{6.6b}
$$

$$
-\vec{d}_{m_b m_s} \cdot \vec{\mathcal{E}}_{sb} = K_{m_b m_s} u_r(\vec{r}_i, t) e^{i(k_r z_i - \omega_r t)} ,
\tag{6.6c}
$$

$$
-\vec{d}_{m_g m_b} \cdot \hat{\vec{\mathcal{E}}}_{gb}^{\dagger} = \sum_{p_2} \int d\vec{k}_2 K_{m_g m_b}^{\vec{k}_2 p_2} \hat{b}_{\vec{k}_2 p_2}^{\dagger} e^{-i(\vec{k}_2 \cdot \vec{r} - \omega_{\vec{k}_2} t)} ,
\tag{6.6d}
$$

where $K_{m_a m_g}$, $K_{m_s m_a}^{\vec{k}_1 p_1}$, $K_{m_b m_s}$, and $K_{m_g m_b}^{\vec{k}_2 p_2}$ are coupling constants for the corresponding

transition.

The temporal evolution of the coupled system consisting of the ensemble and Raman fields is described by the evolution of its density matrix $\hat{\rho}(t)$. In the interaction picture, the corresponding operator $\hat{\rho}_I(t)$ is given by

$$\hat{\rho}_I(t) = \hat{U}_I(t)\hat{\rho}(0)\hat{U}_I^\dagger(t)\,, \tag{6.7}$$

where $\hat{U}_I(t)$ is the temporal evolution operator, and the initial state $\hat{\rho}(0)$ can be written as

$$\hat{\rho}(0) = \hat{\rho}_{F_1}(0) \otimes \hat{\rho}_{F_2}(0) \otimes \hat{\rho}_1(0) \otimes \hat{\rho}_2(0) \otimes \cdots \otimes \hat{\rho}_N(0)\,, \tag{6.8}$$

with $\hat{\rho}_{F_1}(0)$ the initial state of field 1, $\hat{\rho}_{F_2}(0)$ the initial state of field 2, and $\hat{\rho}_i(0)$ the initial state of the ith atom. For most of what follows, we will be interested in the case where the fields 1 and 2 are initially vacuum states, $\hat{\rho}_{F_1}(0) = |vac_{F_1}\rangle\langle vac_{F_1}|$ and $\hat{\rho}_{F_2}(0) = |vac_{F_2}\rangle\langle vac_{F_2}|$, and all atoms are initially in the same incoherent distribution over the Zeeman sublevels of the F_g state:

$$\hat{\rho}_i(0) = \sum_{m_g=-F_g}^{F_g} D_{m_g}|m_g\rangle_i\langle m_g|\,, \tag{6.9}$$

with D_{m_g} giving the probability of finding an atom in the m_g state at $t = 0$. In section 6.4 however, we will consider the case where all the atoms are optically pumped in one of the Zeeman sublevels ($m_F = 0$).

The operator $\hat{U}(t)$ can be written as a Dyson series in the form

$$\hat{U}_I(t) = 1 + \sum_{i=1}^{N} \hat{\mathcal{U}}_i^{(1)}(t) + \sum_{i=1}^{N} \hat{\mathcal{U}}_i^{(2)}(t) + \cdots , \tag{6.10}$$

where

$$\begin{aligned}
\hat{\mathcal{U}}_i^{(1)}(t) &= \left(-\frac{i}{\hbar}\right) \int_0^t dt' \hat{\mathcal{V}}_i(t') , \\
\hat{\mathcal{U}}_i^{(2)}(t) &= \left(-\frac{i}{\hbar}\right)^2 \int_0^t dt' \int_0^{t'} dt'' \hat{\mathcal{V}}_i(t') \hat{\mathcal{V}}_i(t'') ,
\end{aligned} \tag{6.11}$$

and so on. The single-atom interaction operator $\hat{\mathcal{V}}_i(t)$ is defined from the expression for the general interaction Hamiltonian $\hat{V}_I(t)$ in the interaction picture as

$$\hat{V}_I(t) = e^{i\hat{H}_0 t/\hbar} \hat{V}(t) e^{-i\hat{H}_0 t/\hbar} = \sum_{i=1}^{N} \hat{\mathcal{V}}_i(t) . \tag{6.12}$$

6.2.1 Probability for joint detections

We want to calculate in the lowest order of perturbation the probability of detecting a single photon in field 1 followed by another photon in field 2. The first step is then to calculate the restriction of the coupled state $\hat{\rho}(t)$ to the space of states of fields 1 and 2:

$$\hat{\rho}_{F_1 F_2}(t) = \mathrm{Tr}_A \left[\hat{\rho}(t) \right] . \tag{6.13}$$

The symbol Tr_A indicates a partial trace over all atomic states. The probability for detecting two photons, one in mode $\vec{k}_1 p_1$ and the other in mode $\vec{k}_2 p_2$, up to time t is

then given by

$$p_{12}^{th}(t, \vec{k}_1 p_1, \vec{k}_2 p_2) = \langle 1_{\vec{k}_1 p_1}|\langle 1_{\vec{k}_2 p_2}|\hat{\rho}_{F_1 F_2}(t)|1_{\vec{k}_2 p_2}\rangle|1_{\vec{k}_1 p_1}\rangle$$

$$= \langle 1_{\vec{k}_1 p_1}|\langle 1_{\vec{k}_2 p_2}|\text{Tr}_A\left[\hat{\rho}(t)\right]|1_{\vec{k}_2 p_2}\rangle|1_{\vec{k}_1 p_1}\rangle. \tag{6.14}$$

Since all atoms are initially in the ground state F_g, the lowest order term of series (6.10) that results in a single photon in field 1 and another photon in field 2 is the fifth term, which accounts for the four transitions carried successively by the write field, photon 1, read field, and photon 2, respectively. Substituting Eqs. (6.7) and (6.10) into Eq. (6.14) and keeping only the lowest order term, we arrive then at

$$p_{12}^{th}(t, \vec{k}_1 p_1, \vec{k}_2 p_2) =$$
$$\sum_{i,j=1}^{N} \langle 1_{\vec{k}_1 p_1}|\langle 1_{\vec{k}_2 p_2}|\text{Tr}_A\left[\hat{\mathcal{U}}_i^{(4)}(t)\hat{\rho}(0)\hat{\mathcal{U}}_j^{(4)\dagger}(t)\right]|1_{\vec{k}_2 p_2}\rangle|1_{\vec{k}_1 p_1}\rangle. \tag{6.15}$$

Note that $\hat{\mathcal{U}}_k^{(4)}$ acts only over the kth atom. Thus, the trace Tr_A on each term of the double sum can be written as a trace Tr_k over the states of the atoms at which the $\hat{\mathcal{U}}_k^{(4)}$ operator is acting, since all other atoms remain in their initial state. Two different cases are present in Eq. (6.15). If $i \neq j$, the two operators act over two different atoms and the initial state $\hat{\rho}(0)$ simplifies to $\hat{\rho}_{F_1}(0) \otimes \hat{\rho}_{F_2}(0) \otimes \hat{\rho}_i(0) \otimes \hat{\rho}_j(0)$. If $i = j$, then $\hat{\rho}(0) \rightarrow \hat{\rho}_{F_1}(0) \otimes \hat{\rho}_{F_2}(0) \otimes \hat{\rho}_i(0)$. With these observations in mind, we

see that Eq. (6.15) can then be written as

$$
p_{12}^{th}(t, \vec{k}_1 p_1, \vec{k}_2 p_2) =
$$

$$
\sum_{\substack{i,j=1 \\ i \neq j}}^{N} \langle 1_{\vec{k}_1 p_1}| \langle 1_{\vec{k}_2 p_2}| \mathrm{Tr}_i \left[\hat{\mathcal{U}}_i^{(4)}(t) \hat{\rho}_i(0) \right] |vac_{F_2}\rangle |vac_{F_1}\rangle
$$

$$
\times \langle vac_{F_1}| \langle vac_{F_2}| \mathrm{Tr}_j \left[\hat{\rho}_j(0) \hat{\mathcal{U}}_j^{(4)\dagger}(t) \right] |1_{\vec{k}_2 p_2}\rangle |1_{\vec{k}_1 p_1}\rangle
$$

$$
+ \sum_{i=1}^{N} \langle 1_{\vec{k}_1 p_1}| \langle 1_{\vec{k}_2 p_2}| \mathrm{Tr}_i \left[\hat{\mathcal{U}}_i^{(4)}(t) \hat{\rho}_{F_1}(0) \otimes \hat{\rho}_{F_2}(0) \otimes \hat{\rho}_i(0) \right.
$$

$$
\left. \times \hat{\mathcal{U}}_i^{(4)\dagger}(t) \right] |1_{\vec{k}_2 p_2}\rangle |1_{\vec{k}_1 p_1}\rangle. \tag{6.16}
$$

Substituting Eq. (6.9), we have

$$
p_{12}^{th}(t, \vec{k}_1 p_1, \vec{k}_2 p_2) = \left| \sum_{i=1}^{N} \sum_{m_g=-F_g}^{F_g} D_{mg} A_i(m_g, m_g) \right|^2
$$

$$
- \sum_{i=1}^{N} \left| \sum_{m_g=-F_g}^{F_g} D_{mg} A_i(m_g, m_g) \right|^2
$$

$$
+ \sum_{i=1}^{N} \sum_{m'_g=-F_g}^{F_g} \sum_{m_g=-F_g}^{F_g} D_{mg} |A_i(m'_g, m_g)|^2, \tag{6.17}
$$

where

$$
A_i(m'_g, m_g) = \langle 1_{\vec{k}_1 p_1}| \langle 1_{\vec{k}_2 p_2}| \langle m'_g|_i \hat{\mathcal{U}}_i^{(4)}(t) |m_g\rangle_i |vac_{F_2}\rangle |vac_{F_1}\rangle. \tag{6.18}
$$

Note that the first term on the right side of Eq. (6.17) scales as N^2, while the two remaining terms scale with N only. Since we are interested in the limit of large N,

we can then approximate

$$p_{12}^{th}(t, \vec{k}_1 p_1, \vec{k}_2 p_2) = \left| \sum_{i=1}^{N} \sum_{m_g=-F_g}^{F_g} D_{mg} A_i(m_g, m_g) \right|^2 . \tag{6.19}$$

Thus, for large N, only transitions that start and end in the same state contribute to the pair generation. This result can be understood as a constructive interference between all pathways that connect the ensemble back to its initial state, after which it is not possible to distinguish which atom made the transition [78]. Pathways connecting different initial and final states leave a trace in the ensemble, which in principle can give information on which specific atom made the transition. In this last case, the number of possible pathways generating the pair of photons is then linearly proportional to the number of atoms N. Eq. (6.19) expresses the collective enhancement that is essential to the scheme of ref. [22].

Finally, substituting the specific expressions for $\hat{\mathcal{U}}_i^{(4)}(t)$ and $\hat{\mathcal{V}}_i(t)$, we find that $A_i(m_g, m_g)$ can be written as

$$\begin{aligned}
A_i(m_g, m_g) = &\sum_{m_s=-F_s}^{F_s} \frac{d(m_g, ms)}{\hbar^4} e^{i(k_r z_i + k_w z_i - \vec{k}_1 \cdot \vec{r}_i - \vec{k}_2 \cdot \vec{r}_i)} \\
&\times \int_0^t dt' e^{i(\Delta\omega_{\vec{k}_2} - \Delta_r + a_{ig})t'} \\
&\times \int_0^{t'} dt'' u_r(\vec{r}_i, t'') e^{i(\Delta_r - a_{is})t''} \\
&\times \int_0^{t''} dt''' e^{i(\Delta\omega_{\vec{k}_1} - \Delta_w + a_{is})t'''} \\
&\times \int_0^{t'''} dt'^\nu u_w(\vec{r}_i, t'^\nu) e^{i(\Delta_w - a_{ig})t'^\nu} ,
\end{aligned} \tag{6.20}$$

where $\Delta_w = \omega_a - \omega_w$, $\Delta_r = \omega_b + \omega_s - \omega_r$, $\Delta\omega_{\vec{k}_1} = \omega_{\vec{k}_1} - \omega_w - \omega_s$, $\Delta\omega_{\vec{k}_2} = \omega_{\vec{k}_2} - \omega_r + \omega_s$,

and

$$d(m_g, m_s) = \sum_{m_b=-F_b}^{F_b} \sum_{m_a=-F_a}^{F_a} K_{m_g m_b}^{\vec{k}_2 p_2} K_{m_b m_s}^{r} K_{m_s m_a}^{\vec{k}_1 p_1} K_{m_a m_g}^{w} \tag{6.21}$$

gives the strength of an specific excitation pathway in which the atom starts at m_g, then goes to m_s, and ends at m_g again. The Zeeman splittings are written in terms of the parameters $a_{ig} = \mu_B g_g m_g B_{z_i}/\hbar$ and $a_{is} = \mu_B g_s m_s B_{z_i}/\hbar$.

6.2.2 Forward emission

In order to simplify the following analysis while keeping the essential trends of the temporal dynamics, we will focus now on the treatment of the forward, resonant emission from the atomic ensemble. In the forward direction, the light emitted by the sample satisfies the phase-matching condition

$$k_r z_i + k_w z_i - \vec{k}_1 \cdot \vec{r}_i - \vec{k}_2 \cdot \vec{r}_i = 0. \tag{6.22}$$

The resonant conditions for the Raman fields are $\Delta\omega_{\vec{k}_1} = 0$ and $\Delta\omega_{\vec{k}_2} = 0$. A discussion about deviations from these conditions can be found at Ref. [23].

Under these assumptions, and with the slow envelope functions written as

$$u_r(\vec{r}_i, t) = q_r(\vec{r}_i) f_r(t), \tag{6.23a}$$

$$u_w(\vec{r}_i, t) = q_w(\vec{r}_i) f_w(t), \tag{6.23b}$$

Equation (6.20) becomes

$$A_i(m_g, m_g) = q_r(\vec{r}_i)q_w(\vec{r}_i) \sum_{m_s=-F_s}^{F_s} \frac{d(m_g, ms)}{\hbar^4} F(t, z_i) , \tag{6.24}$$

with

$$F(t, z_i) = \int_0^t dt' e^{i(-\Delta_r + a_{ig})t'} \int_0^{t'} dt'' f_r(t'') e^{i(\Delta_r - a_{is})t''}$$
$$\times \int_0^{t''} dt''' e^{i(-\Delta_w + a_{is})t'''} \int_0^{t'''} dt'^\nu f_w(t'^\nu) e^{i(\Delta_w - a_{ig})t'^\nu} . \tag{6.25}$$

Note that the F function depends on the parameters for a specific atom only through z_i that specifies its position along the quantization axis. In this way, after a certain time, atoms in different parts of the ensemble contribute to the probability amplitude of the process with different phases.

If we consider a uniform distribution of atoms throughout the beam path, and neglecting the z dependence on the q functions, the sum over all atoms may be transformed in the following integral

$$\sum_{i=1}^N q_r(\vec{r}_i)q_w(\vec{r}_i) \to \frac{N}{V} \int\int\int dx\, dy\, dz\, q_r(x, y)q_w(x, y)$$
$$= \int\int dx\, dy \frac{q_r(x, y)q_w(x, y)}{A} \frac{N}{L} \int dz$$
$$= \langle q_r(x, y)q_w(x, y) \rangle\, N \int_{-L/2}^{L/2} \frac{dz}{L} , \tag{6.26}$$

where $V = AL$ gives the volume of the excitation region, A its transverse area, and L its length.

Substituting Eqs. (6.24) and (6.26) in Eq. (6.19), we finally obtain

$$p_{12}^{th}(t) = C \left| \sum_{m_g=-F_g}^{F_g} \sum_{m_s=-F_s}^{F_g} D_{m_g} d(m_g, m_s) \int_{-L/2}^{L/2} \frac{dz}{L} F(t, z) \right|^2, \qquad (6.27)$$

where

$$C = N^2 \left| \langle q_r(x, y) q_w(x, y) \rangle \right|^2, \qquad (6.28)$$

is a constant. After the read pulse has left the sample (i.e., when $t \to \infty$), Expression (6.27) is then proportional to the total probability of detecting the pair of photons in one trial. Details on how to compare this expression to the experimental results will be discussed in Sec. 6.3.3. In the experimentally important case of square pulses, it is straightforward to obtain analytical expressions for both $F(t, z)$ and $p_{12}(t)$ in the limit of large Δ_w and Δ_r.

6.2.3 Probability density

Equation (6.27) gives the total probability of detecting one photon in field 2 after detecting a photon in field 1. Now we want to obtain the probability of finding photon 2 between times t_2 and $t_2 + \Delta t_2$ and photon 1 between times t_1 and $t_1 + \Delta t_1$, for small Δt_2 and Δt_1.

The first step in this calculation is to note that Eq. (6.27) can be written as,

$$p_{12}^{th}(t) = |\phi(t)|^2. \qquad (6.29)$$

The function $\phi(t)$ gives then a probability amplitude for the process where the two

photons are found up to time t. It consists of an integral over all possible pairs of detection times (t_2, t_1), representing different excitation pathways, and can in principle also be written as

$$\phi(t) = \int_0^t dt_1 \int_{t_1}^t dt_2 P(t_2, t_1), \tag{6.30}$$

where we considered explicitly $t_2 > t_1$. $P(t_2, t_1)$ represents then a density of probability amplitude.

The probability amplitude for finding photon 2 between times t_2 and $t_2 + \Delta t_2$, and photon 1 between times t_1 and $t_1 + \Delta t_1$, can be obtained then by restricting the limits in the temporal integral in Eq. (6.27). Since all the temporal dynamics in Eq. (6.27) is in the function $F(t, z)$, we need to find out first the restriction on $F(t, z)$ for these specific processes. In order to do so, note that, in the fourth order integral of $F(t, z)$, Eq. (6.25), the emission of photon 2 is described by the integral over t', while photon 1 emission is described by the integral over t'''. The restricted form of $F(t, z)$ for the emission of photon 2 between times t_2 and $t_2 + \Delta t_2$, and photon 1 between times t_1 and $t_1 + \Delta t_1$, is then given by

$$G(t_2, \Delta t_2, t_1, \Delta t_1) = \int_{t_2}^{t_2 + \Delta t_2} dt' e^{i(-\Delta_r + a_{ig})t'} \int_0^{t'} dt'' f_r(t'') e^{i(\Delta_r - a_{is})t''}$$
$$\times \int_{t_1}^{t_1 + \Delta t_1} dt''' e^{i(-\Delta_w + a_{is})t'''} \int_0^{t'''} dt'^\nu f_w(t'^\nu) e^{i(\Delta_w - a_{ig})t'^\nu}. \tag{6.31}$$

Equation (6.31) can also be deduced in a more formal way, beginning by considering that the probability amplitude for detecting photon 2 between t_2 and $t_2 + \Delta t_2$ is given by $\phi(t_2 + \Delta t_2) - \phi(t_2)$, then following all the way down by similar restrictions,

and finally making the approximation of small time intervals.

Equation (6.31) can be directly evaluated for the case of square pulses and large detunings, such that $\Delta_r, \Delta_w >> \Delta t_2^{-1}, \Delta t_1^{-1}$. If the time intervals are also small when compared to the timescale of oscillations determined by the Zeeman shifts (i.e., $\Delta t_2, \Delta t_1 << a_g^{-1}, a_s^{-1}$), then Eq. (6.31) can be written as

$$G(t_2, \Delta t_2, t_1, \Delta t_1) = g(t_2, t_1)\Delta t_1 \Delta t_2 \,, \tag{6.32}$$

with

$$g(t_2, t_1) = -\frac{f_r(t_2)f_w(t_1)}{\Delta_r \Delta_w} \, e^{i(a_g - a_s)(t_2 - t_1)} \,. \tag{6.33}$$

In this case, $F(t, z)$ can be derived by:

$$F(t, z) = \int_0^t dt_1 \int_{t1}^t dt_2 \, g(t_2, t_1) \,. \tag{6.34}$$

An important remark is that, since any pulse envelope can be approximated by a sum of square pulses of different intensities and small duration, Eq. (6.33) is indeed valid for arbitrary pulse shapes, as long as the envelope temporal variation occurs in a much longer timescale than Δt_1 or Δt_2.

The connection between $g(t_2, t_1)$ and the density of probability amplitude $P(t_2, t_1)$

is then made through the relation

$$P(t_2, t_1) = \sqrt{C} \sum_{m_g=-F_g}^{F_g} \sum_{m_s=-F_s}^{F_g} D_{m_g} d(m_g, m_s)$$
$$\times \int_{-L/2}^{L/2} \frac{dz}{L} g(t_2, t_1). \tag{6.35}$$

Finally, the probability density for detecting one photon from field 1 at time t_1 and another from field 2 at t_2 is associated to

$$\mathcal{P}(t_2, t_1) = |P(t_2, t_1)|^2. \tag{6.36}$$

This is the quantity to be compared with the experimental results of Sec. 6.3.4, for the two-photon wavepacket of the photon pair.

6.3   Experiments

Up to this point, the experimental implementation of the DLCZ protocol in MOTs have been plagued by extremely short coherence times [43, 64, 67, 32]. As discussed above, this short coherence time is a result of the action of the MOT quadrupole magnetic field over the Zeeman structure of the hyperfine ground states. In the following, we are going to describe a series of experiments that allowed us to obtain photon pairs from the trapped atomic cloud in a situation of very small magnetic field. In this way, we were able to measure coherence times of more than 10 μs (more than two orders of magnitude longer than the duration of the excitation pulses),

and two-photon wavepackets for the photon pairs that do not exhibit distortion by decoherence even when write and read pulses cease overlapping in time [67].

The crucial point is to turn off the MOT magnetic field and determine the experimental conditions with a best tradeoff between high repetition rate and high optical density. Note that the atoms fly away from the trap and the density starts to decrease when the magnetic field is turned off. Hence, the MOT field has to be turned off as fast as possible, to decrease the transient time and maximize the region with low magnetic field and high density. A fast turning off of the magnetic field in our metallic vacuum chambers, however, is not straightforward and requires special techniques, as will be discussed in Sec. 6.3.1.

Inside each MOT-off period, it is possible to conduct many trials of the photon-pair-generation experiments. These are photon counting measurements that require many events in order to acquire good statistics. Hence, we would like to have as many MOT-off periods as possible to accumulate a large number of trials. However, the MOT needs some time to recover its original density after each off period, and this time limits how often it can be turned off while still keeping a high enough atomic number density.

During the process of turning off the magnetic field and determining the proper conditions for the photon counting experiments, it was essential to be able to perform experiments giving direct access to the ground state broadening by the magnetic field. We chose then to setup a copropagating stimulated Raman spectroscopy apparatus to help us in this process. The results for the Raman spectroscopy measurements and the investigation to determine the best experimental conditions for the photon pair

generation are described in Sec. 6.3.1.

The nonclassical correlation experiments are discussed in Sec. 6.3.2. There we show that the coherence time increases by more than two orders of magnitude once the magnetic field is switched off, and describe measurements of the shape of the two-photon wavepacket in both situations. In this section, we also compare the experimental results with the theory of Sec. 6.2

6.3.1 Characterization and magnetic field nulling

As anticipated above, we use copropagating stimulated Raman spectroscopy [79] to probe directly the broadening of the hyperfine ground states. Our choice for this specific technique is based on the fact that it is insensitive to Doppler broadening, but very sensitive to any broadening caused by magnetic fields, exactly like the spontaneous Raman emission process underlying the photon pair generation in our experiment. Raman stimulated transitions (see Fig. 6.2(a)) are two-photon transitions connecting one ground-state hyperfine level to the other one, in which a single photon is absorbed from one Raman beam and another photon is emitted in the other beam by stimulated emission through a virtual level, which is located 3 GHz below the Cesium D_2 line in our setup.

The Raman process is resonant if the frequency difference of the two Raman beams equals the ground-state hyperfine interval, 9.192631770 GHz for cesium. In the absence of collisions and transit broadening, this two-photon resonance is very sharp, with a linewidth limited only by the power and duration of the Raman beams [79].

In this way, since the specific value of the hyperfine interval for transitions between $|m_g\rangle$ and $|m_s\rangle$ states changes with the magnetic field, scanning the frequency of one Raman beam with respect to the other gives direct information on the frequency distribution of possible two-photon resonances shifted by the magnetic field, i.e., on the broadening of the ground state.

Our setup for Raman spectroscopy is shown in Fig. 6.2(a). The two Raman beams and a probe beam are coupled to the same polarization maintaining fiber, which takes the beams close to the MOT and provides good mode matching between them. The probe beam is coupled with the same polarization as the Raman field connecting the $F = 3$ ground state to the virtual level, the other Raman field is coupled with the orthogonal polarization. The lens at the fiber output focuses the beam to a diameter of 150 μm in the MOT region. After the fiber, the beams pass through a 50-50 beam splitter cube. The transmitted parts of the beams are used as a reference to compensate for power fluctuations. The reflected part is directed to the MOT, forming an angle of about $\theta \approx 3°$ with the quadrupole-field z-axis. The shaded area around the z axis in Fig. 6.2(a) indicates the path of one of our trapping beams. The absorption of the probe beam by the atoms in the MOT is then measured with a second detector by comparing the probe pulse height with MOT on and off.

Before the Raman pulses reach the MOT, an optical pumping cycle moves the whole atomic population to just one of the hyperfine ground states. Note that for the following experiments, we make no attempt to optically pump the atoms into a specific Zeeman state. Hence, the atomic ensemble is unpolarized and all Zeeman substates are populated. The action of the Raman pulses, of about 150 μs duration
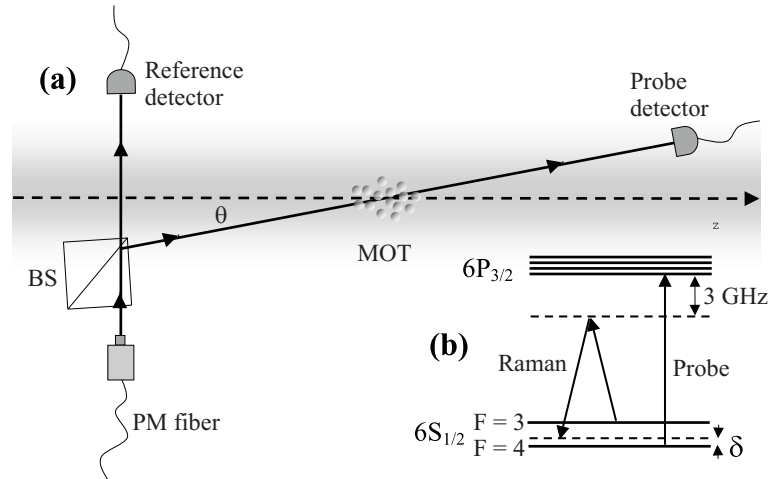
Figure 6.2: (a) Experimental Raman spectroscopy setup. The Raman beams and the probe beam are coupled into a polarization maintaining (PM) fiber and sent through a beam spitter cube (BS). The reflected part is focused into the sample with an angle of 3 degrees with respect to the quadrupole field z axis, while the transmitted part is used as a reference. (b) Relevant level structures and laser frequencies for Raman spectroscopy.

and 10 μW peak power, then transfers some population of atoms to the initially empty level if their relative detuning matches one of the two-photon transitions of the sample. The probe pulse has a duration of 5 μs and goes in the MOT 50 μs after the Raman pulses. It is resonant with the cycling transition connecting the initially empty ground state to the $6P_{3/2}$ level ($F = 4 \rightarrow F' = 5$ if the empty ground state is $F = 4$, $F = 3 \rightarrow F' = 2$ for empty $F = 3$ state). The probe power is about 50 nW, to guarantee a low saturation of the transition. To understand our choice of power for the probe beam, it is important to realize that two main effects can mask the optical depth (OD) results. First, power saturation of the cyclic transition for single atoms, which limits the absorption of light by the medium. Second, even though we are probing a cyclic transition, non-resonant excitation to other hyperfine excited states can still transfer atoms to the other hyperfine ground state, effectively

decreasing the number of atoms in the medium. Note that this second effect can also be understood as a saturation of the medium related to power, since higher probe powers would transfer more atoms to the other ground state. From this analysis, it is clear that it is important to choose a power low enough that both these effects are negligible. In this way, we measured OD as a function of power of the probe beam, and notice that below a certain power the OD reached a constant value. The 50 nW used in the experiment is then the highest power for which we could measure the correct, low power, OD. The probe beam is thus very sensitive to any change in the initial population, and its absorption indicates that the Raman pulses succeeded in transferring some population from one ground state to the other.

In this way, a plot of the medium optical depth (OD) for the probe pulse as a function of the detuning between the two Raman fields gives a direct measure of the ensemble distribution of energies in the ground states. Examples of such plots with the MOT magnetic field on and off are shown in Figs. 6.3(a) and 6.3(b), respectively. In Fig. 6.3(b) the Raman pulses are delayed 4 ms from the moment the magnetic field was turned off, and the nulling of the field was performed using additional Helmholtz coils located around the MOT and looking for a reduced width of the Raman trace. From Fig. 6.3(a) to 6.3(b), the width of the signal is then reduced by more than two orders of magnitude, from 5 MHz to about 20 kHz. The 20 kHz linewidth of Fig. 6.3(b), however, also includes about 10 kHz of power broadening induced by the Raman beams. To measure this power broadening, we applied an extra DC field in the z direction in order to split the central peak between the various $m_F \rightarrow m'_F$ transitions, and then measured the width of the magnetic-field-insensitive transition

$m_F = 0 \rightarrow m'_F = 0$.
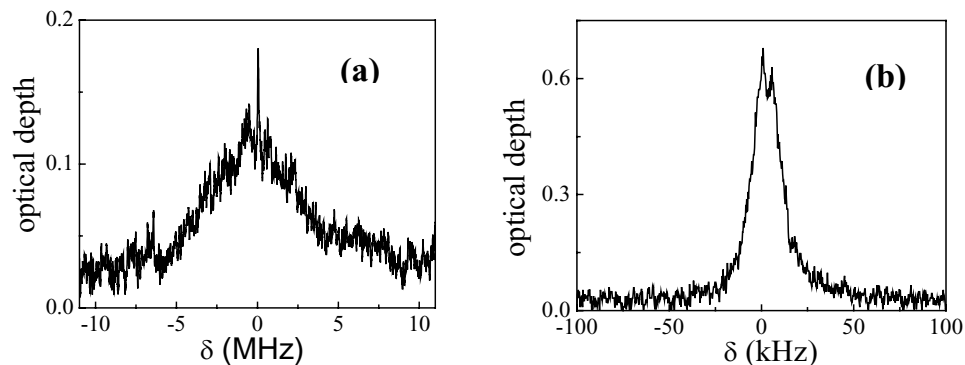
Figure 6.3: (a) Raman trace with the quadrupole MOT magnetic field on. The trace represents the absorbtion of the probe pulse following the Raman beams, as a function of the Raman detuning δ. The FWHM line width is around 5 MHz. (b) Raman trace 4 ms after the quadrupole field has been switched off. The fitted linewidth is 20 kHz, including 10 kHz of power broadening due to the Raman beams

As mentioned above, the quadrupole field of the MOT should be switched off as fast as possible, in order to maintain the high optical density needed for the DLCZ-type experiments. However, switching off the magnetic field generated by the MOT coils is usually retarded for two reasons. First, the current in the coils decays exponentially, with a time constant proportional to the inductance of the coils. Second, the field decay time is increased by eddy currents in the metallic part of our vacuum chamber. Depending on the metallic configuration of chamber and coils, the transient period can last for tens of milliseconds. In order to obtain a faster transient, we use a fast-switching electronic circuit [80, 81]. This circuit allows a quick reversal of the current in the quadrupole coils in order to compensate for the eddy currents, and resulted in a substantial reduction of the transient time in our system.

A detailed description of the magnetic field transient is given in Fig. 6.4(a), which plots the Raman scan linewidth as a function of the delay from the moment the field

was switched off. Figure 6.4(a) then shows the timescale over which the ground state

has its energy-distribution profile changed from Fig. 6.3(a) to Fig. 6.3(b). We can see

that after a few miliseconds, the linewidth asymptotically reaches a plateau, given by

the residual DC field in the chamber, that we estimate in this case to be on the order

of 10 mG. The dashed line in Fig. 6.4(a) indicates the measured power broadening.

Shorter transients can be obtained with a different metallic chamber configuration

(like in Ref. [80]) or using non-metallic vacuum chambers.
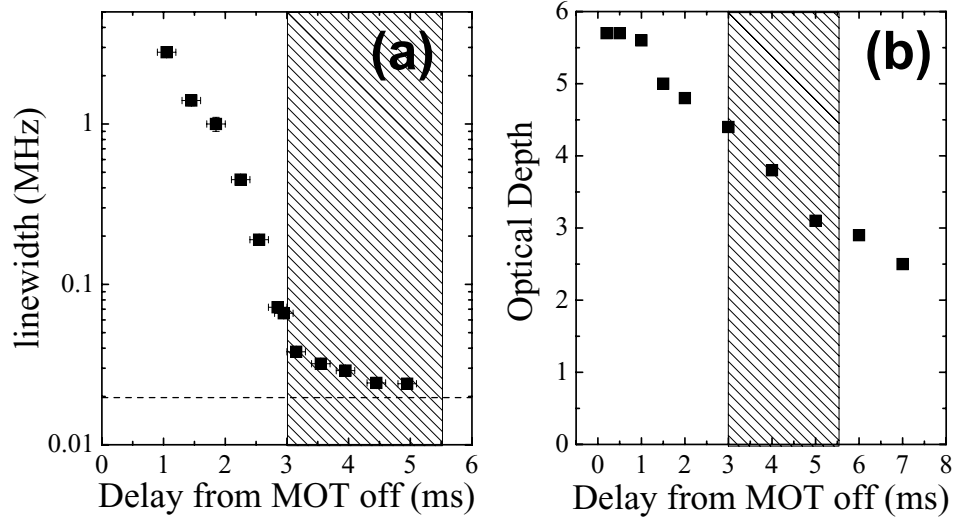
Figure 6.4: (a) Evolution of the ground state linewidth and (b) of the optical depth of the sample as a function of the delay from the time when the current is switched off in the MOT coils. The linewidth is measured with Raman spectroscopy. The dashed line represents the measured power broadening due to the Raman beams. The OD is determined by measuring the absorbtion of a probe pulse in the sample. In both graphs, the dashed area represents the window used for measuring correlations at the single photon level.

In order to estimate the optimal region for photon counting measurements, it is

important to independently measure the decay of the optical depth after the magnetic

field is switched off. In our setup this is done in a straightforward way by turning off the Raman beams and using a probe pulse close to resonance with the ground state that is populated by all the atoms. The results of such measurement are shown in Fig. 6.4(b), for which the population was initially pumped to $F = 4$ and the probe tuned 10 MHz below the $F = 4 \rightarrow F' = 5$ transition. The optical depth measurements in Fig. 6.4(b) were obtained from the absorption at 10 MHz detuning and assuming a Lorentzian lineshape for the atomic transition with a natural linewidth corrected for power broadening by the probe beam.

Together, the results in Figs. 6.4(a) and 6.4(b) allow us to determine an optimal window for the experiments of Sec. 6.3.2, i.e., between 3 and 5.5 ms after the current in MOT coils starts to turn off (shadowed region in both figures). The beginning of this interval is determined by the moment when the residual magnetic field reaches a reasonably small value corresponding to an acceptable decoherence time, and the end by the condition that the density should not vary too much throughout the interval. We accepted a variation of about 30% in the density. The linewidth varies by about 30 kHz in the same interval.

A better cancellation of the magnetic field can in principle lead to even narrower linewidths and, consequently, longer coherence times. However, improvements along this line will eventually be limited by a different problem: the diffusion of atoms out of the excitation region. This effect depends on the temperature of the sample and on the diameter of the excitation beams. In order to directly measure this diffusion time, we use again Raman spectroscopy. In this case, Raman traces are recorded as a function of the delay between the Raman pulses and probe. The measurement is done

when the magnetic field is off, such that there is only one narrow peak in the Raman

trace, like in Fig. 6.2(d). In this case, the area of the peak profile is proportional to

the number of atoms in the excitation region. Figure 6.5 shows a plot of this area as a

function of delay. We see that the population decays with a time constant of 900 μs,

as given by an exponential fit to the data (solid line). Note that this measurement was

done with beams that have 150 μm diameter, while in the correlation measurements

described later we use beams with 60 μm diameter, leading to a diffusion time of the

order of 360 μs.
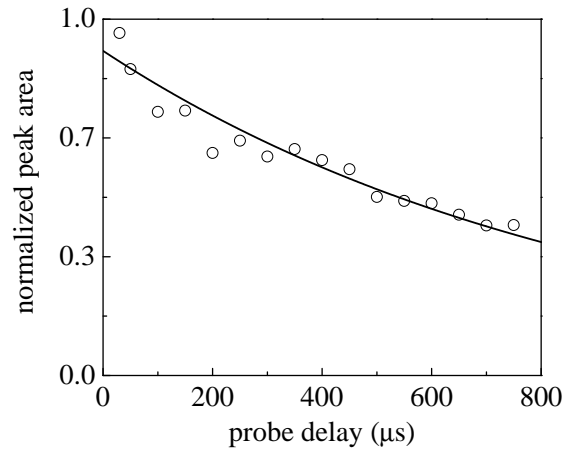
Figure 6.5: Diffusion of atoms out of the excitation region. The solid line is an exponential fit with a time constant of 900 μs. The Raman beam diameter is 150 μm.

6.3.2   Nonclassical correlations

In order to characterize the coherence time of the system for various quantum in-

formation applications, e.g., for the DLCZ protocol or for conditional generation of

single photons, the measurements must be performed at the single-photon level. In

particular, one must know how long a single excitation can be stored in the ensemble.

For this purpose, we perform correlation measurements between fields 1 and 2 as a function of the time delay Δt between write and read pulses, thereby probing how the nonclassical character of these correlations (and hence of the correlations between field 1 and the collective atomic excitations) is preserved during the storage process.

In order to investigate the quantum nature of the correlations, we use the fact that there exists a well-defined border between the classical and quantum domains for fields 1 and 2 that can be operationally accessed via coincidence detection, as was first demonstrated in the pioneering work by Clauser [33] and exploited in Chapters 3 to 5. In particular, we measure the joint detection probability p_{12} for detecting a photon in both fields 1 and 2 in the same trial, and the probabilities p_1 and p_2 to register a single detection event in field 1 and field 2, respectively. By splitting field i with a 50-50 beamsplitter and directing the output to two detectors, the joint probabilities p_{ii} are also measured, where $i = 1$ or 2. Fields for which the Glauber-Sudarshan phase-space function is well-behaved (i.e., classical fields) are constrained by a Cauchy-Schwarz inequality for the various probabilities [33, 30], namely:

$$R = \frac{[g_{12}(t)]^2}{g_{11}\, g_{22}} \leq 1\,, \tag{6.37}$$

where $g_{11} \equiv p_{11}/p_1^2$, $g_{22} \equiv p_{22}/p_2^2$, $g_{12}(t) \equiv p_{12}/(p_1 p_2)$, and t denotes the time separation between the detection of photons 1 and 2. Note that in this chapter we omit the comma between the subscipts of the normalized correlation functions $g_{i,j}$ and the joint detection probabilities $p_{i,j}$. In our system, $g_{11} = g_{22} = 2$ in the ideal case. However, in practice, g_{11} and g_{22} are measured to be smaller than 2, due to various

experimental imperfections. Hence in our case measuring $g_{12} > 2$ heralds nonclassical correlations, and in the following we will use this quantity as another figure of merit to quantify the loss of coherence in the quantum memory.

The experimental setup used to measure nonclassical correlations between fields 1 and 2 is the same as that in Chapter 4, shown in Fig. 6.6.
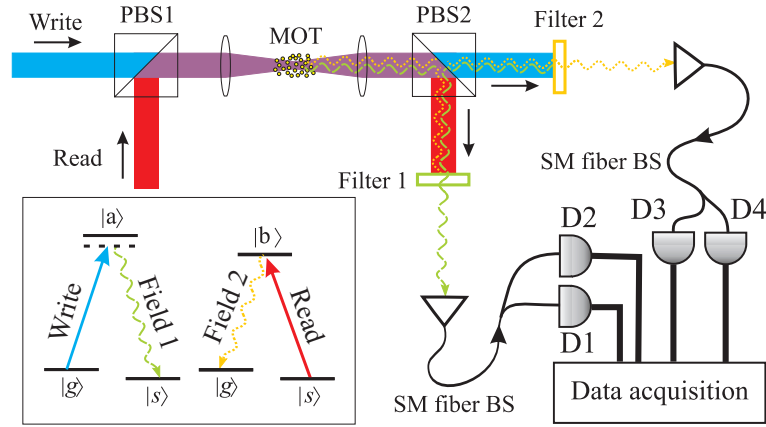
Figure 6.6: Experimental setup. Write and read pulses propagate sequentially into a cloud of cold Cs atoms (MOT), generating pairs of correlated output photons 1 and 2. The write and read pulses have orthogonal polarizations, are combined at polarizing beam splitter PBS1, and then focused in the Cs MOT with a waist of approximately 30 μm. The output fields are split by PBS2, which also serves as a first stage of filtering the (write, read) beams from the (1,2) fields. For example, field 2 is transmitted by PBS2 to be subsequently registered by detector D3 or D4 while the read pulse itself is reflected at PBS2. Further filtering is achieved by passing each of the outputs from PBS2 through separate frequency filters. SM stands for single mode.

6.3.3 Coherence time measurements

In order to characterize the system's coherence time, we measure g_{12} and R as a function of the delay Δt between write and read pulses. We then compare the theoretical quantity $\tilde{p}_{12}(\Delta t) = \xi p_{12}^{th}(\Delta t)$ to the measured $g_{12}(\Delta t)$ by way of a single overall scaling parameter ξ for all Δt, as the rate of single counts in fields 1 and 2 (p_1 and p_2) is

measured to be roughly independent of Δt, with about 20% fluctuation. In Fig. 6.7(a) we show our results for g_{12} with the MOT magnetic field on together with the corresponding theoretical fitting. This figure was the one in [67] (Chapter 5, Fig. 5.5) and shows a fast decay of the coherence between fields 1 and 2, taking place in a time scale of less than 200 ns. Note, however, that the coherence time is actually smaller than 100 ns, since the write pulse itself has a duration of 150 ns. The repetition rate of the trials in this case is 250 kHz. The rate of coincidence events (detection of photon 1 and photon 2 within the same trial) is between 2 and 3 counts per second.

The theoretical joint probability p_{12}^{th} is calculated from Eq. (6.27), assuming $C = 1$. In this way, we need to perform integrals of the F function over the z-coordinate. This function depends on z only through the parameters a_g and a_s. The atomic ensemble is assumed to be initially unpolarized, i.e., with the atoms evenly distributed among all Zeeman states of the $|g\rangle$ level. For the ground states of cesium, we have that the hyperfine Landé factors g_g and g_s of levels $|g\rangle$ and $|s\rangle$, respectively, are given by $\mu_B g_g/h = -\mu_B g_s/h = 0.35\,\mathrm{MHz/G}$, so that we can write

$$a_g = 2\pi K m_g \left(\frac{z}{L}\right) , \qquad\qquad (6.38a)$$

$$a_s = -2\pi K m_s \left(\frac{z}{L}\right) , \qquad\qquad (6.38b)$$

where we considered the magnetic field for the MOT in the form $B_z = bz$, with b the

field gradient in the center of the MOT, and the constant K given by

$$K = \frac{\mu_B g_g bL}{h} . \tag{6.39}$$

The value of Km_F gives an estimate for the inhomogeneous broadening associated with level $|F, m_F\rangle$ due to the magnetic-field gradient b. Note that writing a_g and a_s as in Eq. (6.38) allows us to perform all spatial integrations over the dimensionless coordinate $s = z/L$, and to combine many of the relevant experimental parameters in a single parameter (K). For our experiment, $L = 3.6$ mm and $b = 8.7$ G/cm, so that $K = 1.1$ MHz. This K value is consistent with the measurement of the ground-state broadening shown in Fig. 6.3(a).

The solid curve in Fig. 6.7(a) shows the theoretical fitting of $\tilde{p}_{12}(\Delta t)$ to the experimental data. We considered $K = 1.1$ MHz in the theory, as estimated above for our experimental conditions. The only fitting parameter used was ξ, which was found to be $\xi = 1.05 \times 10^8$. Note that the theoretical quantity p_{12}^{th} gives the probability for joint detection of the two photons, while g_{12} is a measure of this joint probability normalized by the probability of uncorrelated coincidence detections. Thus the scaling factor ξ should be given roughly by the inverse of the probability for these uncorrelated coincidences. A theoretical estimation for this value is given by $\xi^{th} = [p_{12}^{th}(\Delta t \to \infty)]^{-1}$, i.e., the inverse of the theoretical joint probability after the coherence has completely decayed. For the solid curve in Fig. 6.7(a), we find $\xi^{th} = 1.96 \times 10^8$. The difference between ξ and ξ^{th} can be attributed to other sources of uncorrelated coincidences (such as dark counts in the detectors, or leakage from the filters) that are not taken

in to account by the theory, which leads to $\xi < \xi^{th}$. It is also important to have in mind that the noise floor is higher when the pulses are overlapping, since there is more leakage from the filters in this condition. This results in some extra discrepancy when comparing theory to experiment by means of one single scaling parameter to all regions of Fig. 6.7(a).
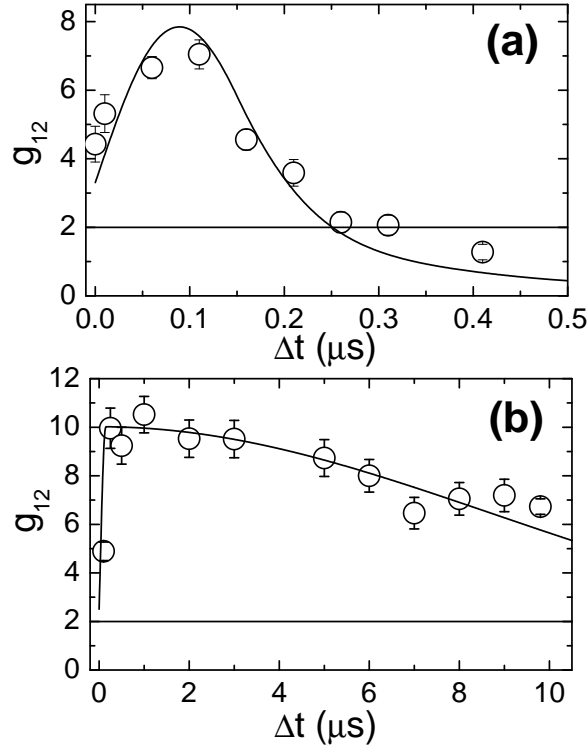
Figure 6.7: Measurement of g_{12} as a function of the storage time, (a) with the quadrupole field on (taken from [67]) and (b) with the quadrupole field off. The observed decay in (b) is consistent with the residual magnetic field in the chamber, as characterized by Raman spectroscopy.

The $g_{12}(\Delta t)$ measurements with magnetic field off are presented in Fig. 6.7(b). In this case, we use the information acquired from the investigation of Sec. 6.3.1 and turn off the magnetic field for a duration of 5.5 ms, at 40 Hz repetition rate. From the magnetic-field-off period, we use only the 2.5 ms window shown in Fig. 6.4 for correlation measurements. This 2.5 ms window is then divided in 208 trial periods of

12 μs, which results in an overall repetition rate of 8.3 kHz. In the beginning of each trial, the trap light of the MOT (tuned in the $F = 4$ to $F' = 5$ transition of the D_2 line) is turned on for 0.6 μs, and its repumper laser (tuned from $F = 3$ to $F' = 4$) for 1 μs. This procedure prepares the system in the proper initial state, with all atoms at the $F = 4$ hyperfine level of the ground state. In this case, the rate of coincidence counts drops to about 0.33 coincidences/s.

Figure 6.7(b) shows then an increase of more than two orders of magnitude on the coherence time of the system, when the magnetic field is turned off. The coherence time is now limited mainly by the rate at which we can turn off the magnetic field, and also to some extent by our ability to magnetically isolate the system. Note that in Fig. 6.4(a) the Raman-trace linewidth indicates that the magnetic field in the measurement window is still decaying. The solid curve in Fig. 6.7(b) gives the decay theoretically expected for a magnetic-field gradient such that $K = 12$ kHz, corresponding to magnetic fields of the order or smaller than 30 mG acting on the ensemble. This gives a reasonable approximation to the behavior of g_{12} under the action of the residual magnetic field, even though the spatial dependence of this field can be more complicated than a simple linear gradient. The change in K from 1.1 MHz to 12 kHz is consistent with the reduction of the ground state linewidth between the two cases, as measured directly by the Raman spectroscopy setup. Finally, for Fig. 6.7(b) $\xi = 0.67 \times 10^8$ and $\xi^{th} = 2.2 \times 10^8$.

From Fig. 6.7(b), we see that the correlations are still highly nonclassical after a storage time of 10 μs. However, from the theoretical fitting we can infer that g_{12} should became smaller than 2 at about 25 μs, which gives an estimation for the

coherence time of non-classical correlation in our system.

As discussed above, the measurements with $g_{12} > 2$ give a strong indication of the nonclassical correlations observed in our system, based on reasonable assumptions for g_{11} and g_{22}. The most appropriate verification of the nonclassical nature of fields 1 and 2, however, is given by the measurement of R as defined in Eq. (6.37). Such measurements with the magnetic field off are shown in Fig. 6.8. More specifically, in Fig. 6.8(a) we show the measurements of g_{11} and g_{22} for the same data points of Fig. 6.7(b). Substituting the results of Figs. 6.7(b) and 6.8(a) in (6.37), we then obtain the values of R shown in Fig. 6.8(b), which confirm the strong nonclassical correlation present in our system for more than 10 μs.

The R measurement presents considerably larger error bars than for g_{12}. This comes from the large statistical uncertainties involved in the determination of g_{22}, which requires measurement of the two-photon component of field 2 [64]. For this reason, we decided to carry out a much longer run of the experiment for the longest coherence time we were able to probe, 10 μs, which resulted in the considerably smaller statistical error of this point.

6.3.4 Two-photon wavepackets

Central to the DLCZ protocol is the ability to write and read collective spin excitations into and out of an atomic ensemble, with efficient conversion of discrete spin excitations to single-photon wavepackets. A critical aspect of such wave packets is that they are emitted into well defined spatiotemporal modes to enable quantum interference between emissions from separate ensembles (e.g., for entanglement-based
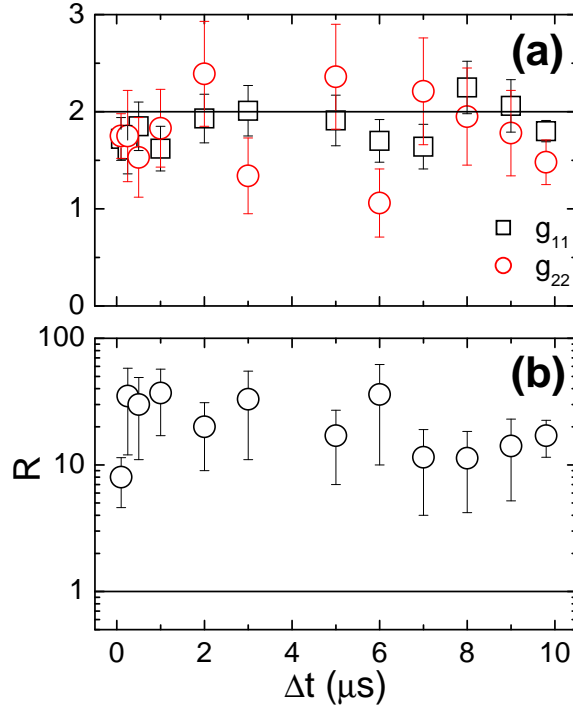
Figure 6.8: (a) Measurement of g_{11} (open squares) and g_{22} (open circles) as a function of the storage time. (b) Measurement of the coefficient R as a function of the storage time. The big statistical errors are mainly due to statistical uncertainties in the measurement of g_{22}. The points at 10 μs have been measured for a much longer time and exhibit smaller statistical errors.

quantum cryptography [22]).

The high efficiencies achieved in the work of Ref. [64] (Chapter 4) enabled us to investigate in detail the temporal properties of the nonclassical correlations between emitted photon pairs [67] (Chapter 5), providing a direct look at various important features of the two-photon wavepacket (field 1 + field 2) generated by the system. In the following analysis, our main quantity of interest is $p_\tau(t_1, t_2)$, the joint probability for photoelectric detection of photon 1 at time t_1 and photon 2 at time t_2 within a time window of duration τ. The times for this quantity are counted starting from the beginning of the write pulse. This quantity is determined from the record of

time-stamped detections on all four photodetectors. The detectors have a timing resolution of 2 ns (minimum bin size), but usually we need to consider larger bins to acquire enough events for the statistics.

In our earlier experiments [67] (Chapter 5), we focused on two cases: (I) nearly simultaneous application of write and read pulses with offset $\Delta t = 50$ ns shorter than the duration of either pulse, and (II) consecutive (nonoverlapping) application of write and read pulses with $\Delta t = 200$ ns. Results for $p_\tau(t_1, t_2)$ are presented in Fig. 6.9. In case (I), Fig. 6.9(a) shows that $p_\tau(t_1, t_2)$ peaks along the line $t_2 - t_1 = \delta t_{12} \simeq 50$ ns with a width $\Delta t_{12} \simeq 60$ ns, in correspondence to the delay δt_{12} and duration Δt_{12} for read-out associated with the transition $|s\rangle \to |b\rangle \to |g\rangle$ given an initial transition $|g\rangle \to |a\rangle \to |s\rangle$ [66]. In case (II) with the read pulse launched 200 ns after the write pulse, the excitation is "stored" in the atomic ensemble until the readout. The production of correlated photon pairs should now be distributed along $t_2 \simeq \Delta t + \delta t_{12}$ with width $\simeq \Delta t_{12}$.
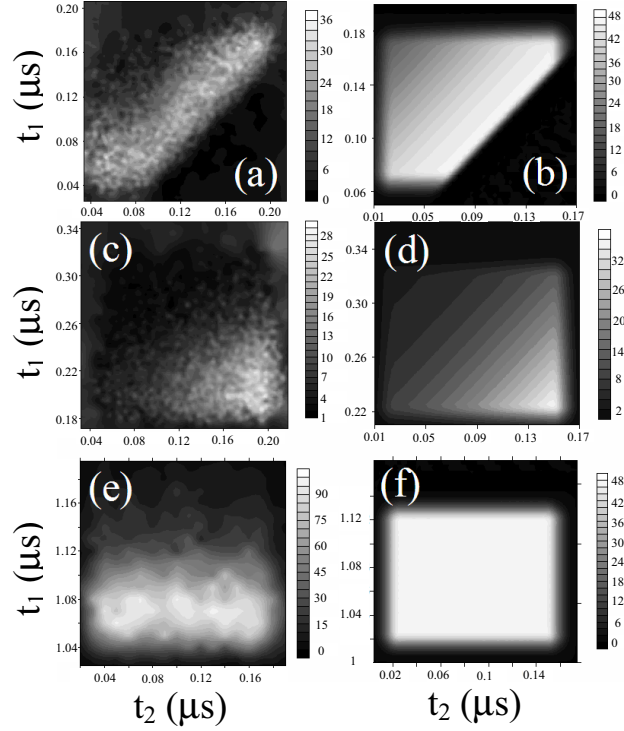
Figure 6.9: Theory and experiment for two-photon wavepackets $P_\tau(t_1, t_2)$. (a) Measured two-photon wavepackets for the case where write and read pulses are partially overlapped with a delay of 50 ns, with the quadrupole magnetic field on. (b) Theoretical predictions for the same conditions as in (a). (c) Measured two-photon wavepackets for the case of consecutive (non-overlapping) write and read puses with a delay of 200 ns, with quadrupole field on. (d) Theoretical predictions for the same conditions as in (c). (e) Measured two-photon wavepackets for non-overlapping write and read pulses, with quadrupole field off. The delay between write and read pulses is 1 μs. (f) Theoretical predictions for the same conditions as in (e). The vertical scales are given in arbitrary units proportional to the joint probability of detecting photons 1 and 2. See text for further details.

Instead, as shown in Fig. 6.9(c), $p_\tau(t_1, t_2)$ peaks towards the end of the write pulse (i.e., $t_1 \gtrsim 100$ ns), and near the beginning of the read pulse (i.e., $200 \lesssim t_2 \lesssim 300$ ns).

Early events for field 1 lead to fewer correlated events for field 2, as $p_\tau(t_1, t_2)$ decays rapidly beyond the line $t_2 - t_1 = \tau_d \simeq 175$ ns. The marked contrast between $p_\tau(t_1, t_2)$ for $\Delta t = 50$ and 200 ns results in a diminished ability for the conditional generation

of single photons from excitations stored within the atomic ensemble [64] (Chapter 4) and, more generally, for the implementation of the DLCZ protocol for larger Δt. The underlying mechanism is again decoherence within the ensemble.

By contrast, when the magnetic field is turned off, this distortion in the two-photon wavepacket is eliminated due to the extended coherence time. We now observe the shape shown in Fig. 6.9(e). The delay in Fig. 6.9(e) is $\Delta t = 1~\mu$s.

The theoretical results corresponding to these three situations are shown in frames (b), (d), and (f) of Fig. 6.9. These are plots of Eq. (6.36) averaged over 4 ns time windows for both t_2 and t_1, the same time window used for the experimental data. We also considered pulses of trapezoidal shape, with 20 ns rising time, and FWHM of 150 ns for the write pulse and 120 ns for the read pulse. These values correspond to the experimental parameters. The only effect of both the time window and pulse rising time is to smooth the edges of the distribution. Different from the case of integrated probabilities, it is necessary here to introduce more details in the description of the pulse shapes, since the theoretical description for this signal predicts that it is directly related to the pulse profiles (see Eq. (6.33)).

The main point that calls our attention in these figures is the fact that the theory offers a reasonable explanation for the data from consecutive pulses ($\Delta t = 200$ ns) with magnetic field on, but not for overlapping pulses or $\Delta t = 1~\mu$s with magnetic field off. This discrepancy can be simply understood, however, if we remember that one of the main approximations of our theory is to consider low intensities for both write and read pulses. At low intensities and zero magnetic field, the theory gives a small and constant probability for the photon 2 emission after photon 1. From Eq. (6.33), we

see that the magnetic field introduces different phases for different groups of atoms. These different phases are proportional to the time difference between the emission of photons 2 and 1, and result in an overall decay of the probability of emission of the second photon over time. In Fig. 6.9(b) and 6.9(f), however, we see that the predicted decay time is much longer than the one inferred from the experimental data.

On the other hand, for the actual experiment, the high intensity of the read pulse should lead to a fast emission of photon 2 once the atom is transferred to level $|s\rangle$. This is consistent with the short duration of correlation $\Delta t_{1,2}$ in Fig. 6.9(a) and 6.9(e), which can be understood as coming from the fast depletion of the $|s\rangle$ state. However, this reasoning cannot explain the shape of Fig. 6.9(c), since the strong excitation alone should result in a similar fast depletion in the beginning of the read pulse for any detection time of photon 1 (as seen in Fig. 6.9(e)). The good comparison between Fig. 6.9(c) and 6.9(d) comes from the fact that the decay due to the magnetic field takes place before the delayed readout process occurs. The shape in Fig. 6.9(c) is then a convolution of a uniform excitation probability over t_1 (like in Fig. 6.9(e)) with the excitation-probability distribution of Fig. 6.9(d).

6.4   Optical pumping

The theory developed to explain the data in Fig. 6.7 can also be used to devise new ways to improve the system. The inclusion of the Zeeman structure in the theory, for example, allows the study of different polarization schemes for both classical excitation and photon detection. It also allows the investigation of the role of the

atomic initial state on the measured correlations. In Fig. 6.10 we give two examples of possible ways to improve the system. The solid and dashed lines in the figure represent the two experimental conditions of Fig. 6.7 (initially unpolarized samples with $K = 1.1$ MHz and $K = 12$ kHz), but now with the same scaling factor. The dash-dotted curve shows how the $K = 12$ kHz curve changes if the system is initially spin polarized, with all atoms in the $|F = 4, m_F = 0\rangle$ state. Note that in this case the value of $\tilde{p}_{1,2}$ considerably increases, and the system develops a plateau coming from the predominant transition $|F = 4, m_F = 0\rangle \rightarrow |F = 3, m_F = 0\rangle \rightarrow |F = 4, m_F = 0\rangle$, which is magnetic-field insensitive. Furthermore, it is possible to devise a polarization scheme of excitation that allows only this specific transition for any Δt, e.g., as when the write pulse and field-1 detection are σ^+ polarized, and the read pulse and field-2 detection are σ^-. This is the case for the dotted curve in Fig. 6.10.
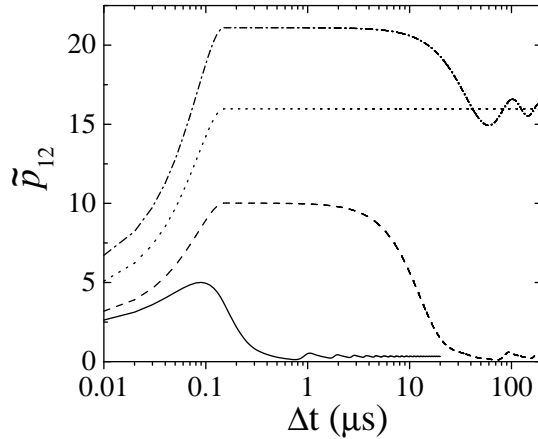
Figure 6.10: Variation of $\tilde{p}_{1,2}$ with the delay Δt between write and read pulses for (solid curve) $K = 1.1$ MHz and an unpolarized sample, (dashed curve) $K = 12$ kHz and an unpolarized sample, and (dash-dotted curve) $K = 12$ kHz and an initially spin-polarized sample with all atoms in $|F = 4, m_F = 0\rangle$. The dotted curve corresponds to an initially spin-polarized sample classically excited by fields with polarizations such that only a magnetic insensitive transition is allowed, see text for details. The same arbitrary scaling factor was used for all curves.

The idealized improvements described by the dotted and dash-dotted curves of Fig. 6.10, however, will probably be limited by two effects which are not taken into account by the theory. First, in our experimental setup we should see a decay with a timescale on the order of 360 μs due to the average time the cold atoms take to cross the 60 μm beam diameter of the classical write and read pulses. Second, the theory assumes the presence of a magnetic field predominantly in the z direction, which defines the quantization axis. This can be obtained by applying an extra DC magnetic field along that direction, [82, 83] but any residual transverse field should lead to some decay of the plateau. In spite of these restrictions, however, we believe that such improvements could lead to an increase of more than an order of magnitude over the largest experimental decoherence time of Fig. 6.7. It is also clear that there is a benefit in the careful preparation of the initial state for the magnitude of the measured correlations. This is an important point that should also be taken into account when considering the implementation of the DLCZ protocol in vapor cells.

6.5   Conclusion

We have presented a detailed study of the decoherence processes in the generation of photon pairs from atomic ensembles, via the DLCZ protocol of Ref. [22]. We have identified the main cause of decoherence for cold atoms in magneto-optical traps as being the inhomogeneous broadening of the hyperfine ground states due to the quadrupole magnetic field used to trap the atoms. A detailed theory has been developed to model this effect. We also reported a series of measurement to characterize

and control the decoherence using copropagating stimulated Raman scattering. These measurement allowed us to switch off the quadrupole magnetic field in a controlled way. With the magnetic field off, we observed highly nonclassical correlations between the two emitted photons, for a storage time up to 10 μs, an improvement of more than two orders of magnitude compared to previous results with cold atoms. Furthermore, the coherence time is now two orders of magnitude larger than the excitation pulses duration. This is a crucial step in order to use atomic ensembles as a quantum memory to store conditional single photon states or entanglement between two distant ensembles.

Chapter 7

Measurement-Induced Entanglement for Excitation Stored in Remote Atomic Ensembles

7.1 Introduction

Entanglement is a uniquely quantum mechanical property of the correlations among various components of a physical system. Initial demonstrations of entanglement were made for photon pairs from the fluorescence in atomic cascades [84, 85] and from parametric down conversion [30]. More recently, entanglement has been recognized as a critical resource for accomplishing tasks that are otherwise impossible in the classical domain [69]. Spectacular advances have been made in the generation of quantum entanglement for diverse physical systems [69, 86], including entanglement stored for many seconds in trapped ions on for distances on the millimeter scale [87, 88], long-lived entanglement of macroscopic quantum spins persisting for milliseconds on the centimeter scale [42], and remote entanglement carried by photon pairs over distances of tens of kilometers of optical fibers [89].

For applications in quantum information science, entanglement can be created deterministically by way of precise control of quantum dynamics for a physical system, or probabilistically by way of quantum interference in a suitable measurement with random instances of success. In the latter case, it is essential that success be heralded unambiguously so that the resulting entangled state is available for subsequent utilization. In either case, quantum memory is required to store the entangled states until they are required for the protocol at hand.

There are by now several examples of entanglement generated "on demand," [69] beginning with the realization of the EPR paradox for continuous quantum variables [90] and the deterministic entanglement of the discrete internal states of two trapped

ions [91]. Important progress has been made towards measurement-induced entanglement on various fronts, including the observation of entanglement between a trapped ion and a photon [92].

Against this backdrop, in this Chapter we report the initial observation of entanglement created probabilistically from quantum interference in the measurement process, with the resulting entangled state heralded unambiguously and stored in quantum memory for subsequent exploitation. As illustrated in Fig. 7.1, the detection of a photon from either of two atomic ensembles (L, R) in an indistinguishable fashion results in an entangled state with one "spin" excitation shared at a distance of 2.8 m between the ensembles and distributed symmetrically among $\sim 10^5$ atoms at each site [22]. Confirmation of entanglement is achieved by mapping this stored excitation onto light fields after a 1 μs delay [22, 77] and by suitable measurements of the quantum statistics of the resulting optical fields. Our results provide the first realization of the capability to transfer a stored entangled state of matter to an entangled state of light.
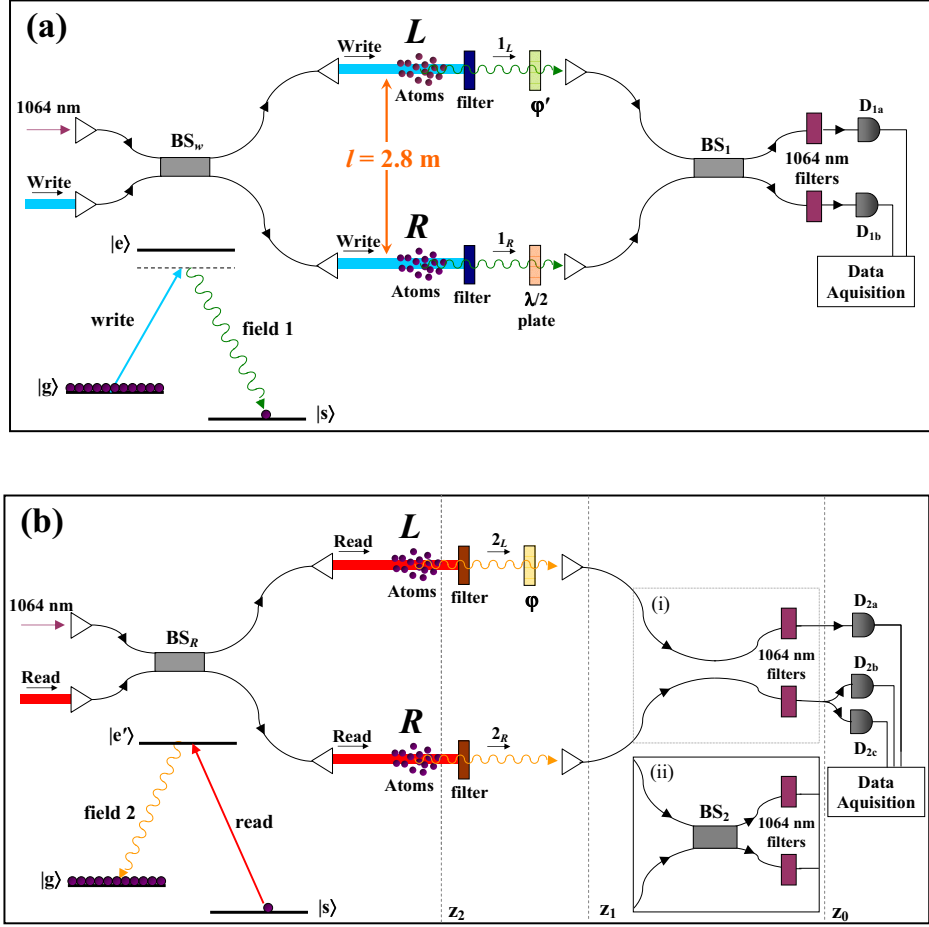
Figure 7.1: An overview of our experiment to entangle two atomic ensembles. (a) Setup for generating entanglement between two pencil-shaped ensembles L and R located within spherical clouds of cold Cs atoms. (b) Schematic for verification of entanglement between the L, R ensembles by conversion of atomic to field excitation by way of simultaneous read pulses obtained from BS_R. The inset (i) shows the configuration used to measure the diagonal elements p_{ij} of $\tilde{\rho}_{2_L,2_R}$ in Eq. (7.6) from the photo-detection events at D_{2a}, D_{2b}, D_{2c}. Reconfiguring the fiber connections we can easily pass from the configuration of inset (i) to the one of inset (ii), which is used to generate interference of the $2_L, 2_R$ fields at beam splitter BS_2 to measure the off-diagonal coherence d in $\tilde{\rho}_{2_L,2_R}$.

Our experiment is motivated by the protocol of Duan, Lukin, Cirac and Zoller (DLCZ) [22] for the realization of scalable quantum communication networks with atomic ensembles. The DLCZ protocol introduced a number of novel ideas for quan-

tum information processing and is the subject of active investigation. In this direction, nonclassical correlations [27, 43, 64, 65, 66, 67, 70, 77] and entanglement [28] have been observed between pairs of photons emitted by a single atomic ensemble. Observations of coherence between two cylindrical volumes of cold Rubidium atoms within a single magneto-optical trap have also been reported [93], although entanglement was not demonstrated between the two regions [94, 95].

This chapter is largely base on Ref. [96].

7.2   Experiment

A simple schematic of our experiment is given in Fig. 7.1, with further details provided in Refs. [64, 67, 77] and Chapter 4. For the writing stage of the protocol, two classical pulses traverse the L, R ensembles in parallel and generate fields $1_L, 1_R$ by spontaneous Raman scattering (see Fig. 7.1a). The intensity of the pulses is made sufficiently weak such that the probability of creating more than one excitation in the symmetric collective mode [22] of the ensemble is very low [64].

The atomic level structure for the writing process consists in the initial ground state $|g\rangle$ ($6S_{1/2}, F = 4$ level of atomic cesium), the ground state $|s\rangle$ for storing a collective spin flip ($6S_{1/2}, F = 3$ level), and the excited level $|e\rangle$ ($6P_{3/2}, F' = 4$). The transition $|g\rangle \rightarrow |e\rangle$ in each ensemble is initially coupled by a write pulse detuned from resonance to generate the forward-scattered anti-Stokes field 1 from the transition $|e\rangle \rightarrow |s\rangle$. The L, R ensembles are excited by synchronized writing pulses obtained from beam splitter BS_w. After filtering, the Stokes fields $1_L, 1_R$ are collected, coupled

to fiber-optic channels, and interfere at beam splitter BS_1, with outputs directed towards two single-photon detectors D_{1a}, D_{1b}.

Entanglement between the L, R ensembles is created by combining the output fields $1_L, 1_R$ on the beam splitter BS_1, with outputs directed to two photodetectors D_{1a}, D_{1b} (see Fig. 7.1(a)). For small excitation probability and with unit overlap of the fields at BS_1, a detection event at D_{1a} or D_{1b} arises indistinguishably from either field 1_L or 1_R, so that the L, R ensembles are projected into an entangled state, which in the ideal case can be written as [22, 23]

$$|\Psi_{L,R}\rangle = \epsilon_L|0\rangle_L|1\rangle_R \pm e^{i\eta_1}\epsilon_R|1\rangle_L|0\rangle_R, \qquad (7.1)$$

where $|0\rangle_{L,R}, |1\rangle_{L,R}$ refers to the two ensembles L, R with 0, 1 collective excitations respectively, ϵ_L (ϵ_R) is the normalized amplitude of photon generation from ensemble L (R), and the sign $\pm$ is set by whichever detector records the event. The phase $\eta_1 = \Delta\beta_w + \Delta\gamma_1$, where $\Delta\beta_w$ is the phase difference of the write beams at the L, R ensembles, and $\Delta\gamma_1$ is the phase difference acquired by the $1_L, 1_R$ fields in propagation from the ensembles to the beam splitter BS_1. Note that to achieve entanglement as in Eq. (7.1), η_1 has to be kept constant from trial to trial.

Experimental details Each of the L, R atomic ensembles is obtained from cesium atoms in a magneto-optical trap (MOT) [64, 77]. Measurements are carried out in a cyclic fashion consisting first of a period of cooling and trapping to form the MOT, followed by an interval during which the magnetic fields for the MOT are switched off. After waiting 3 ms for the magnetic field to decay [77], we initiate a

sequence of measurement trials, where for each trial the atoms are initially prepared in level $|g\rangle$. The write pulse is at 852 nm, with a duration of 150 ns and is detuned 10 MHz below the $|g\rangle \rightarrow |e\rangle$ transition. The read pulse is at 894 nm, with a duration of 130 ns and is resonant with the $|s\rangle \rightarrow |e'\rangle$ transition. At the end of each trial, the sample is pumped back to level $|g\rangle$ by illuminating the atomic cloud with trapping and repumping light for 0.7 μs and 1 μs respectively, and then a new trial is initiated with period of 3 μs. The total duration for a sequence of measurement trials is 5 ms, after which the measurement interval is terminated and a new MOT is formed in preparation for the next sequence of trials. In Fig. 7.1(a) and 7.1(b), the incident write and read beams are orthogonally polarized and combined at a polarizing beam splitter (see Fig. 7.4), and are focused to a waist of about 30 μm in the sample region. All beam splitters BS are polarization-maintaining fiber beam splitters. The arms of the write and read interferometers are both about 12 m long.

7.3 Verifying the entanglement

To verify the entanglement, we map the delocalized atomic excitation into a field state by applying simultaneously strong read beams at the two ensembles (see Fig.1b). The read pulses reach the samples after a programmable delay from the write pulses, and couple the transition $|s\rangle \rightarrow |e'\rangle$ ($|e'\rangle$ being the $6P_{1/2}, F' = 4$ level), leading to the emission of the forward-scattered Stokes fields $2_L, 2_R$ from the transition $|e'\rangle \rightarrow |g\rangle$. If the state transfer were to succeed with unit probability, the conditional state $|\Psi_{L,R}\rangle$ of the ensembles would be mapped to an entangled state of two modes for the Stokes

fields $2_L, 2_R$ given in the ideal case by [22, 23]

$$|\Phi_{LR}\rangle = \epsilon_L|1\rangle_{2_L}|0\rangle_{2_R} \pm e^{i(\eta_1+\eta_2)}\epsilon_R|0\rangle_{2_L}|1\rangle_{2_R} , \qquad (7.2)$$

where $|0\rangle_{2_L,2_R}, |1\rangle_{2_L,2_R}$ refers to the Raman fields $2_L, 2_R$ with 0, 1 photons, respectively. Here, $\eta_2 = \Delta\beta_r + \Delta\gamma_2$, where $\Delta\beta_r$ is the phase difference of the read beams at the L, R ensembles, and $\Delta\gamma_2$ is the phase difference acquired by the $2_L, 2_R$ fields in propagation from the ensembles to the beam splitter BS_2 in Fig. 7.1b. In our experiment, the phases η_1, η_2 can be independently controlled and are actively stabilized by utilizing auxiliary fields at 1.06 μm that copropagate along the paths of the write and read beams and of the $1_L, 1_R$ and $2_L, 2_R$ fields.

Of course, the states in Eqs. (7.1) and (7.2) are idealizations that must be generalized to describe our actual experiment [22, 23, 94]. Specifically, the presence of various sources of noise necessarily transforms these pure states into mixed states. Eqs. (7.1) and (7.2) also neglect the vacuum contribution as well as higher-order terms, which are intrinsic to DLCZ protocol and which otherwise arise due to diverse experimental imperfections. Moreover, the above analysis assumes that all excitations are in the correct "modes" (both for optical fields and for the collective atomic "spin flips"), that excitations of the ensembles map 1-to-1 to photons in fields 1 and 2, and that diverse sources of background light are absent.

The procedure that we have devised to provide a robust, model independent determination of entanglement is based upon quantum tomography of the $2_L, 2_R$ fields. Since entanglement cannot be increased by local operations on either of the two en-

sembles, the entanglement for the state of the ensembles will be always greater than or equal to that measured for the state of the light fields.

7.3.1 Simplifying the density matrix

For convenience of description we assume the two atomic ensembles L and R to be in the hands of Alice and Bob, respectively. The state of the two ensembles conditioned on a click of one of the two detectors D_{1a} or D_{1b} (Fig. 7.1) is mapped onto a state of multiple field modes belonging to Alice and multiple modes belonging to Bob. Because the mapping involves only *local* operations by Alice and Bob, the entanglement (in particular, the entanglement of formation) between their systems cannot increase on average [97]. Hence the entanglement found between Alice's and Bob's field modes is a lower bound on the entanglement between the atomic ensembles. We will use this type of reasoning several times here: certain experimental procedures can be exactly mimicked by imagining Alice and Bob performing LOCC (local operations and classical communication), and those operations can only decrease the entanglement we find. We also sometimes (lower) bound the entanglement analytically using quantities that are more straightforward to measure in the laboratory. That way, we can unambiguously determine the presence of entanglement between the two ensembles, even if we might underestimate its actual magnitude.

On each side there is one main mode (a traveling continuous-wave mode) into which photons are emitted predominantly [22]. Those modes we denote by 2_L and 2_R. Other modes may be populated with very small probability, but in the analysis

we assume all detector clicks arise from modes 2_L and 2_R. In the experiment this reduction from multiple to single modes is mainly accomplished by the use of single mode fibers, which filter out different spatial modes. This is a procedure that can be exactly mimicked by Alice and Bob performing that same spatial filtering on their local modes and hence can only decrease the actual entanglement.

We furthermore assume that all off-diagonal elements of the density matrix between states with different numbers of photons vanish. This is a valid assumption when one takes into account that phases can only be defined relative to a reference laser beam shared by Alice and Bob. Tracing out that laser field sets the off-diagonal elements to zero. Indeed, the experiment makes no use of knowledge of the phases of the various lasers used. Moreover, this can only underestimate the entanglement, since tracing out the laser modes can be exactly mimicked by Alice and Bob performing local operations that makes all those off-diagonal elements zero. Namely, they could each apply a random phase shift to their modes, such that the phase difference is fixed (this requires classical but not quantum communication), and subsequently ignore the information about the individual phase shifts (The phase difference is equal to the phase φ introduced in Sec. 7.3.4.)

This then leaves us with a density matrix of the form

$$\rho_{2_L,2_R} = \begin{pmatrix} p_{00} & 0 & 0 & 0 & 0 & 0 \\ 0 & p_{01} & d & 0 & 0 & 0 \\ 0 & d^* & p_{10} & 0 & 0 & 0 \\ 0 & 0 & 0 & p_{11} & E & F \\ 0 & 0 & 0 & E^* & p_{02} & G \\ 0 & 0 & 0 & F^* & G^* & p_{20} \end{pmatrix}. \tag{7.3}$$

which is written in the basis $|i\rangle_{2_L}|j\rangle_{2_R}$, with the number of photons $\{i,j\} = \{0,1,2\}$. p_{ij} is then the probability to find i photons in mode 2_L and j photons in mode 2_R. The element d gives the coherence between the $|1\rangle_{2_L}|0\rangle_{2_R}$ and $|0\rangle_{2_L}|1\rangle_{2_R}$ states, and similarly for E, F, and G. We can bound the entanglement of formation (EOF) of this state by

$$EOF(\rho_{2_L,2_R}) \geq \tilde{P} EOF(\tilde{\rho}_{2_L,2_R}), \tag{7.4}$$

where

$$\tilde{P} = p_{00} + p_{01} + p_{10} + p_{11}, \tag{7.5}$$

$$\tilde{\rho}_{2_L,2_R} = \frac{1}{\tilde{P}} \begin{pmatrix} p_{00} & 0 & 0 & 0 \\ 0 & p_{01} & d & 0 \\ 0 & d^* & p_{10} & 0 \\ 0 & 0 & 0 & p_{11} \end{pmatrix}. \tag{7.6}$$

In this step we assume that never more than 2 photons populate each mode. This is

an excellent approximation on its own (and is supported by our measurements), but more importantly, this assumption corresponds to lower bounding the entanglement, as detailed below. One obtains this bound by considering the effects of two local operations by Alice and Bob consisting of measuring whether each mode has more than 1 photon or not and communicating this result one to the other. We treat this step explicitly in order to remind ourselves we do have to keep track of the total probability to find more than 1 photon in one of the modes, $1 - \tilde{P}$. Also, we note explicitly this step does not correspond to any procedure in our experiment, but is just an analytic tool to bound the entanglement and express it in terms of quantities that can be easily determined without too large uncertainty (unlike higher-order matrix elements such as p_{12}, etc.)

7.3.2 Quantum state tomography

To experimentally verify the entanglement of the ensembles, we adopt the concept of quantum state tomography and devise measurements to deduce the various components of $\tilde{\rho}_{2_L,2_R}$ (Eq. (7.6)). The concurrence $C(\tilde{\rho}_{2_L,2_R})$ can then be calculated from Eq. (7.6) by way of Ref. [98],

$$C = \max(2|d| - 2\sqrt{(p_{00}p_{11})}, 0)/\tilde{P} \ . \tag{7.7}$$

The entanglement of formation EOF follows directly from C:

$$EOF = h\left(\frac{1 + \sqrt{1 - C^2}}{2}\right), \tag{7.8}$$

where

$$h(x) \equiv -x \log_2 x - (1 - x) \log_2 (1 - x). \tag{7.9}$$

EOF and C both range from 0 to 1 for our system and EOF is a monotonically increasing function of C [98].

7.3.3   The diagonal elements

As a first step in the determination of C we measure the diagonal elements p_{ij}. As shown in Fig. 1b, the field-2 output of each ensemble is directed to different sets of detectors in order to record photon counting probabilities for the fields $2_L, 2_R$ separately. From the record of photoelectric counting events, we then deduce the diagonal elements of $\tilde{\rho}_{2_L, 2_R}$, which are listed in Table 7.1. From Eq. (7.7) and noting that $|d|^2 \leq p_{10}p_{01}$, a necessary requirement for $C > 0$ is that there be a suppression of two-photon events relative to the square of the probability for single-photon events for the fields $2_L, 2_R$ i.e., $h_c^{(2)} \equiv p_{11}/(p_{10}p_{01}) < 1$. For our measurements, we find $h_c^{(2)} = 0.30 \pm 0.04$ for events conditioned on detection at D_{1a}, and $h_c^{(2)} = 0.35 \pm 0.04$ for events conditioned on D_{1b} [64]. In contrast, for non-conditioned events, we find $h_{nc}^{(2)} = 0.99 \pm 0.04$.

The difference in the two sets of probabilities $(p_{01}^{(1a)}, p_{10}^{(1a)})$ and $(p_{01}^{(1b)}, p_{10}^{(1b)})$ results from an asymmetry in the beam splitter BS_1 for detection of the write fields $1_L, 1_R$, with a measured ratio of transmission to reflection $T/R = 0.85$. Hence, in addition to the $\pm$ sign in Eq. (7.1) set by detection at D_{1a} or D_{1b}, the relative amplitudes for the conditional state can also differ, resulting in different values for the concurrence.

Table 7.1: Diagonal elements of the density matrix $\tilde{\rho}_{2_L,2_R}$ [Eq. (7.6)], deduced from the records of photo-electric counts.

Probability	D_{1a}	D_{1b}
p_{00}	0.98510 ± 0.00007	0.98501 ± 0.00007
p_{10}	$(7.38 \pm 0.05) \times 10^{-3}$	$(6.19 \pm 0.04) \times 10^{-3}$
p_{01}	$(7.51 \pm 0.05) \times 10^{-3}$	$(8.78 \pm 0.05) \times 10^{-3}$
p_{11}	$(1.7 \pm 0.2) \times 10^{-5}$	$(1.9 \pm 0.2) \times 10^{-5}$

We expect the ratio $(p_{01}^{(1a)}/p_{10}^{(1a)})(p_{01}^{(1b)}/p_{10}^{(1b)})^{-1}$ to be $(T/R)^2 = 0.73$, which agrees well with the measured value $(7.51/7.38)(8.78/6.19)^{-1} = 0.72$.

The values of p_{ij}, $(i, j) = (0, 1)$, in Table 7.1 are referenced to the locations of detectors $D_{2a,2b,2c}$, and were obtained by considering unit detection efficiency, which gives a more conservative (i.e., smaller) lower bound for the concurrence than the actual (larger) field concurrence for finite efficiency < 1.

7.3.4 The coherence term d

The second step in our tomography protocol is to determine the coherence term d in Eq. (7.6), which we accomplish by adding a relative phase shift φ for the fields $2_L, 2_R$, and by combining them at the beam splitter BS_2 shown in Fig. 7.1b. By recording the conditional count rate after the beam splitter as function of φ, one can measure an interference fringe with a visibility V, with then $|d|$ following from V and the p_{ij}. Roughly, for 50-50 beam splitters and neglecting higher order terms (that are employed in our actual analysis), we would have $|d| \cong V(p_{10} + p_{01})/2$ (see Sec. 7.6.4).

Figure 7.2 shows conditional counts $N_{2a}, N_{2b} + N_{2c}$ as functions of φ. These data demonstrate that the indistinguishable character of measurement events at detectors

D_{1a} (Fig. 7.2a) and D_{1b} (Fig. 7.2b) induces a high degree of coherence between the otherwise independent ensembles L, R [22, 93].

Indeed, we deduce visibilities $V_{1a} = (70 \pm 2)\%$ and $V_{1b} = (71 \pm 2)\%$ for the associated conditional states. Although the interference fringes have comparable visibility, the different sizes arise from unequal quantum efficiencies for detectors D_{2a} (32%)and $D_{2b,2c}$ (40%). The visibility values are obtained from the average of the visibilities of the red and black curves, respectively.

A notable feature of these results is that the interference fringes have relative phase π for the cases of detection at D_{1a}, D_{1b}, in agreement with Eqs. (7.1), (7.2). We also observe similar fringes if the phase η_1 between the write beams is varied instead of φ. Moreover, when the fields $1_L, 1_R$ are combined at the beamsplitter BS_1 with orthogonal polarizations (by way of the half-wave plate in Fig. 7.1a), we find that the visibility from interference of fields $2_L, 2_R$ drops to near zero (Fig. 7.2c and 7.2d), since in this case, there is no longer measurement-induced entanglement associated with quantum interference for detection of fields $1_L, 1_R$. The residual oscillation in the conditional count rate can be explained by the finite polarization extinction ratio in our polarization maintaining fibers. The fibers used in our experiment have a measured extinction ratio of 28 dB between their two orthogonal propagation modes. This can lead to a residual visibility of 8%, which is compatible with the amplitude of the residual oscillation in Fig. 7.2(c,d).
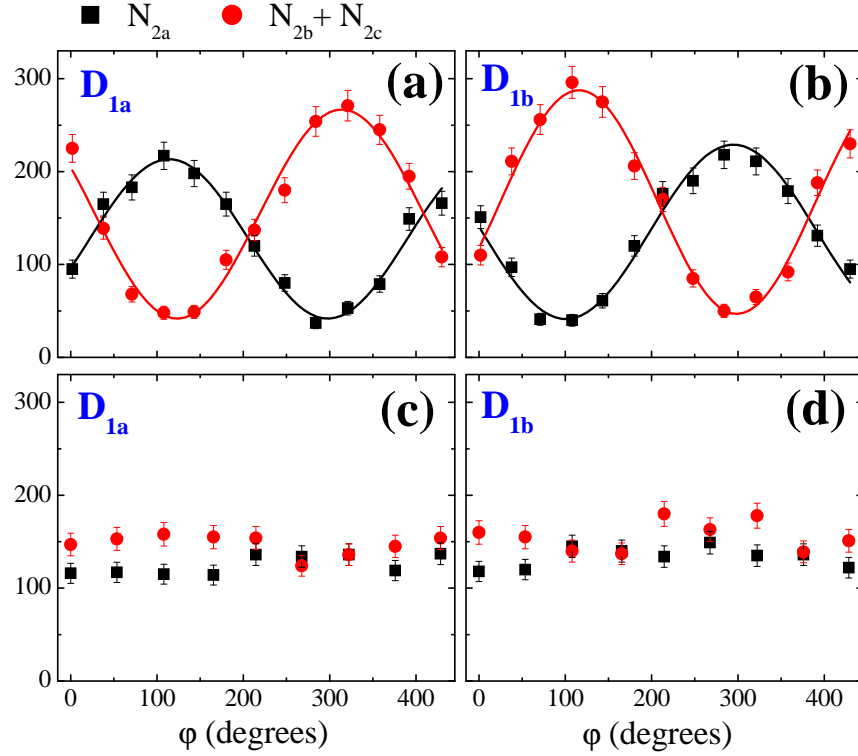
Figure 7.2: Coherence between the atomic ensembles L, R is induced by a measurement event of the fields $1_L, 1_R$ at detector D_{1a} or D_{1b}. Shown is the number of coincidences N_{2a} (circles) and $N_{2b} + N_{2c}$ (triangles) recorded by the respective detectors $D_{2a,2b,2c}$ for the fields $2_L, 2_R$ with the interferometer arrangement of Fig. 7.1b as a function of the relative phase φ. In (a) and (c) $N_{2a,2b,2c}$ are conditioned upon a detection event at D_{1a} with no count at D_{1b}, while in (b) and (d) $N_{2a,2b,2c}$ are conditioned upon an event at D_{1b} with no count at D_{1a}. (a) and (b) show the interference fringe between fields $2_L, 2_R$ as a result of combining fields $1_L, 1_R$ in an approximately indistinguishable fashion with parallel polarizations. (c) and (d) show the results of the same measurement on fields $2_L, 2_R$, but now with fields $1_L, 1_R$ combined with orthogonal polarizations. At each setting of φ, data are acquired for 150 s with a detection window of width 190 ns. Error bars reflect $\pm$ one standard deviation due to the finite number of counts.

7.3.5 Concurrence

With Eq. (7.7), the measured values for the visibility V and for the various p_{ij} are sufficient to deduce a lower bound for the concurrence C for the field state $\tilde{\rho}_{2_L,2_R}$ at the location of detectors $D_{2a,2b,2c}$, with no correction for detection efficiencies or

propagation losses, we find

$$C_{1a}(\tilde{\rho}_{2_L,2_R}) = (2.4 \pm 0.6) \times 10^{-3} > 0 \ , \ C_{1b}(\tilde{\rho}_{2_L,2_R}) = (1.9 \pm 0.6) \times 10^{-3} > 0 \ , \quad (7.10)$$

conditioned upon detection at either D_{1a} or D_{1b}. This conclusively demonstrates a nonzero degree of entanglement between the ensembles, albeit with the concurrence $C_{L,R}$ small. The small difference between the concurrence for the states conditioned on D_{1a} or D_{1b} can be explained by the asymmetry in BS_w (see Sec. 7.3.3).

Beyond the firm lower bound given by Eq. (7.10), we can make a better estimate of the degree of entanglement $C_{L,R}$ between the L, R ensembles by way of detailed measurements of the propagation efficiencies from the atomic ensembles to the plane z_0 of the detectors shown in Fig. 7.1b (see Sec. 7.6). Figure 7.3 gives an inference of the density matrix $\tilde{\rho}_{2_L,2_R}^{z_i}$ and thereby of the concurrence $C^{z_i}(\tilde{\rho}_{2_L,2_R}^{z_i})$ at z_0 and at two other locations $z_{i=1,2}$ along the path from the ensembles to the detectors (see Fig. 7.1b), assuming a constant visibility. Generally, C increases in direct correspondence to the reduced level of losses for the $2_L, 2_R$ fields at locations closer to the ensembles. At location z_2 corresponding to the output edges of the atomic ensembles, we find the result

$$C_{L,R}^{1a} \geq C_{1a}^{z_2}(\tilde{\rho}_{2_L,2_R}^{z_2}) \simeq 0.021 \pm 0.006 > 0 \ , \ C_{L,R}^{1b} \geq C_{1b}^{z_2}(\tilde{\rho}_{2_L,2_R}^{z_2}) \simeq 0.016 \pm 0.006 > 0 \ .$$

$$(7.11)$$

To move beyond this result, we need more detailed information about the efficiencies $\xi_{L,R}$ with which stored excitation in the atomic ensembles is converted to the propa-

gating light fields $2_L, 2_R$. Our earlier measurements included comparisons to a simple model [64] (Chapter 4) and allowed an inference $\xi_{L,R} \sim 0.10 \pm 0.05$. The measurement of the losses together with the values of p_{ij} at the detectors yields $p_{10} + p_{01} \approx 11\%$ at the output of the ensembles (z_2 plane) for our current experiment. This value together with the estimated $\xi_{L,R}$ then indicates that $p_{00} \to 0$ for the conditional state $\rho_{L,R}$ of the ensembles, so that $C_{L,R} \approx V \approx 0.7$, suggesting that $\rho_{L,R}$ is close to the ideal entangled state of Eq. (7.1). The low measured values for the entanglement between fields $2_L, 2_R$ apparently are principally a consequence of the low readout efficiency $\xi_{L,R}$ of the atomic excitation. We stress that this inference of C for the state inside the ensembles must be confirmed by subsequent experiments and is offered here to provide some insight into future prospects for quantum protocols with entangled ensembles. This also emphasizes that a central point in subsequent work should be the improvement of $\xi_{L,R}$.

7.4 Summary

To summarize, we have achieved entanglement between a pair of atomic ensembles separated by 2.8 m, with the entangled state involving one spin excitation within a collective system of roughly 10^5 atoms at each site L, R. The entangled state is generated by and conditioned upon an initial detection event, and is thus produced in a probabilistic fashion. However, this initial event heralds unambiguously the creation of an entangled state between L, R ensembles, which is physically available for subsequent utilization, as, for example, by mapping to propagating optical fields, which can be in principle accomplished with high efficiency. We emphasize that our measurements relate to an actual physical state of the L, R ensembles and of the $2_L, 2_R$ fields, and are not an inference of a state based upon post selection. Our work provides the first example of a stored atomic entangled state that can be transferred to entangled light fields, and significantly extends laboratory capabilities for entanglement generation, with now entangled states of matter stored with separation a hundred-fold larger than was heretofore possible for continuous quantum variables and a thousand-fold larger than for qubits. With our current setup, we have demonstrated $\Delta t_s \simeq 1 \ \mu$s for storing entanglement. However, this should be readily extended to $\Delta t_s \simeq 10 \ \mu$s, and new trapping schemes have the potential to lead to $\Delta t_s \simeq 1$ s [77]. The distance scale for separating the L, R ensembles is limited by the length $l_0 \simeq 2$ km for fiber optic attenuation at our write wavelength 852 nm. Extensions to scalable quantum networks over larger distances requires the realization of a quantum repeater [22], for which we have now laid the essential foundation.
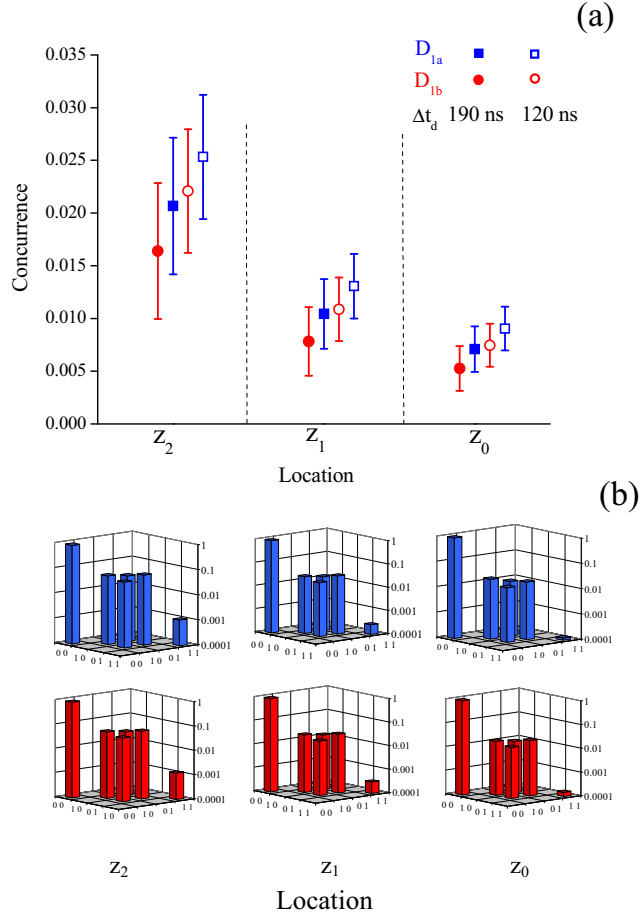
Figure 7.3: The results of our measurements for the concurrence C^{z_i} (a) and density matrix $\tilde{\rho}^{z_i}_{2_L,2_R}$ (b) are shown at the three locations z_i indicated in Fig. 7.1b. At each location, two pairs of results are given corresponding to the measurement-induced state created from detection at D_{1a} and at D_{1b}, and taking into account the efficiency of the detectors and propagation losses. (a) Concurrence C, for two different detection windows Δt_d at $D_{2a,2b,2c}$. Filled symbols are for $\Delta t_d = 190$ ns, enough to acquire the whole temporal wavepacket of field 2. Open symbols are for $\Delta t_d = 120$ ns. We see then that the degree of entanglement can be further enhanced, similar to the increase of nonclassical correlations between fields 1 and 2 reported in Ref. [67] for specific detection windows for these fields. All values shown in this figure, including the ones for z_0, are already corrected for the efficiencies of the detectors. Error bars reflect ± 1 standard deviation, taking into account the finite number of counts and the uncertainties in the efficiency and propagation loss. (b) Density matrix $\tilde{\rho}^{z_i}_{2_L,2_R}$ given in the basis $|n\rangle_{2_L}|m\rangle_{2_R}$ corresponding to Eq. (7.6), with $\{n,m\} = \{0,1\}$.

7.5 Details on the scheme of locking the phases of the interferometers

7.5.1 Introduction

In the experiment, we had to stabilize the phase of the write interferometer to create the same entangled state in every trial, and vary the phase of the read interferometer in a controlled fashion by at least 360 degrees in the protocol verifying entanglement. In the following, I will write down the details on the setup, how the error signals are derived, and how we manage to keep the phases controlled for extended periods of time.

7.5.2 Experimental setup

Fig. 7.4 gives a summary of the setup. Along with the write beam, a laser beam at 1064 nm, derived from a Nd:YAG laser, is injected into the other input port of the fiber beam splitter BS_W, as is similar for the case with the read beam. Since the setup is designed to separate the classical write and read fields from the (1,2) fields by exploiting their polarizations, it is not easy to device a way for the 1064 beams to traverse the paths of the write (read) beams before the ensembles and those of fields 1 (2) after the ensemble to cover the arms of the write (read) interferometer. The solution we adopted is to use polarization beam splitters, PBS-850 from CVI, which have good (>1000:1) extinction ratio at the wavelengths of write and read beams, but transmits about 40% of S polarization (perpendicular to the incident
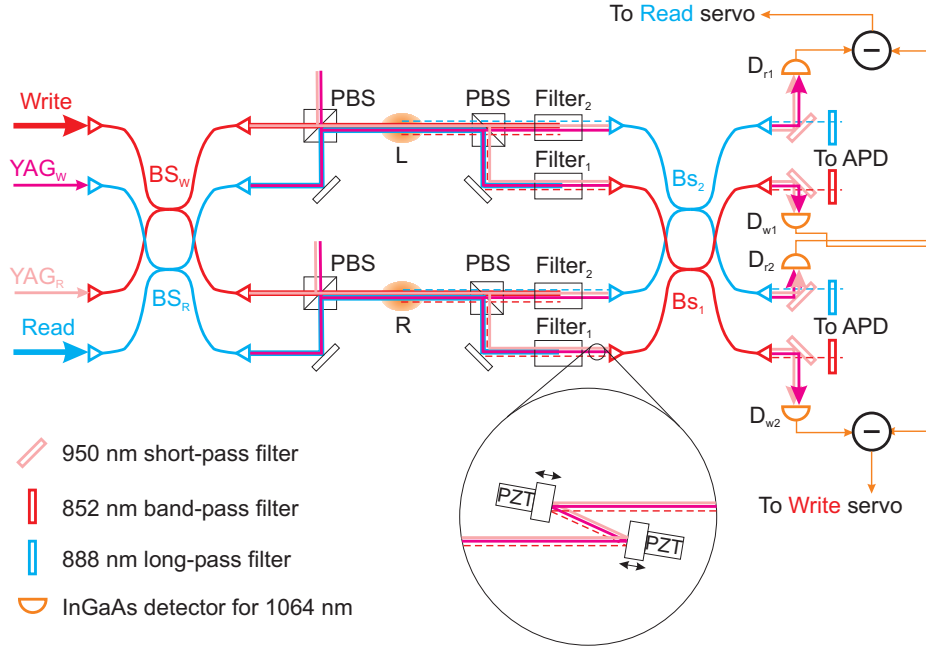
Figure 7.4: The two interferometers. Filter$_{1(2)}$ are paraffin-coated cesium vapor cells, 15 cm in length, and optically pumped to $F = 4(3)$ ground states. The other filters are all from Omega Optical. Two PZT are used in each interferometer for larger dynamic range. The dashed lines denote the nonclassical fields generated by the writing (red) and reading (cyan) processes.

plane) at 1064 nm. The polarization of the two beams at 1064 nm, YAG$_1$ and YAG$_2$, is aligned to the axes of the polarization maintaining fiber beam splitters, BS_W and BS_R, respectively, in such a way that the outputs are S-polarized to the PBS. Thus the PBS both transmits and reflects YAG$_1$ and YAG$_2$ and there is always some light at 1064 nm in the paths of the interferometers so that we can derive error signals for the control of interferometer phases.

7.5.3   Error signal

In this section, I will describe in detail the way of deriving the error signals for the write and read interferometers.

7.5.3.1 Making the channels independent

Because the light from both YAG_1 and YAG_2 beams goes to all four InGaAs detectors (Thorlabs PDA400), we need a way to "distinguish" YAG_1 light from YAG_2 light, so that the two interferometers can be independently controlled. The way we do it is by chopping YAG_1 and YAG_2 beams with two acousto-optic modulators (AOM) and gate the detector signal accordingly. Specifically, the two AOMs work in an alternating fashion: when one is on, the other is off, and vice versa. The RF signals feeding the RF amplifier driving the AOMs are chopped by RF switches (Mini-circuits ZASWA-2-50DR) which are in turn controlled by delay generators (SRS DG535). The delay generators run at a repetition rate of 400 kHz. This is determined by the 10 MHz 3dB bandwidth, and thus the step response, of the InGaAs detectors. Another reason of choosing that repetition rate is that it is far enough from the designed bandwidth of the feedback loop, about 10 kHz, so that it is rather easy to filter away the effect of chopping with low-pass filters. Note that we had to change from Silicon detectors to InGaAs ones for fast response to 1064 nm light. Due to the finite rise and fall times of the detectors, in each period the beams are each turned on for about 1.1 μs instead of half the period, 1.25 μs. The signals from the detectors are each directed into one RF switch (Mini-circuits ZASWA-2-50DR). These RF switches gate the signals in a way that when YAG_1 is on and YAG_2 is off, the signals from D_{w1} and D_{w2} are passed to the subtracters but those from D_{r1} and D_{r2} are blocked by the other switches. For synchronization, the RF switches gating the InGaAs detectors are also controlled by the same delay generators that control the switching of YAG_1 and YAG_2 beams.

7.5.3.2 Countering the effect of power fluctuations

Due to many realistic factors, the light reaching D_w and D_r has about 15% power fluctuation. The factors include the Fabry-Perot effect in the fiber BS with FC-PC connectors, mechanical vibration of the setup, and slow temperature drift. The power fluctuation would show up in the error signal as extra noise and limit the performance of the feedback loop. To counter the effect of power fluctuation, the signals from D_{w1} and D_{w2} are directed to a subtractor, and so are those from D_{r1} and D_{r2}. With carefully balanced gain from each detectors, the effect of common-mode power fluctuation can be minimized. As a bonus, the magnitudes of the error signals are doubled.

In more detail, the signal from detector D_{w1} and D_{w2} can be written as

$$S_{w1} = \alpha_{w1}\left[R_1 I_{wL} + T_1 I_{wR} + 2\sqrt{R_1 T_1 I_{wL} I_{wR}}cos(\phi_w)\right] \tag{7.12}$$

$$S_{w2} = \alpha_{w2}\left[T_1 I_{wL} + R_1 I_{wR} - 2\sqrt{R_1 T_1 I_{wL} I_{wR}}cos(\phi_w)\right], \tag{7.13}$$

where $\alpha_{w1(2)}$ is a proportional constant, $I_{wL(R)}$ is the intensity of the 1064 nm light into the inputs of BS_1 from ensemble L(R). R_1, T_1 are the reflectance and transmittance, respectively, of BS_1. ϕ_w is the relative phase (at 1064 nm) between the two arms of

the write interferometer. Taking the difference

$$S_{w1} - S_{w2}$$

$$= (\alpha_{w1}R_1 - \alpha_{w2}T_1)I_{wL} + (\alpha_{w1}T_1 - \alpha_{w2}R_1)I_{wR}$$

$$+ 2(\alpha_{w1} + \alpha_{w2})\sqrt{R_1 T_1 I_{wL} I_{wR}}cos(\phi_w) \qquad (7.14)$$

We can see that any fluctuation in I_{wL} or I_{wR} would result in noise in the DC level (the two terms independent of ϕ_w) in the error signal. However, we can minimize the effect by tuning the ratio α_{w1}/α_{w2}. In addition, if we choose to lock at the zero crossing ($\phi_w = \pi/2 + n\pi$) of the compensated error signal, the phase is less susceptible to power fluctuation.

In addition, active feedback can also be exploited to stabilize the beam power. This will be elaborated in a following section.

7.5.3.3   Error signal for locking at arbitrary phases

Obtaining the error signal for the read interferometer is trickier. Instead of locking the phase at a fixed value, we need to have the option of locking at arbitrary phases so that we can trace out a full fringe by varying the phase and accumulating the photo-electric events. Since it is the phase of the light on cesium transitions that we need to stablize and we are using another wavelength to lock the interferometers, we have to keep the interferometers locked while acquiring the fringe. Once we lose the lock and re-acquire it, it is quite difficult to know the phases at cesium transition frequencies. Thus we can not afford to unlock the interferometers to change the interferometer

phase. A solution is to derive an error signal whose zero crossing can correspond to variable phase, on the contrary to the case in Sec. 7.5.3.2. The way we do it is by adding two error signals, one obtained in the same way as in Eq. (7.14), the other the derivative. Changing the weighting in the sum, the phase corresponding to the zero crossing would vary accordingly. Fig. 7.5 shows a example. This approach is simpler but has a drawback that the phase does not vary linearly with the weighting in the sum. Note that the magnitude of the signal, and thus the overall gain of the feedback loop, also varies with the weighting. As long as the interferometer can be well locked, this is acceptable. A simple circuit implementation can yield the linear superposition of the direct error signal and the derivative.

We tried two ways to obtain the derivative. The first we tried is modulating the PZT at about 80 kHz and demodulate the signal with a Lock-In amplifier. This approach did not work well since we cannot increase much the modulation frequency due to the bandwidth of the PZT driver (40 kHz, Thorlabs MDT694A) and the modulation cannot be well filtered without affecting the frequency below the desired servo bandwidth, 10 kHz. Thus we switched to another approach: introducing phase modulation to the light fields with a electro-optic modulator (New Focus Model 4002). The modulator has a 100 MHz bandwidth, and we are only limited by the bandwidth of the detectors. The signal can then be demodulated with a mixer. After a low-pass filter, the demodulated signal is just the derivative (see Sec. B.2.2). The modulating frequency was chosen to be 4 MHz to optimize the amplitude of the signal.

With the cosine and sine terms at hand, it is still not enough to trace the whole

360 degrees for the fringe. Specifically, the resultant signal is

$$(1 - X)sin(\phi) + Xcos(\phi)$$

$$= \sqrt{(1 - X)^2 + X^2}\left[cos(\theta)sin(\phi) + sin(\theta)cos(\phi)\right]$$

$$= \sqrt{(1 - X)^2 + X^2}sin(\phi + \theta) \tag{7.15}$$

where

$$cos(\theta) = \frac{1 - X}{\sqrt{(1 - X)^2 + X^2}} \tag{7.16}$$

$$sin(\theta) = \frac{X}{\sqrt{(1 - X)^2 + X^2}} \tag{7.17}$$

When the weighting X is increased from 0 to 1, θ monotonically increases from $0°$ to $90°$. Changing the weighting can only vary the lock point by $90°$ in phase at 1064 nm (about $107°$ at 894 nm). Note that by inverting the cosine and sine terms, we effectively shifted them by $180°$. Thus the following procedure can allow us to trace out a whole fringe without disabling the lock:

1. Change X from 0 to 1. This changes the error signal from $sin(\phi)$ to $cos(\phi)$ and change the lock point from $\phi = 0°$ to $\phi = 90°$.

2. Invert the sine component. $sin(\phi) \Rightarrow -sin(\phi) = sin(\phi + 180°)$. Note that since the weighting of the sine component is zero now, inverting it does not affect the lock.

3. Change X from 1 to 0. The lock point changes from $\phi = 90°$ to $\phi = 180°$.
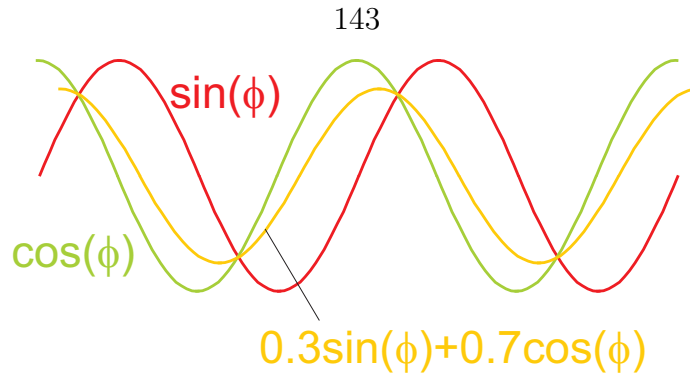
Figure 7.5: The error signal for locking at arbitrary phase

4. Invert the cosine component. $cos(\phi) \Rightarrow -cos(\phi) = sin(\phi + 270°)$. Note that since the weighting of the cosine component is zero now, inverting it does not affect the lock.

5. Change X from 0 to 1. The lock point changes from $\phi = 180°$ to $\phi = 270°$.

6. Invert the sine component. $-sin(\phi) \Rightarrow sin(\phi) = sin(\phi + 360°)$.

7. Change X from 1 to 0. The lock point changes from $\phi = 270°$ to $\phi = 360°$.

Repeating this procedure, we can go even further that a whole fringe. Reversing in phase is also very simple, just go backward in the procedure.

7.5.3.4   Calculating the phase

While tracing a fringe, we need to know the phase to which the number of coincidence corresponds to. Knowing the weighting X and the signs of the sine (difference) and cosine (derivative) components give us enough information to obtain the phase. Fig. 7.6 shows the change in phase, θ, in terms of the weighting, X. The signs tell us which segment we are on the fringe (Fig. 7.7). In practice, we obtained the phase by recording the values and signs of the two signals (difference and derivative).
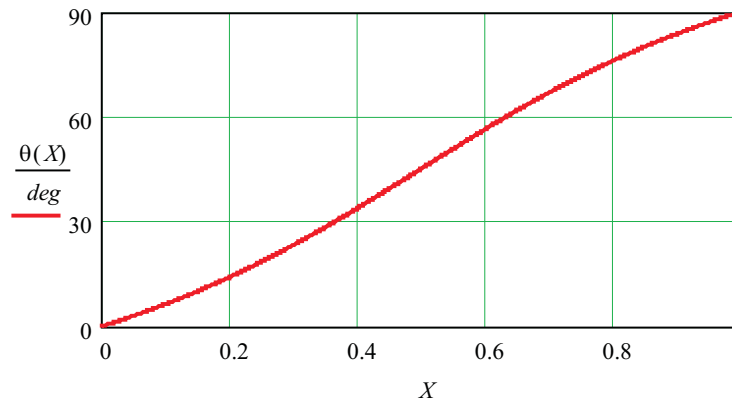
Figure 7.6: Change in the lock point, θ, versus the weighting, X.

The values are read off a digital oscilloscope (Tektronix TDS 2024) with a LabView program (see Appendix E). Along with the signs entered by hand, the program automatically calculates the phase.

7.5.4 Servo design and circuit diagram

Fig. 7.8 shows the circuit diagram for the servo controlling one interferometer. The servo has two branches: one controls the PZTs (shown in the blowup in Fig 7.4) varying optical path length; the other branch drives a voltage-controlled attenuator (Mini-circuits ZFAS-2000) that tunes the power of YAG_1 or YAG_2 beams.

7.5.4.1 The branch controlling PZT

The signals from the two detectors for the interferometer, e.g., D_{w1} and D_{w2}, are fed to the ports In1 and In2. The first Op Amp functions as both a subtracter and a low-pass filter which attenuates the high harmonics of the 400 kHz chopping frequency. The other Op Amps in the branch also attenuate the 400 kHz chopping frequency so
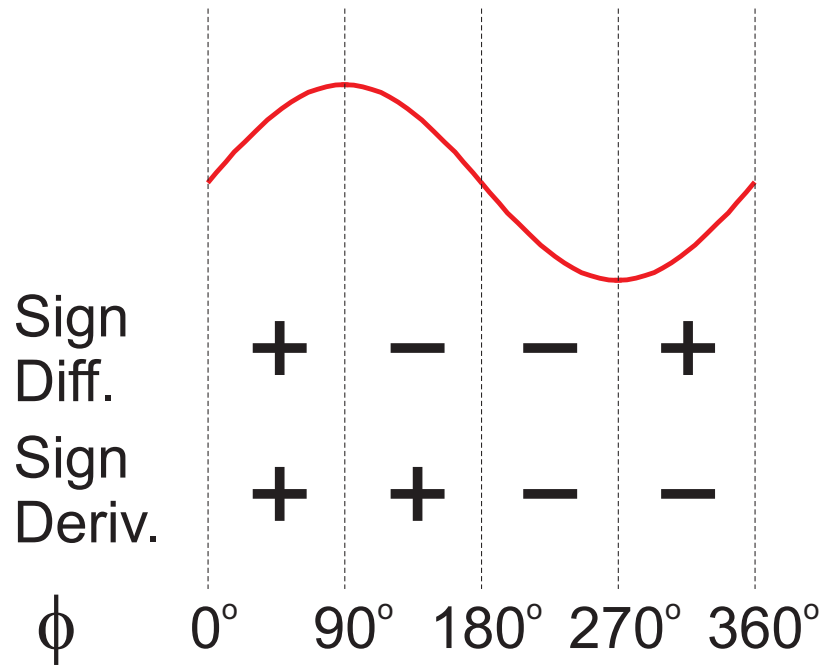
Figure 7.7: The signs of the difference (Diff.) and derivative (Deriv.) signals can tell us the segment of fringe we are sitting on.
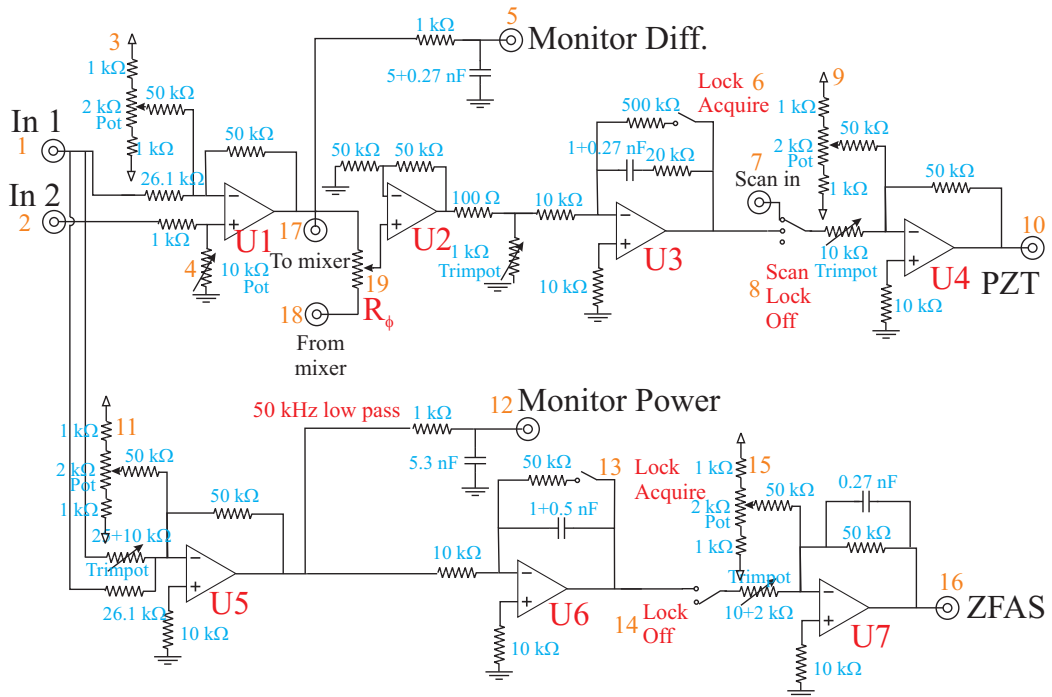
Figure 7.8: Circuit diagram for the servo controlling one interferometer phase.

that only the low frequency components of the error signal are in effect. The output of the first Op Amp is picked off and sent to the mixer. The output of the mixer is low-passed and amplified with proper gain to get the derivative which is in turn fed back to the port "From mixer."

The potentiometer R_ϕ linearly combines the difference output of U1 and the derivative obtained with the mixer. The resistance of R_ϕ directly corresponds to the weighting X. U2 has a large input impedance and does not load R_ϕ. The voltage at the non-inverting port of U2 is amplified by the non-inverting amplifier consisting of U2 and the surrounding resistors and then fed to U3. U3 and the surrounding elements form the heart of the servo. The magnitude of its transfer function behaves like an integrator (low-pass filter) at low frequency when it is set at lock (acquire), and rolls flat at frequency higher than the corner frequency determined by the capacitor and the resistor next to it. U4 is at the center of an inverting amplifier with variable gain and offset. The input to U4 can be chosen by the switch to be a triangular wave (Scan in) for scanning or the output from U3 for locking the phase.

7.5.4.2   The branch controlling power of $YAG_{1(2)}$

In case the power of $YAG_{1(2)}$ beam fluctuates a lot, one would want to stabilize its power. In this branch, the signals from the two detectors are summed by U5 with tunable ratio. The stage with U6 is a integrator (low-pass filter) when the switch is set at lock (acquire). The last stage with U7 is an inverting amplifier with variable gain and offset just like that with U4. This is inverting to enable negative instead of positive feedback.

7.5.5 Extending dynamic range of the servo with extra PZTs

The PZT we use is Thorlabs AE0505D08, which safely provides about 10 μm of displacement. It turns out the optical paths drift relatively more than one PZT can handle and the interferometers fall out of lock every 10 to 20 minutes. After we added extra PZTs in the paths (see the ballon in Fig. 7.4), the interferometers can be locked for more than an hour while, in each interferometer, one PZT is controlled by the servo and the other controlled by hand to compensate for the slow drifts.

7.6 Deriving matrix elements and lower bounds for the concurrence from detection probabilities

7.6.1 Introduction

In the entanglement experiment, all we measured is detection probabilities. In this section I would like to elaborate on how we obtain the density matrix and the lower bound for the concurrence, from detection probabilities.

Sec. 7.6.2 details the derivation of the detection probabilities from a (simplified) density matrix. Sec. 7.6.3 then infers the matrix elements from the actual detection probabilities and the expressions obtained in Sec. 7.6.2. The way to deriving a lower bound for the concurrence is given in Sec. 7.6.4, which is simplified by assuming unity efficiencies in the detectors.
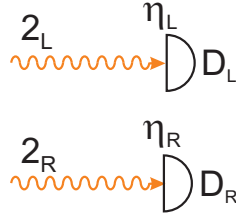
Figure 7.9: The diagonal elements of $\tilde{\rho}_{2_L,2_R}$ are measured with fields 2_L and 2_R directed to two detectors with quantum efficiencies η_L and η_R, respectively. The detection probabilities from this setup are denoted P_{mn}, with m being the number of clicks registered in a trial by the L detector, and n that for the R detector.

7.6.2 Derivation of the detection probabilities from the density matrix

7.6.2.1 Measuring diagonal elements

We start with two fields, denoted 2_L and 2_R, in the state described by the density matrix

$$
\tilde{\rho}_{2_L,2_R} = \begin{pmatrix} p_{00} & 0 & 0 & 0 \\ 0 & p_{10} & d & 0 \\ 0 & d^* & p_{01} & 0 \\ 0 & 0 & 0 & p_{11} \end{pmatrix}
$$

which is written in the number basis $|m\rangle_{2_L}|n\rangle_{2_R}, \{m, n\} = \{0, 1\}$.

To measure the diagonal elements, we direct the two fields to two detectors with efficiencies η_L and η_R (Fig. 7.9). The probabilities P_{mn} that the L detector registers
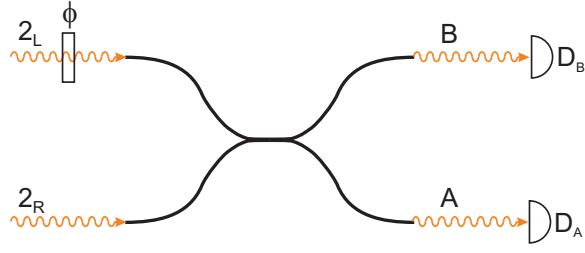
Figure 7.10: Fields 2_L and 2_R are transformed into fields A and B by the beam splitter. The probablility that detector D_A registers 1 click and detector D_B registers none is called Q_{10}. Q_{01} is defined similarly.

m clicks and the R detector registers n clicks are

$$P_{00} = p_{00} + (1 - \eta_L)p_{10} + (1 - \eta_R)p_{01} + (1 - \eta_L)(1 - \eta_R)p_{11} \qquad (7.18a)$$

$$P_{01} = \eta_R p_{01} + (1 - \eta_L)\eta_R p_{11} \qquad (7.18b)$$

$$P_{10} = \eta_L p_{10} + (1 - \eta_R)\eta_L p_{11} \qquad (7.18c)$$

$$P_{11} = \eta_L \eta_R p_{11}, \qquad (7.18d)$$

where η_i stands for the quantum efficiency of detector i, i.e., the probability that the detector gives a click when there is one photon in field i, and $1 - \eta_i$ is the probability that detector i fails to click when there is one photon in field i.

7.6.2.2 Fringe measurement

The logic of this section goes as follows:

1. Start with the density matrix of fields 2_L and 2_R at the input of a beam splitter (the beam splitter in Fig. 7.10 or BS_2 in Fig. 7.1) combining the two modes. We then get the density matrix of the two output modes, A and B.

2. With the output density matrix, we can calculate the probabilities, Q_{mn}, of one

detector registering m clicks and the other n clicks, with $\{m, n\} = \{0, 1\}$.

We start with the density matrix $\tilde{\rho}_{2_L, 2_R}$. The beam splitter and the phase shifter (varying ϕ) perform the following transformation on the creation operators $a_x^\dagger$ for mode x:

$$a_{2_L}^\dagger = Coa_B^\dagger + iSia_A^\dagger \tag{7.19a}$$

$$a_{2_R}^\dagger = e^{i\phi}(iSia_B^\dagger + Coa_A^\dagger) \tag{7.19b}$$

where Co^2 and Si^2 stand for the transmittance and reflectance of the beam splitter. Thus the states are transformed in the following way:

$$|00\rangle_{2_L 2_R} \rightarrow |00\rangle_{AB} \tag{7.20a}$$

$$|10\rangle_{2_L 2_R} = a_{2_L}^\dagger |00\rangle_{2_L 2_R} \rightarrow (Coa_B^\dagger + iSia_A^\dagger)|00\rangle_{AB} \tag{7.20b}$$

$$= Co|01\rangle_{AB} + iSi|10\rangle_{AB} \tag{7.20c}$$

$$|01\rangle_{2_L 2_R} \rightarrow e^{i\phi}(iSi|01\rangle_{AB} + Co|10\rangle_{AB}) \tag{7.20d}$$

$$|11\rangle_{2_L 2_R} \rightarrow (Coa_B^\dagger + iSia_A^\dagger)e^{i\phi}(iSia_B^\dagger + Coa_A^\dagger)|00\rangle_{AB}$$

$$= e^{i\phi}[i\sqrt{2}CoSi(|02\rangle_{AB} + |20\rangle_{AB}) + (Co^2 - Si^2)|11\rangle_{AB}] \tag{7.20e}$$

$$|20\rangle_{2_L 2_R} \rightarrow \frac{1}{\sqrt{2}}(Coa_B^\dagger + iSia_A^\dagger)^2|00\rangle_{AB}$$

$$= (Co^2|02\rangle_{AB} - Si^2|20\rangle_{AB} + \sqrt{2}iCoSi|11\rangle_{AB}) \tag{7.20f}$$

$$|02\rangle_{2_L 2_R} \rightarrow e^{i2\phi}(-Si^2|02\rangle_{AB} + Co^2|20\rangle_{AB} + \sqrt{2}iCoSi|11\rangle_{AB}) , \tag{7.20g}$$

We consider a lossless beam splitter, $Co^2 + Si^2 = 1$, and attribute the actual loss to the efficiencies of the detectors. The transformation in Eq. (7.20) can also be written in the matrix form mapping the bases $|00\rangle$, $|10\rangle$, $|01\rangle$, $|11\rangle$, $|20\rangle$, and $|02\rangle$ of modes $2_L, 2_R$ to those of modes A, B:

$$
T = \begin{pmatrix}
1 & 0 & 0 & 0 & 0 & 0 \\
0 & iSi & e^{i\phi}Co & 0 & 0 & 0 \\
0 & Co & e^{i\phi}iSi & 0 & 0 & 0 \\
0 & 0 & 0 & e^{i\phi}(Co^2 - Si^2) & i\sqrt{2}CoSi & e^{i2\phi}i\sqrt{2}CoSi \\
0 & 0 & 0 & e^{i\phi}i\sqrt{2}CoSi & -Si^2 & e^{i2\phi}Co^2 \\
0 & 0 & 0 & e^{i\phi}i\sqrt{2}CoSi & Co^2 & -e^{i2\phi}Si^2
\end{pmatrix}
\tag{7.21}
$$

The density matrix at the output of the beam splitter is then $\rho_{AB} = T\rho_{LR}T^\dagger$. The diagonal elements of ρ_{AB} are

$$p'_{00} = p_{00} \tag{7.22a}$$

$$p'_{10} = Si^2 p_{10} + Co^2 p_{01} + 2CoSi|d|sin(\phi - \phi_d) \tag{7.22b}$$

$$p'_{01} = Co^2 p_{10} + Si^2 p_{01} - 2CoSi|d|sin(\phi - \phi_d) \tag{7.22c}$$

$$p'_{11} = (Co^2 - Si^2)^2 p_{11} \tag{7.22d}$$

$$p'_{20} = 2Co^2 Si^2 p_{11} \tag{7.22e}$$

$$p'_{02} = 2Co^2 Si^2 p_{11} \tag{7.22f}$$

where $\phi_d = arg(d)$. Denoting η_A and η_B the detection efficiencies of the two output arms, we find the detection probabilities Q_{ij} that detector D_A register i clicks and D_B j clicks are

$$
\begin{aligned}
Q_{10} &= \eta_A p'_{10} + \eta_A(1 - \eta_B)p'_{11} + [2\eta_A(1 - \eta_A) + \eta_A^2]p'_{20} \\
&= \eta_A[Si^2 p_{10} + Co^2 p_{01} + 2CoSi|d|sin(\phi - \phi_d)] \\
&\quad + p_{11}[\eta_A(1 - \eta_B)(Co^2 - Si^2)^2 + (2\eta_A - \eta_A^2)2Co^2Si^2] ,
\end{aligned} \tag{7.23a}
$$

$$
\begin{aligned}
Q_{01} &= \eta_B[Co^2 p_{10} + Si^2 p_{01} - 2CoSi|d|sin(\phi - \phi_d)] \\
&\quad + p_{11}[\eta_B(1 - \eta_A)(Co^2 - Si^2)^2 + (2\eta_B - \eta_B^2)2Co^2Si^2] .
\end{aligned} \tag{7.23b}
$$

Note that in η_A and η_B we include the 80% total transmission of the beam splitter. Define $\Delta \equiv Q_{10} - Q_{01}$ and $\Sigma \equiv Q_{10} + Q_{01}$, and visibility $V \equiv \frac{\Delta_{max} - \Delta_{min}}{\Sigma_{max} + \Sigma_{min}}$. Assuming equal efficiencies, $\eta_A = \eta_B \equiv \eta$, the visibility is then represented by

$$
V = \frac{4SiCo|d|}{p_{01} + p_{10} + p_{11}[4Si^2Co^2(2 - \eta) + 2(Co^2 - Si^2)^2(1 - \eta)]} . \tag{7.24}
$$

7.6.3 Deriving the matrix elements from detection probabilities

7.6.3.1 Diagonal elements

By inverting the expressions in Sec. 7.6.2.1 (Eq. (7.18)), we can obtain the diagonal elements p_{ij}

$$p_{11} = P_{11}/(\eta_L \eta_R) \tag{7.25a}$$

$$p_{01} = P_{01}/\eta_{1R} - (1 - \eta_{1L})P_{11}/(\eta_L \eta_R) \tag{7.25b}$$

$$p_{10} = P_{10}/\eta_{1L} - (1 - \eta_{1R})P_{11}/(\eta_L \eta_R) \tag{7.25c}$$

$$p_{00} = P_{00} - (1 - \eta_{1R})P_{01}/\eta_{1R} - (1 - \eta_{1L})P_{10}/\eta_{1L}$$

$$+ (1 - \eta_{1R})(1 - \eta_{1L})P_{11}/(\eta_L \eta_R) \tag{7.25d}$$

7.6.3.2 Off-diagonal element

We can obtain the off-diagonal element $|d|$ from the fringe visibitily V (Eq. (7.24)):

$$|d| = \frac{V\{p_{01} + p_{10} + p_{11}[4Si^2Co^2(2 - \eta) + 2(Co^2 - Si^2)^2(1 - \eta)]\}}{4SiCo} \tag{7.26}$$

7.6.4 Lower bound for the concurrence

With the matrix elemets, we can calculate the concurrence. If we can precisely determine the quantum efficiencies of the detectors, we can obtain the value of the

concurrence to similar precision. However, measuring detector efficiency can be tricky. So we want a affirmative way of checking if the concurrence is positive independent of the detector efficiencies.

In order to give a lower bound for the off-diagonal element $|d|$ independent of the detector efficiencies, we consider the detectors to be of unity-efficiency and non-number-resolving. Substituting $\eta = 1$ in Eq. (7.26), we get

$$|d| = \frac{V(p_{01} + p_{10} + p_{11}4Si^2Co^2)}{4SiCo} \tag{7.27}$$

This sets a lower bound for $|d|$ since any $\eta < 1$ would increase the quantity multiplying p_{11} in the expression for $|d|$.

The next factor we need to consider is the beam splitter splitting ratio, Co and Si. Taking equal splitting ratio, $Co^2 = Si^2 = \frac{1}{2}$, sets a lower bound to $|d|$ since the denominator attains its maximum. Although the quantity $4Si^2Co^2$ in the numerator also reaches its maximum, 1, it multiplies p_{11} which is experimentally determined to be neglegible compared to $p_{01} + p_{10}$. Thus we have

$$|d| = \frac{V(p_{01} + p_{10} + p_{11})}{2} \approx \frac{V(p_{01} + p_{10})}{2} \; , \tag{7.28}$$

which gives a lower bound of $|d|$. This is the expression we use to estimate $|d|$ in Sec. 7.3.4.

Note that for a given set of detection probabilities P_{mn} and Q_{ij}, the inferred concurrence decreases with the values of ηs (Fig. 7.11). Thus simply assuming that
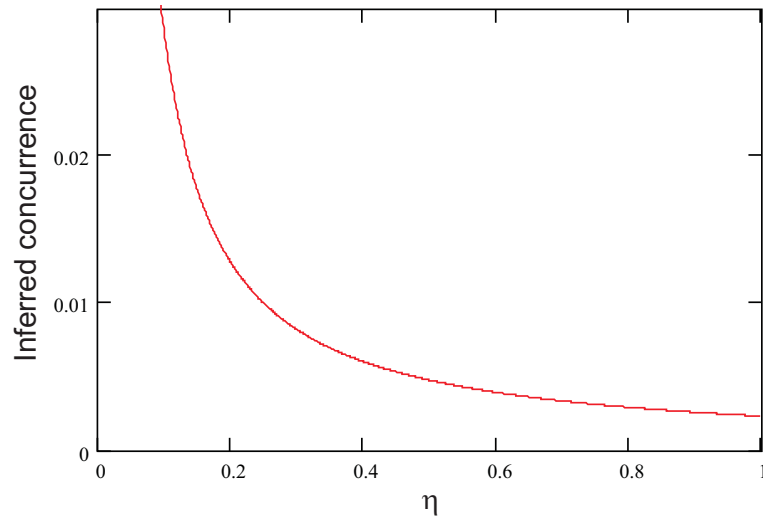
Figure 7.11: Inferred concurrence as a function of the detection efficiency used in the inversion. The detection probabilities in the cases when detector D_{1a} clicks are used in the plot. The plot assumes 70% fringe visibility for all values of η.

the detectors have unity efficiencies gives us a lower bound for the concurrence without the uncertainty introduced by the detector efficiencies.

The positive lower bound for the concurrence in Sec. 7.3.5 confirms that when either D_{1a} or D_{1b} registers a photo-electric click, the two ensembles are entangled. To gain more understanding on the entanglement stored in the ensembles, we try to characterize the propagation loss and infer the concurrence for the fields at various locations of the experimental setup. The solid symbols in Fig. 7.3(a) are the resulting concurrence assuming that the fringe visibility does not depend on the loss. In other words, the plot is done by figuring out the detection efficiency at various locations of the setup and reading the inferred concurrence off plots similar to Fig. 7.11. Fig. 7.3b shows all the inferred matrix elements on log scale.

7.7 Error propagation in estimating the entangle-

ment

In this section I write down the formula for error propagation and expressions of error in entanglement in terms of errors in the measured quantities.

7.7.1 Error propagation

A simple way to get errors of a compound quantity consisting of various measured variables is to take the partial derivative. For the statistically independent variables, the errors have to be summed in quadrature. That is:

$$(\Delta A(x_1, x_2, ...))^2 = \sum_i (\frac{\partial A}{\partial x_i} \Delta x_i)^2 \qquad (7.29)$$

Where ΔX denotes the uncertainty in determining the quantity X. For example, for $A = x_1^3 x_2^{-2} - x_3$,

$$(\Delta A(x_1, x_2, x_3))^2 = (3x_1^2 x_2^{-2} \Delta x_1)^2 + (-2x_1^3 x_2^{-3} \Delta x_2)^2 + (-\Delta x_3)^2 \qquad (7.30)$$

7.7.2 Errors in determining the diagonal elements

To estimate the error in the measured concurrence, first we need to determine the errors in the diagonal elements. From Eq. (7.25) we can obtain p_{00}, p_{10}, etc. from the measured Ps; if we assume that the APDs have unity quantum efficiency, Ps are just equal to ps. However, when we try to infer ps at various locations of the experimental

setup, the errors in the efficiencies would then result in larger errors in the diagonal elements and thus in the entanglement.

The uncertainties in ps are

$$\Delta p_{11} = p_{11}\sqrt{\frac{1}{N_{11}} + 2(\frac{\Delta\eta}{\eta})^2} \tag{7.31a}$$

$$\Delta p_{01} = p_{01}\sqrt{\frac{1}{N_{01}} + (\frac{\Delta\eta}{\eta})^2} \tag{7.31b}$$

$$\Delta p_{10} = p_{10}\sqrt{\frac{1}{N_{10}} + (\frac{\Delta\eta}{\eta})^2} \tag{7.31c}$$

$$\Delta p_{00} = \sqrt{(\Delta p_{10})^2 + (\Delta p_{01})^2 + (\Delta p_{11})^2} \tag{7.31d}$$

I took N as exact and no uncertainty is associated with it. Even it is not exact, the error is negligible. The efficiencies in the two arms are taken as statistically independent when determining Δp_{11}. The tiny contribution of the uncertainty from p_{11} is neglected when calculating Δp_{01} and Δp_{10}.

7.7.3 Error in the concurrence C

The concurrence, if greater than zero, is

$$C = 2|d| - 2\sqrt{p_{00}p_{11}} \tag{7.32}$$

in which (see (7.26))

$$|d| = \frac{V x_1}{4 SiCo}$$

$$x_1 = p_{01} + p_{10} + p_{11} x_2$$

$$x_2 = 4Si^2Co^2(2 - \eta) + 2(Co^2 - Si^2)^2(1 - \eta) \qquad (7.33)$$

So

$$(\Delta C)^2 = (2\Delta|d|)^2 + \left(-\sqrt{\frac{p_{11}}{p_{00}}}\Delta p_{00}\right)^2 + \left(-\sqrt{\frac{p_{00}}{p_{11}}}\Delta p_{11}\right)^2 \qquad (7.34)$$

where

$$
\begin{aligned}
(\Delta|d|)^2 &= [\Delta(V\frac{x_1}{4SiCo})]^2 \\
&= (\frac{x_1}{4SiCo}\Delta V)^2 + \left(\frac{V}{4SiCo}\Delta x_1\right)^2 \\
&\quad + \left[-\frac{V x_1}{4(SiCo)^2}\Delta(SiCo)\right]^2 \\
(\Delta x_1)^2 &= (\Delta p_{01})^2 + (\Delta p_{10})^2 + (x_2\Delta p_{11})^2 + (p_{11}\Delta x_2)^2 \\
(\Delta x_2)^2 &= \left[4(2-\eta)\Delta(Si^2Co^2)\right]^2 + \left[2(1-\eta)\Delta((Co^2 - Si^2)^2)\right]^2 \\
&\quad + \left[(-4Si^2Co^2 - 2(Co^2 - Si^2)^2)\Delta\eta\right]^2 \qquad (7.35)
\end{aligned}
$$

Note that the errors in Co^2 and Si^2 are not independent, so when we calculate the errors of quantities consisting of these variables, we should add the errors before taking the square. To avoid the uncertainty associated with beam splitter splitting ratio, we can take the ratio to be 50/50, which would underestimate $|d|$ for given visibility, ps, and η, etc. (see Sec. 7.6.4).

Chapter 8

Proposal toward Quantum Cryptography with Atomic Ensembles

8.1   Introduction

For quantum cryptography in the DLCZ protocol, two chains of ensembles are involved. As described in Sec. 2.6, we only need to maintain the stability of the relative phase ($\eta'_D - \eta'_U$ in Eq. (2.15)) between the two chains, which can potentially spare us the trouble of locking long-arm interferometers. In this Chapter I will lay down the basic ideas on how we can use the two ensembles as four to perform quantum cryptography by either following the DLCZ protocol or generating polarization entangled photons. Specifically, I write down the details on using two cylinders in one MOT as two ensembles and performing quantum cryptography with two MOTs, without the requirement of locking the path lengths of the interferometers.

8.2   Details on the scheme

As described in Sec. 2.6, the quantum cryptography scheme with entangled ensembles consists of first entangling two pairs of ensembles, heralded by two detection clicks. The excitations are then transferred to light fields. Conditioned on the heralding clicks, the coincidence rate that each communication party obtains a click in their detectors, revealing the transferred excitation, is dependent on the difference between the phases the parties introduce locally to the fields. The fourfold coincidences can then be exploited to violate a Bell's inequality and/or perform quantum cryptography.

To perform quantum cryptography following DLCZ, we need to meet the following criteria:

1. Effective four ensembles, two at each communicating party, constituting two
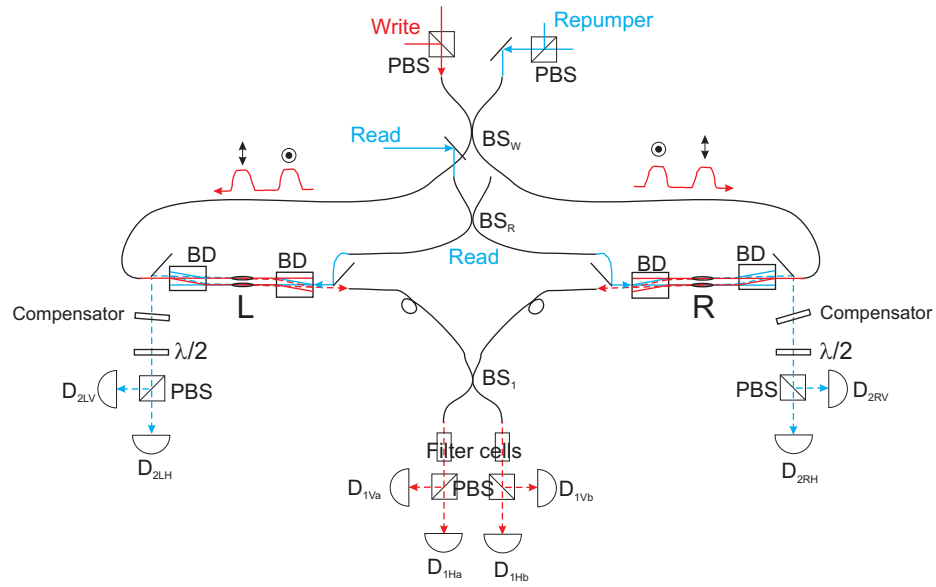
Figure 8.1: System schematic for the demonstration of quantum communication with atomic ensembles. Write, Read, field 1, and field 2 are coded as solid red, solid blue, dashed red, and dashed blue lines, respectively. PBS: a polarizing beam splitter; BS_W and BS_1: single-mode fiber beam splitters; BS_R: a polarization-maintaining fiber beam splitter; BD: a beam displacer; Compensator: birefringent plates varying the relative phase of the two polarization components of the transmitted beam; L (R): the MOT at the communication party with two cylindrical regions used as two ensembles.

entangled pairs.

2. Ability to address each ensemble at either party, including the writing, reading,

and re-initializing processes.

3. Known or stabilized relative phase between the two entangled pairs.

4. Phase coherent retrieval processes.

5. Memory to ensure polynomial scalability.

The proposed scheme is shown in Fig. 8.1. The features in the setup satisfying

the criteria are explained in detail in the rest of the section.

8.2.1 Using one MOT as two ensembles

To use one MOT as two ensembles, I adopt the idea from [93], and consider two spatially separated cylindrical regions in one ensemble as two independent one. We use a beam displacer (BD) to divide the write pulse into two orthogonal polarizations. The resultant beams are separated at millimeter scale. This setup should provide passive relative interferometric stability between the two paths. The paths between the BDs are polarization encoded. We can choose which cylinder to address by using different polarizations for the classical pulses.

8.2.2 Filtering and retrieval efficiency

Adopting the configuration in [27, 28], with counter-propagating writing and retrieval processes, near-uniform illumination from the classical beams, and non-collinear collection of the scattered (1,2) fields for each addressed cylinder, we should get higher retrieval efficiency [26], and the noise should be reduced with the angular separation between the classical and scattered fields.

8.2.3 Phase stability

The two pairs of entangled ensembles might not have the same relative phases between the two terms in the entangled state (Eq. (2.11)). With single-mode (SM) fibers and stable small interferometers formed by the BDs, the relative phase between the two entangled pairs can be fixed for the duration when the small interferometers are stable. Specifically, we use a single-mode fiber beam splitter to derive the write pulses and

deliver them to the two parties. Single-mode fibers have much lower birefringence than the polarization-maintaining ones so that even if the lengths of the fibers vary with time, the two polarization components of the light pick up the same phase shift at the same time. The two components can arrive at the same time if we direct the outputs of the fiber beam splitter to two PBS and detect photon 1 clicks separately, or we can time multiplex the detectors by sending the two polarizations consecutively. Thus the setup in Fig. 8.1 consists of two almost overlapping interferometers, whose paths are different only in the segments involving the BDs. The relative phase between the two interferometers needs to be stable for the duration of the memory time to ensure identical relative phase between the two entangled pairs when the excitations are ready for readout. The readout process depends on the long term stability of the BD interferometers. This has to last for the duration of the whole data acquisition.

8.2.4 Controlling the polarization for stable phases

In this proposal single-mode (SM) fibers are employed to ensure stability of the relative phase between the two polarization components. We can either use fiber polarization controllers or sets of wave plates to perform polarization transformation for the alignment of axes. The transformation will need to be checked from time to time. The fibers have to be fixed to rigid objects to avoid high frequency disturbance.

In the following, I will write down the detailed derivation for the phases of the two entangled pairs. I will refer to the two pairs as pair U and pair D (for up and down, as in Sec. 2.6). The two communicating parties are denoted L and R as usual. Denote the

propagation phase differences in the two output arms of BS_W as $\Delta\phi_{WH}$ and $\Delta\phi_{WV}$ for the two polarization H and V, respectively. Call the phase difference resulted from propagation between the BDs and through free space $\Delta\phi_{BDU}$ and $\Delta\phi_{BDD}$. Finally, the phase differences in the two input arms of BS_1 are called $\Delta\phi_{1H}$ and $\Delta\phi_{1V}$ for the two polarization H and V, respectively. When one of the $D_{1V}(D_{1H})$ clicks, the $D(U)$ pair is entangled. To the lowest order in the excitation probability, the state of the pair can be written as:

$$|\Phi_{LR}\rangle_{D(U)} = \left[\frac{1}{\sqrt{2}}(|1_L0_R\rangle + e^{i\Delta\phi_{D(U)}}|0_L1_R\rangle)\right]_{D(U)}, \qquad (8.1)$$

where

$$\Delta\phi_D = \Delta\phi_{WH} + \Delta\phi_{BDD} + \Delta\phi_{1V}, \qquad (8.2)$$

$$\Delta\phi_U = \Delta\phi_{WV} + \Delta\phi_{BDU} + \Delta\phi_{1H}. \qquad (8.3)$$

In the following, I would like to argue that the difference $\Delta\phi \equiv \Delta\phi_U - \Delta\phi_D$ can be constant if all phases involved in $\Delta\phi$ are taken within sufficiently short time intervals. First, the output polarization state of a SM fiber can be fixed over time with proper isolation from the environment, irrespective of the ellipticity. This is just saying that the relative phase between two polarizations is fixed. Thus we have

$$\Delta\phi_{WH} = \Delta\phi_{WV} + const., \qquad (8.4a)$$

$$\Delta\phi_{1H} = \Delta\phi_{1V} + const., \qquad (8.4b)$$

within the same trial in the experiment. However, the above relation can still hold for the case of different trials as long as the fiber length stays the same. This can be achieved by isolating the fibers passively to eliminate high frequency fluctuation in length. With memory time at tens of microsecond range, we only need to worry about fluctuation in fiber length within that time scale and this should be easily taken care of with moderate shielding. Certainly this claim needs to be tested to make sure that the other factors, such as stress-induced birefringence, are not large enough to invalidate it. Note that since polarization-maintaining (PM) fibers have much larger birefringence, the setup would be much more sensitive in variation of fiber lengths if we use PM instead of SM fibers.

A short note on the polarization properties of SM fibers With the help of polarization controllers or waveplates, two perpendicular linear polarizations launched into a SM fiber can stay the same at the output (Fig. 8.2), ensuring the independence of the two channels. However, an extra phase will inadvertently be introduced between the two components. This can be seen when a beam linearly polarized at 45° from the axes is launched through the fiber. The output would in general be elliptically polarized. This should be fine for the experiment as long as the relative phase stays fixed. To be safe, we can check and compensate this extra phase by using a Berek compensator, which is a plate made of uniaxial material with the extraordinary axis normal to the surface. By tilting the compensator, we can change the relative phase between the two polarizations without mixing them. By checking from time to time that the output is linearly polarized when the input is linearly polarized at 45° from the axes, we can be sure that the relative phase between the two H and V polarizations
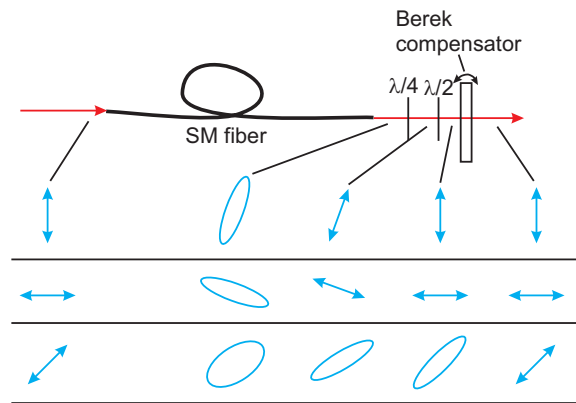
Figure 8.2: Compensating for the birefringence of a SM fiber. The figure shows the polarization states of the output beam for various input polarization states. A SM fiber generally turns linear polarizations into elliptical polarizations. Two orthogonal polarizations can remain orthogonal to each other after passing through a SM fiber with the help of a quarter-wave plate ($\lambda/4$). A half-wave plate can further rotate the polarizations. After the waveplates, the two orthogonal polarizations pick up different phases, thus a input beam polarized at 45° will in general be transformed into an elliptically polarized beam. The Berek compensator, which varies the relative phase between the two orthognal linear polarizations, can cancel the relative phase experienced by the two orthogonal polarizations and thus, together with the waveplates, remove any birefringence induced by the SM fiber.

is fixed over time.

Tilting of the Berek compensator might shift the two polarizations in space differently and degrade the visibility of the beams after combined by a BD. A way to avoid that is to use two birefringent plates, e.g., waveplates with crystal axes aligned horizontally, as compensators. The waveplates need to be tilted in a complimentary way so that the beam displacement caused by one waveplate is canceled by that caused by the other (see Fig. 8.3).

Now we are left with the phase differences involving BDs. Since the BDs introduce
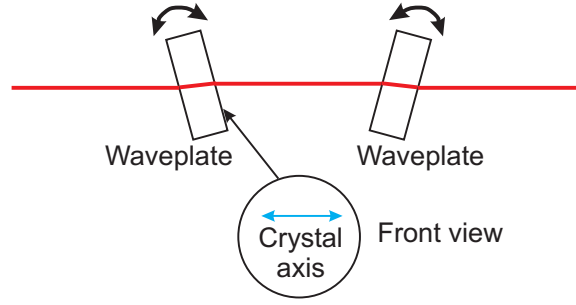
Figure 8.3: Two waveplates can serve as a compensator with minimal beam displacement.

phase drift in the U and D paths in a common-mode fashion, we can get

$$\phi_{BD,LU} - \phi_{BD,LD} = const.,$$

$$\phi_{BD,RU} - \phi_{BD,RD} = const.,$$

$$\Delta\phi_{BDU} - \Delta\phi_{BDD}$$

$$= \phi_{BD,RU} - \phi_{BD,RD} - (\phi_{BD,LU} - \phi_{BD,LD})$$

$$= const. \tag{8.5}$$

The above relations hold in the same trial. The phases of the BD interferometers might drift from trial to trial similar to the relative phase between the two polarization in a SM fiber. Through vibration isolation, we should be able to keep the phase stable over the period of memory time. To characterize noise spectrum for the phases, we can look at the beat note for the interferometer formed by BS_W, two pairs of BDs and BS_1, with two half-wave plates inserted between the BDs to rotate the polarizations of the write fields from BS_W and deliberately steer them into BS_1. The paths of the resultant interferometer are close to those of the one of interest given that the angular separation between the write field and the scattered field 1 is small. Note that the
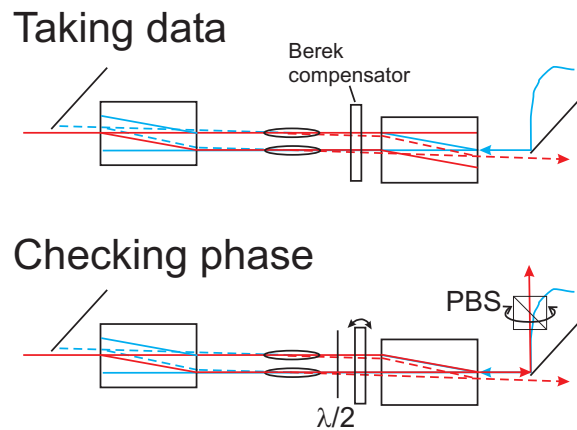
Figure 8.4: Check the phase of the BD interferometer. Instead of using a Berek compensator, we can replace its function by tilting one of the BDs.

free-space paths from the SM fibers to the BDs should also be shielded to avoid high frequency phase fluctuation.

From the above argument we can see that $\Delta\phi$ can be kept constant as long as the setup does not move too much within the memory time. The noise spectrum of the fluctuation of the effective length of the fiber will give us the information about this limit, in addition to the memory time of the ensembles, on how long one pair of ensemble can store an entangled state and wait for the other pair.

We have tested the stability of the BD interferometers and find less than 3 degree RMS (root-mean-square) phase fluctuation over an hour of observation. The long term drift is slow enough to be compensated by hand. The vibration noise spectrum of the test setup has a bandwidth around 10 kHz, while the RMS phase deviation still needs to be determined in the actual setup. We will need to device more shielding to attenuate high-frequency disturbance on the setup for better stability.

8.2.5 Readout stage and verification of entanglement

After we get a click for both pairs, the state of the entangled pairs is then (to the lowest order and omitting the cases with minus signs)

$$|\Psi\rangle_{UD} = \frac{1}{2}\Big[(|10\rangle + e^{i\Delta\phi_U}|01\rangle)_U \otimes (|10\rangle + e^{i\Delta\phi_D}|01\rangle)_D\Big] \qquad (8.6)$$

We then map the state to fields 2. By using linearly polarized read pulses, the additional phase between the U and D pairs associated with the readout process is determined only by the phases of the BD interferometers. From Eq. (8.5) and the discussion following the equation, these phases can be kept constant. Even if the BD phases drift, we should be able to compensate for the drift by tilting the BDs.

Details of the compensation scheme As shown in Fig. 8.4, we can put a Berek compensator between the BDs (or outside the BD interferometer; they just need to cover all fields) to compensate the phase drift. To check for any phase drift, we insert a $\lambda/2$ plate to rotate the polarization of the write beams so that they are combined in the 2nd BD. If the phase of the BD interferometer does not drift, the polarization of the combined write beam should stay the same. We should start with the case that the combined write beam is linearly polarized so that we can check with a PBS. We can then compensate the phase drift by minimizing the transmission through the PBS when tilting the Berek compensator and rotating the PBS. To address the problem of beam displacement when tilting a Berek compensator, we can simply spare the compensator and horizontally tilt one of the BDs by a PZT to adjust the path difference.

Actually, the read pulses do not even have to be derived from a common source. The effective state of fields 2 that would result in a coincidence, one in D_{2L}s and the other in D_{2R}s, can be written as

$$e^{i\Delta\phi_D}e^{i(\phi_{BD,LU}+\phi_{BD,RD})}|1_{2L}0_{2R}\rangle_U|0_{2L}1_{2R}\rangle_D + e^{i\Delta\phi_U}e^{i(\phi_{BD,RU}+\phi_{BD,LD})}|0_{2L}1_{2R}\rangle_U|1_{2L}0_{2R}\rangle_D.$$

$$(8.7)$$

At the outputs of the BDs, the effective state is

$$|\Psi_{eff}\rangle \equiv \frac{1}{\sqrt{2}}\Big(|H_LV_R\rangle + e^{i\theta}|V_LH_R\rangle\Big), \qquad (8.8)$$

$$\theta = \Delta\phi + (\phi_{BD,RU} + \phi_{BD,LD}) - (\phi_{BD,LU} + \phi_{BD,RD}) = const. \qquad (8.9)$$

This is a Bell state within an extra phase θ. With this state, we have two ways (for now) of violating a Bell inequality. The first approach is intuitive: use the polarization bases. First, use H-V basis for the L analyzer and get fringes of coincidences by rotating the half-wave plate of the R analyzer. Then use 45° basis for the L analyzer and get another fringe. The visibility of the fringes can then be plugged into a CHSH inequality. This scheme has the advantage that from the orientation of the wave plates, we know how far we go on the fringes. The other approach is the one proposed by DLCZ. We can vary the relative phase of the H-V components on either side by tilting a birefringent plate (Berek compensator). The half-wave plates then need to rotate the polarization by 45° to mix the components so that the PBS works just like a non-polarizing BS. We might have difficulty implementing this because there is not a clear way to know how much we vary the phase when tilting the plates.

One way around this is to obtain a fringe at high count rates to gain information about the phase and then decrease the excitation probability to obtain a fringe with high visibility at a lower count rate. The violation of the Bell's inequality guarantees the security of quantum cryptography, in which each communication party is given access to one set of ensembles (L or R) and randomly chooses the analyzer between H-V or 45-degree bases. After comparing the choices of bases, the communication parties collect the measurement outcomes when the bases match. The outcomes can then be utilized as a secret key to encode information to be exchanged.

8.2.6   Higher-order terms

As discussed in Chapter 7, after getting clicks from detectors at the outputs of BS_1, one can transfer the state of the ensembles to scattered fields using read pulses. The state of the scattered fields should be described by a density matrix:

$$\rho_{UD} = \rho_U \otimes \rho_D. \tag{8.10}$$

Keeping the terms that can result in the desired fourfold coincidences with relatively high probability, we have

$$
\begin{aligned}
\rho_{U(D)} \;=\; & \Big[(1 - p - \frac{h_c^{(2)} p^2}{4})|0_L 0_R\rangle\langle 0_L 0_R| \\
& + \; \frac{p}{2}\big(|1_L 0_R\rangle + e^{i\Delta\phi}|0_L 1_R\rangle\big) \otimes \big(\langle 1_L 0_R| + e^{-i\Delta\phi}\langle 0_L 1_R|\big) \\
& + \; \frac{h_c^{(2)} p^2}{4}|1_L 1_R\rangle\langle 1_L 1_R| + O(p^3)\Big]_{U(D)} \;,
\end{aligned}
\tag{8.11}
$$

where p stands for the probability of detecting the ideal entangled states with only one excitation involved, roughly equivalent to $p_{01} + p_{10}$ in Chapter 7, and $h_c^{(2)}$ is the same as that defined in Sec. 7.3.3. Note that the $|0_L 2_R\rangle$ and $|2_R 0_L\rangle$ components will also result in fourfold coincidences, but with lower probability $(O(p^3))$, and thus are omitted. To the lowest order in p, there are three terms in ρ_{UD} that will result in the final fourfold coincidences. One corresponds to the ideal case in Eq. (8.6), which results in a fourfold coincidence with probability $\frac{1}{2} \times p^2 = p^2/2$. The other two terms are cross terms between the vacuum (00) and the two-photon (11) terms, with the corresponding probability $\approx (1 - p - \frac{h_c^{(2)} p^2}{4})(\frac{h_c^{(2)} p^2}{4} + \frac{h_c^{(2)} p^2}{4}) = (1 - p - \frac{h_c^{(2)} p^2}{4})\frac{h_c^{(2)} p^2}{2}$. The latter case will lead to fourfold coincidences independent of the setting of the analyzing apparatus (angles of waveplates or relative phases between two polarization components), which uniformly offset the entanglement fringes and reduce the visibilities and thus the inferred degree of entanglement. The resultant fringes will have maxima $\propto \frac{p^2}{2} + (1 - p - \frac{h_c^{(2)} p^2}{4})\frac{h_c^{(2)} p^2}{2}$ and minima $\propto (1 - p - \frac{h_c^{(2)} p^2}{4})\frac{h_c^{(2)} p^2}{2}$. Thus the visibility is given by

$$Vis = \frac{\frac{p^2}{2}}{\frac{p^2}{2} + 2(1 - p - \frac{h_c^{(2)} p^2}{4})\frac{h_c^{(2)} p^2}{2}} = \frac{1}{1 + 2(1 - p - \frac{h_c^{(2)} p^2}{4})h_c^{(2)}} . \qquad (8.12)$$

To violate the CHSH inequality, we need $Vis \geq \frac{1}{\sqrt{2}}$, which means

$$1 + 2(1 - p - \frac{h_c^{(2)} p^2}{4})h_c^{(2)} \leq \sqrt{2}$$

$$\Rightarrow h_c^{(2)} \leq \frac{1}{p^2}(2 - 2p - \sqrt{4 - 8p + 6p^2 - 2p^2\sqrt{2}}) \to \frac{\sqrt{2} - 1}{2} = 0.21 \text{ when } p \to 0 .$$

$$(8.13)$$

8.2.7 Timing and logic

The logic for exploiting memory is as follows: getting a click for one pair of ensembles, U or D, we stop all classical pulses going to that pair and wait for the other pair to be entangled. When we get a click from the other pair or reach the memory time, we read out the state of the ensembles and reset the system. This is elaborated in Sec. 8.6.

8.3 Estimate of coincidence rate

Further progress in implementing the DLCZ protocol beyond entangling two ensembles would require detection of at least fourfold coincidences. Verification of entanglement connection with quantum state tomography would even require good statistics of 5-fold coincidences. Here I would like to estimate the coincidence rate for the quantum cryptography and Bell inequality experiments with and without memory effect.

Assuming that the singles' detection probability in fields 1 from one pair of ensembles is p_1 and the repetition rate of the trials is Rep, the rate Rc_2 that 2 pairs of ensembles are both entangled in the same trial (2-fold coincidence rate) is

$$Rc_2 = p_1^2 Rep, \tag{8.14}$$

The three- and fourfold coincidence rates in the Bell inequality experiment are

$$Rc_3 \;=\; p_c Rc_2 = p_c p_1^2 Rep, \tag{8.15}$$

$$Rc_4 \;=\; \frac{1}{2} p_c Rc_3 = \frac{1}{2} p_c^2 p_1^2 Rep, \tag{8.16}$$

where p_c is the conditional probability for a click in field 2, given a click from field 1.

With memory, assume that we can hold an entangled state in one pair of ensembles and wait for up to M trials. The rate of getting two pairs of ensembles entangled at the same time is then

$$
\begin{aligned}
Rc_{2M} \;&=\; p_1\Big[p_1 + 2[(1-p_1)p_1 + (1-p_1)^2 p_1 + ... + (1-p_1)^{(M-1)}p_1]\Big] \\
&=\; p_1^2(1 + 2\frac{(1-p_1) - (1-p_1)^M}{p_1}) \approx (2M-1)p_1^2 \text{ when } p_1 \ll 1. \quad (8.17)
\end{aligned}
$$

The factor 2 in the above expression accounts for the two possible orders that the coincidences can occur in the two pairs of ensembles. The coincidence rates become

$$Rc_{3M} = p_c Rc_{2M} = (2M-1)p_c p_1^2 Rep = (2M-1)Rc_3, \tag{8.18a}$$

$$Rc_{4M} = \frac{1}{2} p_c Rc_{3M} = (2M-1)\frac{1}{2} p_c^2 p_1^2 Rep = (2M-1)Rc_4, \tag{8.18b}$$

The memory merely increases the coincidence rates by a factor of $2M-1$, which comes from the ability of each pair of ensembles to store the entangled state up to M trials. We need to subtract "1" to avoid double counting the coincidences in the

same trial. The realistic numbers (for now) are

$$M = 8, \; Rep = 44 \text{ kHz}, \tag{8.19a}$$

$$p_1 = 7.4 \times 10^{-3}, \; \tilde{g}_{1,2} = 20, \tag{8.19b}$$

$$p_c = 11.4\%, \tag{8.19c}$$

$$Rc_{2M} = 35 \text{ Hz}, \; Rc_{3M} = 4 \text{ Hz}, \; Rc_{4M} = 0.23 \text{ Hz}. \tag{8.19d}$$

If we keep track of which two of the D_1's click, we might attribute all the fourfold coincidences to one fringe.

8.4 Demonstration of entanglement connection

It is good to keep in mind that the setup in Fig. 8.1 can also be used for demonstrating entanglement connection. Set the half-wave plate of, say L, to rotate the polarizations by 45 degree. After two clicks heralding that the two pairs are entangled, getting a third click at L would entangle the two ensembles at R.

Getting the third click, the state of the system consisting of fields 2_{UL}, 2_{DL} and ensembles UR and DR becomes

$$
\begin{aligned}
\frac{1}{2\sqrt{2}} \Big(a_{2UL} \;\; &\pm \;\; a_{2DL} \Big) \Big[(e^{i\phi_{BD,LU}} |1_{2L}0_R\rangle + e^{i\Delta\phi_U} |0_{2L}1_R\rangle)_U \\
&\otimes \;\; (e^{i\phi_{BD,LD}} |1_{2L}0_R\rangle + e^{i\Delta\phi_D} |0_{2L}1_R\rangle)_D \Big] \\
= \;\; &e^{i\phi_{BD,LU}} |0_{2L}0_R\rangle_U \otimes (e^{i\phi_{BD,LD}} |1_{2L}0_R\rangle + e^{i\Delta\phi_D} |0_{2L}1_R\rangle)_D \\
\pm \;\; &(e^{i\phi_{BD,LU}} |1_{2L}0_R\rangle + e^{i\Delta\phi_U} |0_{2L}1_R\rangle)_U \otimes e^{i\phi_{BD,LD}} |0_{2L}0_R\rangle_D \quad (8.20)
\end{aligned}
$$
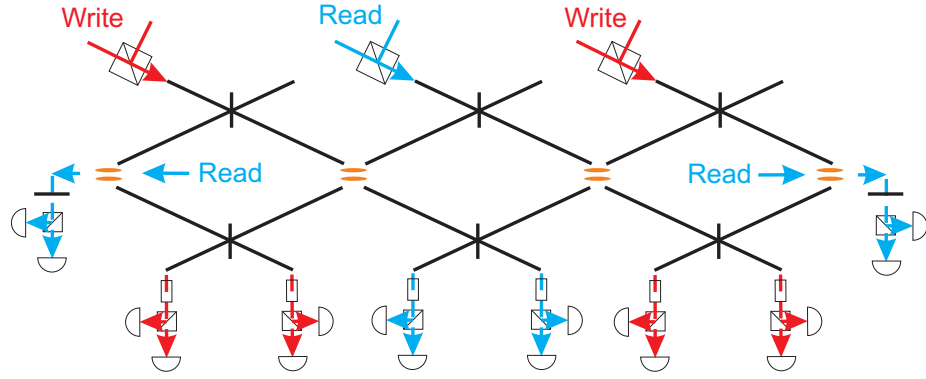
Figure 8.5: Scaling up.

Tracing over the state of fields 2_{UL} and 2_{DL}, the state of the ensembles at R is then

$$\frac{1}{2}\rho(|0_U 1_D\rangle_R \pm e^{i\Phi}|1_U 0_D\rangle_R) + \frac{1}{2}\rho(|0_U 0_D\rangle_R) \tag{8.21}$$

$$\Phi = \Delta\phi + \phi_{BD,LD} - \phi_{BD,LU} = const. \tag{8.22}$$

where I denote $|\psi\rangle\langle\psi|$ as $\rho(|\psi\rangle)$. This is a density matrix with the same form as in [96] (Chapter 7), so we can verify entanglement in the same way. However, we will need to boost up the three- (success rate of entanglement connection), four- (fringe) and fivefold (p_{11}) coincidences so that the experiment can be done in reasonable time.

8.5 Scaling up

To extend the distance between communication parties, we can connect the entangled pairs. Two chains of ensembles connected through SM fibers can maintain the phase stability in the same fashion discussed in Sec. 8.2.4. The idea is shown in Fig. 8.5.

8.6   Logic for exploiting quantum memory

8.6.1   Introduction

In the DLCZ protocol, the scalability relies on the the ability to store a quantum state. It is suggested that the long communication distance is broken into much shorter segments. One tries to prepare entanglement within the segments and extend the distance by entanglement connection. Due to the probabilistic nature, the success rate of creating two remote entangled ensembles in that fashion decreases exponentially with the distance, unless quantum memory is exploited so that the segments of the communication channel do not have to succeed in entangling the ends within the same trial. This notion also applies to any other schemes with finite success probability. For example, if we want to obtain a Hong-Ou-Mandel (HOM) type of interference from two probabilistic sources of single photons, the ability to store the excitation until we need it can significantly increase the data rate.

In this section, the details on how to exploit the quantum memory in our experiment are described. First, the logic flow is explained. After that follows the tentative setup including the circuits gating the laser pulses.

8.6.2   Logic flow

The logic flow is best explained with a flowchart. Fig. 8.6 shows the flowchart for the experiment on the HOM dip. In the experiment, we need two independent ensembles as the single photon sources. During initialization, the trapping beams and the re-pumpers are pulsed on for a short period to cool the MOT. The trapping beams are

first turned off, with the repumpers remaining on for hundreds of nanoseconds longer, which deplete the $F = 3$ ground states. The ensembles are now ready for the protocol. We send in the write pulses in each trial and try to detect a photon 1. If none of the detectors for fields 1 clicked, we go back to the initialization stage and start over. If a photon 1 is detected from, say, ensemble X, we immediately stop all beams going to X to store the excitation, and keep trying at the other ensemble, called Y, to get a photon 1. If the memory time is reached, we read out the state of the ensembles and go back to initialization. Within the memory time, if we register another photon 1 from ensemble Y, two excitations are successfully prepared in X and Y. We can then read out the excitations and go back to initialization. The resultant single photons from the two ensembles are combined on a beam splitter to get a HOM dip. Only the events preceded by two photon-1 clicks within one memory time contribute to the HOM dip.

The logic for the quantum cryptography experiment is the same as that of the HOM dip, except that each system is a pair of ensembles instead of just one.

8.6.3 Implementing the logic

The logic described in Sec. 8.6.2 can be implemented with simple digital electronics. Fig. 8.7 shows the simplified scheme for the circuit implementing the logic in Fig. 8.6. The system is triggered by repetitive TTL pulses. The TTL pulses are in turn gated by controlling pulses reflecting the status of the ensembles. The controlling pulses are created with monostable multivibrators (MM, part number: 74LS123),
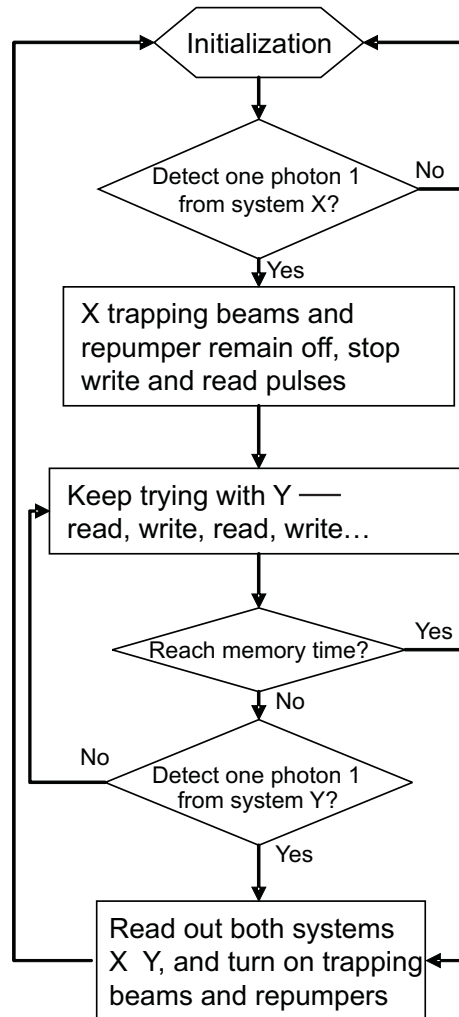
Figure 8.6: The flowchart for the logic of the HOM dip experiment.
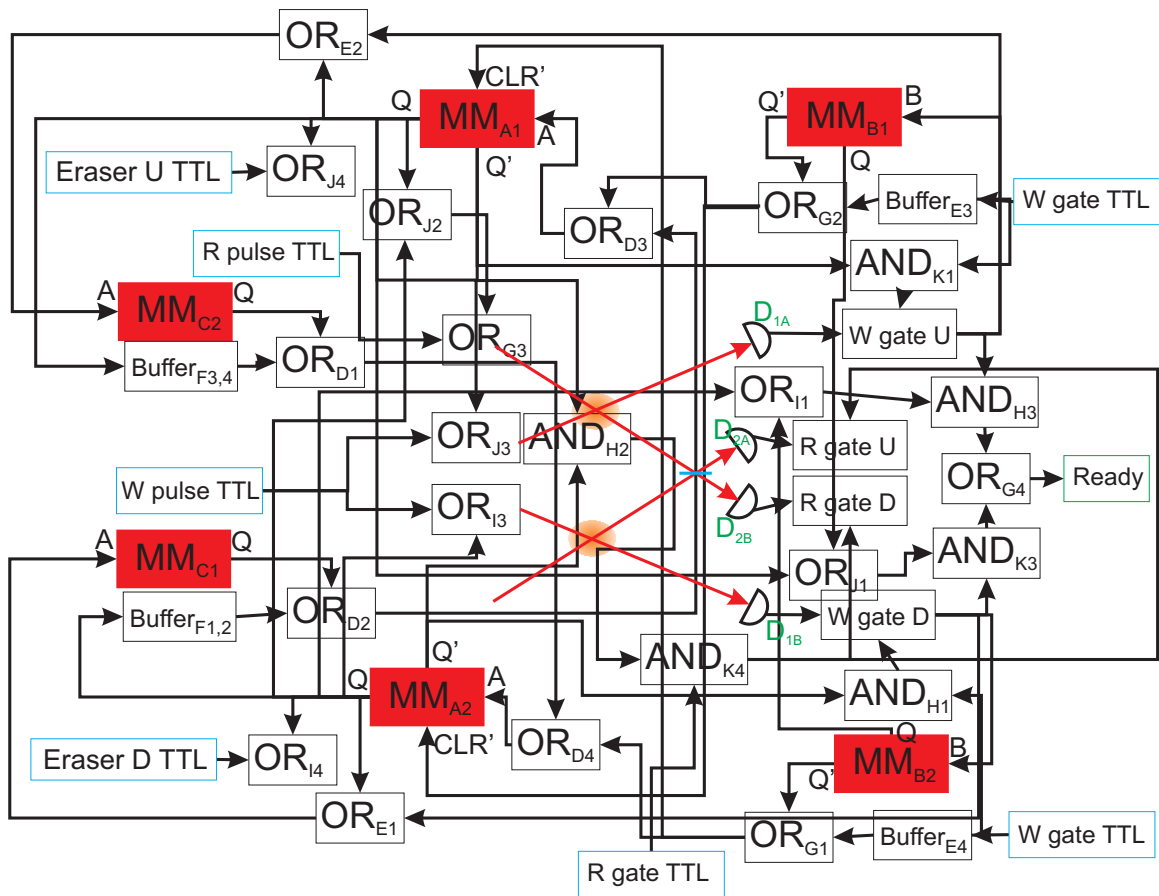
Figure 8.7: The circuit for the logic in HOM dip experiment. The two ovals stand for the ensembles. Fields 1 from the ensembles are directed to detectors D_{1A} and D_{1B}. Fields 2 are combined on a beam splitter, outputs of which are directed to detectors D_{2A} and D_{2B}. MM: monostable multivibrator

which basically behave as triggerable pulse generators with variable pulse durations.

Specifically, the circuit works as following:

1. A and B denote the trigger inputs for the MM. Port A is falling edge triggered and Port B is rising edge triggered.

2. The Q outputs of MM_{A1} and MM_{A2} serve as indicators of memory status for the upper and lower ensembles, respectively. A logic-high state means the memory is activated.
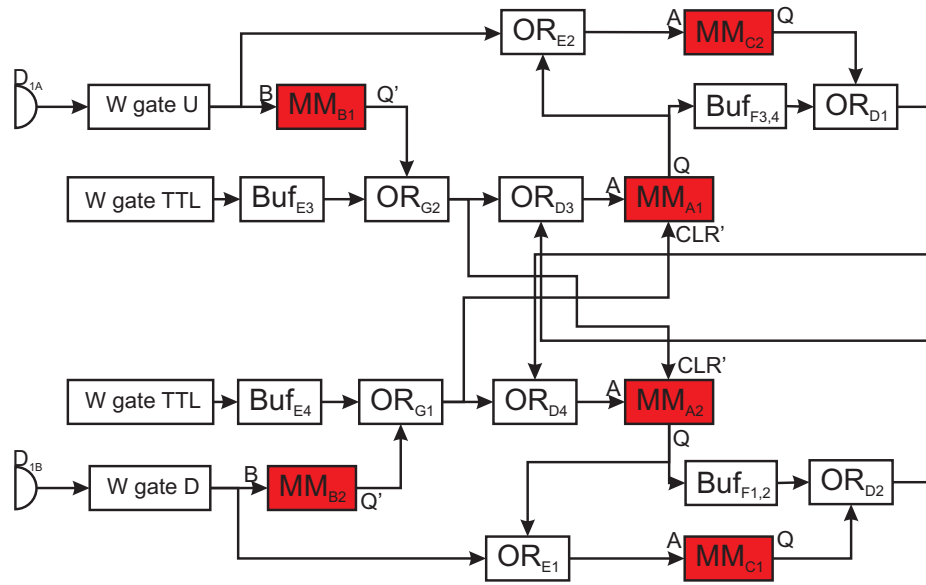
Figure 8.8: The part of the circuit in Fig. 8.7 responsible for the conditioning logic.

3. At the initialization stage, the output ports (Q) of MMs stay logic low, while the inverted output ports (Q') stay logic high. All the pulses: write, read, trapping beams, and repumpers, go in the ensembles repetitively.

4. Memory is activated by the falling edge of the write-gate pulse (gating photon-1 clicks) so that the write window containing the activating photon-1 click is not affected by the memory indicators (Q ports of MM_{A1} and MM_{A2}). The activating pulse is formed by ORing the write-gate pulse and the extended version of the photon-1 click given by either B1 or B2. The pulse durations of B1 and B2 ($\sim$340 ns) are determined by the criterion that if the photon-1 click happens at the beginning of the write gate window, the pulse will not end until after the falling edge of the write-gate pulse. Using the write gate itself has a shortcoming in that the photon-1 clicks appearing at the end of the write gate window create the extended pulse with falling edge from Q' ports of B1 and

B2 after the falling edge of the write-gate pulse. This means the memory is not activated at a fixed time relative to the write gate. This can be remedied by using a TTL pulse synchronized with the write-gate pulse at the inputs of E3 and E4 but with the falling edge later than the write-gate pulse so that its falling edge is always later than that of the extended photon-1-click pulse. How much later it has to be is determined by how far the falling edge of the extended photon-1-click pulses at the end of the write window is from the falling edge of the write-gate pulse and needs to be characterized in the lab. This will introduce about 50 ns of extra delay that is not usable and limits how short the trial period can be.

5. Buffers consist of OR gates with two inputs tied together to introduce extra propagation delay so that the delay introduced by the MM can be compensated.

6. The memory activating pulses from G1 and G2 for one ensemble disables the memory of the other ensemble. If the memory was not activated when the CLR' ports receive a falling edge, the memory status remains unaffected. If one ensemble is in storage mode and the other registers a photon-1 click, the storage mode is disabled by the pulse into the CLR' port from the 2nd ensemble. While the Q port of the ensemble exiting storage mode coming back from high to low, the combinations of C1, F1,2, D2 or C2, F3,4, D1 extend the indicator pulse to gate the activating pulse (preventing any falling edges) to the 2nd ensemble to make sure it is not activated. C1 (C2) is triggered by the falling edge of the pulse to give a pulse 600 ns in duration. The output is then combined by D2

(D1) with the original pulse delayed by F1,2 (F3,4) for about 40 ns.

7. Preventing the memory from being mistakenly activated is tricky when the two ensembles both have photon-1 click within the same trial, since the activation and disabling both occur at the falling edge of the write-gate pulse. OR gates E1 and E2 are added so that C1 and C2 can also be triggered by the falling edge of the photon-1 clicks. Since C1 and C2 put out pulses 600 ns long, the activating pulses are disabled when the opposite ensemble registers a photon-1 click.

8. The indicator pulses are used to gate the pulses in the trials. For the inverted TTL pulses, e.g., write (J3 and I3), and eraser (J4 and I4), the pulses from ports Q are used to gate them with OR gates. For the non-inverted TTL pulses, e.g., write gate (K1 and H1) and read gate (H2 and K4), the pulses from ports Q' are used to gate them with AND gates. The read pulse is set to fire whenever the two ensembles are not in the storage mode, so it is gated by the ORed (J2) Q pulses with an OR gate (G3). Similarly the read gate is activated with the read pulse.

The part of the circuit in Fig. 8.7 responsible for the conditioning logic is shown in Fig. 8.8.

8.6.4 Data processing

With memory, data processing is trickier. We are no longer working with coincidences happening in the same trials. To simplify data acquisition, a ready signal is prepared.
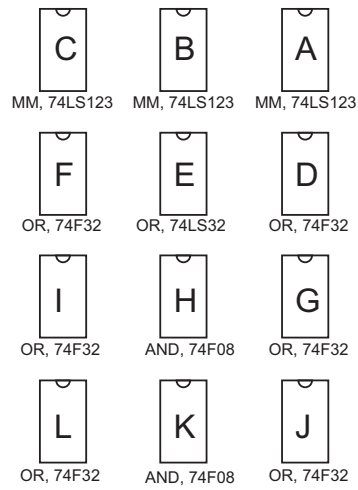
Figure 8.9: The chips layout of the finished circuit shown in Fig. 8.7.
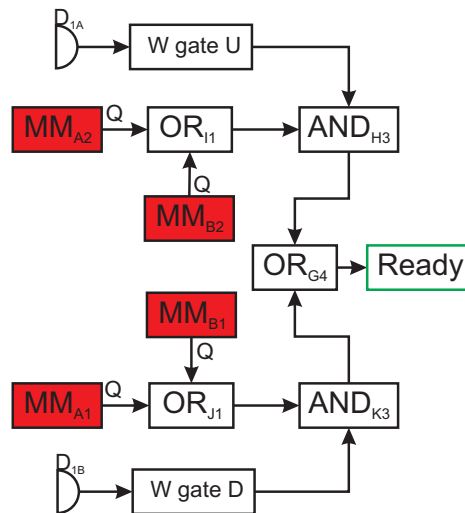
Figure 8.10: The part of the circuit in Fig. 8.7 deriving the ready signal.

The ready signal is high when both ensembles have a excitation to be read out. As shown in Fig. 8.10, it is obtained by gating (with H3 and K3) the photon-1 click from one ensemble with the memory indicator pulse ORed (I1 and J1) with the extended photon-1-click pulses from the other ensemble and then combining the gate outputs with a OR gate (G4). This can be generalized to the cryptography experiment when 4 detectors are involved in the writing process. Just combine the photon-1 clicks from each ensemble with OR gates and feed the output to H3 and K3. When processing the data, we can just look for coincidences between D_2's in the same trial with these pulses present. More precisely, we should consider the coincidence probability per successful trial for proper normalization.

Chapter 9

Conclusion and Outlook

9.1   Conclusion

We have successfully demonstrated capabilities proposed in the DLCZ protocol, including the generation of two light fields with nonclassical correlation, storage of the correlation in an atomic memory, and converting a stored atomic excitation into a single photon. The nonclassical correlation between a scattered field and an atomic ensemble has been exploited to entangle two atomic ensembles. The entangled state has been stored in the atomic memory of the ensembles and later transferred from the atoms to light fields. The memory effect in atomic ensembles has been extensively characterized. A scheme for performing quantum cryptography has been proposed and is being implemented. These experiments demonstrate a simple and promising approach toward building a large-scale quantum network.

9.2　Outlook

At the time of writing, the retrieval efficiency of the stored state has been improved from the 10% level reported in Chapter 4 and 7 to above 50%, by arranging the writing and reading processes in a counter-propagating configuration [26, 27, 28]. The improved retrieval efficiency in turn significantly increases the coincidence rate in the experiment, since every time a photon is registered in field 1, there is an increased likelyhood to register a photon in field 2. The counter-propagating configuration opens the possibility of non-collinear detection schemes [27, 28]. The non-collinear configuration permits better filtering of the classical write (read) pulse from field 1 (2), resulting in lower noise levels. With this scheme, much improved nonclassical correlation between the (1,2) fields has been observed [28]. Despite these advantages, the new scheme has a critical drawback, that is, the idea of using auxiliary fields to lock the interferometers exploited in Chapter 7 is no longer applicable. The auxiliary fields would follow the paths of classical write and read pulses and will not be useful in locking the interferometers which comprise of the paths of the classical pulses and the (1,2) fields. The scheme in Chapter 8 was developed with all the observations above taken into consideration. Compared to the protocols exploiting polarization entanglement utilizing a single ensemble [28], my scheme still has a major shortcoming in that interferometric stability is required over the span of memory time of the ensembles. However, by taking the entangling steps by parts, the DLCZ protocol is expected to yield better scalability than single ensemble polarization schemes. Specifically, for systems generating, at probability p, polarization entanglement between photons

and excitations in ensembles, the heralded entanglement between ensembles involves combining the photon from each ensemble on a beam splitter and detecting one photon at both output ports, which happens with probability $p^2/2 + p^2 = 3p^2/2$, where the two terms correspond to the cases that each ensemble contribute one photon and that both photons are from one ensemble, respectively. After the clicks heralding the entanglement, the probability to read out one photon from each ensemble is $(p^2/2)/(3p^2/2) = 1/3$ in the ideal case. The DLCZ protocol exploits the memory effect which would allow us to reach the same distance and similar state for four ensembles with probability $(2M - 1)(2p)^2$ (see Sec 8.3 and note that p here is the probability for one ensemble to scatter a photon 1), where M is the number of trials for which one pair of ensembles can store the entangled state. In this case, after the heralding clicks, ideally the probability for each communication party to read out one excitation is $1/2$. These factors occur at every level of connection and leads to higher success probability and thus better scalability for the DLCZ protocol.

The next steps toward building a large-scale quantum network via the DLCZ protocol should be in two directions. The first is to extend the memory time of the ensembles. As described in Chapter 6, even with a well-controlled magnetic field, memory time of the current setup with MOT will reach the limit at hundreds of microseconds due to the diffusion of atoms into and out of the regions addressed by the classical pulses. For longer memory time, a new trap scheme is necessary. For example, with a dipole-force trap, the atoms can be confined in a small region, virtually eliminating the diffusion effect. By carefully managing the magnetic field, memory time on the order of seconds should be possible, and the range of a quantum

network can then be further extended. Note that, with longer memory time, the requirement on path stability is more stringent. In addition to passive stabilization, active feedback may be employed to ensure path stability within the memory time.

The other direction one should work toward is multiplexing the nodes. Even with long memory time, the DLCZ protocol still suffers from the low success probability required to suppress the multiphoton processes. With multiple ensembles at each node, the entangling steps can be done in parallel, thus increasing the success probability of creating entangled ensembles at two nodes. Multiplexing also allows additional purification on top of the built-in purification in the DLCZ protocol. Specifically, with two ensembles at each node one can generate a pair of polarization-entangled photons (Ch. 8). With multiple entangled photon pairs, one can perform entanglement purification to compensate for the effect of technical imperfection [99], such as the degradation of entanglement due to path fluctuation, and obtain one final pair of photons with a higher degree of entanglement.

Once these two aspects above are addressed, a long-distance quantum network is well within reach. Other subjects in the application of a quantum network, such as interfacing between different species of quantum nodes, distributed quantum communication, and quantum teleportation [22] across a quantum network will definitely result in more fruitful physics when the quantum network is scaled up.

Appendix A

Calculation of Detection Probabilities and Correlation Functions

A.1 Introduction

In order to interpret the observations in the experiments, we usually need to construct a model and try to gain information about the system, such as the quantum state, noise level, and efficiencies. We can assume a quantum state including noise and introduce losses while calculating the observable detection probabilities. This appendix documents the expressions of relevant quantities for the ideal state including the fringe visibility in the entanglement experiment for two ensembles. The effect of noise can be included by incorporating additional modes into consideration.

A.2   Assuming ideal initial state

Start with the ideal state:

$$|\Phi_{12}\rangle = \sqrt{1-p}\left[|0_10_2\rangle + \sqrt{p}|1_11_2\rangle + O(p)\right] = \sqrt{1-p}\sum_{n=0}^{\infty} p^{\frac{n}{2}}|n_1n_2\rangle. \tag{A.1}$$

$\tilde{g}_{1,2}$ for this state can be calculated from

$$\tilde{g}_{1,2} \equiv \frac{\langle : \hat{I}_1\hat{I}_2 : \rangle}{\langle \hat{I}_1\rangle\langle \hat{I}_2\rangle}. \tag{A.2}$$

In this expression,

$$\hat{I}_i \equiv \xi_i\hat{a}_i^\dagger\hat{a}_i, \tag{A.3}$$

$$: \hat{I}_1\hat{I}_2 : = \xi_1\xi_2\hat{a}_1^\dagger\hat{a}_2^\dagger\hat{a}_2\hat{a}_1, \tag{A.4}$$

where $\hat{a}_i^\dagger$ ($\hat{a}_i$) is the creation (annihilation) operator, and ξ_i is the proportional constant between the intensity operator $\hat{I}_i$ and the photon number operator $\hat{a}_i^\dagger\hat{a}_i$ for mode i.

Define

$$|a_1\Phi_{12}\rangle \equiv \hat{a}_1|\Phi_{12}\rangle = \sqrt{1-p}\sum_{n=1}^{\infty}\sqrt{n}p^{\frac{n}{2}}|(n-1)_1n_2\rangle. \tag{A.5}$$

With the identity

$$\sum_{n=1}^{\infty}np^n = p\frac{\partial}{\partial p}\sum_{n=1}^{\infty}p^n = p\frac{\partial}{\partial p}\frac{p}{1-p} = \frac{p}{1-p} + \frac{p^2}{(1-p)^2} = \frac{p}{(1-p)^2}, \tag{A.6}$$

we can get

$$\langle \Phi_{12}|\hat{I}_1|\Phi_{12}\rangle = \xi_1\langle a_1\Phi_{12}|a_1\Phi_{12}\rangle = \xi_1\xi_2(1-p)\sum_{n=1}^{\infty} np^n = \xi_1\frac{p}{1-p} \qquad (A.7)$$

and

$$\langle \Phi_{12}|\hat{I}_2|\Phi_{12}\rangle = \xi_2\frac{p}{1-p}. \qquad (A.8)$$

Similiarly, define

$$|a_1a_2\Phi_{12}\rangle \equiv \hat{a}_2\hat{a}_1|\Phi_{12}\rangle = \sqrt{1-p}\sum_{n=1}^{\infty} np^{\frac{n}{2}}|(n-1)_1(n-1)_2\rangle. \qquad (A.9)$$

With the identity

$$\sum_{n=1}^{\infty} n^2p^n = p\frac{\partial}{\partial p}\sum_{n=1}^{\infty} np^n = p\frac{\partial}{\partial p}\frac{p}{(1-p)^2} = \frac{p}{(1-p)^2} + \frac{2p^2}{(1-p)^3} = \frac{p+p^2}{(1-p)^3} , \quad (A.10)$$

we arrive at

$$\langle \Phi_{12}| : \hat{I}_1\hat{I}_2 : |\Phi_{12}\rangle = \xi_1\xi_2\langle a_1a_2\Phi_{12}|a_1a_2\Phi_{12}\rangle = \xi_1\xi_2(1-p)\sum_{n=1}^{\infty} n^2p^n = \xi_1\xi_2\frac{p+p^2}{(1-p)^2}$$
$$(A.11)$$

and from Eq. (A.2), (A.7), (A.8), and (A.11),

$$\tilde{g}_{1,2} = 1 + \frac{1}{p}. \qquad (A.12)$$

To calculate $\langle : \hat{I}_1^2 : \rangle$ and $\langle : \hat{I}_2^2 : \rangle$, we can start with the fact that when traced over the other field, the state of field 1 (2) is just a thermal state, so $\tilde{g}_{1,1} = 2$ and $\tilde{g}_{2,2} = 2$.

Thus

$$\langle : \hat{I}_1^2 : \rangle \;=\; 2\langle : \hat{I}_1 : \rangle^2 = \xi_1^2 \frac{2p^2}{(1-p)^2} \; , \tag{A.13}$$

$$\langle : \hat{I}_2^2 : \rangle \;=\; \xi_2^2 \frac{2p^2}{(1-p)^2} \; . \tag{A.14}$$

To verify, we start with $\langle : \hat{I}_1^2 : \rangle = \xi_1^2 \langle \hat{a}_1^{\dagger 2} \hat{a}_1^2 \rangle$ and get

$$\hat{a}_1^2 |\Phi_{12}\rangle = \sqrt{1-p} \sum_{n=2}^{\infty} \sqrt{n(n-1)} p^{n/2} |(n-2)_1 n_2\rangle . \tag{A.15}$$

Thus we find that

$$
\begin{aligned}
\langle \hat{a}_1^{\dagger 2} \hat{a}_1^2 \rangle &= (1-p) \sum_{n=2}^{\infty} n(n-1) p^n \\
&= (1-p) p^2 \left(\frac{\partial}{\partial p} \right)^2 \sum_{n=0}^{\infty} p^n = (1-p) p^2 \frac{2}{(1-p)^3} = \frac{2p^2}{(1-p)^2} . \quad \text{(A.16)}
\end{aligned}
$$

A.3 Fringe visibility for the entanglement experiment

In the entanglement experiment, the ideal state of the fields emitted by the ensembles is

$$|\Phi_{LR}\rangle = |\Phi_{12}\rangle_L |\Phi_{12}\rangle_R \tag{A.17}$$

where

$$|\Phi_{12}\rangle_x = \sqrt{1-p_x} \sum_{n=0}^{\infty} p_x^{\frac{n}{2}} |n_1 n_2\rangle_x \tag{A.18}$$

$x=\{L,R\}$.

To get a fringe, we measure the coincidence between outputs of the interferometer for field 1 and field 2, that is, we measure quantities such as $\langle: \hat{I}_{1\pm}\hat{I}_{2\pm} :\rangle = \xi_1\xi_2\langle\hat{a}^\dagger_{1\pm}\hat{a}^\dagger_{2\pm}\hat{a}_{2\pm}\hat{a}_{1\pm}\rangle$ with $\hat{a}_{i+} = \sqrt{r_i}\hat{a}_{iL} + \sqrt{t_i}e^{i\phi_i}\hat{a}_{iR}$, $\hat{a}_{i-} = \sqrt{t_i}\hat{a}_{iL} - \sqrt{r_i}e^{i\phi_i}\hat{a}_{iR}$, ϕ_i the relative phase between field iL and iR, r_i (t_i) as the reflectivity (transmission) of the beam splitter BS$_i$, $r_i^2 + t_i^2 = 1$ (lossless), and $i = \{1, 2\}$.

For example,

$$\begin{aligned}
\langle: \hat{I}_{1+}\hat{I}_{2-} :\rangle &= \xi_1\xi_2\langle\hat{a}^\dagger_{1+}\hat{a}^\dagger_{2-}\hat{a}_{2-}\hat{a}_{1+}\rangle \\
&= \xi_1\xi_2\langle((\sqrt{r_1}\hat{a}^\dagger_{1L} + \sqrt{t_1}e^{-i\phi_1}\hat{a}^\dagger_{1R})(\sqrt{t_2}\hat{a}^\dagger_{2L} - \sqrt{r_2}e^{-i\phi_2}\hat{a}^\dagger_{2R}) \\
&\quad (\sqrt{t_2}\hat{a}_{2L} - \sqrt{r_2}e^{i\phi_2}\hat{a}_{2R})(\sqrt{r_1}\hat{a}_{1L} + \sqrt{t_1}e^{i\phi_1}\hat{a}_{1R})\rangle \quad\quad (A.19)
\end{aligned}$$

which has 16 terms of the form $\sqrt{\alpha\beta\gamma\delta}\hat{a}^\dagger_{1A}\hat{a}^\dagger_{2B}\hat{a}_{2C}\hat{a}_{1D}$, where $\{\alpha, \delta\} = \{r_1, t_1\}, \{\beta, \gamma\} = \{r_2, t_2\}$,, and $\{A, B, C, D\} = \{L, R\}$. The initial state is now $|\rho_0\rangle_L \otimes |\rho_0\rangle_R$. For $_R\langle\Phi_{12}|_L\langle\Phi_{12}|\sqrt{\alpha\beta\gamma\delta}\hat{a}^\dagger_{1A}\hat{a}^\dagger_{2B}\hat{a}_{2C}\hat{a}_{1D}|\Phi_{12}\rangle_L|\Phi_{12}\rangle_R$ the non-vanishing terms are those with $\{A, B, C, D\}$ satisfying (1) $A = B$, $C = D$, but $A \neq C$ (2) $A = D, B = C$, but $A \neq B$ (3) $A = B = C = D$.

Case (1) $A = B$, $C = D$, but $A \neq C$

$$\langle\hat{a}^\dagger_{1R}\hat{a}^\dagger_{2R}\hat{a}_{2L}\hat{a}_{1L}\rangle = \langle\hat{a}^\dagger_{1R}\hat{a}^\dagger_{2R}\rangle\langle\hat{a}_{2L}\hat{a}_{1L}\rangle$$

With

$$
\begin{aligned}
\langle \hat{a}_{2L}\hat{a}_{1L} \rangle &= \sqrt{1-p_L}\sum_{n=0}^{\infty} p_L^{\frac{n}{2}}\langle n_1 n_2 | \sqrt{1-p_L}\sum_{n'=1}^{\infty} n' p_L^{\frac{n}{2}}|(n_1'-1)(n_2'-1)\rangle \\
&= \sqrt{1-p_L}\sum_{n=0}^{\infty} p_L^{\frac{n}{2}}\langle n_1 n_2 | \sqrt{1-p_L}\sum_{n'=0}^{\infty} (n'+1) p_L^{\frac{n'+1}{2}}|n_1' n_2'\rangle \\
&= (1-p_L)\sum_{n=0}^{\infty}(n+1)p_L^{n+\frac{1}{2}}
\end{aligned}
$$

$$
= (1-p_L)p_L^{\frac{1}{2}}\left[\sum_{n=0}^{\infty} n p_L^n + \sum_{n=0}^{\infty} p_L^n\right] = (1-p_L)p_L^{\frac{1}{2}}\left(\frac{p_L}{(1-p_L)^2}+\frac{1}{1-p_L}\right) = \frac{\sqrt{p_L}}{1-p_L}
$$

$$(A.20)$$

we can get

$$
\langle \hat{a}_{1R}^{\dagger}\hat{a}_{2R}^{\dagger}\hat{a}_{2L}\hat{a}_{1L}\rangle = \langle \hat{a}_{1R}^{\dagger}\hat{a}_{2R}^{\dagger}\rangle\langle \hat{a}_{2L}\hat{a}_{1L}\rangle = \frac{\sqrt{p_L}}{1-p_L}\frac{\sqrt{p_R}}{1-p_R}
$$

and

$$
\langle \hat{a}_{1L}^{\dagger}\hat{a}_{2L}^{\dagger}\hat{a}_{2R}\hat{a}_{1R}\rangle = \langle \hat{a}_{1L}^{\dagger}\hat{a}_{2L}^{\dagger}\rangle\langle \hat{a}_{2R}\hat{a}_{1R}\rangle = \frac{\sqrt{p_L}}{1-p_L}\frac{\sqrt{p_R}}{1-p_R}
$$

Case (2) $A=D$, $B=C$, but $A \neq B$

$$
\langle \hat{a}_{1R}^{\dagger}\hat{a}_{2L}^{\dagger}\hat{a}_{2L}\hat{a}_{1R}\rangle = \langle \hat{I}_{1R}\rangle\langle \hat{I}_{2L}\rangle = \frac{p_R}{1-p_R}\frac{p_L}{1-p_L} \tag{A.21}
$$

$$
\langle \hat{a}_{1L}^{\dagger}\hat{a}_{2R}^{\dagger}\hat{a}_{2R}\hat{a}_{1L}\rangle = \frac{p_L}{1-p_L}\frac{p_R}{1-p_R} \tag{A.22}
$$

Case (3) $A=B=C=D$

$$
\langle \hat{a}_{1L}^{\dagger}\hat{a}_{2L}^{\dagger}\hat{a}_{2L}\hat{a}_{1L}\rangle = \langle \hat{I}_{1L}\hat{I}_{2L}\rangle = \frac{p_L + p_L^2}{(1-p_L)^2} \tag{A.23}
$$

$$
\langle \hat{a}_{1R}^{\dagger}\hat{a}_{2R}^{\dagger}\hat{a}_{2R}\hat{a}_{1R}\rangle = \langle \hat{I}_{1R}\hat{I}_{2R}\rangle = \frac{p_R + p_R^2}{(1-p_R)^2} \tag{A.24}
$$

Combining these terms, we get (omitting ξ from now on):

$$\langle : \hat{I}_{1+}\hat{I}_{2-} : \rangle$$

$$= -e^{-i(\phi_1+\phi_2)}\sqrt{t_1 r_2 t_2 r_1}\langle \hat{a}^\dagger_{1R}\hat{a}^\dagger_{2R}\hat{a}_{2L}\hat{a}_{1L}\rangle - e^{i(\phi_1+\phi_2)}\sqrt{r_1 t_2 r_2 t_1}\langle \hat{a}^\dagger_{1L}\hat{a}^\dagger_{2L}\hat{a}_{2R}\hat{a}_{1R}\rangle$$

$$+ \sqrt{t_1 t_2 t_2 t_1}\langle \hat{a}^\dagger_{1R}\hat{a}^\dagger_{2L}\hat{a}_{2L}\hat{a}_{1R}\rangle + \sqrt{r_1 r_2 r_2 r_1}\langle \hat{a}^\dagger_{1L}\hat{a}^\dagger_{2R}\hat{a}_{2R}\hat{a}_{1L}\rangle$$

$$+ \sqrt{r_1 t_2 t_2 r_1}\langle \hat{a}^\dagger_{1L}\hat{a}^\dagger_{2L}\hat{a}_{2L}\hat{a}_{1L}\rangle + \sqrt{t_1 r_2 r_2 t_1}\langle \hat{a}^\dagger_{1R}\hat{a}^\dagger_{2R}\hat{a}_{2R}\hat{a}_{1R}\rangle$$

$$= \sqrt{r_1 t_2 r_2 t_1}\left[-e^{-i(\phi_1+\phi_2)}\frac{\sqrt{p_L}}{1-p_L}\frac{\sqrt{p_R}}{1-p_R} - e^{i(\phi_1+\phi_2)}\frac{\sqrt{p_L}}{1-p_L}\frac{\sqrt{p_R}}{1-p_R}\right]$$

$$+ (t_1 t_2 + r_1 r_2)\frac{p_R}{1-p_R}\frac{p_L}{1-p_L} + r_1 t_2\frac{p_L + p_L^2}{(1-p_L)^2} + t_1 r_2\frac{p_R + p_R^2}{(1-p_R)^2}$$

$$= -2\sqrt{r_1 t_2 r_2 t_1}\cos(\phi_1+\phi_2)\frac{\sqrt{p_L}}{1-p_L}\frac{\sqrt{p_R}}{1-p_R}$$

$$+ (t_1 t_2 + r_1 r_2)\frac{p_R}{1-p_R}\frac{p_L}{1-p_L} + r_1 t_2\frac{p_L + p_L^2}{(1-p_L)^2} + t_1 r_2\frac{p_R + p_R^2}{(1-p_R)^2} \tag{A.25}$$

Consider the simplest case when $p_L = p_R = p$, and $r_1 = t_1 = r_2 = t_2 = 1/2$. We have

$$\langle : \hat{I}_{1+}\hat{I}_{2-} : \rangle$$

$$= -\frac{1}{2}\cos(\phi_1+\phi_2)\frac{\sqrt{p}}{1-p}\frac{\sqrt{p}}{1-p} + \frac{1}{2}\frac{p}{1-p}\frac{p}{1-p} + \frac{1}{2}\frac{p+p^2}{(1-p)^2}$$

$$= \frac{p}{2(1-p)^2}\left[1 + 2p - \cos(\phi_1+\phi_2)\right]. \tag{A.26}$$

The visibility of the fringe

$$V \equiv \frac{Max - min}{Max + min} = \frac{(2+2p) - 2p}{(2+2p) + 2p} = \frac{1}{1+2p}. \tag{A.27}$$

From Eq. (A.12), $p = 1/(\tilde{g}_{1,2} - 1)$. We can get a relation between V and $\tilde{g}_{1,2}$:

$$V = \frac{1}{1 + \frac{2}{\tilde{g}_{1,2}-1}} = \frac{\tilde{g}_{1,2} - 1}{\tilde{g}_{1,2} + 1}. \tag{A.28}$$

A.4   Incorporating noise

Follow the standard quantum optics approach and model the noise as coherent states combined with the ideal state with beam splitters. Assuming that the noise in field 1 (2) is caused by a noise field 3 (4) in a coherent state $|\alpha_3\rangle$ ($|\alpha_4\rangle$), the state of the fields can be written as

$$|\psi_0\rangle_{1,2,3,4} = |\Phi_{1,2}\rangle|\alpha_3\rangle|\alpha_4\rangle. \tag{A.29}$$

All the quantities given in Sec. A.2 and A.3 can then be calculated in the same fashion taking the state in Eq. (A.29) as the initial state for the fields.

Appendix B

General Introduction to Feedback Control in Quantum Optics

B.1   Introduction

In experimental quantum optics, one often needs to counter the effect of external disturbance and stabilize certain physical quantities. The standard procedure begins with obtaining an "error signal" which is proportional to the deviation between the physical quantity of interest and its desired value. According to the error signal, one then controls the "actuators" which tune the physical quantity. With properly tailored "transfer function" (frequency response) of the control system, we can minimize the deviation. In this Appendix, the standard procedure will be described in more detail with the examples of daily applications including locking the frequency of a diode laser and the relative phase between two laser beams.

B.2 Deriving the error signal

B.2.1 Introduction to error signal

Given a physical quantity X of a system that needs to be kept at X_0, we will first need an indicator of how far X is from X_0. In most cases, a voltage signal V as a function of X will suffice for this purpose. Around the value X_0, the function $V(X)$ can be expanded in terms of the deviation $X - X_0$:

$$V(X) = V(X_0) + V'(X_0)(X - X_0) + \frac{1}{2!}V''(X_0)(X - X_0)^2 + ... \quad \text{(B.1)}$$

At the region close to X_0, $V(X)$ is linear in $X - X_0$:

$$V(X) - V(X_0) \approx V'(X_0)(X - X_0) \quad \text{(B.2)}$$

which is just saying that the change in V is linearly proportional to that in X. Within that region, we can apply the linear control theory to the system. Intuitively, simply invert the sign of $V(X) - V(X_0)$ and feed that signal back to the actuator controlling X, we can keep X at X_0. However, more sophisticated processing is necessary for desired results. We will see that the transfer function of the feedback loop has to be optimized in order to avoid oscillation and minimize residual fluctuation.

B.2.2 Taking the derivative

In many cases, it is easier to get a signal $A(X)$ that has a extreme (maximum or minimum) at X_0, that is, $A'(X_0) = 0$. In that case, a modulation based technique can derive the derivative of $A(X)$, which is linear around X_0. In more detail, suppose that we can sinusoidally modulate the quantity X with angular frequency ω_{mod}; we get the signal

$$A(X + \delta X cos(\omega_{mod}t)) \approx A(X) + A'(X)\delta X cos(\omega_{mod}t) \qquad \text{(B.3)}$$

to the lowest order in the small modulation amplitude δX. We then obtain the derivative by measuring the amplitude of the cosine term. This can be done by multiplying the modulated signal with a signal (local oscillator or LO) oscillating at the same frequency as the modulation source, followed by proper filtering. The LO can be expressed as $LO(t) = A_{LO}cos(\omega_{mod}t + \phi)$ since the amplitude A_{LO} and phase ϕ uniquely characterize a sinusoidal wave with frequency ω_{mod}. Using the identity

$$cos(\alpha)cos(\beta) = \frac{1}{2}(cos(\alpha + \beta) + cos(\alpha - \beta)), \qquad \text{(B.4)}$$

the product becomes

$$A(X)A_{LO}cos(\omega_{mod}t + \phi) + A'(X)\delta X A_{LO}\frac{1}{2}\left[cos(2\omega_{mod}t + \phi) + cos(\phi)\right] \qquad \text{(B.5)}$$

Original function
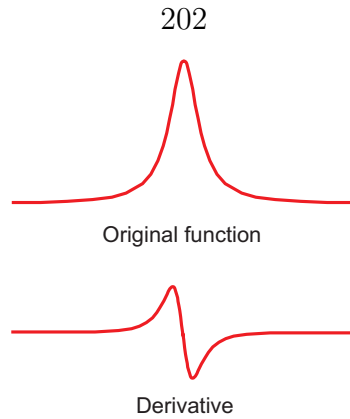
Derivative

Figure B.1: Taking the derivative of a function

Using a low pass filter, we can extract the third term and obtain

$$V(X) = \frac{1}{2}A'(X)\delta X A_{LO}cos(\phi) \propto A'(X). \tag{B.6}$$

Since $A(X)$ has an extreme at X_0, $A'(X_0) = 0$, $V(X) \propto X - X_0$ at the region near X_0.

B.2.3   Practical consideration

A usual mistake in designing a servo is that the error signal can be excessively filtered. The error signal should reflect the status of the system with high fidelity. So care has to be taken when one tries to filter the applied modulation. The modulation needs to be much higher than the desired bandwidth of the error signal so that one can easily remove it without attenuating or phase-shifting frequency components within the bandwidth. If the modulation has to be low, one can consider using a notch filter to attenuate the monochromatic modulation. The notch filter would have to be carefully designed so that the notch frequency coincides with the modulation and the attenuation region does not extend into the frequency range of interest.

B.3 Tailoring servo transfer function

Getting the error signal, we then want to characterize the response of the system to external perturbation and design a suitable feedback mechanism to control the system. First we need to have some basic idea about control theory.

B.3.1 Basic control theory

The response X of a linear system to an external drive Y is dominated by a linear differential equation

$$\left[a_n \frac{d^n}{dt^n} + a_{n-1} \frac{d^{n-1}}{dt^{n-1}} + ... + a_1 \frac{d}{dt} + a_0 \right] X(t) = Y(t). \tag{B.7}$$

Taking a Laplace transform and assuming $X(t) = 0$ for $t < 0$, we have

$$\left[a_n s^n + a_{n-1} s^{n-1} + ... + a_1 s + a_0 \right] \tilde{X}(s) = \tilde{Y}(s). \tag{B.8}$$

Solving for $\tilde{X}(s)$,

$$\begin{aligned} \tilde{X}(s) &= \frac{1}{\left[a_n s^n + a_{n-1} s^{n-1} + ... + a_1 s + a_0 \right]} \tilde{Y}(s) \\ &\equiv T(s)\tilde{Y}(s). \end{aligned} \tag{B.9}$$

Thus the transfer function $T(s)$ carries the information on the governing equation of the system.

In the context of control theory, people use block diagrams to denote the setup.
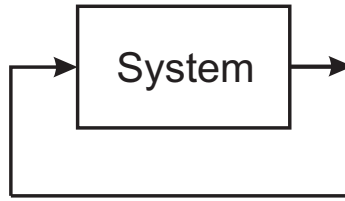
Figure B.2: Block diagram of a system driven by its response.

In a block diagram a system is denoted with a box. The drive and response can be "delivered" using arrows. Fig. B.2 shows a system driven by its response.

The simplest control is done by picking off the output of the system, checking it against the desired value, and feeding the difference back to the input (Fig. B.3). We can derive the effective transfer function from input to output with feedback through some simple algebra:

$$\tilde{X} = T(\tilde{Y} - \tilde{X})$$

$$\Rightarrow \quad \tilde{X} = \frac{T}{1+T}\tilde{Y}. \tag{B.10}$$

Eq. (B.10) elucidates some interesting properties of the system with feedback. First, in the frequency range where $|T| \gg 1$, $\tilde{X} \approx \tilde{Y}$, the output closely follows the input. So if we can somehow modify the transfer function so that its magnitude is much larger than unity in the desired frequency range, the system can be easily controlled. Second, if at some frequency $1 + T \rightarrow 0$, the magnitude of the effective transfer function tends to infinity. This means that the system is unstable. Even when the input is absent, we can still get finite output. In this case, the system tends to oscillate at the frequency satisfying $1 + T \rightarrow 0$.

Unfortunately, this simple scheme cannot counter the effect of noise directly af-
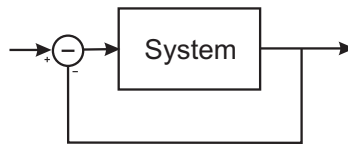
Figure B.3: The simplest feedback scheme.
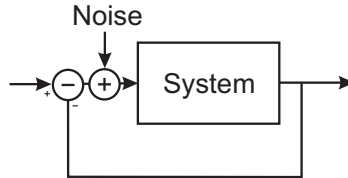
Figure B.4: The way to include noise.

fecting the system. Fig. B.4 includes the noise affecting the system. The transfer function for the noise is just T. If we simply modify T to get $|T| \gg 1$, the noise will also be amplified.

This is where servo comes in. Fig. B.5 shows the block diagram with servo. The effective transfer function for the input is

$$T_S = \frac{ST}{1 + ST},$$
(B.11)

and that for the noise is

$$T_N = \frac{T}{1 + ST}.$$
(B.12)

Thus we can include a servo whose transfer function S gives $|S| \gg 1$ in the frequency range of interest and make $T_s \approx 1$ and $T_N \to 0$, so that the output follows the input and the effect of the noise is minimized.
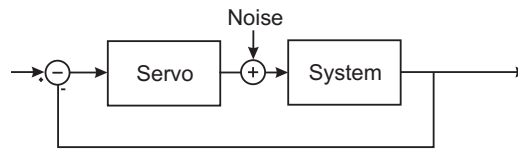
Figure B.5: Feedback with servo.

B.3.2 Characterizing system transfer function

Driving a linear system with a sine wave, the response will be a sine wave with phase shift (delay) and modified magnitude. The transfer function is a complex function of frequency whose magnitude and argument stand for the magnification in amplitude and phase shift, respectively, of the system response. Since a time-varying input to the system can be decomposed into frequency components, the transfer function fully characterizes how a system would react to any input.

To measure the transfer function of a system, intuitively we can drive the system with a sine wave, compare the output to the input, and measure the amplitude magnification/attenuation and phase delay while varying the frequency of the sine wave. This can be quite tedious without the help of automated equipment. A computer controlled lock-in amplifier can handle the task. Fortunately, in our group we have a SR780 network analyzer which has a built-in function for measuring transfer functions.

Note that the system has to be kept in the linear range when measuring its transfer function. Specifically, the value of the parameter to be controlled needs to stay within the range where the error signal is linear with the deviation. For stable systems, slow drift out of the linear range can be countered by hand. For systems seriously perturbed by the environment, a preliminary servo can be installed first to hold the system to a

limited parameter space. The preliminary servo is usually a low-pass filter with large

(100 to 1000) gain at DC and low 3 dB frequency (below 300 Hz) to counter the slow

drift.

In our experiments, the system is usually some sort of optics, either a mirror or a

grating, driven by a piezo-electric transducer (PZT). We can model the system as a

mass on a spring, thus a second order system. The transfer function (from the input

voltage of the PZT driver to the output voltage of a position sensor, usually that of

a photo-detector) has the general form

$$T_S(s) = \frac{b}{a_2 s^2 + a_1 s + a_0} \tag{B.13}$$

People plot the magnitude and phase of a transfer function with log-log and lin-log

scales, respectively, and call the resultant diagram "Bode plot." Fig. B.6 shows a

typical Bode plot of a second order system. The magnitude is basically flat from DC

all the way up to near the resonance frequency, where it peaks. At frequencies higher

than the resonance, the magnitude rolls off at a slope of around 40dB/decade, since

at high frequency, $T_S \propto 1/s^2$. The phase starts at $0°$ at DC, quickly rolls down across

the resonance, crossing $-90°$ at the resonance frequency, and reaches $-180°$ at high

frequencies.

B.3.3 Designing servo transfer function

With the transfer function of the system at hand, we can design a servo to drive the

system so that the output follows the input and the effect of noise is minimized. A
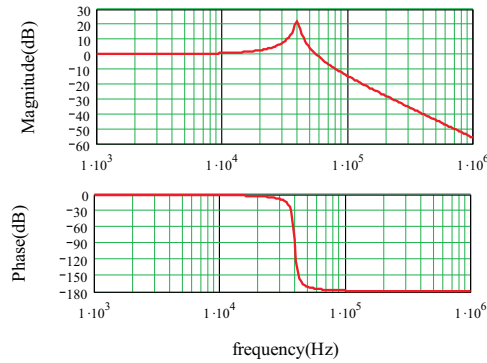
Figure B.6: Bode plot of a typical second-order system.

few guidelines are as follows:

1. **The magnitude at DC should be as high as possible,** so that the DC error (Out − In at DC) is minimized. Thus the servo should behave like an integrator with magnitude approaching infinity at DC. Practically, the DC magnitude is limited by the open loop gain of the Op Amp in the servo circuit.

2. **Avoid oscillation and instability.** The open loop transfer function is now the product of that of the system and that of the servo, i.e., ST, instead of T in the absence of a servo. For the feedback loop to be stable and free of oscillation, ST can not be too close to -1 (refer to Eq. (B.10) and the following paragraph). One way to take this into account is to check on the Bode plot that the magnitude of ST is not 0 dB where its phase is close to 180 degree.

3. **Get high closed-loop bandwidth.** Closed-loop bandwidth is a benchmark of how fast the feedback loop can respond to the input. Noise within the closed-loop bandwidth can be reduced by the servo. The closed-loop bandwidth is roughly determined by the "unity gain point" of the open-loop transfer function

(the frequency at which the magnitude reaches unity). The bandwidth of the loop needs to be wide enough to counter the whole spectrum of external noise.

The most common actuator we deal with is a PZT. In practice, the lowest resonance frequency is often the upper limit of the useful bandwidth of a PZT. One can see many resonances above the lowest resonance frequency and the phase changes erratically. Thus when designing a servo, one is usually forced to set the unity gain frequency below that resonance. The lowest resonance frequency inversely depends on the square root of the mass loading the PZT, so a key to increase the bandwidth is to use small optics. When dealing with a PZT, which can be approximated by a second order system for frequencies below the lowest resonance, a servo would need to pull the resonance peak below 0 dB to avoid oscillation. The reason is that near resonance the system phase rapidly sweeps from 0 to 180 degree and the magnitude rolls off really fast. A servo unavoidably introduces extra phase shift and it is very likely that around the resonance the feedback loop will become unstable. An integrator makes a modest servo. However, the height of the resonance puts a limit on the bandwidth. In order to pull the resonance peak below 0 dB, the unity gain frequency, f_{unity} would have to satisfy

$$f_{unity} = \frac{f_{res}}{h_{res}} \ , \tag{B.14}$$

where f_{res} is the resonance frequency and h_{res} is the maximal magnitude, or the height of the resonance. To increase f_{unity} without causing instability, we will need to reduce the height of the resonance. One way is to insert a notch filter that cancels the resonance and introduce acceptable amount of phase delay. Fig. B.7(a) shows

(a)

(b)
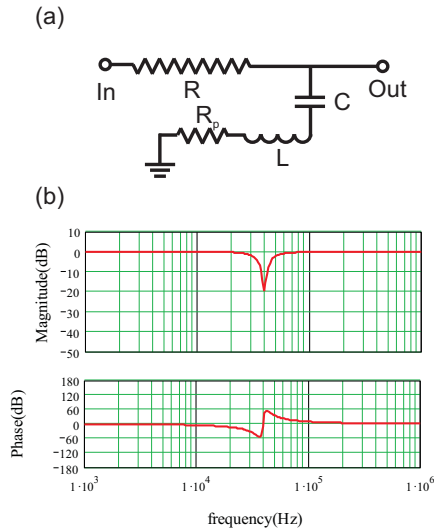
Figure B.7: (a) Circuit diagram (b) Bode plot of a notch filter.

the circuit diagram of a notch filter, and (b) is the Bode plot. R_p is the parasitic resistance in the inductor. The ratio R_p/R determines the depth of the notch. R_p also controls the width of the dip. A notch filter also introduces extra phase delay so one would have to make compromises between resonance height and phase delay. With the help of a notch filter, we can push the unity gain point closer to the resonance frequency.

Sometimes the system has too much phase delay at the desired unity gain frequency that we can not afford the 90-degree phase shift introduced by a simple integrator. In that case, a servo with transfer function show in Fig. B.8 could be handy. However, it has the drawback that it can not pull down much the resonance peak, so a notch filter is usually a necessity.

The mount holding the PZT has to be firm and massive, otherwise one can see a resonance at lower frequency corresponding to the case that a spring with both ends free. Sometimes additional weight has to be attached to the mount to eliminate the
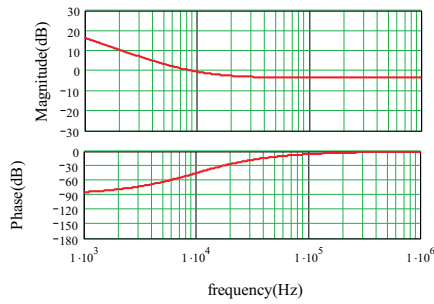
Figure B.8: The transfer function of a servo introducing less phase delay than a simple integrator.

two-body resonance.

B.4   Implementing the design

With a design of the servo transfer function, we need to implement it as a circuit. The impedance models for basic circuit elements such as resistors, capacitors, and inductors are very useful. Fig. B.9 lists the symbols and impedances of the elements. Combined with the fact that the transfer function of the circuit shown in Fig. B.10 is $-Z_2/Z_1$, we can implement most of the transfer functions.

A useful tip: design the servo with two modes, acquire and lock, which correspond to a low-pass filter and an integrator at DC, respectively. The reason is that although an integrator can eliminate DC error, it also requires a small deviation from the lock point to begin with. If the deviation is so large that the system is not in the linear range of the error signal and the negative feedback does not work, turning on the integrator would immediately bring the voltage output of the servo to the rails (upper or lower limit of the output voltage), disabling the servo. Using the servo first in acquire mode enables the feedback at high frequencies with higher tolerance
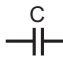
Symbol   Impedance

R

R

L

sL

C

$1/sC$

Figure B.9: Impedance of the basic circuit elements.

$V_{out}/V_{in}=-Z_2/Z_1$

Z_2

V_{in} Z_1 − V_{out}

+
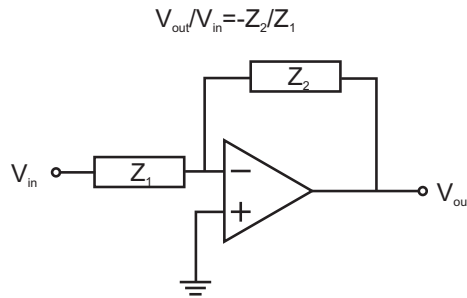
Figure B.10: The circuit that can implement most of the transfer functions.

on the initial deviation. Thus one can tune the system offset and the system would be "sucked" into the linear range. One can then switch to the lock mode and the residual DC error is eliminated.

B.5   Characterizing the performance

With the feedback loop set up, we need to check if it is up to specification. The first thing to check is if the system can be locked. The error signal should be fuzzy around zero. The fuzziness shows how well the system is locked. Ideally the error signal should be a flat line on the oscilloscope with thickness limited only by the electronic noise of the loop deriving the error signal. The RMS value of the error signal can be converted to that of the controlled parameter to estimate the in-loop residual errors. To completely characterize the quality of the lock, we will need to perform measurements independent of the feedback loop. For example, one way to

check the residual frequency noise of a locked laser is to beat two lasers locked in the same way. From the beat note one can then calculate the RMS frequency excursions of the lasers.

B.6 Real-world applications

B.6.1 Locking the frequency of a diode laser with an error signal derived from saturation spectroscopy

In our labs, the most visited servo is the one locking the frequency of diode lasers. It is straightforward to get a saturation spectroscopy trace (Fig. B.11(a)). However, we usually want to exploit the narrow feature of the little dimples, so we need a signal which is linear near the regions around the little peaks. The derivative of the trace can be derived by slightly modulating the current driving the diode, the frequency of the laser is in turn modulated. We then multiply the signal from the detector with a signal in phase with the modulating signal using a RF mixer. The output of the mixer is then passed through a low pass filter to extract only the low frequency components, which is proportional to the derivative of the original trace (Fig. B.11(b)). Selecting the modulation frequency can be tricky. Usually it is chosen to tune the relative phase between the LO and the modulation to zero, i.e., ϕ in Eq. (B.5), optimizing the magnitude of the derived signal. But it cannot be too close to the bandwidth of the servo, usually around 10 kHz, otherwise the low pass filter would introduce extra attenuation to the error signal in the frequency range of interest.
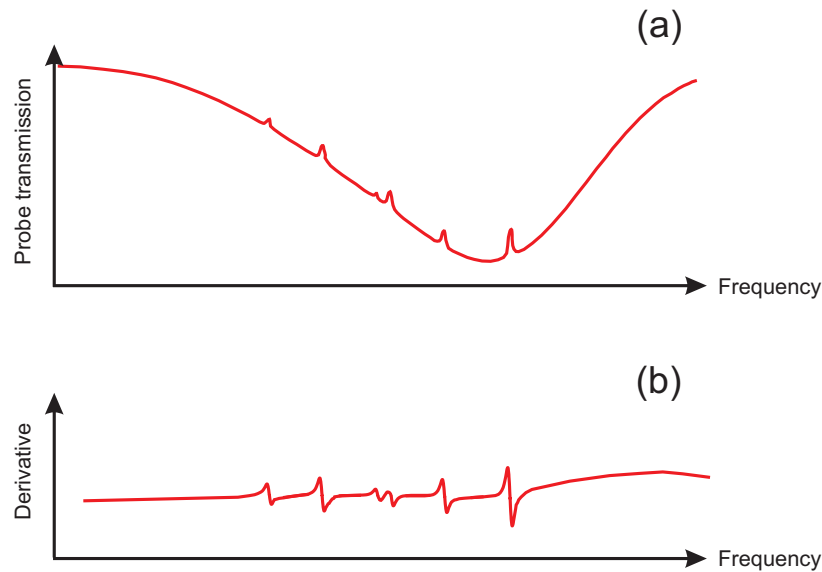
Figure B.11: Saturation spectroscopy of cesium D_2 line. (a) Transmission of the probe beam versus the frequency, (b) The derivative of the curve in (a), which can be used as the error signal for the frequency servo of the laser.

Due to the noise characteristics of an external cavity diode laser, the frequency servo needs to handle a noise spectrum with about 1 MHz bandwidth. We have two ways of adjusting the laser frequency. One is through tilting the feedback grating. This approach usually leads to a 3 dB bandwidth < 10 kHz for an applied modulation. The other way is by varying the diode current, which directly affects the frequency of the laser. Frequency modulation through modulating the diode current can achieve > 1 MHz bandwidth. It is generally not a good idea to control the frequency of a diode laser merely through modulating the current, because the laser diode is vulnerable to large abrupt current variation and the output power is also dependent on the diode current. Two branches of servos are commonly used together. One is an integrator driving the PZT with low unity gain point to roughly keep the laser frequency around the desired value, removing the DC error. The residual high-frequency excursion is canceled by the other servo branch controlling the diode current. This high-frequency

branch is usually a high pass filter whose gain rolls off at around 1 MHz. In practice, engaging the feedback to the PZT alone can achieve moderate frequency lock after finding the proper sign and gain for the servo. The proper sign of the current feedback can then be easily found. The transfer function, in particular, gain and corner frequencies, of the current feedback loop need to be further optimized for the best result.

B.6.2   Locking the relative phase between two laser beams

In experiments on quantum optics, one often needs to fix the relative phase of two laser beams. For example, to measure one particular quadrature amplitude of a beam with a homodyne detector, the phase of the local oscillator beam needs to be locked at a certain value relative to the signal beam. The two beams in question are usually combined on a beam splitter. The interference fringes at the outputs are natural candidates for the error signal. Power fluctuation of the beams can introduce discrepancies in the error signal since the variation cannot be easily attributed to power or phase fluctuation. As described in Sec. 7.5.3.2, to alleviate the effect of power fluctuation, one can exploit the difference of the beam splitter outputs as the error signal.

The common way to adjust the relative phase between two laser beams is through changing the path length for one of the beam by moving a mirror with a PZT. With a 1/2 inch mirror, one would need to add extra weight on the other end of the PZT, i.e., the mirror mount, to get rid of resonances at few kHz regime associated with

the vibration mode of a PZT with two free ends. Such setting can usually push the lowest resonance to >20 kHz. If the resonance is too sharp, it will put a upper bound on the bandwidth of the feedback loop. In that case, a notch filter can be designed to cancel the resonance with minor reduction in the phase margin.

Appendix C

Electronic Gates for Photon Counting Experiments

C.1 Introduction

The single-photon counting modules (SPCM) we used in the experiments put out TTL pulses when they register photons, with the rising edges of the pulses corresponding to the instants of detection. In the experiments, the signals of interest usually occur within some well-defined period. Any TTL pulses coming at the time other than the period are considered noise. An electronic gate that passes the TTL pulses if their rising edges are within the period for signals but blocks them otherwise is very useful in the experiments. In order to avoid complicated NIM modules, a senior graduate student, (Dr.) David Boozer came up with a simple circuit with the function described above. This Appendix serves as a detailed document on the circuit.
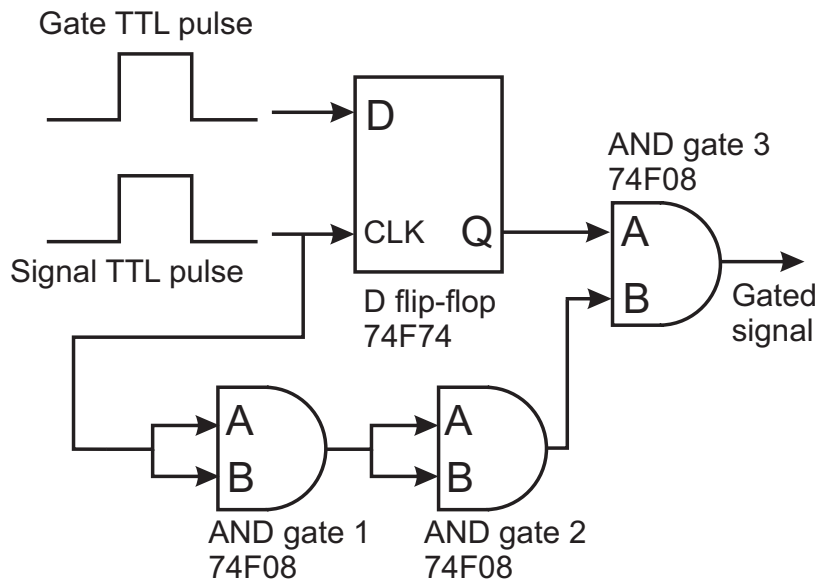
Figure C.1: The circuit diagram of the electronic gate.

C.2 Description of the circuit

The circuit consists of two kinds of logic elements. The D flip-flop relays the status (high or low) of the D port to Q port whenever the CLK (clock) port receives a rising edge. The AND gates perform the logic AND function on the two input ports, A and B. When the rising edge of the signal TTL pulses happen within the gate TTL pulse, the Q port of the D flip-flop will be high. AND gates 1 and 2 have their two inputs tied together and work as buffers to introduce propagation delay. This is to compensate the propagation delay within the D flip-flop. The delayed copies of the signal TTL pulses are ANDed by AND gate 3 with the Q port of the D flip-flop, which is high only if the signal rising edges are within the gate pulse. Thus the output will be delayed copies of the signal pulses or stay low depending on whether the rising edges are within the gate window or not.

Appendix D

The List Files and the Programs Processing Them

D.1   Introduction

Within the acquisition card (p7888) we use in the experiments, there is a really useful feature. The card allow us to keep in a list file the records of all the arrival times of the input pulses which are converted from the detected photons in the single photon counting modules (SPCM). The list files are usually referred to as click files (for recording the detection "clicks"). A click file itself does not provide us with much information. Only after proper processing, we can extract useful information such as the singles rate, g_{12}, $g^{(2)}$, etc. In this appendix, the structure of a list file recording the arrival times of all the photo-electric detection events. The programs which compress and extract the detection probabilities of interest are also described.

D.2 The structure of a list file

The beginning of a list file is a header showing the setting of the acquisition card at the time the list file is taken. After "[Start of Data]" is a long list of numbers. The numbers stand for 5 possible events: 1 start signal triggering the clock of the card, and stops from the 4 input channels of the card that prompt the card to register the clock readings. We can tell which event a number stands for by looking at its format. If the list file is recorded in the ASCII format, the number -1073741824 $(= (-1)^1 2^{30}$, referred to as "Start" in the programs) stands for a start event. In binary form, "Start" is experssed as 11000...0 (31 bits) with the first bit indicating the sign. The "Start event generation" box in the p7888 is usually checked so the card writes a -1073741824 into the list file whenever its start channel receives a pulse. With the start events, we know how far in time events are from one another. That is how we track the time. The other forms of numbers correspond to stops registered by the 4 channels. The correspondence can be found in Table D.1.

Table D.1: The correspondence between a recorded number, the channel recording the stop, and the actual arrival time in the list files.

Number	Channel	Arrival time
> 0 and $\leq$ length of trial	1	Number
$> -$Start and $\leq$ length of trial$-$Start	2	Number$-$Start
$<$-2000000000	3	Number+2147483648
$>$ Start and $\leq$ length of trial+Start	4	Number+Start

In binary form, the correspondence is simpler, as show in Table D.2. The recorded numbers are actually encoded in binary form with the first two bits indicating the channels registered the start and the rest of the bits storing the arrival time. Thus

Table D.2: The correspondence between a recorded number in binary form, the channels recording the stop, and the actual arrival times in the list file. Not(Start) is the bitwise-flipped version of Start.

First two bits of Number in binary form	Channel	Arrival time
00	1	Number & Not(Start)
01	2	Number & Not(Start)
10	3	Number & Not(Start)
11	4	Number & Not(Start)

the operation "Number & Not(Start)" just sets the first two bits of Number to zero and the result is the time of arrival.

D.3 The compression program

Due to the low excitation probability in the experiments, almost all the numbers in a click file are Starts. The Starts are written as clock ticks to keep track of elapsed time. We just need to know how many Starts are between Stops to get the time separation between them. To reduce the size of a click file and facilitate later processing, sequences of Starts separated by Stops can be substituted with the total numbers of Starts, keeping all information. For a common click file, this program can achieve about 99% compression.

A compression program in MATLAB using the correspondence in Table D.1 is as follows:

```
%This program reads one small portion of the list file at a time,
%save the compressed version to a buffer (compressed_data), and write
```

```
%to the compressed file every time the read portion is processed.

%The process is repeated until the whole file is reached

%(feof(fid_data)!=0)

%tic; %This can be unremarked along with a toc at the end

%to benchmark the speed of the processing

fid_data = fopen('FILE_IN.lst');

%Open the list file with ' ' specifying the filename

fid_target = fopen('FILE_C.lst','w');

%Open a file with ' ' specifying the filename to store the compressed version

while (fscanf(fid_data,'%c',1)==']')==0

%skip the header which ends with ']'

end

read_length=50000;

%Specify the number of data points the program reads at a time

data=zeros(1,read_length);

%Initialize the buffer for the data

data_temp=0;

%Initialize the variable temporarily storing the data point processed

%at the time

compressed_data=zeros(1,read_length);

%Initialize the buffer for the compressed data

Start=-1073741824;

%A data point with value -1073741824 marks a start
```

```
Length_of_trial=1500;

%Specify the trial period in unit of bin size (1 or 2 ns)

same_trial=0;

%Initialize the indicator showing whether the data point under processing

%is within the same trial as the former one

%(whether there is a start between them)

N_start=0;

%Initialize the counter for the number of starts between stops

Total_start=0;

%Initialize the counter for the total nubmer of starts

N1=0;

%Initailize the counters Ni for stops in detector i, i={1,2,3,4}

N2=0;

N3=0;

N4=0;

while feof(fid_data)==0

    %Keep looping before reaching the end of file

    data=fscanf(fid_data,'%i',read_length);

    %Read from the file a sequence of data points with "read_length"

    %of them, and store them in the buffer "data"

    Data_size=size(data);

    %Find out how many points were actually read, the last sequence

    %might not have exacly "read_length" of points.
```

```
n=1;

%Reset the index for the loops

i=1;

%Reset the index for the compressed data buffer

while  n <= Data_size(1)

    %Loop until the last point

data_temp=data(n);

%Store the n-th data into "data_temp"

if (data_temp == Start & same_trial == 0)

    %The number is a start and the number before it is also a start

    %(same_trial==0)

        N_start=N_start+1;

        %Add 1 to number of start, "N_start", between stops

        Total_start=Total_start+1;

        %Add 1 to the total number of starts, "Total_start"

elseif (data_temp == Start & same_trial ==1)

    %The number is a start and the number before it is not a start

    %(same_trial==1)

        Total_start=Total_start+1;

        %Add 1 to the total number of starts, "Total_start"

        N_start=1;

        %Reset N_start to 1 (the start at hand)

        same_trial = 0;
```

```
        %Not in the same trial any more

elseif data_temp ~= Start & same_trial == 0

    %The number is not a start and the number before it is a start

    %(same_trial==0)

        same_trial=1;

        %Now we are in a trial

        compressed_data(i)=N_start+2000000000;

        %All the starts before this stop and the stop before it can be

        %replaced by their total number. N_start is augmented by

        %2000000000 to identify it.

        compressed_data(i+1)=data_temp;

        %The stop is recorded without modification

        i=i+2;

        %Add two to the index for the compressed data buffer

        if  data_temp > 0 & data_temp <= Length_of_trial

            %Stop from detector 1?

            N1=N1+1;

        end

        if  data_temp + Start > 0 & data_temp + Start <= Length_of_trial

            %Stop from detector 2?

            N2=N2+1;

        end

        if  data_temp - Start > 0 & data_temp - Start <= Length_of_trial
```

```matlab
            %Stop from detector 3?

            N3=N3+1;

        end

        if  data_temp < -2000000000

            %Stop from detector 4?

            N4=N4+1;

        end

    elseif data_temp ~= Start & same_trial == 1

        %The number is not a start and the number before it is not a start

        %either(same_trial==1)

        compressed_data(i)=data_temp;

        i=i+1;

        if  data_temp > 0 & data_temp <= Length_of_trial

            %Stop from detector 1?

            N1=N1+1;

        end

        if  data_temp + Start > 0 & data_temp + Start <= Length_of_trial

            %Stop from detector 2?

            N2=N2+1;

        end

        if  data_temp - Start > 0 & data_temp - Start <= Length_of_trial

            %Stop from detector 3?

            N3=N3+1;
```

```
        end

        if  data_temp < -2000000000

            %Stop from detector 4?

            N4=N4+1;

        end

    end

    n=n+1;

end

    i=1;

    while compressed_data(i)~=0

        %Not 0 means altered

            fprintf(fid_target,'%-10.10g \n',compressed_data(i));

            %Keep writing the number from the buffer to the file

            %for the compressed data

            i=i+1;

    end

    compressed_data=zeros(1,read_length);

    %Reset the buffer for the compressed data

end

if same_trial==0

    %The list file ends with a start?

    fprintf(fid_target,'%-10.10g \n',N_start+2000000000);

    %Most of the time the list file does not end with a stop, and thus the
```

```
    %last starts are not recorded. This line remedies that.

end

fclose(fid_data);

%Close the files

fclose(fid_target);

Total_start

%The outputs of the program: Total_start: total number of trials

N1

%Number of stops from each detector. These can be checked against the

%histograms recorded by the card for consistency.

N2

N3

N4

Total_start+N1+N2+N3+N4

%This should yield the total number of data points in the list file for

%consistency check

%toc

%For benchmarking the processing time
```

A compression program in C composed by Daniel Felinto using the correspondence in Table D.2 and exploiting the binary operations is much simpler:

```
#include <stdio.h>

#include <stdlib.h>
```

```c
#include <math.h>

#include <time.h>



#define    start        -1073741824



long int    ch[4] = {0,1073741824,-2147483648,-1073741824};

%ch is a indicator for the channels. In binary form, the first two bits of

%the numbers are {00, 01, 10, 11}, with the first bit setting the sign.
void        detection(int p);

FILE        *arq2;



int main()
{
    long int    p1;

    int         c2;

    FILE        *arq1;


    arq1=fopen("FILE_IN.lst","r");

    %Read numbers from FILE_IN.lst

    arq2=fopen("FILE_C.lst","w");

    %Write to the compressed file FILE_C.lst

    while(getc(arq1) != ']');

    %Skip the header
```

```
fscanf(arq1,"%d",&p1);

%Read a number and store it in the buffer p1

while(!feof(arq1)){

%Keep looping until the end of file

    if(p1 == start){

   %If the number is a Start

          c2=0;

      %Reset the counter for consecutive Starts

            while(p1 == start && !feof(arq1)){

                %Keep looping if the number is a Start

                    ++c2;

                    %Count the number of Starts in a row.

                    fscanf(arq1,"%d",&p1);

            }

            fprintf(arq2,"%d\t%d\n",0,c2);

%At the last consecutive %Start, write to the file the channel number

%'0' and the number of Starts

            if(!feof(arq1)) detection(p1);



    }

    else  detection(p1);

  %If the number is not a Start and the end of file is not
```

```
    %reached, find out in which channel the number is recorded

     %by calling the subroutine "detection"

        fscanf(arq1,"%d",&p1);

     }



     fclose(arq1);

     fclose(arq2);



     printf("%u",clock()/CLOCKS_PER_SEC);

     return 0;

}



void detection(int p)

%This subroutine determines the channel registering the number

{

     int    c2,c3;



     c2 = c3 = 0;

     %Initialize the indicator c2 for if the channel has been found

     %and the index c3 for the channel search

     while(c2==0){

         %If the channel is still undetermined

          if((p & start) == ch[c3]){
```

```
%Check the first two bits of p to match that of the channels

        fprintf(arq2,"%d\t%d\n",c3+1,p & ~start);

%If match, c3+1 is the channel and "p & ~start" will set the first

%two bits of p to 0 and yield the time of arrival.

        c2=1; %The channel has been determined.

 }

 else  ++c3;  %Otherwise, try next channel.

}
}
```

D.4   The analyzing program

After compression, the click files are ready for analysis. One of the most useful information is the detection probability. The detection probability can be extracted from the click file by counting the numbers of occurrence for each event. For example, the joint detection probability for two detectors is obtained by first counting the number of the trials with two numbers each corresponding to the detection event in one detector. The total number of occurrences is then divided by the total number of trials in the experment, and converted to the detection probability. One way to implement the task of counting the number that each event shows up is to look for the trials in which something happens. In the compressed files, this is simple since the trials in which nothing happens are all collapsed to numbers keeping only the number of trials between two stop events. Specifically, it is done with a counter/indicator

variable "Same_trial," which stands for the total number of Stop events in one trial, and can be at most 6 in the cases where six detectors are used. We consider the SPCM as non-photon-number resolving. Even if more than one stop is registered by one SPCM within the same trial and they are separated by an interval longer than the dead time ($\approx$50 ns), the second click is ignored. This is done to simplify the problems involving afterpulsing, which refers to the falsely triggered avalanche process in the SPCM and the resultant electrical pulse after an avalanche process is induced by a photon. The numbers of occurrence of each event are stored in the buffer variable, Event(n_1,n_2,n_3,n_4,n_5,n_6), in which $n_m \in \{0, 1\}$ denote the number n of clicks recorded at detector m in the same trial. From this outcome, various quantities such as numbers of coincidences and $h_c^{(2)}$ can be obtained.

```
%For files compressed by compressfile.m

%Software gates set by the variable "Gate"

%6-detector configuration to get entanglement

%field 2s are combined on a BS, and the outputs are split with BSs,

%Detector assignment: 1->1a Ch_4, 2->1b Ch_1, 3->2a Ch_3, 4->2b Ch_3, 5->2c

%Ch_2,6->2d Ch_2

fid_data=fopen('FILE_C.lst','r');

%Open the compressed file

tic;

[a, b]=fscanf(fid_data,'%f',inf);

%Read the whole file into the vetor a, the number of point is read to b
```

b

%Output the total number of data points, can be checked against the output

%of the compressfile program

same_trial=0;

%Reset indicators and counters

Total_start=0;

Start_aug = 2000000000;

%The augment to start used in the compressfile program

Start=-1073741824;

%The number correspond to a Start

Length_of_trial=1500;

%Length of trial in the program, in unit of bin size

%Detector assignment: Det 1->1a Ch_4, Det 2->1b Ch_1, Det 3->2a Ch_3, Det

%4->2b Ch_3, Det 5->2c Ch_2, Det 6->2d Ch_2.

%The stops from D2a and D2b (D2c and D2d) are combined into Ch_3 (Ch_4)

%with an OR gate. D2b (D2c) has an extra long cable at its output to add

%~250 ns delay to distinguish its stops from those of D2a (D2d).

Gate=[298 410;292 404; 776 891; 907 1021; 909 1024; 788 904];

%The start and end time points of the gate windows for each detector.

%unit: bin size. Need to be read off from the histogram recorded by

%the card.

Single=[0 0 0 0 0 0];

%Buffer for the number of stops in each detector within one trial.

```
Single_event=[0 0 0 0 0 0];

%Buffer for the number of events in each detector within one trial.

%At most one in each detector.

click=[0 0 0 0 0 0];

%index for clicks in the same trial, can be [2 1 0 0],

%[1 0 0 0], [3 1 2 0], etc.

exist=[0 0 0 0 0 0];

%indicate if a click from each channel exists in the same trial under test,

%e.g., [1 0 0 1 1 0] means a click is registered in D1, D4, and D5

Double=zeros(6); %12 13 14 23 24 34

After_pulsing=[0 0 0 0 0 0];

%The number of extra (>1) clicks in each detector in the trial

TArr=[0 0 0 0 0 0];

%Time of arrival for each click in the trial

Ch3_beginning=-2147483648;

%We need to substract this number from the stops in Ch3 to get the actual

%time of arrival from the beginning of the trial

length_a=length(a);

%The length of the file


%%%%%%%%%%%%%%%%%%%%%%%%%%%%%%%%%%%%%%%%%%%%%%

%Need to be changed

Gate_T0=[298 292 776 907 909 788];
```

```
%The beginning of each gate window


%%%%%%%%%%%%%%%%%%%%%%%%%%%%%%%%%%%%%%%%%%%%


T_offset=[0 0 0 0 0 0];

%The detectors looking at one field might need extra time offset to

%compensate the different electronic and cable delay

% tau_W=0;

% tau_R=0;

%Indices for the detectors

D1a=1; D1b=2; D2a=3; D2b=4; D2c=5; D2d=6;

ed=0; %Index for the entangling detector

%%%%%%%%%%%%%%%%%%%%%%%%%%%%%%%%%%%%%%%

%Initiate counters

Event=zeros(2,2,2,2,2,2);

%%%%%%%%%%%%%%%%%%%%%%%%%%%%%%%%%%%%%%%%%%%

index_a=1;

data_temp=0;

while index_a <= length_a

    data_temp=a(index_a);

   if (data_temp > Start_aug & same_trial == 0)

       %data_temp > Start_aug means this data point is a "Start"

       %same_trial == 0 means since the last stop, no stop is encountered
```

```
        Total_start=Total_start+data_temp-Start_aug;

    elseif (data_temp > Start_aug & same_trial >=1)

        Total_start=Total_start+data_temp-Start_aug;

        %For unconditioned statistics********************************

        Event(exist(1)+1,exist(2)+1,exist(3)+1,

        exist(4)+1,exist(5)+1,exist(6)+1)

        =Event(exist(1)+1,exist(2)+1,exist(3)+1,

        exist(4)+1,exist(5)+1,exist(6)+1)+1;

        %Event(1,2,1,1,2,1) gives the number of trials in which D2 and D5

        %click

        %End unconditioned statistics********************************


        same_trial = 0;        %reset the counter and buffers

        exist=[0 0 0 0 0 0];

        click=[0 0 0 0 0 0];

    elseif (data_temp < Start_aug & same_trial == 0)

        %This point is a Stop and the one before it is a Start.

        same_trial = 1;

%Detector assignment: Det 1->1a Ch_4, Det 2->1b Ch_1, Det 3->2a Ch_3,

%Det 4->2b Ch_3, Det 5->2c Ch_2, Det 6->2d Ch_2

            if  data_temp - Start > 0 & data_temp - Start <= Length_of_trial

    & data_temp - Start > Gate(1,1) & data_temp - Start < Gate(1,2) %Ch 4

                Single(1)=Single(1)+1;
```

```
    TArr(1)=data_temp - Start;

     exist(1)=1;

     click(1)=1;

  end

  if  data_temp > 0 & data_temp <= Length_of_trial

      & data_temp > Gate(2,1) & data_temp < Gate(2,2) %Ch 1

     Single(2)=Single(2)+1;

      exist(2)=1;

      click(1)=2;

  end

  if  data_temp < -2000000000

      & data_temp - Ch3_beginning > Gate(3,1)

      & data_temp - Ch3_beginning < Gate(3,2) %Ch 3

     Single(3)=Single(3)+1;

      exist(3)=1;

      click(1)=3;

  end

  if  data_temp < -2000000000

      & data_temp - Ch3_beginning > Gate(4,1)

      & data_temp - Ch3_beginning < Gate(4,2) %Ch 3

     Single(4)=Single(4)+1;

      exist(4)=1;

      click(1)=4;
```

```
        end

        if  data_temp + Start > 0 & data_temp + Start <= Length_of_trial

            & data_temp + Start > Gate(5,1)

            & data_temp + Start < Gate(5,2) %Ch 2

            Single(5)=Single(5)+1;

             exist(5)=1;

             click(1)=5;

        end

        if  data_temp + Start > 0

            & data_temp + Start <= Length_of_trial

            & data_temp + Start > Gate(6,1)

            & data_temp + Start < Gate(6,2) %Ch 2

            Single(6)=Single(6)+1;

             exist(6)=1;

             click(1)=6;

          end


 elseif (data_temp < Start_aug & same_trial >= 1)

%This point is a Stop and the one before it is also a Stop.

        same_trial=same_trial+1;

%Detector assignment: Det 1->1a Ch_4, Det 2->1b Ch_1, Det 3->2a Ch_3,

%Det 4->2b Ch_3, Det 5->2c Ch_2, Det 6->2d Ch_2

          if  data_temp - Start > 0 & data_temp - Start <= Length_of_trial
```

```
        & data_temp - Start > Gate(1,1)

        & data_temp - Start < Gate(1,2) %Ch 4

        Single(1)=Single(1)+1;

         if exist(1) == 1

             After_pulsing(1)=After_pulsing(1)+1;

%The second stop from one channel is considered an afterpulsing

         else

             exist(1)=1;

     %Indicates that a stop from detector 1 exists in this trial

             click(sum(exist))=1;

             %The sum(exist)'th stop is from detector 1

         end

    end

    if  data_temp > 0 & data_temp <= Length_of_trial

        & data_temp > Gate(2,1) & data_temp < Gate(2,2) %Ch 1

        Single(2)=Single(2)+1;

         if exist(2) == 1

             After_pulsing(2)=After_pulsing(2)+1;

         else

             exist(2)=1;

             click(sum(exist))=2;

         end

    end
```

```matlab
if  data_temp < -2000000000

    & data_temp - Ch3_beginning > Gate(3,1)

    & data_temp - Ch3_beginning < Gate(3,2) %Ch 3

    Single(3)=Single(3)+1;


     if exist(3) == 1

         After_pulsing(3)=After_pulsing(3)+1;

     else

         exist(3)=1;

         click(sum(exist))=3;

     end

end

if  data_temp < -2000000000

    & data_temp - Ch3_beginning > Gate(4,1)

    & data_temp - Ch3_beginning < Gate(4,2) %Ch 3

    Single(4)=Single(4)+1;

    if exist(4) == 1

         After_pulsing(4)=After_pulsing(4)+1;

     else

         exist(4)=1;

         click(sum(exist))=4;

         TArr(sum(exist))=data_temp - Ch3_beginning;

     end
```

```
end

if  data_temp + Start > 0

    & data_temp + Start <= Length_of_trial

    & data_temp + Start > Gate(5,1)

    & data_temp + Start < Gate(5,2) %Ch 2

    Single(5)=Single(5)+1;


     if exist(5) == 1

         After_pulsing(5)=After_pulsing(5)+1;

      else

         exist(5)=1;

         click(sum(exist))=5;

         TArr(sum(exist))=data_temp + Start;

      end

end

if  data_temp + Start > 0

    & data_temp + Start <= Length_of_trial

    & data_temp + Start > Gate(6,1)

    & data_temp + Start < Gate(6,2) %Ch 2

    Single(6)=Single(6)+1;

    if exist(6) == 1

         After_pulsing(6)=After_pulsing(6)+1;

      else
```

```
                exist(6)=1;

                click(sum(exist))=6;

          end

       end

   end

   index_a=index_a+1;

end

fclose(fid_data);

Total_start

After_pulsing
```

Appendix E

The LabView Program Reading the Phase of the Interferometer

E.1 Introduction

In the experiment in Chapter 7, we used a LabView program to convert the interferometer error signals to the phase variation for the interferometers. This appendix documents the details of the program.

E.2 Description of the front panel

Fig. E.1 shows the front panel of the program. Before we start an experiment measuring fringes by locking the interferometer at various phases, we need to scan the phase of the interferometer, examine the two error signals, difference and derivative, adjust the offsets to near zero, and mark the maxima and minima of the two signals. The "Sign" switch stands for the sign of the difference signal, and the "Invert" switch corresponds to whether the derivative signal is inverted or not. We usually start with the "Sign" switch flipped up and the "Invert" off, which corresponds to the first, that
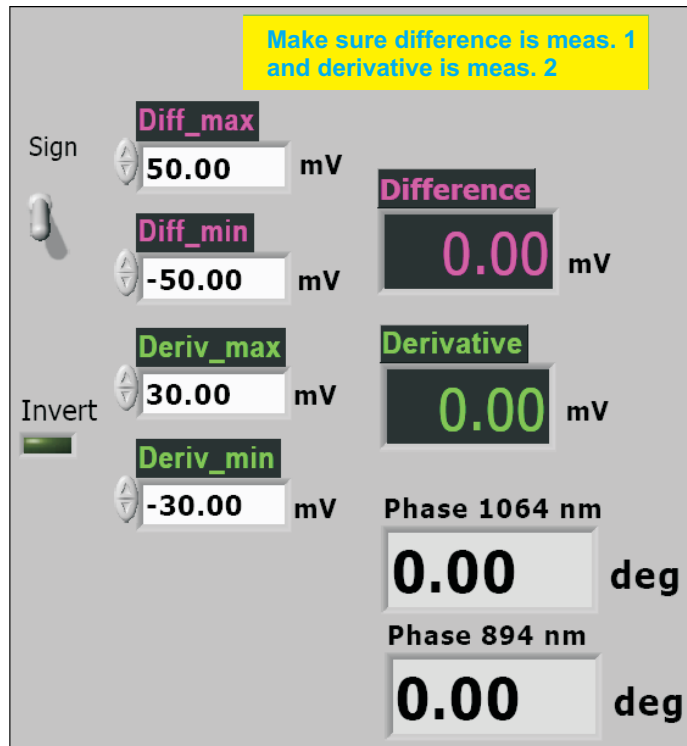
Figure E.1: The front panel of the program reading the phase of the interferometer.

is, 0° to 90°, interval in Fig. 7.7. When we invert the error signals, we also modify the
"Sign" and "Invert" switch so that the program knows which segments on the fringe
the interferometer is locked.

E.3   Description of the program diagram

Fig. E.2 shows the diagram for the program. When executed, the program keeps
looping. The sequence loop reads the values of the difference and derivative signals
from the oscilloscope. The "Sign" and "Invert" determine if the values needs to be
multiplied by −1 before they are relayed to the "MATLAB Script." The "MATLAB
Script" first determines if the values are out of the ranges permitted by the predeter-
mined maxima and minima, and replaces them with the values of proper extremes.

The phase of the interferometer is then calculated by taking the appropriate arcsine (phase1) or arccosine (phase2) values. The two quantities, phase1 and phase2, can then be converted to be on the same segment of the fringe. Ideally, after this conversion, phase1 and phase2 will yield the same number. In practice, the signal closer to be a maximum or minimum, that is, further from zero, is less sensitive to the phase of the interferometer, thus at the end of the "MATLAB Script," we choose the value from the signal that is closer to zero. Specifically, if after the conversion phase1 is closer to $0°$ ($360°$) or $180°$, we choose phase1 to be the estimate for the phase of the interferometer. Otherwise, phase2 is chosen.
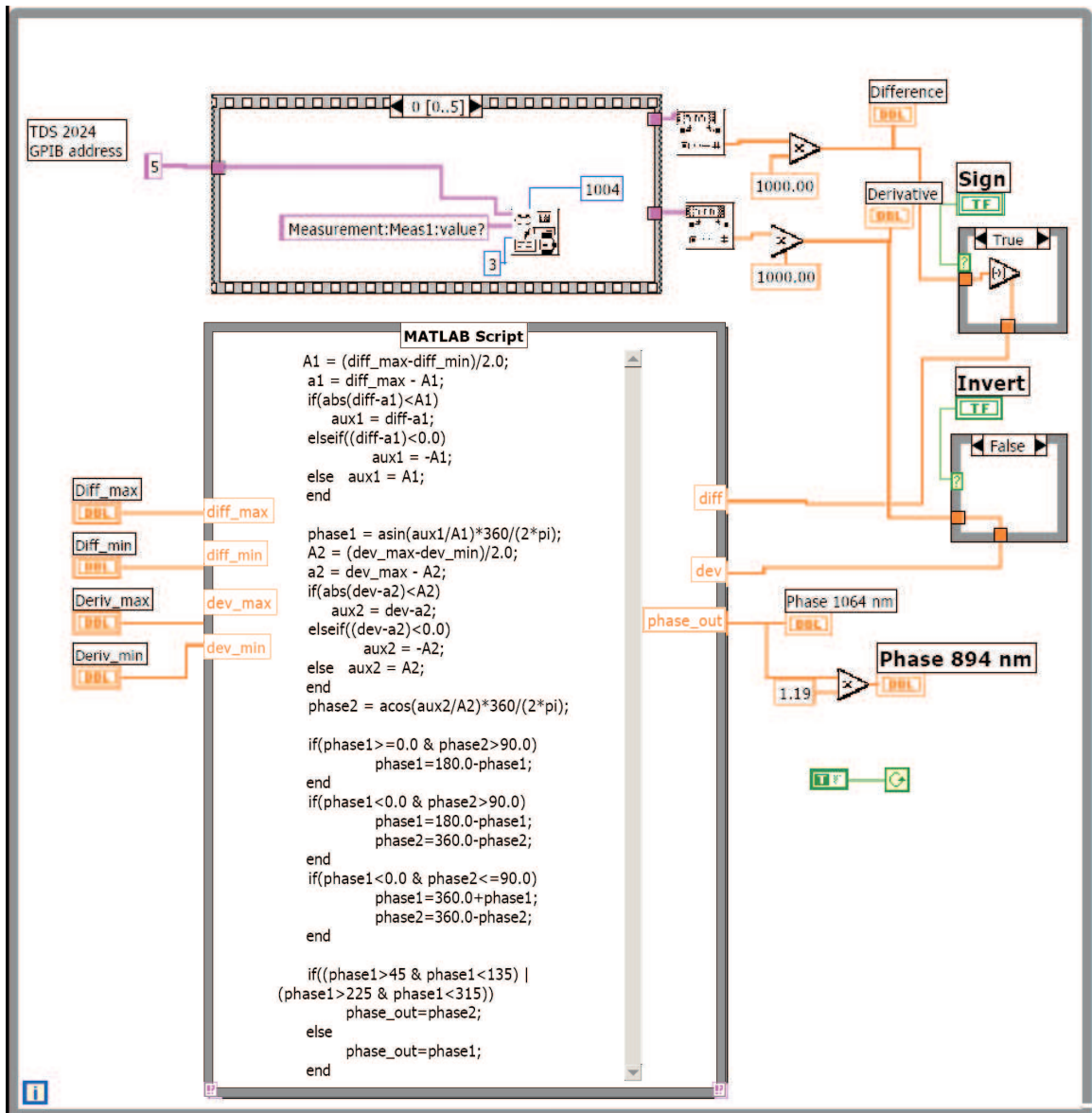
Figure E.2: The diagram of the program reading the phase of the interferometer.

Bibliography

[1] D. Bouwmeester, A. Ekert, and A. Zeilinger, editors. *The Physics of Quantum Information.* Springer-Verlag, Berlin, Germany, 2001.

[2] I. Marcikic, H. de Riedmatten, W. Tittel, H. Zbinden, M. Legré, and N. Gisin. Distribution of time-bin entangled qubits over 50 km of optical fiber. *Phys. Rev. Lett.*, 93:180502, 2004.

[3] See the website of the companies *MagiQ* (www.magiqtech.com) and *id Quantique* (www.idquantique.com).

[4] N. Gisin, G. Ribordy, W. Tittel, and H. Zbinden. Quantum cryptography. *Rev. Mod. Phys.*, 74:145, 2002.

[5] C. Gobby, Z.L. Yuan, and A.J. Shields. Quantum key distribution over 122 km of standard telecom fiber. *Appl. Phys. Lett.*, 84:3762, 2004.

[6] K. J. Resch, M. Lindenthal, B. Blauensteiner, H. R. Bhm, A. Fedrizzi, C. Kurtsiefer, A. Poppe, T. Schmitt-Manderbach, M. Taraba, R. Ursin, P. Walther, H. Weier, H. Weinfurter, and A. Zeilinger. Distributing entanglement and single photons through an intra-city, free-space quantum channel. *Opt. Exp.*, 13:202, 2005.

[7] C.-Z. Peng, T. Yang, X.-H. Bao, J.-Zhang, X.-M. Jin, F.-Y. Feng, B. Yang, J. Yang, J. Yin, Q. Zhang, N. Li, B.-L. Tian, and J.-W. Pan. Experimental free-space distribution of entangled photon pairs over 13 km: Towards satellite-based global quantum communication. *Phys. Rev. Lett.*, 94:150501, 2005.

[8] B. C. Jacobs and J. D. Franson. Quantum cryptography in free space. *Opt. Lett.*, 21:1854, 1996.

[9] C. Kurtsiefer, P. Zarda, M. Halder, H. Weinfurter, P. M. Gorman, P.R. Tapster, and J. G. Rarity. A step towards global key distribution. *Nature*, 419:450, 2002.

[10] G. Brassard, N. Lütkenhaus, T. Mor, and B.C. Sanders. Limitations on practical quantum cryptography. *Phys. Rev. Lett.*, 85:1330, 2000.

[11] W. K. Wootters and W. H. Zurek. A single quantum cannot be cloned. *Nature*, 299:802, 1982.

[12] C. H. Bennett, G. Brassard, S. Popescu, B. Schumacher, J. A. Smolin, and W. K. Wootters. Purification of noisy entanglement and faithful teleportation via noisy channels. *Phys. Rev. Lett.*, 76:722, 1996.

[13] D. Deutsch, A. Ekert, R. Jozsa, C. Macchiavello, S. Popescu, and A. Sanpera. Quantum privacy amplification and the security of quantum cryptography over noisy channels. *Phys. Rev. Lett.*, 77:2818, 1996.

[14] H.-J. Briegel, W. Dür, J. I. Cirac, and P. Zoller. Quantum repeaters: The role of imperfect local operations in quantum communication. *Phys. Rev. Lett.*, 81:5932, 1998.

[15] W. Dür, H.-J. Briegel, J.I. Cirac, and P. Zoller. Quantum repeaters based on entanglement purification. *Phys. Rev. A*, 59:169, 1999.

[16] C. H. Bennett, G. Brassard, C. Crépeau, R. Jozsa, A. Peres, and W. K. Wootters. Teleporting an unknown quantum state via dual classical and Einstein-Podolsky-Rosen channels. *Phys. Rev. Lett.*, 70:1895, 1993.

[17] M. Zukowski, A. Zeilinger, M. A. Horne, and A. K. Ekert. Event-ready-detectors Bell experiment via entanglement swapping. *Phys. Rev. Lett.*, 71:4287, 1993.

[18] P. Berman, editor. *Cavity Quantum Electrodynamics*. Academic Press, San Diego, 1994.

[19] H. Mabuchi and A. C. Doherty. Cavity quantum electrodynamics: Coherence in context. *Science*, 298:1372, 2002.

[20] J. I. Cirac, P. Zoller, H. J. Kimble, and H. Mabuchi. Quantum state transfer and entanglement distribution among distant nodes in a quantum network. *Phys. Rev. Lett.*, 78:3221, 1997.

[21] S. J. van Enk, J. I. Cirac, and P. Zoller. Photonic channels for quantum communication. *Science*, 279:205, 1998.

[22] L.-M. Duan, M. D. Lukin, J. I. Cirac, and P. Zoller. Long-distance quantum communication with atomic ensembles and linear optics. *Nature*, 414:413, 2001.

[23] L.-M. Duan, J. I. Cirac, and P. Zoller. Three-dimensional theory for interaction between atomic ensembles and free-space light. *Phys. Rev. A*, 66:023818, 2002.

[24] M. Fleischhauer and M. D. Lukin. Dark-state polaritons in electromagnetically induced transparency. *Phys. Rev. Lett.*, 84:5094–5097, 2000.

[25] M. D. Lukin. Colloquium: Trapping and manipulating photon states in atomic ensembles. *Rev. Mod. Phys.*, 75:457, 2003.

[26] A. André. *Nonclassical states of light and atomic ensembles: generation and new applications.* PhD thesis, Harvard University, 2005.

[27] V. Balic, D. A. Braje, P. Kolchin, G. Y. Yin, and S. E. Harris. Generation of paired photons with controllable waveforms. *Phys. Rev. Lett.*, 94:183601, 2005.

[28] D. N. Matsukevich, T. Chanelière, M. Bhattacharya, S.-Y. Lan, S. D. Jenkins, T. A. B. Kennedy, and A. Kuzmich. Entanglement of a photon and a collective atomic excitation. *Phys. Rev. Lett.*, 95:040405, 2005.

[29] D. A. Braje, V. Balić, S. Goda, G. Y. Yin, and S. E. Harris. Frequency mixing using electromagnetically induced transparency in cold atoms. *Phys. Rev. Lett.*, 93:183601, 2004.

[30] L. Mandel and E. Wolf. *Optical Coherence and Quantum Optics.* Cambridge Univ. Press, Cambridge, UK, 1995.

[31] B. C. Jacobs, T. B. Pittman, and J. D. Franson. Quantum relays and noise suppression using linear optics. *Phys. Rev. A*, 66:052307, 2002.

[32] D. N. Matsukevich and A. Kuzmich. Quantum state transfer between matter and light. *Science*, 306:663, 2004.

[33] J. F. Clauser. Experimental distinction between quantum and classical field-theoretic predictions for photoelectric effect. *Phys. Rev. D*, 9:853, 1974.

[34] H. J. Metcalf and P. van der Straten. *Laser Cooling and Trapping.* Springer-Verlag, Berlin, 1999.

[35] M. Kitagawa and M. Ueda. Nonlinear-interferometric generation of number-phase correlated fermion states. *Phys. Rev. Lett.*, 67:1852–1854, 1991.

[36] D. J. Wineland, J. J. Bollinger, W. M. Itano, and F. L. Moore. Spin squeezing and reduced quantum noise in spectroscopy. *Phys. Rev. A*, 46:R6797–R6800, 1992.

[37] A. Kuzmich, K. Mølmer, and E. S. Polzik. Spin squeezing in an ensemble of atoms illuminated with squeezed light. *Phys. Rev. Lett.*, 79:4782, 1997.

[38] A. Kuzmich, N. P. Bigelow, and L. Mandel. Atomic quantum non-demolition measurements and squeezing. *Europhys. Lett.*, 42:481–486, 1998.

[39] K. Mølmer. Twin-correlations in atoms. *Eur. Phys. J. D*, 5:301–305, 1999.

[40] J. Hald, J. L. Sørensen, C. Schori, and E. S. Polzik. Spin squeezed atoms: a macroscopic entangled ensemble created by light. *Phys. Rev. Lett.*, 83:1319–1322, 1999.

[41] A. Kuzmich, L. Mandel, and N. P. Bigelow. Generation of spin squeezing via continuous quantum nondemolition measurement. *Phys. Rev. Lett.*, 85:1594–1597, 2000.

[42] B. Julsgaard, A. Kozhekin, and E. S. Polzik. Experimental long-lived entanglement of two macroscopic objects. *Nature*, 413:400–403, 2001.

[43] A. Kuzmich, W. P. Bowen, A. D. Boozer, A. Boca, C. W. Chou, L.-M. Duan, and H. J. Kimble. Generation of nonclassical photon pairs for scalable quantum communication with atomic ensembles. *Nature*, 423:731, 2003.

[44] E. B. Alexandrov, M. V. Balabas, A. S. Pasgalev, A. K. Verkhovskii, and N. N. Yakobson. Double-resonance atomic magnetometers: From gas discharge to laser pumping. *Laser Physics*, 6:244–251, 1996.

[45] Supplementary Information accompanying Ref. [43] at http://www.nature.com/nature/journal/v423/n6941/suppinfo/nature01714.html.

[46] C. Schori, B. Julsgaard, J. L. Sørensen, and E. S. Polzik. Recording quantum properties of light in a long-lived atomic spin state: Towards quantum memory. *Phys. Rev. Lett.*, 89:057903–1–057903–4, 2002.

[47] M. Pelton, C. Santori, J. Vuckovic, B. Zhang, G. S. Solomon, J. Plant, and Y. Yamamoto. Efficient source of single photons: A single quantum dot in a micropost microcavity. *Phys. Rev. Lett.*, 89:233602, 2002.

[48] E. Knill, R. Laflamme, and G. J. Milburn. A scheme for efficient quantum computation with linear optics. *Nature*, 409:46–52, 2001.

[49] I. L. Chuang and Y. Yamamoto. Simple quantum computer. *Phys. Rev. A*, 52:3489, 1995.

[50] Q. A. Turchette, C. J. Hood, W. Lange, H. Mabuchi, and H. J. Kimble. Measurement of conditional phase shifts for quantum logic. *Phys. Rev. Lett.*, 75:4710–4713, 1995.

[51] N. Lutkenhaus. Security against individual attacks for realistic quantum key distribution. *Phys. Rev. A*, 61:052304, 2000.

[52] D. Bouwmeester, A. Ekert, and A. Zeilinger, editors. *The Physics of Quantum Information*, chapter 6.2 and 8.6. Springer-Verlag, Berlin, Germany, 2001.

[53] L.-M. Duan and H. J. Kimble. Scalable photonic quantum computation through cavity-assisted interaction. *Phys. Rev. Lett.*, 92:127902, 2004.

[54] P. Michler, A. Kiraz, C. Becher, W. V. Schoenfeld, P. M. Petroff, Lidong Zhang, E. Hu, and A. Imamoglu. A quantum dot single-photon turnstile device. *Science*, 290:2282, 2000.

[55] E. Moreau, I. Robert, J. M. Gérard, I. Abram, L. Manin, and V. Thierry-Mieg. Single-mode solid-state single photon source based on isolated quantum dots in pillar microcavities. *Appl. Phys. Lett.*, 79:2865, 2001.

[56] J. McKeever, A. Boca, A. D. Boozer, R. Miller, J. R. Buck, A. Kuzmich, and H. J. Kimble. Deterministic generation of single photons from one atom trapped in a cavity. *Science*, 303:1992, 2004.

[57] P. Grangier, G. Roger, and A. Aspect. Experimental-evidence for a photon anti-correlation effect on a beam splitter—a new light on single-photon interferences. *Europhys. Lett.*, 1:173, 1986.

[58] C. K. Hong and L. Mandel. Experimental realization of a localized one-photon state. *Phys. Rev. Lett.*, 56:58, 1986.

[59] A. I. Lvovsky, H. Hansen, T. Aichele, O. Benson, J. Mlynek, and S. Schiller. Quantum state reconstruction of the single-photon Fock state. *Phys. Rev. Lett.*, 87:050402, 2001.

[60] T. B. Pittman, B. C. Jacobs, and J. D. Franson. Single photons on pseudodemand from stored parametric down-conversion. *Phys. Rev. A*, 66:042303, 2002.

[61] J. B. Altepeter, D. Branning, E. Jeffrey, T. C. Wei, P. G. Kwiat, R. T. Thew, J. L. O'Brien, M. A. Nielsen, and A. G. White. Ancilla-assisted quantum process tomography. *Phys. Rev. Lett.*, 90:193601, 2003.

[62] A. B. U'Ren, C. Silberhorn, K. Banaszek, and I. A. Walmsley. Efficient conditional preparation of high-fidelity single photon states for fiber-optic quantum networks. *Phys. Rev. Lett.*, 93:093601, 2004.

[63] B. Julsgaard, Schori C, J. L. Sorensen, and E. S. Polzik. Atomic spins as a storage medium for quantum fluctuations of light. *Q. Inf. and Computation*, 3:518, 2003.

[64] C. W. Chou, S. V. Polyakov, A. Kuzmich, and H. J. Kimble. Single-photon generation from stored excitation in an atomic ensemble. *Phys. Rev. Lett.*, 92:213601, 2004.

[65] W. Jiang, C. Han, P. Xue, L.-M. Duan, and G.-C. Guo. Nonclassical photon pairs generated from a room-temperature atomic ensemble. *Phys. Rev. A*, 69:043819, 2004.

[66] C. H. van der Wal, M. D. Eisaman, A. André, R. L. Walsworth, D. F. Phillips, A. S. Zibrov, and M. D. Lukin. Atomic memory for correlated photon states. *Science*, 301:196, 2003.

[67] S. V. Polyakov, C. W. Chou, D. Felinto, and H. J. Kimble. Temporal dynamics of photon pairs generated by an atomic ensemble. *Phys. Rev. Lett.*, 93:263601, 2004.

[68] K. M. Gheri, K. Ellinger, T. Pellizzari, and P. Zoller. Photon-wavepackets as flying quantum bits. *Fortschr. Phys.*, 46:401, 1998.

[69] M. A. Nielsen and I. L. Chuang. *Quantum Computation and Quantum Information.* Cambridge University Press, Cambridge, United Kingdom, 2003.

[70] M. D. Eisaman, L. Childress, A. André, F. Massou, A. S. Zibrov, and M. D. Lukin. Shaping quantum pulses of light via coherent atomic memory. *Phys. Rev. Lett.*, 93:233602, 2004.

[71] M. A. Bouchiat and J. Brossel. Relaxation of optically pumped rb atoms on paraffin-coated walls. *Phys. Rev.*, 147:41, 1966.

[72] E. B. Alexandrov, M. V. Baladas, D. Budker, D. English, D. F. Kimball, C.-H. Li, and V.V. Yashchuk. Light-induced desorption of alkali-metal atoms from paraffin coating. *Phys. Rev. A*, 66:042903, 2002.

[73] B. Julsgaard, J. Sherson, J. I. Cirac, J. Fiurášek, and E. S. Polzik. Experimental demonstration of quantum memory for light. *Nature*, 432:482, 2004.

[74] B. Julsgaard, J. Sherson, J. L. Sorensen, and E. S. Polzik. Characterizing the spin state of an atomic ensemble using the magneto-optical resonance method. *J. Opt. B: Q. Semiclass. Opt.*, 6:5, 2004.

[75] S. Kuhr, W. Alt, D. Schrader, I. Dotsenko, Y. Miroshnychenko, W. Rosenfeld, M. Khudaverdyan, V. Gomer, A. Rauschenbeutel, and D. Meschede. Coherence properties and quantum state transportation in an optical conveyor belt. *Phys. Rev. Lett.*, 91:213002, 2003.

[76] M. F. Andersen, A. Kaplan, T. Grünzweig, and N. Davidson. Suppression of dephasing of optically trapped atoms. *Phys. Rev. A*, 70:013405, 2004.

[77] D. Felinto, C. W. Chou, H. de Riedmatten, S. V. Polyakov, and H. J. Kimble. Control of decoherence in the generation of photon pairs from atomic ensembles. *Phys. Rev. A*, 72:053909, 2005.

[78] S. van Enk, private communication.

[79] J. Ringot, P. Szriftgiser, and J. C. Garreau. Subrecoil Raman spectroscopy of cold cesium atoms. *Phys. Rev. A*, 65:013403, 2001.

[80] C. J. Dedman, K. G. H. Baldwin, and M. Colla. Fast switching of magnetic fields in a magneto-optic trap. *Rev. Sci. Instr.*, 72:4055, 2001.

[81] C. L. Garrido Alzar, D. Oblak P. G. Petrov, J. H. Müller, and E. S. Polzik. Compensation of eddy-current-induced magnetic field transients in a MOT. Submitted for publication.

[82] G. Avila, V. Giordano, V. Candelier, E. de Clercq, G. Theobald, and P. Cerez. State selection in a cesium beam by laser-diode optical-pumping. *Phys. Rev. A*, 36:3719, 1987.

[83] S.-I. Ohshima, Y. Nakadan, and Y. Koga. Development of an optically pumped cs frequency standard at the NRLM. *IEEE Trans. Instrum. Meas.*, 37:409, 1988.

[84] J. F. Clauser and A. Shimony. Bell's theorem: Experimental tests and implications. *Rep. Prog. Phys.*, 41:1881–1927, 1978.

[85] A. Aspect, J. Dalibard, and G. Roger. Experimental test of Bell's inequalities using time-varying analyzers. *Phys. Rev. Lett.*, 49:1804–1807, 1982.

[86] For a comprehensive overview of experimental progress, see *Quantum Information and Computation Roadmap*, http://qist.lanl.gov/qcomp_map.shtml.

[87] C. Langer, R. Ozeri, J. D. Jost, J. Chiaverini, B. DeMarco, A. Ben-Kish, R. B. Blakestad, J. Britton, D. B. Hume, W. M. Itano, D. Leibfried, R. Reichle, T. Rosenband, T. Schaetz, P. O. Schmidt, and D. J. Wineland. Long-lived qubit memory using atomic ions. *Phys. Rev. Lett.*, 95:060502, 2005.

[88] H. Haffner, F. Schmidt-Kaler, W. Hansel, C. F. Roos, T. Korber, M. Chwalla, M. Riebe, J. Benhelm, U. D. Rapol, C. Becher, and R. Blatt. Robust entanglement. *App. Phys. B*, 81:151–153, 2005.

[89] I. Marcikic, H. de Riedmatten, W. Tittel, H. Zbinden, Legré, M., and N. Gisin. Distribution of time-bin entangled qubits over 50 km of optical fiber. *Phys. Rev. Lett.*, 93:180502, 2004.

[90] Z. Y. Ou, S. F. Pereira, H. J. Kimble, and K.-C. Peng. Realization of the Einstein-Podolsky-Rosen paradox for continuous variables. *Phys. Rev. Lett.*, 68:3663–3666, 1992.

[91] Q. A. Turchette, C. S. Wood, B. E. King, C. J. Myatt, D. Leibfried, W. M. Itano, C. Monroe, and D. J. Wineland. Deterministic entanglement of two trapped ions. *Phys. Rev. Lett.*, 81:3631–3634, 1998.

[92] B. B. Blinov, D. L. Moehring, L.-M. Duan, and C. Monroe. Observation of entanglement between a single trapped atom and a single photon. *Nature*, 428:153–157, 2004.

[93] D. N. Matsukevich and A. Kuzmich. Quantum state transfer between matter and light. *Science*, 306:663–666, 2004.

[94] S. van Enk and H. J. Kimble. Comment on "Quantum state transfer between matter and light." *Science*, 309:1187b, 2005.

[95] D. N. Matsukevich and A. Kuzmich. Response to comment on "Quantum state transfer between matter and light." *Science*, 309:1187c, 2005.

[96] C. W. Chou, H. de Riedmatten, D. Felinto, S. V. Polyakov, S. J. van Enk, and H. J. Kimble. Measurement-induced entanglement for excitation stored in remote atomic ensembles. *Nature*, 438:828–832, 2005.

[97] C. H. Bennett, D. P. DiVincenzo, J. A. Smolin, and W. Wootters. Mixed-state entanglement and quantum error correction. *Phys. Rev. A*, 54:3824, 1996.

[98] W. K. Wootters. Entanglement of formation of an arbitrary state of two qubits. *Phys. Rev. Lett.*, 80:2245–2248, 1998.

[99] J.-W. Pan, S. Gasparoni, R. Ursin, G. Weihs, and A. Zeilinger. Experimental entanglement purification of arbitrary unknown states. *Nature*, 423:417–422, 2003.